ACHIEVING LITHIUM-ION CELLS WITH IMPROVED PERFORMANCE AND LIFETIME

By

Connor Aiken

Submitted in partial fulfilment of the requirements
for the degree of Doctor of Philosophy

at

Dalhousie University,
Halifax, Nova Scotia
September 2023

TABLE OF CONTENTS

LIST OF TABLES

LIST OF FIGURES

ABSTRACT

For commercial use, lithium-ion batteries must deliver sufficient calendar- and cycle-life. Increased lifetime can enable the adoption of advanced batteries with higher energy density or lower cost, compounded with the possibility of reducing levelized energy cost and waste. For cells with optimized electrode materials, electrode-electrolyte reactions are the predominant source of failure. Improvements to electrolyte formulation can help mitigate these reactions and extend cell lifetime. This can include the concentration and type of salt, solvent and electrolyte additive.

Understanding the role of the electrolyte salt, $LiPF_6$, additives and solvents, in high voltage operation of $Li[Ni_{0.5}Mn_{0.3}Co_{0.2}]O_2$ (NMC532)/graphite cells and high state of charge operation of $LiFePO_4$ (LFP)/graphite cells is discussed in the context of improving cell lifetime. When $LiPF_6$ is selected as an electrolyte salt, NMC cells and LFP cells achieve longer lifetime with higher and lower concentrations of $LiPF_6$, respectively. Additionally, the role of two salts, $LiPF_6$ and LiFSI, in unique, low voltage $Li[Ni_{0.5}Mn_{0.3}Co_{0.2}]O_2$/graphite cells is discussed, and unprecedented lifetime potential is demonstrated with the use of LiFSI.

LIST OF ABBREVIATION AND SYMBOLS USED

A	SEI thickness growth rate
Ah	Ampere hour
AWG	American wire gauge
B	Fitting constant for SEI growth models
BTS	Battery testing system
C	Linear capacity loss rate, unit of relative current
CCCV	Constant current, constant voltage
Cdl	Double layer capacitance
CE	Coulombic efficiency
CEI	Cathode electrolyte interphase
CIE	Coulombic Inefficiency
CQ	Constant capacity
CT	Computer tomography
CV	Constant voltage
D	Fitting constant for Sigmoidal SEI growth model
DEC	Diethyl carbonate
DFT	Density functional theory
DiFEC	Difluoro ethylene carbonate
DMC	Dimethyl carbonate
DTA	Differential thermal analysis
DTD	1,3,2-Dioxathiolane 2,2-dioxide
EA	Ethyl acetate
E_a	Activation energy
EC	Ethylene carbonate
EIS	Electrochemical impedance spectroscopy
EMC	Ethyl methyl carbonate

eV	Electron volt
FEC	Fluoroethylene carbonate
FTIR	Fourier transform infrared spectroscopy
g	Gram
h	Hour
HOMO	Highest occupied molecular orbital
I	Current
K	Electron energy level
k	Parabolic growth law rate constant
kB	Boltzmann's constant
kHz	Kilohertz
kPA	Kilopascal
kV	Kilovolt
L	Liter
LFO	Lithium difluoro phosphate
LFP	$LiFePO_4$
LiBOB	Lithium bis(oxalato) borate
LiDFDOP	Lithium difluoro di(oxalato) phosphate
LiFSI	Lithium bis(fluorosulfonyl)imide
LiTFOP	Lithium tetrafluoro oxalato phosphate
LiTFSI	Lithium bis(trifluoromethanesulfonyl)imide
LMP	$LiMnPO_4$
LUMO	Lowest unoccupied molecular orbital
M	Unspecified transition metal, moles per liter, electron energy level
m_-	Negative electrode active mass
m_+	Positive electrode active mass
MA	Methyl acetate

mAh	Milliampere hour
mBar	Millibar
mg/cm^2	Milligrams per square centimeter
mHz	Millihertz
mm	Millimeter
mV	Millivolt
NCA	Li[Ni$_{1-x-y}$Co$_x$Al$_y$]O$_2$
nm	Nanometer
NMC	Li[Ni$_{1-x-y}$Mn$_x$Co$_y$]O$_2$
NMC111	Li[Ni$_{1/3}$Mn$_{1/3}$Co$_{1/3}$]O$_2$
NMC442	Li[Ni$_{0.42}$Mn$_{0.42}$Co$_{0.16}$]O$_2$
NMC532	Li[Ni$_{0.5}$Mn$_{0.3}$Co$_{0.2}$]O$_2$
NMC622	Li[Ni$_{0.6}$Mn$_{0.2}$Co$_{0.2}$]O$_2$
NMC640	Li[Ni$_{0.6}$Mn$_{0.4}$]O$_2$
NMC811	Li[Ni$_{0.8}$Mn$_{0.1}$Co$_{0.1}$]O$_2$
NMR	Nuclear magnetic resonance spectroscopy
OC	Open circuit
ODTO	1,2,6-oxadithiane 2,2,6,6-tetraoxide
PC	Propylene carbonate
PES	1-propene-1,3-sultone
Q	Capacity
q$_-$	Negative electrode specific capacity
q$_+$	Positive electrode specific capacity
Q$_0$	Initial capacity
R	Unspecified chemical side chain
RC	Resistor-capacitor circuit element
R$_{ct}$	Charge transfer resistance

RF	Radio frequency
R_s	Series resistance
RTD	Resistance temperature detector
RW	Resistor-warburg circuit element
sCMOS	Scientific complementary metal–oxide–semiconductor
SEI	Solid electrolyte interphase
STEM	Scanning tunneling electron microscopy
T	Temperature
t	Time
TAP	Triallyl phosphate
TFEC	bis(2,2,2-trifluoroethyl) carbonate
TM	Transition metal
TWh	Terawatt hour
UHPC	Ultra high precision charger/Ultra high precision coulometry
USD	United States Dollar
V	Voltage, Volt
V_-	Negative electrode voltage
V_+	Positive electrode voltage
V_{ch}	Charge endpoint voltage
VC	Vinylene carbonate
W	Watt, Warburg circuit element
x	Fractional site occupation
XPS	X-ray photoelectron spectroscopy
XRF	X-ray fluorescence
y	Year, calendar year, fractional site occupation
α	Tunneling attempt frequency constant
β	Tunneling barrier height constant

γ	Arrhenius Law frequency factor
μ_-	Chemical potential of lithium in the negative electrode
μ_+	Chemical potential of lithium in the positive electrode
μA	Microampere
μm	Micrometer
ρ_{water}	Density of water
Δm	Mass change
ΔV	Voltage polarization
Δv	Volume change

ACKNOWLEDGEMENTS

First and foremost, I would like to acknowledge and thank my supervisor, Prof. Jeff Dahn, for not only the supervision and continuous support during this degree, but also my introduction to the research and this field of study a decade prior. Jeff's legacy is so clearly his students, evidenced by the patience, effort, and devotion he shows to their education and development. It has been a pleasure and an honor to have been one of his students.

I would like to thank the entirety of the Dahn lab students and staff for their support, camaraderie, and collaboration. Specifically, to Eric Logan and Jessie Harlow, for always being available to chat and committed to a state of perpetual caffeination. To Ahmed Eldesoky, Ines Hamam and Saad Azam for being willing to exchange ideas, share expertise and contribute to good times both in and outside the lab. I would like to thank Julian Oxner for his considerable assistance in completing work that is detailed throughout this thesis. I would also like to thank Mike Johnson for his invaluable and tireless efforts managing lab infrastructure and ensuring experiments operate smoothly.

Finally, to Patty: thank you for being by my side throughout this time and more, while continually inspiring me to take the next step. Thank you for being a positive distraction when needed and understanding throughout. I'm excited to see where new paths will take us.

CHAPTER 1 INTRODUCTION

1.1 Motivation

Lithium ion (Li-ion) batteries experienced a period of rapid development and widespread use after commercial introduction by Sony Corporation in 1991 for use in portable electronics.[1] Li-ion cells have been and continue to be well suited for portable electronics, owing to the fact that they have excellent volumetric and gravimetric energy and power densities compared with other battery technologies, which enable smaller and more lightweight devices with more powerful electronics and longer runtimes.[2,3] Li-ion batteries have undergone continual improvements to essentially any measurable quantity and have become an enabler behind the technological advancements that have become commonplace and define modern society. Devices such as cell phones, portable computers, and wireless peripherals, all enabled by Li-ion batteries, serve as personal access points to the global information network and are used by nearly all citizens in the developed world.

Beyond enabling information transfer and connectivity, Li-ion batteries have emerged as a viable energy storage candidate that can support the widespread deployment of energy production technologies that can disrupt the global socio-economic dependence on fossil fuel combustion as an energy source. Personal transportation and the electrification of vehicles is one such area where Li-ion battery technology is beginning to displace the direct combustion of fossil fuel. At the time of writing, many nations have set policy targets to prohibit the future sale of new petroleum fueled vehicles or alternately promote the sale of electrically driven vehicles.[4–9] Li-ion batteries have also found application as stationary, grid-attached energy storage for multiple applications, including

to alleviate the temporal mismatch between supply and demand associated with renewable but intermittent energy sources, such as solar photovoltaic or wind.[10] Electrified transportation and energy generation from renewable sources are two significant and interrelated measures that are required with widespread adoption and great urgency to prevent the ever-worsening climate and environmental impact of continued fossil fuel consumption.

Production of the cells necessary to support these two measures is constrained both by scale up of manufacturing capabilities and availability of raw materials from which batteries are made. Availability, or at the very least availability at a profitable margin, is a concern for the metals lithium, cobalt and nickel[11,12] to the extent that battery production could become resource limited. At the time of writing, the infrastructure and throughput for Li-ion battery production is assessed as 0.747 TWh in 2020[13] and any further production is infrastructure limited. Meanwhile, 130 000 TWh of fossil fuels were consumed globally for energy production in 2019 and represented over 80% of total energy produced.[14] Consider the following hypothetical situation, adapted with permission from J. Electrochem. Soc. **169** 090523 (2022), copyright The Journal of the Electrochemical Society, 2022[15]. Every time a cell phone or laptop is upgraded, or an electric vehicle undergoes a battery replacement due to degradation of the original battery, some fraction of the global battery production capacity is consumed in an application which does not expand the total amount of globally deployed energy storage. The greater the frequency with which batteries end up being replaced, or the shorter their lifetimes, the less energy storage will be available for grid-attached and renewable energy enabling applications.

As previously stated, 2020 global Li-ion battery production has been assessed at 0.747 TWh. This is projected to increase to 2.492 TWh by 2025.[13] Furthermore, Benchmark Mineral Intelligence projects that this number will increase in a mostly linear fashion, and reach an estimate of 6 TWh by 2030.[16] An convenient, approximate linear trend to these three points, suitable for general discussion and the basis of a simple model, is

$$P = \frac{1}{2}(y - 2020) \tag{1.1},$$

where P is the annual production in units of TWh, for a given calendar year, y. Only considering production beginning in 2022, and future years, Equation 1.1 remains positive and therefore physically sensible. To understand the influence of battery lifetime on global deployment quantity, consider a model that adheres to the following rules:

1. For simplicity and convenience, assume no batteries exist in the field prior to 2022,

2. Global annual production capabilities, described in quantity of energy storage that can be produced (not number of cells, mass of cells, etc.), is given by Equation 1.1,

3. The global annual production capabilities are fully utilized and deployed, subject to no material or natural resource quantity limitations,

4. All batteries are produced with a lifetime that is constant and independent of the year of assembly,

5. When a battery reaches end-of-life, it is replaced with a new battery produced in the same year the first battery reached end of life, and

6. Any batteries not utilized to replace expired batteries at end-of-life are allocated into new applications that are categorized simply as increasing the net energy storage deployment, or energy storage "fleet" size.

The practical interpretation of this model can be explained by economic consumption driving individuals to replace their devices and hence batteries, but never eliminate that application (i.e., cell phone or vehicle battery) from their life. The available production that is not allocated for replacement needs is assumed to be available for public good and can service applications such as the grid or renewable energy production facilities. This ignores the economics of installing such storage and assumes that sufficient renewable energy and grid infrastructure exists. This model also overlooks the inevitable future population growth and increase in consumption that will surely occur with an increasingly portable and electrified world. This would consume more production that could otherwise enable renewable energy production. While beyond the scope of this model, it is encouraging that there is research dedicated to means of allowing batteries to simultaneously service personal and utility needs,[17,18] as well as second-life usage to extend utility beyond the originally intended lifetime.[19]

The functioning of this model can be understood by examining the case where batteries with a lifetime of 2 years are produced. In 2022, according to Equation 1, 1 TWh of batteries are constructed. Those cells reach end-of-life in 2024. Therefore, of the 2 TWh produced in 2024, 1 TWh is required to replace the end-of-life cells produced in 2022, and 1 TWh can contribute to new applications. The model is computed between 2022 and the year 2100 for a selection of cell lifetimes. Figure 1.1a shows the net contribution to expanding the quantity of energy storage installed and in service globally, as a function of

year. Comparing each trace in a given year, as cell lifetime increases, the net energy storage deployed is higher. When lifetime is large, it gives time for production to increase and grow, before cells reach end-of-life and need to be replaced. Therefore, as lifetime is increased, a much smaller fraction of the production capacity, at the time of replacement, is consumed for replacement and diverted from increasing net deployment or total installed capacity. As an alternate but equivalent view, the time required to reach a particular threshold, such as the 400 TWh threshold indicated, is lower, up to a limit, as the cell lifetime is increased, for the same reasons. 400 TWh is the daily energy usage of the entire planet, rounded to the nearest 100 TWh[14] and therefore is a possible target threshold with some practical significance. Figure 1.1b explicitly shows the time to reach 400 TWh, as a function of cell lifetime. For cell lifetimes beyond approximately 30 years, the time to reach 400 TWh is constant. This is because for these long lifetime cells, the annual production is fully utilized and energy storage deployment over this time is limited by production capacity and not the amount of replacement required. This can be observed in Figure 1.1a, as the highest lifetime traces follow the same trajectory as the dashed reference trace, representing the quantity of batteries produced.

Figure 1.1b also shows the relationship between cell lifetime and the average annual production capacity required to sustain 400 TWh of deployed batteries. This average assumes that the replacement needs can be evenly distributed. For instance, if cells had a lifetime of 4 years, even distribution of the replacement needs would require 100 TWh of production each year. The necessary production capacity decreases monotonically as cell lifetime increases. Within the range of parameters considered, the lowest required production capacity of 8 TWh is achieved when cell lifetimes are 50 years. This is

particularly troubling because the production capacity needed to achieve 400 TWh in a

timely manner is much greater than the production capacity needed to maintain 400 TWh.

At the time of writing, neither commercial cells with 50 year lifetimes nor 8 TWh of annual

global cell production have been achieved, , and do not project to be in the immediate

future.[16]
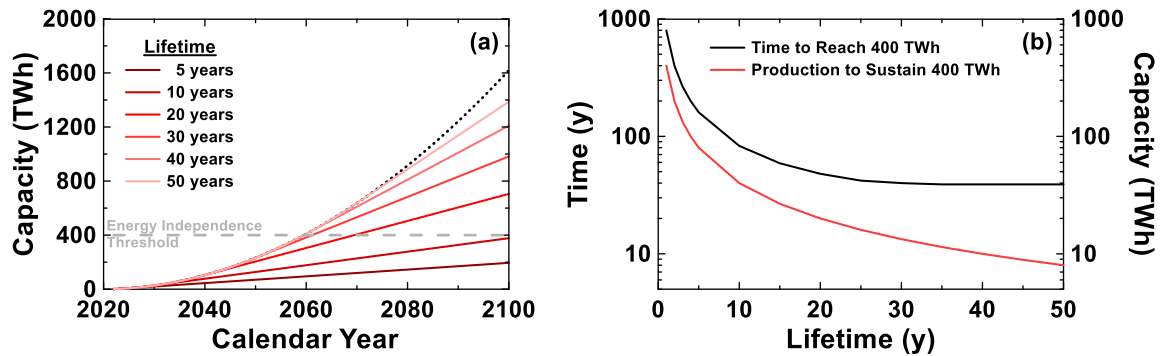
Figure 1.1. Model calculation results illustrating battery lifetime needs. (a) Net cumulative deployment of global lithium-ion battery energy storage as a function of calendar year. Net deployment is based on linear growth of production capabilities, fully utilized production and one-for-one replacement of cells that reach end-of-life. A proposed energy independence threshold of 400 TWh is indicated with a horizonal dashed line, based approximately on the global energy needs for a single day. (b) The time required to reach net deployment of 400 TWh of lithium-ion battery energy storage and the average annual production capacity to sustain 400 TWh, once the energy independence threshold is reached, as a function of battery lifetime.

It should be clear that increasing the lifetime of lithium-ion cells will be critical in

ensuring battery energy storage can make a meaningful contribution to achieving energy

independence from fossil fuels. This is the underlying motivator, central to all the work in

this thesis. The simple ideas conveyed by Figure 1.1 and the accompanying discussion do

not capture any of the economic, ethical, or operational constraints that are considered

when comparing types of lithium-ion batteries for use in a given application. Lithium-ion

batteries can be constructed using a variety of materials, as will be discussed later in this

chapter. The selection of these materials can determine electrochemical performance metrics such as the maximum energy stored or power delivered per unit volume, and socioeconomic metrics such as cost and ethical material acquisition. Certain applications may place higher priority on a selection of these or other metrics and therefore prefer lithium-ion batteries made with certain materials. To help overcome the ongoing global energy and climate crisis, improving the lifetime of batteries suitable for any and all applications is necessary.

1.2 Li-ion Batteries and Cells

1.2.1 Operation and Assembly

A lithium-ion (Li-ion) battery is a secondary battery[20], in that it is rechargeable and accepts/delivers electrical energy that is transformed and stored in chemical bonds. The fundamental electrochemical unit of a Li-ion battery is referred to as a cell, consisting of a positive and negative electrode, isolated from electronic connection by a separator but connected ionically by a liquid electrolyte.[3]

Figure 1.2 shows a perspective schematic of a lithium-ion cell. The positive electrode is typically a layered, lithium-containing transition metal oxide. The archetypal and first discovered positive electrode material for Li-ion cells is $LiCoO_2$[21]. The negative electrode is conventionally graphite. The conventional electrode materials, both crystalline solids, serve as intercalation hosts, with vacant lattice sites into which lithium ions can reversibly be inserted and removed[22,23]. Upon assembly and in the discharged state, all lithium ions reside exclusively in the positive electrode. When the cell is charged, some fraction of lithium from the positive electrode is removed and hosted in the negative

7

electrode[23]. To travel from one electrode to the other, lithium, in a host lattice site separates from a localized electron, shared with the lattice. Lithium, now as a singularly charged cation, can traverse the lithium-ion conducting electrolyte to the opposite electrode. The previously bonded electron travels, outside the cell through external circuitry, and re-enters the cell at the opposite electrode where it recombines with a lithium ion to facilitate a new bond with the lattice of the new electrode. In this manner, the operation of a Li-ion cell simply involves to reversible movement of lithium ions and electrons from one electrode to the other, earning it the colloquial description of "rocking chair" battery[23–25].
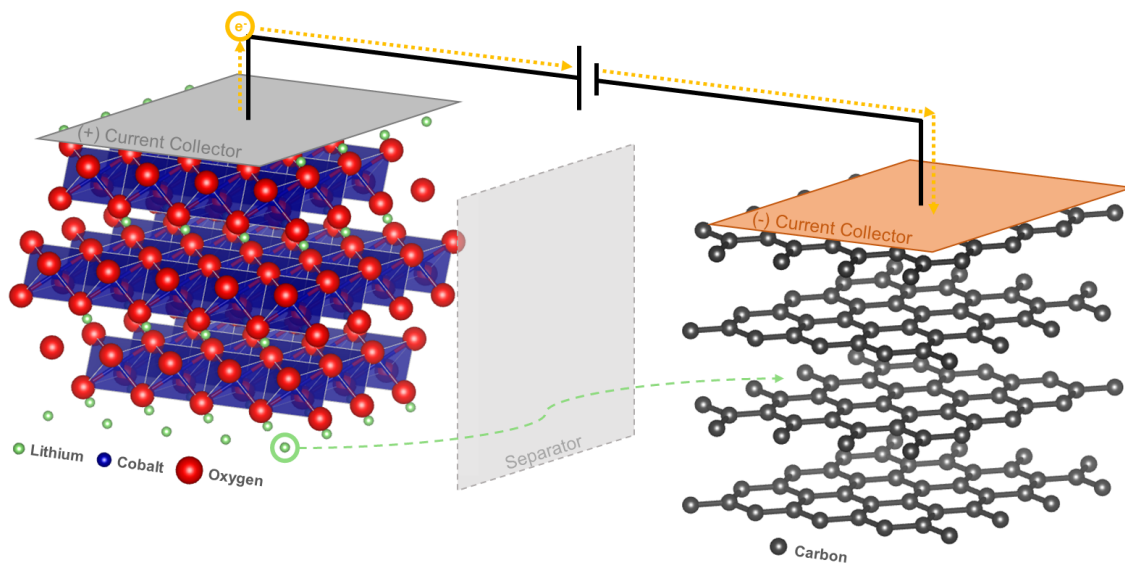
Figure 1.2 Schematic diagram of a lithium-ion cell in the discharged state. Positive and negative electrode materials are represented by crystallographic models of archetypes $LiCoO_2$ and graphite respectively. The space between and surrounding the electrode materials is assumed to be filled with a liquid electrolyte, not shown. The schematic indicates the direction of electron and ion travel during the charging process.

Energy is stored and released during this motion of charges, due to a difference in chemical potential of lithium between each electrode. The chemical potential of lithium stored in the positive electrode is much lower than the negative electrode[22,23], therefore

moving lithium from the positive electrode to the negative electrode represents an increase in potential energy of the lithium. The energy input required to increase the lithium potential energy, usually work performed by electrical energy, is thus stored in the chemical and structural configuration of the electrodes. Allowing lithium to return to the positive electrode causes both electrodes to revert to their original structural and chemical configurations and liberates this stored energy, which can be used to perform work. Figure 1.2 shows the motion of a lithium ion and electron pair from the positive electrode to the negative electrode, or during the energy storage or charging process.

Conventional Li-ion cells are constructed from a three-layer stack of positive and negative electrode foils, with a polymer separator film between them.[26] The primary function of this stack is to facilitate alignment in close proximity and electronic isolation of the electrodes, so that electrons are forced to travel through external circuitry when ions move from one electrode to the other. Sections of this stack can be repeatedly layered or alternately wound into a flat or cylindrical "jelly roll" and inserted into the cell housing (with necessary electrical connections) depending on the cell size and geometry[26]. Cells are filled with a lithium-ion-containing electrolyte and sealed to prevent exposure to ambient atmosphere. Electrodes are constructed by coated as a slurry onto metallic foils that serve as electronic current collectors. The slurry is formulated from a mixture of active electrode materials, conductive carbon diluent and polymeric binder, all dispersed in a volatile carrier solvent. The slurry is coated on aluminum or copper foil for the positive and negative electrode, respectively, and heated to remove the solvent. Of the remaining solid coating, $\geq 94\%$ by mass is typically active material[27,28]. Aluminum foil is economical

and lightweight, whereas copper is required for the negative electrode current collector due to superior low potential stability[29] that cannot be afforded by aluminum.[30]

While the fundamental electrochemical unit of a Li-ion battery is the cell, batteries can consist of a single cell to a large and complex arrangement of parallel and series connected cells. Generally, studies of Li-ion batteries at the cell level yield insight into intrinsic properties, particularly the roles and interactions of various materials. Intrinsic properties are unchanged between a single cell and a larger battery comprised of many of those same cells, hence the electrochemistry of materials can be well studied at the cell level. The use of larger batteries tends to affect extrinsic properties alone, meaning the study of materials in large batteries is not convenient and generally wasteful. At the cell level, direct experimental measurables are the current flowing into or out of the positive terminal of the battery and the electric potential difference or voltage between the positive and negative terminals. By continuously measuring the current flowing into or out of the positive terminal, the charge capacity stored, Q, can be calculated by

$$Q = \int_{t_1}^{t_2} I(t) \mathrm{d}t \tag{1.2}$$

where $I(t)$ is the current as a function of time, t. The interval over which the measurement takes place is defined by t_1 and t_2. The capacity is related to the lithium concentration in either host electrode by

$$Q = x q_- m_- = (1 - x') q_+ m_+ \tag{1.3}$$

where x and $(1 - x')$ are the fractional lithium concentrations or lattice site occupations, q_- and q_+ are the gravimetric specific capacities and m_- and m_+ are the mass contained

in the cell, of the negative and positive electrodes respectively. Equation 1.3 is written in a manner to imply that as a full Li-ion cell is charged, the negative electrode is lithiated while the positive electrode is delithiated. The fractional occupations x and x' are noted to be possibly different depending on the cell design. Generally, interactions between intercalant species in an intercalation host result in chemical potentials that vary as a function of the fractional occupation of sites within the host.[22] Given that lithium is a singularly charged cation, the cell voltage, V, is given by

$$V = \frac{1}{-e}\left(\mu_+(1-x') - \mu_-(x)\right) \tag{1.4}$$

where $-e$ is the charge of an electron and $\mu_+(1-x')$ and $\mu_-(x)$ are the chemical potentials of lithium in the positive and negative electrode respectively. Eq. 1.4 can be viewed as describing the chemical potential energy difference per unit charge in a cell, and approximately follows the prescription of McKinnon and Hearing.[22] Distributing the electron charge to the chemical potential of each electrode, Eq. 1.4 can be rewritten as

$$V = V_+(Q) - V_-(Q) \tag{1.5}$$

where $V_+(Q)$ and $V_-(Q)$ and the positive and negative electrode voltages, respectively, as a function of the cell capacity. The fractional occupation, x, in Eq. 1.4 has been replaced with the cell capacity, Q, for convenience, according to Eq. 1.3. Eq. 1.5 implies that the cell voltage is dependent on the voltage-capacity relationship of each individual electrode. Generally, the potential of an individual electrode, in the context of a lithium host is referenced to the Li$^+$/Li redox couple (-3.040 V referenced to the standard hydrogen electrode).

Figure 1.3 shows the voltage as a function of capacity, or voltage curve, of a representative Li-ion cell, along with the voltage curves of the two electrodes which comprise the cell. As constructed (not shown in Figure 1.3), a cell is typically within a few 100 mV of 0 V, although the value varies considerably. As the cell is charged, the capacity value increases. Lithium is removed from the positive electrode and inserts into the negative electrode. As lithium is removed from the positive electrode, the positive electrode voltage, versus Li^+/Li, increases. As lithium is inserted in the negative electrode, the negative electrode voltage, versus Li^+/Li, decreases. As such, throughout the entire charge process, the full cell voltage increases as more capacity is stored.
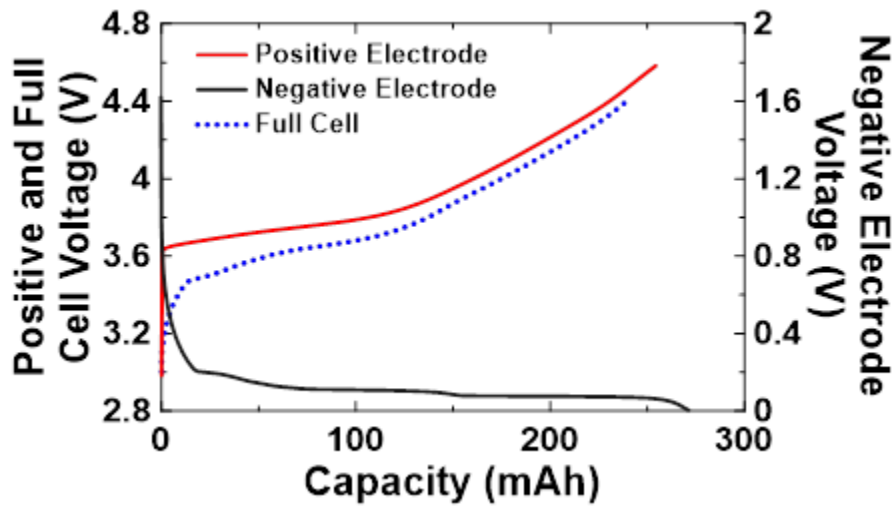
Figure 1.3. Voltage as a function of capacity for a representative Li-ion full cell, and constituent positive and negative electrodes. The lithium-ion cell has a $Li[Ni_xMn_yCo_{1-x-y}]O_2$ (where $1-x-y \leq 1$, $x \leq 1$, $y \leq 1$) positive electrode and graphite negative electrode.

1.2.2 Positive Electrode Materials

The positive electrode serves as the source of lithium in Li-ion cells[20]. Due to the relatively low variability in viable negative electrode materials[30], the voltage behaviour as a function

of lithium concentration in the positive electrode generally determines the operating voltage of the cell[23]. This a consequence, of Eq. 1.5, assuming the term, $V_-(Q)$ is the same in nearly all cells or varies less from cell-to-cell than $V_+(Q)$. While many electrode materials are possible[23,31,32], two general types of materials see the majority use in contemporary, commercially produced cells.

The first type of positive electrode materials is the group that is classified as layered oxide structures. These materials have the chemical formula $LiMO_2$ where M is one or more transition metals and dopant metals.[20,21,33–36] Generally, the layered materials are described by the $R\bar{3}m$ space group,[21,34,36] although certain formulations and synthesis conditions can yield a superlattice that diminishes the $R\bar{3}m$ symmetry. Visually, the delithated, or lithium-free, structure can be described as slabs consisting of two layers of oxygen atoms, separated by a layer of transition metal atoms. When completely lithiated, lithium arranges in layers between otherwise adjacent oxygen layers. Figure 1.2 shows the structure of a representative layered positive electrode material, $LiCoO_2$. The first layered oxide material discovered and commercialized as a Li-ion battery positive electrode was $LiCoO_2$.[21] While $LiCoO_2$ has acceptable electrochemical performance and saw use in portable personal electronics in the 1990s and 2000s, expensive cobalt prices,[37] relatively poor safety[38] and lower usable energy density[39] than alternatives, and the existence of phase transitions when too much lithium is removed[21] have led researchers and manufacturers to replace Co in $LiCoO_2$ in search of improvements. Substitution of some fraction of Co with Ni and Mn yields $Li[Ni_xMn_yCo_{1-x-y}]O_2$ (1-x-y≤1, x≤1, y≤1) or NMC materials. NMC materials are typically referred to by shorthand based on the fractions of each transition metal. For instance, $Li[Ni_{0.5}Mn_{0.3}Co_{0.2}]O_2$ is referred to as NMC532. The relative amounts

of Ni, Mn and Co determine the cost, safety, energy density in a given voltage range and lifetime.[40,41] For instance, NMC532-containing cells have demonstrated among the longest lifetimes in laboratory settings[28,42] while using less Co, superior safety and greater usable energy density than $LiCoO_2$ cells.[39] Increasing the Ni content, compared to NMC532, can yield compounds like NMC811. High Ni NMC materials offer even greater energy density[39,43], but compromise on lifetime and safety compared to NMC532 or similar materials, while still showing better safety than $LiCoO_2$.[39] Some of the latest efforts have been into NMC materials where all the Co has been replaced with Ni and Mn, in an effort to decrease costs as much as possible while preserving excellent performance inherent to NMC types which still contain some Co.[44] Another class of layered positive electrode materials is $Li[Ni_{1-x-y}Co_xAl_y]O_2$ ($1-x-y\leq1$, $x\leq1$, $y\leq1$) or NCA materials.[35] Generally, NCA materials are made with high amounts of Ni and function most similarly to high Ni NMC materials.[39] Due to less commercial relevance than NMC cells, and no relevance to this thesis, NCA materials will not be mentioned further.

The second type of positive electrode materials of both academic and commercial interest is the olivine materials, particularly $LiMPO_4$, where M is Fe, Mn, Ni or Co.[45] The most commercially relevant formulation among this family of materials is $LiFePO_4$ or LFP, described by the Pnma space group[45]. The material arranges with phosphate tetrahedra and FeO_6 octahedra, leaving a series of channels in which lithium resides and travels. For years after its discovery, LFP was seen as inferior to $LiCoO_2$ and NMC materials due to lower energy density[45] along with ionic and electronic conductivity problems[40]. Conductivity issues were addressed by nano-sizing and carbon-coating the LFP particles[40], which unlocked the utility of the material. Specifically, LFP is significantly cheaper than NMC

materials due to the abundance and pricing of Fe compared to Ni and Co[46–48] and has superior safety characteristics.[49,50] Olivine materials with Mn and Co as alternative to Fe are technologically immature at the time of writing and do not presently afford cycling stability necessary for commercial relevance and have no relevance to this thesis, therefore are not mentioned.
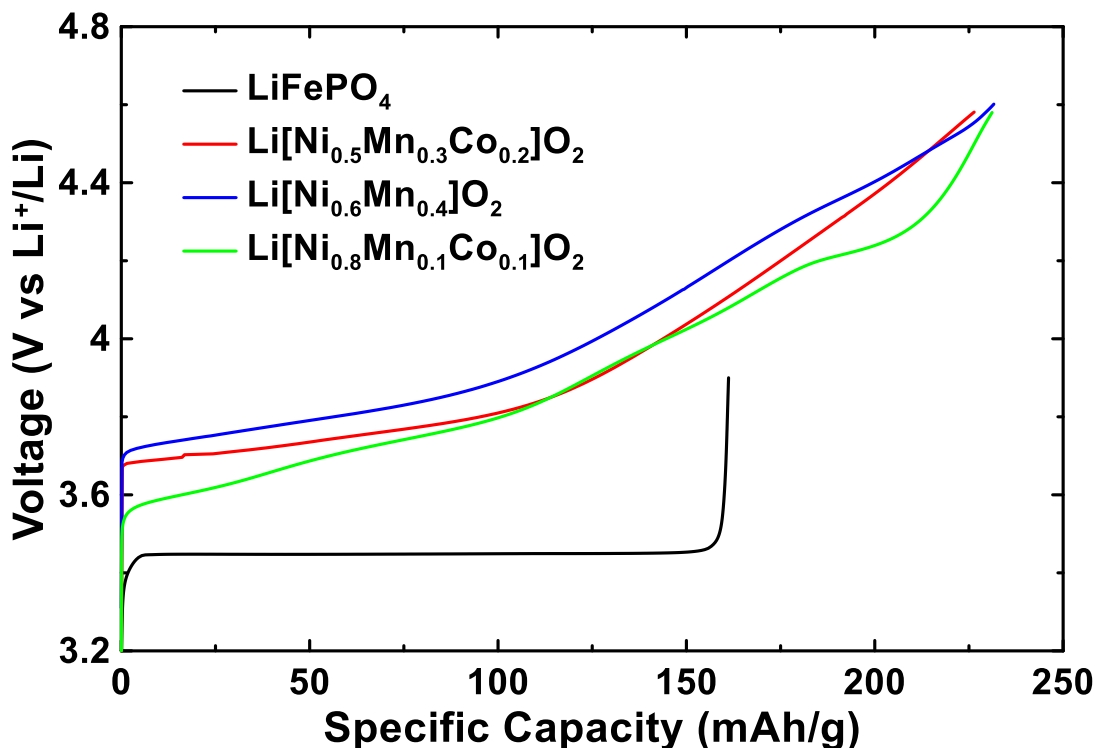
Figure 1.4. Voltage as a function of specific capacity for positive electrode active materials relevant to this thesis.

While NMC and LFP positive electrode materials are both found in Li-ion batteries and share common features like greater energy density than other battery chemistries, such as Lead-Acid or Nickel-Metal Hydride, they have considerably different electrochemistry. Figure 1.4 shows the voltage curve of LFP and three varieties of NMC that are mentioned in later chapters. NMC cells have a sloped voltage curve, generally indicating single-phase,

voltage-mediated (de)lithiation, while LFP shows a flat voltage curve, indicating two-phase co-existence of lithiated and delithiated regions. The theoretical capacity of LFP is 172 mAh/g, while NMC materials can deliver well in excess of 200 mAh/g if charged to sufficiently high voltage, although this is usually accompanied by undesirable side effects that impact lifetime.[51,52] Typically NMC materials are only delithiated to a certain extent, balancing energy density and lifetime as needed for a particular application. Figure 1.2 also clearly shows that NMC materials can store more capacity, at a higher voltage than LFP cells. Since energy stored is the integral of the voltage curve, this explains the fact that NMC cells have a greater gravimetric energy density. LFP also has a lower density than NMC materials, which translates to lower volumetric energy density as well. Among NMC cells, different fractions of the three transition metals can result in different behaviours. Higher Ni concentrations result in depression of the voltage curve[39,43], resulting in more capacity stored below a certain upper charging voltage limit. High concentrations of any single metal can lead to structural phase transitions.[21,43] Relatively equal mixtures have relatively facile synthesis[34,53,54], good safety[38,55] and long lifetime[28,42]. Generally, a compromise is made when selecting NMC formulation between desirable performance metrics and cost.

1.2.3   Negative Electrode Materials

The negative electrode is the lithium host in the charged state. The advent of the Li-ion cell is accompanied by the unprecedented, at the time, use of an intercalation negative electrode[20]. Earlier lithium metal cells contained metallic lithium with an intercalation positive electrode. The presence of metallic lithium resulted in handling and safety

concerns[56] remedied by Li-ion cells. The earliest negative electrodes were various carbonaceous materials,[57–60] from which graphitized carbon has emerged as the contemporary choice in a large majority of commercial Li-ion cells. Lithium reversibly intercalates into the van der Waals space between adjacent graphene layers in graphite, up to a maximum lithium concentration of LiC_6, providing a theoretical specific capacity of 372 mAh/g.[60] Lithiated graphite also has a low average voltage of 125 mV versus Li^+/Li[30,60] meaning it contributes positively to a greater cell voltage and higher energy density. Two sources of graphite are used in modern Li-ion negative electrodes, identified by their production method. Natural graphite is mined from naturally occurring surface and subterranean deposits, while synthetic or artificial graphite is obtained from heating soft carbon precursors under inert atmosphere beyond 2500°C.[60] Natural graphite electrodes can improve cell energy density, because it responds well to densification but yields inferior lifetime compared to artificial graphite.[61] It is believed that the artificial graphite particle morphology and structure makes it more robust to expansion and mechanical degradation.[61] All cells included in this thesis use artificial graphite as the negative electrode active material.

Research and development of next-generation batteries with higher energy density and lower cost has identified one strategy as replacing graphite with another, usually a non-intercalating negative electrode material.[30,62] Leading candidates, which do not require significant changes in other materials or cell assembly are a return to lithium metal negative electrodes,[62] specifically the use of zero-excess lithium metal cells,[63] or the use of alloying electrodes, specifically Si.[30,64] Lithium and silicon have specific capacities of 3860 mAh/g[62] and 3579 mAh/g,[30] and average voltages of 0 V and 0.4 V versus Li^+/Li,

respectively,[30,62] yielding desired improvements in energy density. Cells made with either lithium metal or silicon negative electrodes suffer considerably shorter lifetimes than graphite cells, due to mechanical and morphological instability that results in deleterious reactions with the electrolyte.[64-66] As such, modern commercial use of lithium metal negative electrodes is yet to be realized, and use of Si is typically as part of a composite electrode[67], in heterogenous combination with graphite, where the mass and capacity fractions skew in favour of graphite.

1.2.4 Electrolytes

The primary purpose of the electrolyte is to facilitate ionic conduction and transport of lithium from one electrode to the other. Conventional Li-ion cells, and all the cells in this thesis, utilize a liquid electrolyte. At its simplest, a liquid electrolyte is a solution of a salt in a liquid solvent. The liquid serves to dissociate the salt into charged ions that can carry current, and to fill the internal of space of the cell and ensure contact with all active material particles. Once dissociated, the salt serves as charge carriers through the electrolyte solution. To function properly. electrolyte should have excellent thermal and electrochemical stability, to prevent unwanted reactions that may harm the electrodes or consume the active lithium capacity. The solvent dielectric constant should be high, to ensure sufficient solubility towards the salt of choice and achieve full dissociation. The conductivity, lithium transference number (fraction of current carried by Li^+) and viscosity of the solution should be high, high, and low respectively, to enable fast lithium diffusion and increased current capabilities. Finally, the electrolyte should be free of phase transitions over the usable temperature range of the cell.

As both electrodes can individually react with water, and the stability voltage window of water is exceeded by the voltage difference between the charged electrodes, water is an unsuitable electrolyte solvent. As such, polar, aprotic solvents are commonly selected as they can still dissolve the necessary salts, without the same reactivity concerns of water. Mixtures of carbonate solvents are most used, due to the variety of suitable carbonate species that can be combined to tune the properties of the final electrolyte and the fact that carbonate solvents can passivate the charged electrodes, providing kinetic stability.[68–70] Figures 1.5a and 1.5c show a selection of popular solvents used in electrolytes for Li-ion cells. Cyclic carbonates, such as ethylene carbonate (EC), typically have high dielectric constant required for full dissociation of salts but have higher viscosity (at temperatures where liquid phases exist) than linear carbonates.[71] EC is inconveniently solid at room temperature[71] and propylene carbonate (PC) use is detrimental to graphite electrodes due to solvent co-intercalation and subsequent mechanical damage to the active material.[72] Linear carbonates such as dimethyl carbonate (DMC) and ethyl methyl carbonate (EMC) have poor dielectric constants, but exhibit acceptably low melting points and relatively low viscosity.[71] A combination of 15-30%(v/v) of EC 70-85%(v/v) of DMC and/or EMC yields sufficient salt dissociation with low enough viscosity to achieve excellent conductivity, and remains liquid below 0°C.[73] Mixtures in this range are among the most common for modern Li-ion cells. Alternate solvents, such as esters[73–75] are used, but with much less prevalence.

Electrolyte salts are typically selected on the bases of cost, conductivity, and relative stability/reactivity. Ideally the salt is dissociated completely in solution and simply allows charge transport by allowing the removal of lithium at the surface of one electrode

to be matched by the insertion of lithium at the other electrode, with no other role in cell performance. As will be discussed in Chapter 2, the stability, and reactions of the electrolyte, including both salts and solvents, with the charged electrodes largely determine the lifetime of a cell along with many performance metrics. The most common salt found in Li-ion cells is $LiPF_6$ and has been since the 1990s and early 2000s.[76–78] $LiPF_6$ has long been known to have thermal stability concerns,[78–80] but gives excellent conductivity and solubility in carbonate solvents[73] and cells that demonstrate among the longest lifetimes utilize $LiPF_6$.[28,81] Alternate salts have been tested, but typically do not show enough merit to supplant $LiPF_6$. $LiAsF_6$ performs very similarly to $LiPF_6$ but has toxicity concerns due to the presence of As,[82] $LiBF_4$ provides lower conductivity than $LiPF_6$,[83] lithium bis-oxalatoborate (LiBOB) has low solubility and diminished conductivity in carbonate solvents,[84] $LiClO_4$ is known to have violent reactivity in certain circumstances,[85,86] and both lithium bis(trifluoromethanesulfonyl)imide (LiTFSI) and lithium bis(fluorosulfonyl)imide (LiFSI) salts catastrophically corrode the aluminum that serves as the positive electrode current collector when cells are charged to moderate-high voltage.[87,88] The use of these salts, particularly LiFSI, results in excellent lifetime capabilities in cells that remain at low voltage, however.[42,89]

In addition to the minimum components, a salt and a solvent, necessary to form an electrolyte, it is convenient and commonplace to add chemicals to the electrolyte that react with favorable products or outcomes at the surface of either electrode.[90] Referred to as electrolyte additives, these chemicals are sacrificially consumed[91], alter the electrode surface chemistry[69,92] or morphology[93], and consequently tune cell performance metrics such as lifetime[94–96], high voltage tolerance[97,98], cell impedance,[99] safety[96,100] or

temperature stability[101,102]. Countless additives have been tested by the academic community. The task of testing and understanding additives has become increasingly complex, as ternary and quaternary additive systems[96,103] have become common and comparative studies of nearly 100 different additive combinations exist.[103] It is not uncommon for an entire cell design, including electrodes and electrolyte, to require cohesive optimization for a given application, and if a single detail is changed (perhaps solvent type), the optimized cell design may be entirely different.
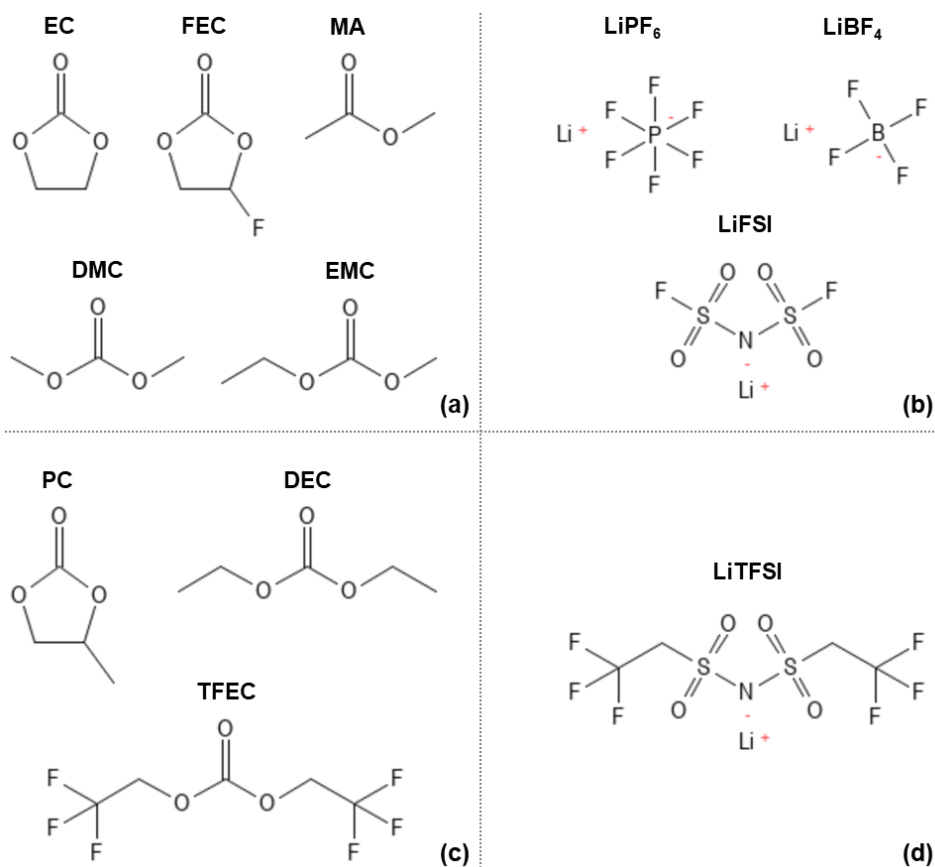
Figure 1.5. Chemical structures of common Li-ion (a,c) solvents and (b,d) salts. Structures in (a) and (b) are used in cells that are detailed in this thesis.

Despite the prevalence and success of liquid electrolytes, considerable research effort has been dedicated to developing solid electrolytes for next generation cells which

may yield enhanced safety and improved lifetimes for otherwise unstable materials.[104,105] Practical use of these solid electrolytes has yet to be realized. Nevertheless, electrolyte work is essential to unlocking the capabilities of existing and next-generation materials. Typically, electrodes determine the possible energy density and have a role in the power capability and lifetime of the cells in which they are used. Electrolyte chemistry and controlling the interaction between the electrolyte and electrodes is key to allowing those materials to store energy for a long lifetime, without excessive capacity loss. Perfectly functioning electrode materials will be hindered in their operation and lifetime performance if an unstable or unsuitable electrolyte formulation is used.

1.3 Scope of Thesis

The preceding text hopefully motivated the need for long lifetime Li-ion cells in the context of accumulating a global fleet of energy storage that can be used to enable energy generation from renewable but intermittent sources and achieve independence from fossil fuels as an energy source. An introduction has been given to the assembly, operation and materials featured in Li-ion cells, particularly materials with relevance to other chapters. This work seeks to explore the role of electrolyte components, particularly salts, in achieving improved lifetime in a variety of cell types, some under unique use-cases.

Chapter 2 of this thesis will give a description of electrode-electrolyte reactions, the solid electrolyte interphase, and the role of electrolyte components in tuning cell performance. The current understanding and body of work, with emphasis on the electrodes

and electrolytes relevant to this thesis, will be reviewed. That is, layered or olivine positive electrodes, artificial graphite negative electrodes and carbonate solvents.

Chapter 3 will detail the experimental materials and methods used throughout. Materials include the cells, electrodes and electrolytes. A detailed explanation of various electrochemical cycling methods and their merits is given. Finally, a description of analysis techniques, including electrochemical impedance spectroscopy, differential voltage analysis, ultra high precision coulometry, X-ray fluorescence microscopy and isothermal microcalorimetry, is given.

Chapter 4 of this thesis will present the effect of salt, electrolyte additives and solvent in terms of both types and concentrations on NMC532/artificial graphite subject to an aggressive cycling protocol that imposes long time duration at high voltage. Cycling and analysis results are presented to elucidate the mechanism of failure and the source of electrolyte-derived performance improvements.

Chapter 5 will discuss efforts to improve lifetime of cells that require high voltage charging to provide competitive energy density compared to contemporary cells, namely NMC640/artificial graphite cells. The effect of electrolyte additives, temperature and charging voltage limit are explored.

Chapter 6 will present the effect of salt concentration LFP/artificial graphite cells subject to a unique high state-of-charge cycling protocol. The qualities demonstrated by the cells detailed in this chapter will be contrasted with the qualities of the NMC532/artificial graphite cells detailed in Chapter 4 and provide insight into the difference in electrolyte design for olivine versus layered positive electrode cells.

Chapter 7 will present a novel, low voltage NMC532/artificial graphite cell design and the role of salt type in achieving ultra-long lifetimes. These cells will be compared with LFP and conventional NMC532 cells. A method of capacity fade compensation to achieve extended use is described. Finally, these experiments are extended to low voltage cells with a NMC811 positive electrode, and cells with composite layered/olivine positive electrodes with proof-of-concept results.

Chapter 8 will present the conclusions of this work as a whole and both the academic and commercial implications. Future work to understand the electrolyte-mediated failure and extend the lifetime in these cells and natural progressions to other cell types will be recommended.

CHAPTER 2 ROLE OF ELECTROLYTE IN LI-ION CELL PERFORMANCE

2.1 Parasitic Reactions and Kinetic Passivation

The operation of a Li-ion cell, as described in Section 1.2.1, involves lithium intercalation or deintercalation processes at both electrodes, along with ion conduction through the cell. This description is idealized, in that there is no account of detrimental processes or explanation of the imperfections inherent to Li-ion cells. Li-ion cells store relatively large amounts energy because of the large chemical potential difference between lithium stored in graphite (~0.1 eV vs. Li$^+$/Li) and lithium stored in the positive electrode (~3.8 eV vs. Li$^+$/Li). When the cell is charged, the result is a highly reactive lithiated negative electrode that can supply electrons and lithium to electrolyte species at the electrode surface. delithiated positive electrode that can react with species in the electrolyte which is accompanied with a gain of electrons. As such, the charged electrodes are strong reducing and oxidizing agents respectively and both electrodes can react irreversibly with components of the electrolyte[68,106–109]. Such reactions can be accompanied by a plethora of deleterious effects, but of primary concern is that the lithium that is used for charge and energy storage, often referred to as the lithium inventory of the cell, is irreversibly consumed by some of the reactions. This results in the loss of some amount of cell capacity,[107,110,111] equal to the charge of one electron per lithium consumed. It is a logical conclusion that if the rate of these reactions is not arrested, the cell will rapidly lose capacity and cease to function. These reactions are often referred to as parasitic reactions, or side reactions.

The reactions between the charged negative electrode and the electrolyte are of historic significance as controlling them was an enabling breakthrough for Li-ion cells. In 1990, it was observed that in a carbonate electrolyte, lithium could reversibly intercalate into carbonaceous materials, including graphite. This was accompanied by irreversible, charge consuming reactions that occurred at 1.2 V versus Li^+/Li, in a quantity proportional to the surface area of the carbon electrode. The irreversible reactions fortuitously result in the deposition of a Li-conducting passivating film that largely limits such reactions to the first charge.[112] This passivation layer is referred to as the solid electrolyte interphase, or SEI,[68,112,113] due to the similarity to the passivation film formed on Li metal electrodes in similar electrolytes.[109] The implication is that when graphite electrodes are lithiated and the potential drops below 1.2 V, the electrolyte is thermodynamically susceptible to reduction at the electrode surface.

The passivation afforded by the SEI therefore constitutes a kinetic barrier against further reactions between the electrodes and electrolyte, along with accompanying lithium consumption. Without the protection of the SEI, Li-ion cells would experience uncontrolled electrolyte reduction and rapid capacity. Without the lithium conductivity of the SEI, charge transfer from the negative electrode to the electrolyte beyond the first cycle would not be possible. The development of a stable SEI on graphite was originally unlocked through the purposeful use of the electrolyte solvent ethylene carbonate (EC), suggesting the formation of the film and its characteristics are in some way dependent on electrolyte formulation. The passivation provided by the SEI is imperfect, as capacity loss still occurs slowly over the life of the cell. In this regard, many of the characteristics of the cell are determined by the nature and efficacy of the SEI.

Many efforts to quantify the thickness-time dependence of SEI growth find it roughly follows a parabolic growth law, with thickness being proportional to $t^{1/2}$,[114–116] which matches conceptually with passivation of metals by oxide layer growth[117] and the suggests that the passivation mechanism is rooted in transport limitation.[116] Characterization of the chemical makeup and morphology of the SEI is challenging, owing to its air and moisture sensitivity[69,118], along with its dynamic nature[119,120] all presenting handling difficulties. Harris and Lu demonstrated that the SEI on graphite can have a two-layer structure, with a dense, inner layer and a porous, outer layer.[121–123] Electrolyte, namely solvation structures, can diffuse through outer porosity, before the transport mechanisms changes to bare Li^+ diffusion through the inner layer. The outer layer contains a larger proportion of semi- and poly-carbonates, along with polyolefins, while the inner layer is comprised of lithium-containing species, such as Li_2CO_3 and Li_2O.[121–123]

This agrees well with comprehensive reviews by the groups of Brett Lucht[124] and Emanual Peled.[125] Peled explains that electrons and lithium ions, supplied by the charged negative electrode, reduce solvents, salt anions and impurities to form the SEI and the reactivity of these electrolyte components towards solvated electrons can determine which components react and in which order, determining the SEI structure and chemistry. Reduction of carbonate solvents tends to yield Li_2CO_3, semi-carbonates and polymeric specifies, while salt anion reduction is responsible for inorganic compounds such as LiF.[125] Peled also remarks that ideal properties of an SEI are electronic insulation, mechanical flexibility, perfect lithium transport, strong surface adhesion, rapid formation and complete surface coverage. These properties are structure and chemistry dependent, and therefore determined by the cell chemistry, including electrolyte and electrode formulations.[125]

Lucht remarks that initially, reduction of ethylene carbonate yields a 50 nm thick SEI, primarily composed of lithium ethylene dicarbonate, accompanied by LiF from decomposition of the PF_6^- anion. If present in the electrolyte, linear carbonates can be reduced to form lithium alkyl carbonate and lithium alkoxides. It is also noted that as the SEI ages, lithium alkyl carbonates react to produce inorganic species, typically more LiF and Li_2CO_3.[124] These broad characteristics of the SEI are common to most Li-ion cells due to the near-ubiquitous nature of the $LiPF_6$ salt in carbonate solvents electrolyte formulation. The development of a performance-determining passivation film of solid reaction products naturally depends on the concentration and types of reactants available at the electrode surface. Additionally, the SEI composition and structure is regarded as dynamic, over the state-of-charge of a cell,[119] evolves over time[126] and can vary due to the environmental conditions, such as temperature, the cell is exposed to, particularly at beginning-of-life.[127] Descriptions and illustrations of the SEI structure and composition are therefore often situational.

Passivating the negative electrode against reactions with the electrolyte is immediately important for the successful operation of a Li-ion cell. The reduction of electrolyte components at the negative electrode involves electron transfer that is accompanied by lithium consumption, thereby depleting the capacity of the cell. Electrolyte oxidation processes can similarly occur at the positive electrode, although they often can occur without the consumption of lithium.[111] It has been shown that common Li-ion electrolyte components, including EC, DMC and $LiPF_6$ can be oxidized against Au, Pt and Al electrodes at 4.0 V versus Li^+/Li,[128] which does not happen continuously at considerable rates in well-built Li-ion cells.[111] This suggests that there is also a passivation

mechanism that provides a kinetic barrier against thermodynamically favorable electrolyte reactions at the positive electrode surface, like the SEI at the negative electrode.

The group of Goodenough noted the formation of a polymer surface coating on charged $LiCoO_2$ that was exposed to PC-containing electrolyte, and it was inferred that this film must contain Li-ions to facilitate conduction. Lastly, it was noted that such a film was absent in the Li_xTiS_2 intercalation system, which is far less oxidizing than $LiCoO_2$.[129] Guyomard and Tarascon correlated the capacity associated with electrolyte oxidation and the surface area of the positive electrode, suggesting the necessity of a surface coverage for a positive electrode passivating film.[130] Solid films of reaction products have been observed to occur on other positive electrode materials, including NMC-type materials, but to distinguish it from the film formed on the negative electrode, it is often referred to as a cathode electrolyte interphase,[131,132] or CEI. Like the SEI, the properties of an ideal CEI have been summarized as to provide a kinetic barrier that prevents further reactions between the positive electrode and the electrolyte, excellent mechanical properties to accommodate particle volume changes, sufficient lithium conductivity and electronic insulation.[132,133] Also like the SEI, the CEI structure and chemistry depends on electrolyte and electrode formulation, and includes decomposition products from both the solvents and salt.[131,134]

Characterization of the CEI is viewed as more challenging than the SEI. For instance, chemical constituents can include Li_2CO_3 and $LiOH$, however these can result from atmospheric contaminants, synthesis impurities, or reaction with electrolyte components.[133,134] Discerning the sources and understanding the mechanisms of CEI formation are therefore difficult. Inorganic compounds such as LiF, Li_xPF_y, and $LiPO_xF_y$

are believed to be from direct oxidation of salts, the reaction of salts with existing CEI Li_2CO_3, or the reaction of salt decomposition products (e.g. HF) with existing CEI Li_2CO_3.[133,134] Generally, the thermodynamics formation of a CEI is a function of the proximity of the electron energy levels of lowest unoccupied molecular orbital (LUMO) of the positive electrode material and the highest occupied molecular orbital (HOMO) of the electrolyte.[134] Positive electrode types can be highly varied in each cell design, and within a particular positive electrode type different ratios of transition metals are possible, changing its possible LUMO levels. Similarly, electrolyte formulations vary significantly. The decomposition of linear carbonates, cyclic carbonates and salt can occur through many possible mechanisms.[134] In all, it makes the structure and composition of any CEI and the voltage and rate at which it is formed fairly unique to a complete cell design.[133] Nevertheless, it is illustrative to consider a simple example, described by Ye et al.[135] Equation 2.1 shows a possible reaction for the hydrolysis of $LiPF_6$ in the presence of trace water.

$$LiPF_6 + H_2O \rightarrow Li^+ + HF + PF_5^- \qquad (2.1)$$
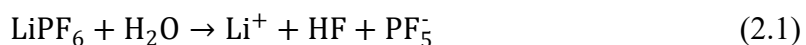
HF can react with either lithium or the transition metals in the charged negative electrode to leave solid LiF or a transition metal fluoride, such as NiF, on the surface of the positive electrode.[135]

The consequences of unmitigated electrolyte reactions with negative electrode are rapid capacity loss, electrolyte depletion or increased resistance to charge transfer as the SEI thickens. Similarly, continuous oxidation of electrolyte can lead to eventual electrolyte depletion and increased resistance due to a thick CEI. In addition to film forming reactions

at the positive and negative electrode, the electrolyte can participate in shuttle reactions where the electrolyte is reduced at the negative electrode to produce a species that can migrate to the positive electrode, where oxidation regenerates the original electrolyte component, in a cyclic and continuous product. The result is a cell that suffers from self-discharge. The interaction of the electrolyte and the positive electrode has been shown to govern the rates of both transition metal dissolution and the growth of resistive surface phases. Generally, these and other electrode-electrolyte interactions, along with their accompanying failure modes, are highly dependent on the electrode and electrolyte formulations. Specific reaction mechanisms and resultant cell properties that arise can often be unique to a given electrode and electrolyte combination, but broad trends can be observed and help direct intelligent electrolyte design.

2.2 Salts

The primary role of an electrolyte salt in a Li-ion cell is to facilitate ionic conduction through the electrolyte. Upon mixture of a lithium containing salt with a non-aqueous solvent system, dissociation of the salt occurs and Li^+ interacts with solvent molecules to form a solvation sphere or sheath. Li^+ is thought to be attracted to nucleophilic sites on solvent molecules and the solvent-cation solvation structure contributes most significantly conductivity, while evidence has been presented to suggest that in conventional non-aqueous Li-ion electrolytes, the accompanying anion remains mostly unsolvated and participates very little in bulk transport.[136] In high dielectric constant solvents, dissociation occurs readily as salt is added to the solvents. In low dielectric constant solvents, low

concentrations of salt readily dissolve, but exist in solution as ion-pairs, resulting in low overall conductivity.[137–139] Increasing salt concentrations are known to increase bulk conductivity and viscosity, through an increase in charge carriers and an increase in solvent molecules participating in a solvation structure, respectively. This holds up to a limit where further increasing viscosity inhibits ion mobility and thus decreases conductivity.[73,136] Logan et al. found that $LiPF_6$ solutions in EC/EMC and EC/DMC solvent mixtures had viscosity that increased monotonically with $LiPF_6$ concentration, whereas conductivity increased with $LiPF_6$ concentration only until around 1 mol/L, decreasing afterwards.[73]

Understanding solution structures in realistic electrolyte systems across a wide temperature range, with binary or ternary solvent blends, multiple salt species and concentrations, and being able to link them to cell performance and reaction mechanism has been described by Xu as a complex problem with a five-dimensional phase space that requires hundreds of experiments to properly map and understand.[140] This remains a research topic that requires more exploration. The most accepted view is that cyclic carbonate species form the primary solvation shell, with 4-6 coordinating a Li^+, and linear carbonates contributing to a secondary or outer solvation structure. Xu notes, however, that deviations from this model are common.[140]

Due to the reactivity of the electrodes, the salt ions can also participate in electrochemistry and side reactions that determine cell characteristics and performance. Endo et al. found that, using electron spin resonance and molecular orbital calculations, the reduction of lithium salt anions, including PF_6^-, has a highly endothermic reduction enthalpy on carbonaceous electrodes.[141] It has also been shown in *ab initio* calculations that with metal oxide positive electrodes in carbonate solutions, $LiPF_6$ has stability against

oxidation up to 5.1 V vs Li$^+$/Li.[142] Nevertheless, side reactions involving or mediated by lithium salts are known to occur.

Chung et al. showed that increasing the concentration of LiPF$_6$ in EC/DEC solutions caused greater irreversible capacity loss associated with SEI formation on carbon electrodes.[143] Increased LiPF$_6$ concentration was also correlated with decreasing cell impedance, suggesting greater amounts of lithium incorporation into the SEI causing improved conductivity.[143] Nie et al. showed that high LiPF$_6$ concentrations could enable the use of electrolytes with PC as a sole solvent against a graphite electrode. At lower concentrations of LiPF$_6$ ($\leq$ 2.4 mol/L), LiPF$_6$ existed fully dissociated in solution, PC reduction occurred, yielding a lithium propylene dicarbonate surface product and a complete lack of passivation. At higher concentrations of LiPF$_6$ ($\geq$ 3.0 mol/L), the solution structure contains solvated ion-pairs, which react at the graphite surface to form a LiF-rich surface film with excellent passivation, enabling reversible cycling.[144] The notion that solution structure is essential to negative electrode passivation and SEI formation is commensurate with the SEI formation model proposed by Winter et al., which states that SEI formation on graphite is initiated by intercalation of the entire Li$^+$-solvent solvation structure, followed by preferential reduction of some solvating molecules.[145] Varying salt concentration can affect the constituents and energy levels of solvent molecules participating in a solvation structure, thereby presenting a means of controlling or altering the SEI.

Similarly, investigations on the effect of salt concentration at the positive electrode have revealed similar influence on the CEI. Liu et al. showed using voltammetry with a scan rate of 1 mV/s that electrolyte of 1M LiPF$_6$ in EC/DMC had oxidative stability up to

6.5 V versus Li^+/Li against a Pt electrode, whereas a 6.5M $LiPF_6$ in EC/DMC electrolyte had stability against oxidative electron transfer beyond 6.5 V versus Li^+/Li.[146] Using X-ray photoelectron spectroscopy (XPS), it was shown that the surface film formed on a $Li[Ni_{0.6}Mn_{0.2}Co_{0.2}]O_2$ electrode was found to have more Li_2CO_3, unassigned species containing C-O-C bonding, Li_2O, Li_xPO_y and $Li_xPO_{y-1}F_{z+1}$, but less LiF and organic species when 6.5M $LiPF_6$ electrolyte was used. Cells constructed with 6.5M $LiPF_6$ electrolyte showed better capacity retention during room temperature, C/5 cycling between 2.8 V and 4.6 V than cells using 1M $LiPF_6$ electrolyte. This was attributed to changing HOMO levels of the electrolyte as varied salt concentration resulted in different solution structures.[146]

In addition to the influence of salt concentration on the passivation film, it has also been shown to participate in other positive electrode failure modes. Thermal decomposition of $LiPF_6$ or exposure to trace water in the electrolyte can result in HF generation in the electrolyte. Sahore et al. showed that transition metal (TM) dissolution from a pristine NMC532 electrode was due to acid attack by HF, from $LiPF_6$.[147] They also showed that transition metal dissolution from a charged NMC532 electrode was greater when $LiPF_6$ was replaced with lithium acetylacetonate. Transition metal dissolution was also greater when oxidatively unstable molecules were added to the electrolyte. Lithium acetylacetonate is described as more oxidatively unstable, compared to $LiPF_6$, and transition metal-acetylacetonate complexes are more soluble in carbonate solvents than transition metal-PF_6 complexes. It was concluded that the mechanism of TM dissolution from charged positive electrodes was oxidation of electrolyte components, accompanying reduction of TM ions in the positive electrode, and subsequent dissolution from the electrode into the electrolyte.[147] This suggests that $LiPF_6$ decomposition can damage the

positive electrode prior to charging, but once charging and cycling is underway, the oxidative stability of electrolytes with high $LiPF_6$ concentrations may protect the positive electrode from further, continuous TM dissolution. Use of a concentrated, 3M $LiPF_6$ in EC/EMC/DMC electrolyte was shown to reduce TM dissolution from a Li1.2Ni0.15Fe0.1Mn0.55O2 positive electrode.[148]

Klein et al. showed that the products of $LiPF_6$ thermal decomposition, namely PF_5 and HF, can even interact with the ceramic coatings that are common on Li-ion separators. The reaction of $LiPF_6$ with boehmite (γ-AlOOH) coated separators was shown to produce the PO_2F_2 anion,[149] which, as part of the compound $LiPO_2F_2$ (LFO) has been shown to be an excellent electrolyte additive than enables excellent cycle life in conventional[81,150] and high voltage[150–154] Li-ion cells. Klein et al. observed that γ-AlOOH reacted more readily with $LiPF_6$ decomposition products than α-Al_2O_3 and use of γ-AlOOH coated separators enabled better capacity retention in NMC532//graphite cells, compared to α-Al_2O_3 coated separators.[149] This was attributed to reaction with otherwise deleterious $LiPF_6$ decomposition species and the production of beneficial $LiPO_2F_2$.[149] Li et al. found using accelerating rate calorimetry that $Li_{0.5}CoO_2$ had greater thermal stability when heated with 1.5M $LiPF_6$ in EC/DEC (1:2) electrolyte than electrolytes with lower $LiPF_6$ concentrations. [155] It was speculated that the presence of salt altered the surface coating on the $Li_{0.5}CoO_2$ particles[155] Guo et al. used limited oxygen concentration wick combustion to show that the addition of $LiPF_6$ to DMC reduced solution flammability and DMC solutions containing $LiPF_6$ exhibited some self-extinguishing behavior that was not observed when other salts, $LiBF_4$ and LiTFSI, were used.[156] Qiao et al. reported similar results, namely superior

combustion properties for EC/PC/EMC solutions containing $LiPF_6$ when compared to $LiBF_4$.[157]

The prior discussion should strongly demonstrate that use and concentration of $LiPF_6$ can affect electrolyte properties, control the surface electrochemistry and modify the properties of resultant passivation films on both the positive and negative electrodes. In turn, the performance of the cell is affected. In addition to salt concentration, the type of salt is strongly tied to cell performance and SEI or CEI chemistry. As discussed by Xu, $LiPF_6$ is not necessarily the best electrolyte salt to suit all possible performance metrics individually, but it is the near-ubiquitous choice in modern Li-ion cells because it can satisfy most metrics very well and its use comes with far fewer compromises than other options.[133,140] Nevertheless, some alternate salts show merit in specific situations that are worth brief mention.

The use of the lithium imide salts, LiFSI and LiTFSI, are attractive because they do not exhibit thermal stability problems or reactivity towards trace water like $LiPF_6$. They also exhibit high dissociation constants and excellent solubility.[133,140] As such, they are often candidates for highly concentrated electrolytes which offer enhanced electrochemical stability[158–160], but are accompanied by high viscosity and low ion diffusivity[161]. Additionally, use of imide salts beyond cell voltages of 4.0 V has been observed to yield catastrophic corrosion of the aluminum positive electrode current collector.[140] Nevertheless, excellent performance with imide salts, superior to $LiPF_6$, in low voltage applications, such as LFP//graphite cells has been demonstrated.[89] Finally, $LiBF_4$ also does not have thermal decomposition problems that $LiPF_6$ does, but sees limited use in modern cells due to lower dissociation constant and higher viscosity than $LiPF_6$. It also does not

passivate graphite as well as $LiPF_6$,[133,136] but sees application in cells with lithium metal negative electrodes.

2.3 Solvents

Solvents primarily serve to dissolve salts and fill the inner space of the cell with an ionically conducting medium that contacts all active particles. As was discussed in Section 2.1, reversible lithiation of a graphite negative electrode was enabled by electrolyte containing EC as a co-solvent, due to passivating film formed from EC reduction products against the charged negative electrode.[112] As the combined electrolyte chemistry has a significant role in Li-ion cell performance, it is only natural that solvent formulation has been leveraged in the effort to improve cell design. Solvent choice is often primarily motivated by physical properties: sufficient dielectric constant to dissociate salts, low viscosity, high conductivity and wide liquid temperature range when salts are dissolved. Common, modern electrolyte formulations are detailed in Section 1.2.4, but unsurprisingly considerable effort has been devoted to improved solvent systems.

Initially, ethylene carbonate was thought to be necessary for graphite passivation. Ein-Eli et al. showed 1M $LiPF_6$ in EMC electrolyte would support ion conduction and lithium intercalation in graphite, but inadequate passivation led to excessive cell volume expansion, likely due to gas production from EMC reduction due to inadequate passivation.[162] Gmitter et al. studied electrolytes without EC with an aim to create electrolytes with lower freezing temperatures.[163] 1M $LiPF_6$ in EMC was shown to allow reversible cycling of carbon and $LiCoO_2$ electrodes if 5 wt% of either fluoroethylene

carbonate (FEC) or vinylene carbonate (VC) was added to the electrolyte.[163] Both common electrolyte additives, FEC[164] and VC[165,166] have been shown to be preferentially reduced on graphite, before EC and contribute to superior SEI formation. Linear carbonates, such as DMC, EMC and diethyl carbonate (DEC), have low reactivity against Li-ion electrodes[167] and therefore do not react on graphite to form an adequate passivation layer.

With the SEI sourced from either VC or FEC reduction, EC was not necessary to meet the passivation requirements for stable cycling.[163] Work by Petibon et al. showed that 1M LiPF$_6$ in EMC electrolyte with either 2 wt% or 5 wt% of either VC or FEC was a superior high voltage electrolyte in Li[Ni$_{0.42}$Mn$_{0.42}$Co$_{0.16}$]O$_2$//graphite (NMC442) cells when charged to 4.4 V and 4.5 V, compared to 1M LiPF$_6$ in EC/EMC (3:7).[168] Cyclability, storage, gas production and safety were all improved with EC-free electrolyte.[168] This work was further optimized by Ma et al. who presented an optimized electrolyte formulation of 1M LiPF$_6$ in EMC with 5 wt% FEC in the same cells, and similar experiments.[169] Xia et al. showed 1M LiPF$_6$ in EMC electrolyte with various additives yielded less gas production, less impedance growth and less charge endpoint capacity slippage, compared to 1M LiPF$_6$ in EC/EMC (3:7), in NMC442 cells tested with charging to 4.5 V.[170] These results yielded the conclusion that EC oxidation at high voltage is likely and deleterious to high voltage lifetime.

Historically, electrolytes for Li-ion cells contained approximately 30% cyclic carbonate, such as EC, and 70% linear carbonate, such as DMC or EMC, due to favorable physical properties such as conductivity and liquid range.[133] At the time of writing, anecdotes from commercial cell makers have suggested that they have adjusted electrolyte formulations to 15% EC or less. This improves certain physical properties such as

viscosity[73] and liquid range[71,171], but also improves the electrolyte stability, oxidation resistance and cell lifetime at high voltage. Finally, Xu et al. showed that varying EC concentration in solvent mixtures of EC/EMC or EC/DMC changed the composition of the primary Li^+ solvation structure, which determines the available species present at the electrode surface to react during Li^+ desolvation and intercalation.[172] EC concentrations of 35% or greater should result in Li^+ solvated exclusively by EC, resulting in an SEI on graphite composed primarily of EC reduction products. At lower EC concentrations, the amount of DMC in the solvation structure and DMC reduction products in the SEI is increased.[172] While this work was not extended to reaction at the positive electrode, it stands to reason that the improved oxidative stability of low-EC or EC-free electrolyte may have connections to the solvation structure at low EC concentration.

As an alternate route of improving conventional electrolytes for use in high voltage cells, it has been suggested that solvents with oxidation potentials greater than 5 V versus Li^+/Li should be explored, necessitating the replacement of alkyl carbonates.[173] A common method is to fluorinate carbonate solvents, such as FEC, a mono-fluorinated analogue of EC, to achieve superior oxidation resistance or anodic stability, while maintaining the physical properties, like dielectric constant, of the original carbonate.[174] Fluorine is electron withdrawing, which tends to simultaneously raise the resistance to oxidation and lower the resistance to reduction.[140] This prevents oxidation at the positive electrode and encourages preferential reduction at the negative electrode, which often yields a superior, fluorine-rich SEI.[133,175] Many studies of fluorinated solvents for Li-ion electrolytes exist,[175–180] with benefits in addition to improved oxidation resistance being lower freezing point,[167,176,177] increased ion conduction[179] lower SEI impedance,[175] and improved CEI

passivation quality[180]. Generally, fluorinated solvents have not seen much use in commercial cells in large quantities, as a co-solvent due to increased cost and handling and synthesis safety concerns[181]. There are also examples of poor capacity retention,[174] impedance growth[178] and excessive gas production[182] when certain fluorinated solvents are used.

In addition to improvements to the interfacial reactions between electrolytes and electrodes, solvent choices made to improve electrolyte physical properties can result in increased parasitic reaction at either electrode surface. Low viscosity esters, such as methyl acetate[73,75] (MA) and ethyl acetate[74,183] (EA), have been used to produce low viscosity, high conductivity electrolytes, particularly well-suited for improving fast charge capabilities.[184,185] Glazier et al. showed using a combination of ultra-high precision coulometry and isothermal microcalorimetry that the use of MA in NMC532 cells decreased coulombic efficiency and increased the rate of parasitic reactions. It was concluded that MA decreases the anodic stability of the electrolyte, leading to ongoing oxidation on the positive electrode.[186] Li et al. reported nearly identical results, also noting that the use of MA caused an increase in cell impedance[75], possibly due to accumulation of oxidation products on the positive electrode. With the use of electrolyte additives and managing charge voltage limits, use of acetate solvents appears manageable in a practical context.[74,75,186]

Many other solvents have been researched for use in Li-ion cells, including proprionates,[183] ethers,[187] nitriles[163,188] and glymes.[189] These solvents generally have a notable redeeming quality that inspires their use, but compromises in other areas, such that their use cannot be justified over carbonate solvents that compromise very little across most

physical and electrochemical properties.[133,140] Furthermore, Section 2.2 and Section 2.3 (this section) have hopefully illustrated that electrolyte optimization and the effect of electrolyte typically needs to be considered as full formulation in a specific cell for a specific application. This will become more apparent in Section 2.4, where the influence of small quantities of chemical additives to the electrolyte can alter the electrochemistry and nature of passivation on both electrodes will be discussed. In this sense, a conventional electrolyte formulation, with excellent additives may have performance so great, it does not require replacement of carbonate solvents with newer, for instance, more stable solvents. Alternately, electrolyte additives can enable solvents that have superior physical properties, but inferior electrochemical properties. Regardless of the approach, it should be stressed that full cell and electrolyte chemistry is often necessary to consider when undertaking electrolyte design.

2.4 Additives

Chemicals added to the electrolyte that react preferentially or simultaneously, over solvents or salts, on either electrode surface can be used as electrolyte additives if the reaction products provide passivation or modify an existing passivating film. Electrolyte additives are a simple and effective means of improving electrolyte and cell performance, without necessitating significant changes to existing formulations and processes.[140] There have been an overwhelming number of studies to date, involving many different additives, in many electrolyte systems, for use in a variety of cells. It is impossible to concisely review

all of them and carefully detail their influence, so what follows in this section will only cover a few representative examples, particularly those relevant to this thesis.

The most well-known additive and among the first to be utilized and understood is vinylene carbonate. Aurbach et al. found that 1M $LiAsF_6$ in EC/DMC (1:1) with 5 wt% VC reacted at artificial graphite, $LiNiO_2$ and $LiMn_2O_4$ electrode surfaces. Fourier transform infrared spectroscopy (FTIR) and XPS were used to show that VC is preferentially reduced on graphite and yields an SEI composed of a variety of polymerized lithium alkyl carbonates, with much less LiF than VC-free electrolyte. Electrochemical measurements showed that cyclability and irreversible capacity loss of graphite was improved with the VC-containing electrolyte, and impedance spectra showed lower resistance to charge transfer at the graphite surface. Benefits to $LiNiO_2$ and $LiMn_2O_4$ positive electrodes, charged to 4.2 V versus Li^+/Li at room temperature, were much less striking. It was concluded that VC formed an excellent SEI on graphite, far better than the SEI formed in the presence of VC-free electrolyte, primarily caused by EC reduction.[165] Wang et al. performed density functional theory (DFT) calculations that suggest VC participates in the Li^+ solvation sheath, alongside EC, and is reduced preferentially on graphite, rather than EC. It was proposed that an initial reduction of VC takes place, to form intermediaries that are reduced again to form lithium divinylene dicarbonate, lithium vinylene dicarbonate, R-O-Li compounds and oligomeric or polymeric vinylene compounds.[91]

VC is arguably the most commonly used electrolyte additive for cells containing a graphite negative electrode, featured in many studies, usually independent of positive electrode choice.[42,52,89,97,99,169,183,190–192] Despite the incredible performance benefits

offered to graphite negative electrodes, some drawbacks have been noted. For instance, Liu et al. showed using symmetric cells and impedance spectroscopy, that VC can contribute to increased positive electrode impedance[193] meaning it may not be suitable at higher voltages or temperatures in certain applications. This suggests that alternate additives to VC and/or combinations of additives may be required to provide more significant improvements to specific performance metrics that may be valuable in a particular application.

An additive that has seen increasing research and use in modern cells over the last five years is $LiPO_2F_2$ (LFO).[150–154,193] Martinez et al. showed that LFO is oxidatively stable up to 6 V versus Li+/Li in 1M $LiPF_6$ in EC/DEC/EMC (1:1:1 v/v) electrolyte, in cyclic voltammetry experiments against a Pt electrode.[154] Cycling experiments in $Li[Ni_{0.6}Mn_{0.2}Co_{0.2}]O_2$//graphite pouch cells showed reduced capacity fade with a 1M $LiPF_6$ in EC/DEC/EMC electrolyte with 0.2M LFO, compared to electrolyte without LFO. Examining the differential capacity during the first cycle showed no differences to the electrochemical signatures associated with SEI and CEI formation, and FTIR spectra showed no significant changes to the CEI when LFO-containing electrolyte was used, but small amounts of additional alkyl phosphate, phosphate and fluorophosphate species were observed in the SEI. The conclusion was that LFO is not preferentially consumed before solvents, and does not provide passivation, but makes a small contribution to the existing SEI. It was suggested that LFO reacts with solvent-derived SEI components such as Li_2CO_3 and lithium alkyl carbonates, to yield a modified SEI with more LiF and lithium organo-fluorophosphates. It was also suggested that LFO can react with the charged

Li[Ni$_{0.6}$Mn$_{0.2}$Co$_{0.2}$]O$_2$ to form transition metal fluoro or organophosphate surface species.[154]

Ma et al. found similar results in NMC532//graphite pouch cells.[150] XPS showed that SEI layers formed in cells using an electrolyte of 1.2M LiPF$_6$ in EC/EMC (3:7 w/w) with 1% LFO were thinner than the same electrolyte without LFO, and more fluorophosphate species were found. Like Martinez et al., no electrochemical signs of first cycle reduction or oxidation of LFO were found. When electrolyte containing LFO was extracted from cells after the first cycle and examined using nuclear magnetic resonance (NMR) spectroscopy, a small amount but not all LFO was consumed. This led the authors to conclude that LFO prevents carbonate breakdown to a certain degree[194]. This conclusion somewhat disagreed with conclusions from Martinez et al.[154] The use of LFO did not seem to affect the composition or thickness of the CEI, according to Ma et al. using XPS. They also noted lower charge transfer resistance, less charge transfer resistance growth, and less capacity fade for cells containing electrolyte with 1% LFO, compared to either 2% VC or additive-free electrolyte when cycled at both 20°C and 40°C with charging to 4.3 V.

Further studies by Liu et al.[193] and Aiken et al.[153] have shown the use of electrolytes containing 1% LFO offer superior protection against positive electrode impedance growth in cells containing NMC532 positive electrodes.[153,193] Finally, Liu et al. showed that electrolytes containing 0.2M LFO can yield dramatically better capacity retention than LFO-free electrolyte in NMC811/Li-metal cells over 120 cycles with charging to 4.5 V. This was attributed to the use of LFO preventing impedance growth and transition metal dissolution from the positive electrode. It was observed using XPS that after 120 cycles, the positive electrode surface exposed to electrolyte containing 0.2M LiPF$_6$ had fewer

solvent decomposition products, more LiF and the presence of $Li_xPO_yF_z$, possibly from $LiPF_6$ or LFO decomposition.[151] Layered positive electrodes containing large Ni concentrations, such as NMC811, have been noted to have crystal structure contraction, accompanied by impedance growth,[43] therefore, the results by Liu et al.[151] suggest electrolyte composition and specifically the use of LFO can protect from structural problems as well. Similar results were obtained, where Li et al., showed that growth of a crystallographic surface reconstruction on NMC811 positive electrodes could be controlled using different electrolyte additives, pro-1-pene-1,3-sultone (PES) or VC, when compared with additive-free electrolyte.[52]

In Section 1.2, the aspects of cell performance where additives have been used to affect improvements are listed, with references. To avoid redundancy, they will not be listed again here. Suffice it to say that for any measurable, additives are among the first materials screened and tested to achieve either direct or indirect improvements. An example of a direct improvement may be improved power capability of an existing cell chemistry, by way of an additive-generated SEI with lower impedance. An indirect improvement may be achieving higher energy density cells, by enabling a higher energy density electrode material via longer lifetime, that has insufficient lifetime without the additive.

The works covered in this section show electrolyte additives can affect electrode surface chemistry, control cell impedance, affect electrode surface structure, and more. As detailed in Sections 2.2 and 2.3, this is true of other changes to electrolyte formulation, such as salt and solvent choice. The two prior sections and this section repeatedly mention the notion of the complete electrolyte formulation and particularly the electrolyte

components solvating lithium ions as the key determining factor in cell performance. Electrolyte additives are very powerful because they allow significant changes to the electrolyte electrochemistry, without making significant changes to the electrolyte formulation. An additive such as VC can participate in the Li^+ solvation structure and react preferentially at the electrode surface. Only a small amount of VC is necessary to alter the SEI chemistry and in turn allow improved operation while the salt and co-solvents remain the same. The result is largely unchanged electrolyte physical properties, but vastly superior electrochemical performance. Nevertheless, to achieve a truly optimized and advanced electrolyte formulation, testing and understanding needs to be developed that includes the role of all three main electrolyte components. With that being said, the detailed, mechanistic understanding behind electrode-electrolyte interactions that would allow perfect, *a priori* electrolyte design does not yet exist. For a select few electrolyte formulations, reaction mechanisms have been elucidated and the chemical species that can be found in the SEI or CEI have been measured and reported. The ideal SEI or CEI thicknesses, fraction of each reaction product, and film microstructure, along with how to achieve those ideals are not well understood. Research into electrolytes for Li-ion cells therefore relies highly on screening, trial and error, and piecing together limited understanding in small steps.

CHAPTER 3 EXPERIMENTAL METHODS

3.1 Lithium-Ion Pouch Cells

Electrochemical measurements performed throughout this thesis were made on commercial quality, machine made pouch cells obtained from LiFUN Technology (Zhuzhou City, Hunan Province, People's Republic of China). LiFUN sources electrode active materials, formulates electrode slurries, coats electrodes, winds "jelly rolls" and handles final cell assembly, except for filling with electrolyte. Cells are made to requested specification, in terms of active material types and amounts, electrode geometries along with final cell size, capacity and operating voltage. Academic, laboratory scale research often utilizes coin-type cells with handmade electrodes as the electrochemical workhorse. Coin cells work well with small amounts of materials and can be assembled with simple equipment,[27] but are often difficult to make with high repeatability and precise control over electrode and cell parameters.[195] Furthermore, to make a sufficient number of coin cells required for large studies is particularly laborious. Alternately, the equipment and manufacturing expertise offered by a manufacturer like LiFUN enables studies at a scale and with ease that would not be possible using hand-made cells.

Cells are supplied sealed and without electrolyte. This is for two reasons. Firstly, these cells are typically a test vehicle to study the effect of changes to electrolyte formulation. Given dry cells, it is easy and efficient to mix small quantities of different electrolytes as needed for each experiment. Secondly, cells that do not have electrolyte are effectively not batteries. This makes them easy and safe to ship, while cells only start aging

and undergoing parasitic reactions once filled. In this sense, full control over experiment timing is afforded.

Table 3.1. Cell chemistry, balance, cycle testing parameters and a chapter reference, for LiFUN pouch cells used in this thesis. Detailed specifications of the materials and assembly of each cell type can be found in Appendix A. *The cells listed as NMC811 are best represented by this nominal formulation, but known to have 83 atomic percent Ni, and correspondingly less Mn/Co, rather than 80% Ni, 10% Mn, 10% Co.

Positive Electrode	Negative Electrode	Cell Balance (V)	Cycle Test	Temperature (°C)	Chapter
NMC532		4.40	Cycle-Hold, Cycle-Store	20, 40	4
NMC640		4.50	CCCV	20, 40, 55	5
LFP	Artificial Graphite	3.65	CCCV, Cycle-Hold	40, 55, 70	6,7
NMC532		3.80	CCCV, Cycle-Hold	40, 55, 70	6,7
NMC640/LFP		3.80	CCCV	40, 55, 70	7
NMC811*		4.06	CCCV	40, 55, 70	7

Figure 3.1c shows a photograph of a pouch cell, as obtained from LiFUN. The cells are denoted by the size 204035, meaning a 20 mm × 40 mm × 3.5 mm sized prismatic volume occupied by the jellyroll and casing immediately housing the jellyroll. These cells are constructed with some excess casing, labeled in Figure 3.1 as the gas bag, which allows for the collection of any gases produced. The casing is an aluminized polymer, capable of sealing against itself under the application of sufficient heat and pressure. Typically, this cell size allows for reversible storage of 240-250 mAh when NMC-type positive electrodes are used. Exact electrode materials, loadings and capacities vary for different cells used in this thesis. Table 3.1 offers a summary of the cells used, in terms of composition and testing

parameters. Precise details of the specifications of electrode materials, electrode, and cell assembly, along with material suppliers for all cells used throughout can be found in Appendix A. Additional details related to cell construction, test procedures and electrolyte formulations are included in this chapter and the chapters where results for each cell type are presented as needed.
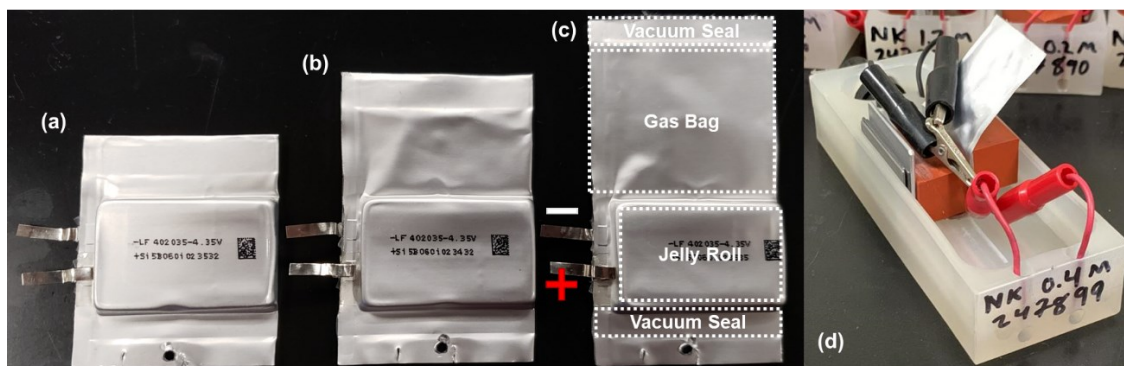
Figure 3.1. Photograph of Li-ion pouch cells (a) after degassing and ready for testing, (b) after drying and filling with electrolyte, and (c) as obtained from LiFUN. (d) Photograph of a Li-ion pouch cell constrained and four wire connected in a polypropylene cell holder.
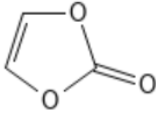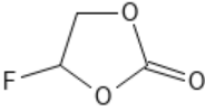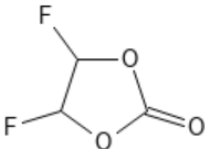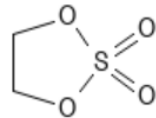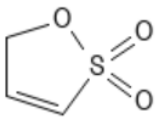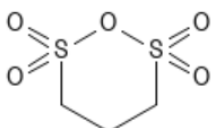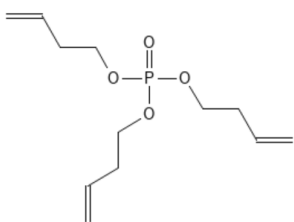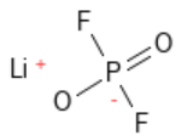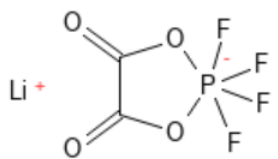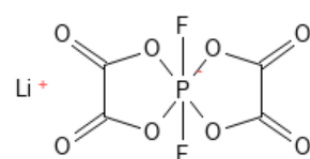
The pouch cells used in this thesis are treated as identical, when among the same batch (e.g. same electrode materials, coating specifications, etc.). This is due to the combination of high quality construction from the manufacturer and many years of collective experience working with cells of this type at Dalhousie University. Anecdotally, extrinsic properties, such as the mass or capacity of a cell, can vary slightly from cell-to-cell by an amount of at most a few percent. Quantities that can be represented as a fraction of the initial mass, capacity or some other value, or intrinsic properties tend to show far less cell-to-cell variation. Examples of this could include the rate of fractional capacity loss or the electrode voltage at which a reaction takes place. Furthermore, trends and differences of behavior between cells that are identically prepared other than large changes of a single

parameter along a gradient, such as a series of cells made with increasing electrolyte salt concentrations, are typically immune to any cell-to-cell variation effects. Due to limitations on available cells and available test equipment that are encountered in a shared laboratory environment, compromises on ensemble sizes were made. There are often instances where it is not economical to work in large batches of cells. In these cases, individual cells per variation are tested or a single cell from a batch is allowed to continue under test while duplicates are removed to free up charger space. These individual cells are considered an adequate representation of the experimental parameters being studied and the variation among duplicate cells is very small, particularly in case where experiments are designed with large changes to varied parameters.

3.2 Electrolyte Preparation

Electrolytes were prepared in an argon-filled glovebox. Solvents were measured and dispensed by volume using a micropipette (Mettler Toledo, Columbus, Ohio, USA), while solids including the salt were measured using by weight using a Shimadzu AUW-D analytical balance (Shimadzu Corp., Kyoto, Japan). Electrolyte solvents and salts were initially supplied by BASF and later by Shenzhen Capchem Technologies. All materials were high purity, battery grade where possible, and used as received from the manufacturers.

Table 3.2. Additives used in this thesis, described by name, acronyms found in this text, chemical structure, and supplier.

Name	Acronym	Structure	Supplier
Vinylene carbonate	VC		BASF/Capchem
Fluoro ethylene carbonate	FEC		BASF/Capchem
Difluoro ethylene carbonate	DiFEC		Jiangsu HSC New Energy Materials
1,3,2-Dioxathiolane 2,2-dioxide	DTD		Guangzhou Tinci New Materials Technology
1-Propene 1,3-Sultone	PES		Lianchuang Medicinal Chemistry
1,2,6-oxadithiane 2,2,6,6-tetraoxide	ODTO		Guangzhou Tinci New Materials Technology
Triallyl phosphate	TAP		TCI America
Lithium difluoro phosphate	LFO		Shenzhen Capchem Technologies
Lithium tetrafluoro oxalato phosphate	LiTFOP		Zhuhai Smoothway Electronic Materials
Lithium difluoro di(oxalato) phosphate	LiDFDOP		Zhuhai Smoothway Electronic Materials

The baseline formulation used was a solution $LiPF_6$ in EC/DMC (3:7 w/w). The concentrations of $LiPF_6$ used in each experiment varied and will be denoted where necessary. Additionally, some deviations from this formulation occurred in many experiments. These will also be denoted where necessary, accompanying relevant results. Finally, to the baseline electrolyte formulation, electrolyte additives specific to each experiment were included. These will also be noted where relevant, but for completeness, the names, structures, and suppliers have been included in Table 3.2. As mentioned in Chapters 1 and 2, countless electrolyte additives have been tested, including many various types of materials. Table 3.1 shows that the additives used in this work can generally be sorted into three major groups: functionalized carbonates, sulfur-containing compounds, and phosphorous-containing compounds. Among the phosphorous containing compounds, a group of lithium salt additives exist, which are related to the structure of $LiPF_6$, with various degrees of replacement of F by O atoms, or oxalate groups.

3.3 Cell Assembly and Preparation

In preparation for filling with electrolyte, cells were transferred to an argon-filled glovebox and cut open. The opened cells were transferred to a vacuum oven attached to the glovebox and heated at 120°C for 14 h to remove any excess moisture that can remain trapped in the porosity of the electrodes and separator. This may cause poor cell performance due to the moisture sensitivity of the cells once filled with electrolyte and charged.[196] Ensuring that cells are only cut open once in an inert atmosphere prevents any exposure of the positive

electrode to oxygen and moisture, to which it can be sensitive, even as a pristine coating before electrolyte is added.[197]

After drying, a micropipette (Mettler-Toledo, Columbus, Ohio, USA) was used to dispense approximately 4 g/Ah of electrolyte into each cell. This quantity varied slightly depending on the density of electrolyte. The jellyroll was manually massaged in an effort to expel any argon gas trapped in the electrodes and encourage preliminary wetting of the electrodes and separator by the electrolyte. Cells were next transferred to a sealed metal canister, which was evacuated for approximately one minute in further effort to remove any trapped argon bubbles and facilitate wetting. Finally, the cells were transferred to a vacuum sealer (MSK-115, MTI Corp., Richmond, California, USA) where a vacuum of -90 kPa gauge pressure is applied before the cell is sealed. The cells were removed from the sealer and glovebox. The actions of cutting the cell open and resealing are done at the top of the gas bag, therefore the cell has a smaller gas bag after filling and sealing. This is shown in Figure 3.1b.

Prior to any electrochemical testing, the cells were mounted in cell holders originally described by Dahn et al.[198] The cell holder is formed from a milled piece of polypropylene, forming a low thermal mass, insulating structure. The cell holder allows for four-wire or Kelvin connections that allow for the independent measure of current and voltage when connected to electrochemical test equipment, preventing inaccuracy in the voltage measurement when current is flowing. The cells were constrained in the holder, as shown in Figure 3.1d, using rubber blocks (orange) such that pressure was exerted on the jellyroll and any gases produced during testing were forced out of the jellyroll, up into the

gas bag. Steel shims were used to ensure a snug fit, achieving an applied pressure to the jellyroll, estimated by Louli et al. to be less than 75 kPa.[199]

Cells were then connected to a constant voltage power supply, set to 1.5 V. This does not result in appreciable current flow to or charging of the cell, but depresses the voltage of the negative electrode sufficiently to avoid dissolution of the copper current collector into the electrolyte that is known to happen at high negative electrode potentials, or correspondingly low cell potentials.[200,201] Cells were left at 1.5 V for 24 h, to allow time for electrolyte to diffuse into the jellyroll and wet any areas yet to achieve contact with the electrolyte. Finally, cells underwent a first electrochemical cycle prior to any other testing. This first cycle, completed at elevated temperature to form an excellent SEI, hence is referred to as the formation cycle. The formation cycle was completed on a Maccor Series 4000 charger with a current of C/20, or current such that the full capacity of the cell is achieved in 20 h, in a temperature-controlled chamber set to $40.0 \pm 0.1°C$. Once a single charge and discharge, or cycle, was completed between appropriate voltage limits for the cell chemistry, the cell was recharged to approximately 50% of the full capacity and removed from the charger. To remove any gases produced during SEI forming reactions, the cells were returned to the glovebox, cut opened, and resealed under vacuum. The removal of gases is referred to as degassing. Figure 3.1a shows a cell after being formed and degassed. After degassing, the cells completed various forms testing and/or characterization.

3.4 Electrochemical Cycling

The most common mode of testing full cells is to repeatedly charge and discharge, or cycle, the cell. The capacity discharged as a function of cycle number, the capacity as a function of applied current, the charge or coulombic efficiency and the voltage polarization are among the many measurables of interest that can be determined via cycling experiments. The methodology and programming behind the cycling protocol can affect cell performance and measured quantities.

A battery charger or cycler typically functions as a programmable power supply with variable current and voltage outputs, along with a precision multimeter. Cells are commonly (dis)charged with constant currents in laboratory testing. The charger adjusts the output to ensure the current matches the set point, using the measured voltage and current from the multimeter as feedback parameters. Conventional to the battery field, currents are typically specified relative to the full cell capacity in a language that indicates the time a charge or discharge will take. If a 1 Ah cell is charged and discharged with a current of 1 A, the complete charge or discharge will take 1 h. If the same 1 Ah cell is charged and discharged with a current of 50 mA, the complete charge or discharge will take 20 h. For this hypothetical cell, 1 A and 50 mA are referred to as 1C and C/20 respectively, where the general format is C/X given a current the completes a charge in X h. The amount of capacity a cell can store is understood to be between a particular set of voltage limits. The upper cutoff or charge endpoint voltage is the voltage at which the charge is stopped, and the lower cutoff or discharge endpoint voltage is the voltage at which the discharge is stopped.

3.4.1 Constant Current-Constant Voltage Cycling

Cells which are subject to an applied current show a polarization voltage drop proportional to the magnitude of the applied current. This is due to kinetic limitations within the cell for processes such as Li diffusion and charge transfer at interfaces. This can be conceptualized very simply, by considering a Li-ion battery as a voltage source connected in series with an internal resistance. The voltage drop associated with current flow is simply the product of the current with that internal resistance. As such, a cell that is charged at a constant current (CC) may reach the charge endpoint voltage, but when the current is turned off, the voltage of the cell drops to some lower value. To allow the cell to equilibrate at and properly reach the charge endpoint voltage, cells are typically held at constant voltage (CV) at the charge endpoint voltage. Current continues to flow, although diminishes as the effect of the internal resistance is overcome, until becoming negligibly small. There is no CV step at the end of discharge, because for practical usage in a device, power is the most important quantity, so extracting more capacity at a low voltage with a diminishing current is of no value.

Figure 3.2a shows the cell voltage as a function of time for a cell undergoing a CCCV charge protocol. In the work detailed in this thesis a typical CCCV protocol was to charge at constant current of C/3. When the charge endpoint voltage is reached, the cell is held in a CV step until the current diminishes to a value less than or equal to C/20. In cells with low internal resistance and when the currents are not large ($\geq$ 1C), the amount of time spent in the CV step is very small, and difficult to visualize. This is the case in Figure 3.2a. CCCV protocols were utilized in Chapters 5 and 7, and specific currents, voltage limits and test temperatures will be mentioned there, as appropriate.

3.4.2 Cycle-Hold Testing

Figure 3.2a shows that CCCV charging protocols are generally very symmetric, with nearly equal time spent charging and discharging, with very little time spent near the charge endpoint voltage. For reference, the average voltage of the cell undergoing CCCV testing typically turns out to be the voltage that corresponds to approximately 50% state of charge, because the voltage-time profiles are symmetric, and no additional time is spent at any particular state-of-charge. In an NMC532 cell balanced for operation to 4.4 V, this is a time-averaged voltage of approximately 3.8 V. By spending more time at the charge endpoint voltage, the electrochemical stress placed on the cell is increased. A method demonstrated by Nelson et al. was to include long duration (20-24 h) CV steps or "CV Holds" at the charge endpoint voltage, after completing a CC charge.[190,202]

Here, a modification of the procedure by Nelson et al. was implemented, as described by Aiken et al.[153] Figure 3.2b shows the cell voltage as a function of time for a cell undergoing a cycle-hold test protocol. The cell is charged and discharged using a constant current of C/3. Every second cycle, at the end of charge, the cell is held at constant voltage at the charge endpoint voltage for 24 h. An NMC532 cell balanced for operation to 4.4 V undergoing cycle-hold testing spends two-thirds of its life at the charge endpoint voltage and experiences a time averaged voltage of 4.2 V. This is much more aggressive than the CCCV protocol described in Section 3.4.1. Cycle-hold protocols are designed to induce greater rates of electrolyte oxidation, more electrode material stress, and overall faster rates of failure. Cycle-hold testing is generally completed at 40°C, where elevated temperature complements the increased electrochemical stress, however some examples at 20°C will be noted where relevant. Cycle-hold testing is utilized in Chapters 4 and 6.

3.4.3 Cycle-Store Testing

Figure 3.2c shows the cell voltage as a function of time for a cell undergoing cycle-store testing. A cycle-store test protocol is programmed almost identically to a cycle-hold test protocol, described in Section 3.4.2, except that every second cycle, at the end of charge, the cell is effectively disconnected from the charger for 24 h, rather than holding at constant voltage for 24 h. This effectively places the cell in an open circuit condition. Cells in storage, and cells undergoing storage testing are similarly in an open circuit condition, therefore this test is given the name cycle-store.

A cell experiencing an open circuit will self-discharge at a rate that is dependent on many factors, including temperature, storage voltage and cell chemistry. This self-discharge causes the time averaged cell voltage to be lower than an identical cell undergoing cycle-hold testing, but still much higher than conventional CCCV cycling. As such, cycle-store testing is less aggressive than cycle-hold testing, but still an effective means of probing high voltage behavior of cells and accelerated failure. Cycle-store testing is mentioned in Chapter 4.
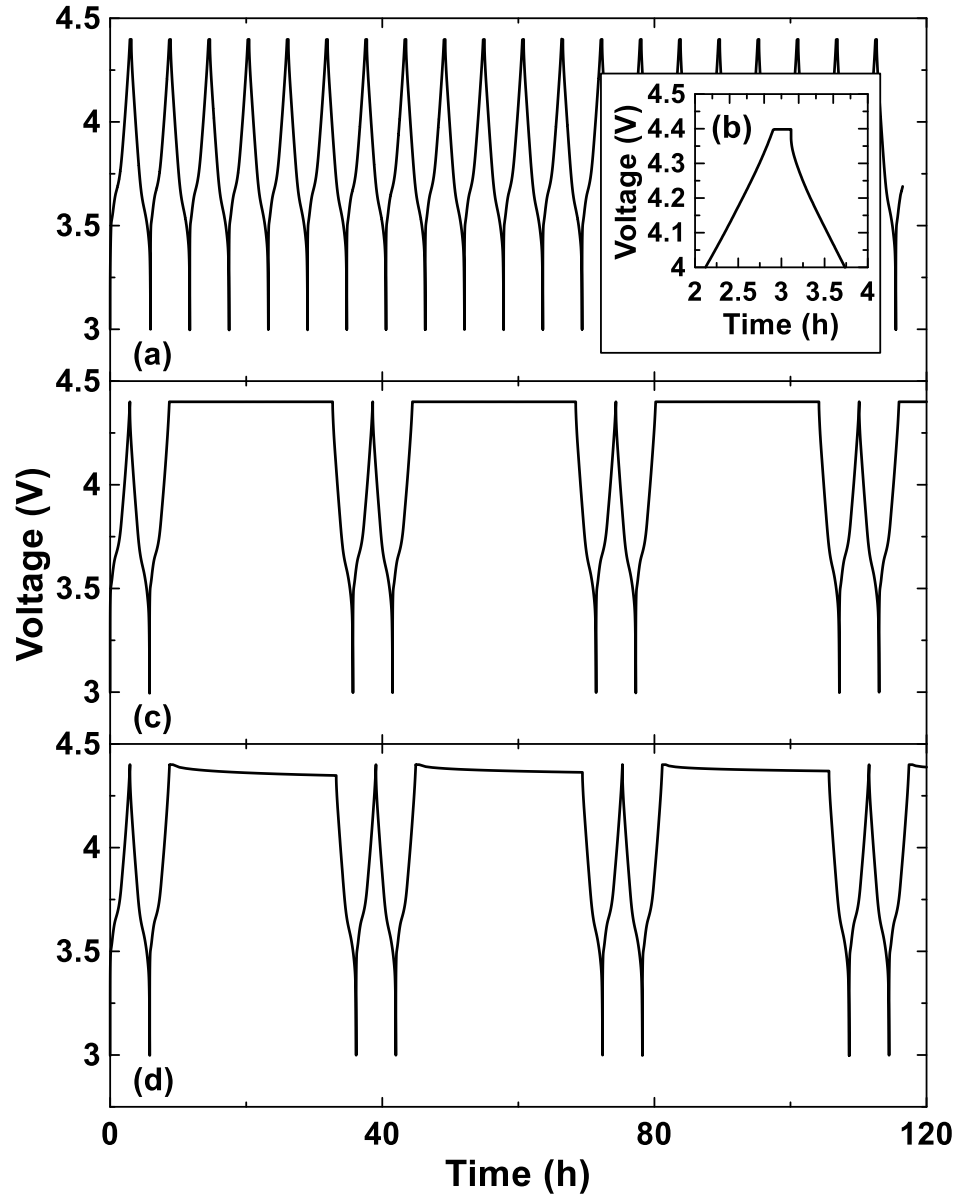
Figure 3.2. Voltage as a function of time for NMC532 cells charging to 4.4 V with C/3 current, under (a) constant current-constant voltage (CCCV), (c) cycle-hold or (d) cycle-store protocols.

3.4.4 Constant Capacity Cycling

Constant capacity cycling, or more correctly, cycling with a constant charge capacity delivery is a novel cycling protocol that takes advantage of a unique cell construction. This has been published by Aiken et al.[15] and will be described in greater detail in Chapter 7. A

visualization of the positive and negative electrode voltage curves in a full Li-ion cell and how they combine to yield the cell voltage curve was shown in Figure 1.3. Among the modes of capacity loss, lithium consumption at the negative electrode due to imperfect passivation can have the effect of the negative electrode shifting horizontally to the right, relative to the positive electrode on the capacity axis. When charging between constant voltage limits, such as CCCV, described in Section 3.4.1, this results in reduced cell capacity. In cells that are constructed with excess positive electrode capacity, that excess capacity can be accessed by charging to higher voltage and can be used to offset the capacity loss due to negative electrode slippage.
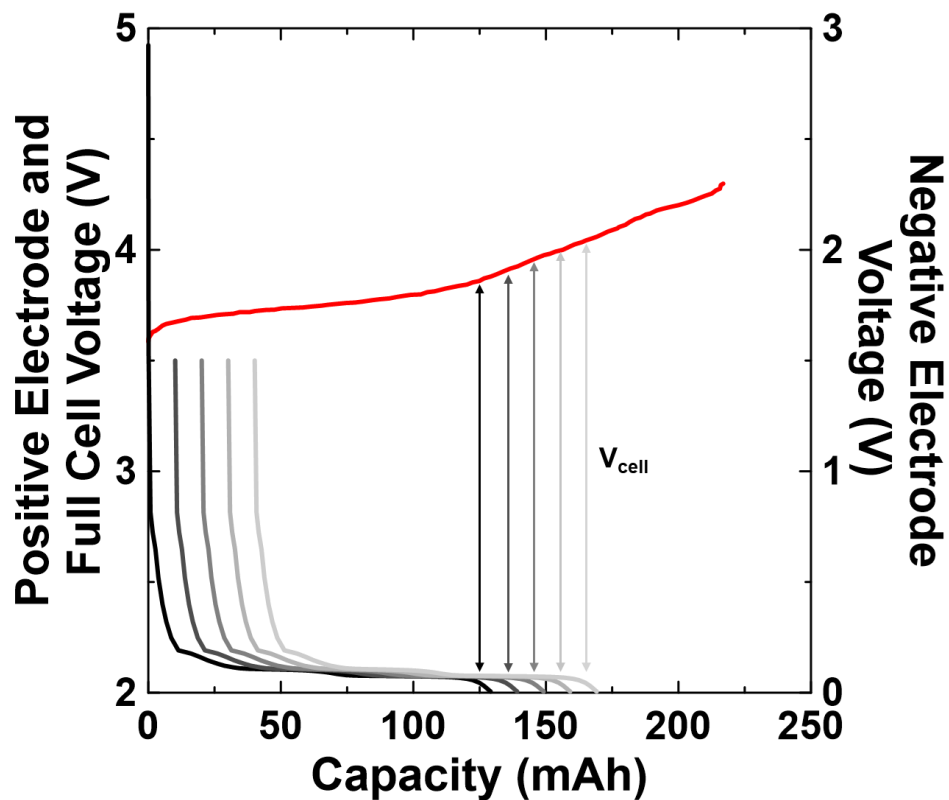
Figure 3.3. Positive electrode (red, left axis) and negative electrode voltage curves (greyscale, right axis) for an NMC811/graphite cell balanced for operation to approximately 3.8 V. The negative electrode is considered with varying amounts of slippage. The cell voltage corresponding to full graphite usage is indicated in a color matched arrow.

Figure 3.3 shows the voltage curves in a cell with excess positive electrode capacity, where several negative electrode voltage curves are shown in a greyscale color series to indicate increasing amounts of shift loss or slippage. If the cell is charged enough to fully utilize the graphite capacity, the voltage of the positive electrode and the corresponding charge endpoint voltage must increase as the amount of negative electrode slippage increases. To implement this in a charging protocol, it is sufficient to charge the cell at constant current for a constant amount of time, thereby delivering a charging a constant amount of capacity. It is necessary that this amount of charge be less than the graphite capacity, otherwise Li-plating would occur. The cell can then be discharged normally, using a constant current until the set discharge endpoint voltage is reached. Through this method, monitoring the charge endpoint voltage, or the voltage reached at the end of charge that results from charging a constant capacity, can provide insight into the state of the cell. It can determine how much of the positive electrode capacity reservoir is accessed as the test matures, can help indicate when new failure modes are likely to arise (e.g., electrolyte oxidation or impedance growth), and can be used to predict or schedule the end-of-life. In this case, end-of-life during constant capacity charging was determined to be when the charge endpoint voltage reaches 4.3 V, since beyond this voltage a host of deleterious effects are expected to occur at increasing rate.

This was implemented in Chapter 7 on a cell that had lost 20% of its beginning-of-life capacity or had 80% capacity remaining. The cell then completed constant capacity cycling with the constant capacity delivered during the charge set at this same 80% value. This means that in the absence of any negative electrode active mass loss, there is a buffer against lithium plating, equal to 20% of the graphite capacity.

3.4.5 Long-Term Cycling Equipment

Most of the electrochemical cycling was performed on various Neware Battery Test Systems (BTS). Various models of different ages with nearly identical functionality were used, with a suitable representative model being a Neware BTS4000. The chargers are typically capable of 5V 1A output, but the current ranges vary slightly among the various models. These chargers can execute all cycling methods described in the previous four sections with some modification to the software configuration and provide sufficient data quality. Some of the results obtained in Chapter 4 were collected using a high precision charger built in-house using Keithley Instruments 2602 source-measure units. This specific instrument is described in Aiken et al.[153] and draws heavily from the design originally implemented by Smith et. al.[203] This was originally assembled to provide a high degree of control and measurement precision during the 24 h hold or open circuit storage implanted in cycle-hold and cycle-store testing. It was quickly determined that this quality of equipment was excessive for the needs of cycle-hold and cycle-store experiments.

All cycling experiments are done in temperature-controlled environments. The lowest cycling temperature in this work is room temperature. Cycling at room temperature was done in an air-conditioned room set at 20°C, with a closed door. The actual temperature has been measured as 18.1 ± 0.3°C. There is a relatively large fluctuation, but this fluctuation is not large compared to the temperature difference to hotter test temperatures. Cycling at 40°C, 55°C and 70°C is completed in temperature chambers built in house, or repurposed laboratory-grade ovens. Both are designed to minimize temperature gradients and maintain the set temperature to within 0.1°C.

3.4.6 Ultra-High Precision Coulometry

Long-term cycling measurements, as previously described, can be complemented by short-term measurements made with high precision and accuracy. Smith et al. detailed the design and use of a high precision charger in 2010,[203] which has been in use and seen improvements[204] in the time since. Ultra-high precision coulometry (UHPC) can allow for the careful measurement of the rate of capacity loss in very few cycles, along with transformation of the voltage curves. This provides non-destructive insight into degradation mechanisms in the cell and their rates.

The primary metric typically associated with UHPC measurements is the coulombic efficiency (CE), or the ratio of capacity discharged to the capacity charged. The rate of capacity loss, or fade, and the rate of change of the charge endpoint capacity (or slippage) have been used to provide insight into the rate of parasitic reactions at the negative and positive electrodes, respectively.[111] These constitute secondary metrics which can be used to provide underlying context to a CE measurement. Such measurements were made on cells immediately after formation and degas. Cells were cycled at a rate of C/20 at 40°C for 16-20 cycles to allow for sufficient SEI maturation, ideally yielding CE, fade and charge endpoint slippage that had reached nearly constant values. In cases where these quantities are reported as single point values, those values were obtained from averaging the final three cycles of each experiment.

Careful measurement of a full cell voltage curve, by a UHPC system, along with measurement of the individual electrode voltage curves can allow the calculation and fitting of the full cell voltage curve, using the constituent electrode voltage curves. To increase the sensitivity to features in the voltage curve, the calculation and fitting process

is generally done using the derivative of the voltage curve, dV/dQ versus Q, rather than the voltage curve itself. This technique, referred to as differential voltage , developed with contributions from Bloom et al,[205–208] Honkura et al.[209] and Dahn et al.,[210] allows for the determination of the amount of active mass and relative shift between the positive and negative electrode voltage curves.[210] The quantification of active mass loss and shift loss allows for non-destructive and facile study of cell failure. Measurements for differential voltage analysis were completed on a UHPC system at 40°C, using a C/40 rate. Two cycles were completed, and fitting of differential voltage curves was done using an updated version of the software detailed by Dahn et al.[210] Positive and negative electrode reference voltage curves were taken from an internal library, with measurements originally performed by Jing Li.

3.5 Electrochemical Impedance Spectroscopy and Symmetric Cells

Electrochemical impedance spectra (EIS) were collected for cells at beginning- and end-of-life using a Biologic VMP3 potentiostat. Measurements were made using an applied signal with 10 mV amplitude and frequency that varied from 10 mHz to 100 kHz. EIS measurements were performed on cells that were charged to approximately 50% state-of-charge and held in 10.0 ± 0.1°C temperature-controlled chambers. Cells were charged to approximately 50% state-of-charge (approximately 3.8 V for NMC cells, or 3.3 V for LFP cells) in accordance with convention and due to the fact that both the positive and negative electrodes become increasingly blocking in the fully charged or discharged state.

Impedance spectra are measured as a function of frequency. The frequency response of various simple circuit elements (e.g., capacitors) is determined by measuring the current response to an applied voltage stimulus that is periodic, with variable frequency. Because the current can be out of phase with voltage, visualization of impedance is aided by representation on the complex plane. Impedance spectra are commonly represented as Nyquist plots where the impedance is plotted as a two-dimensional quantity with a real and imaginary component, where the angle relative to the real axis is understood to be the phase angle and the distance from the origin is the magnitude of the impedance. Figure 3.4 shows calculated, representative Nyquist plots. The impedance of a Li-ion cell is conventionally described with a Randles equivalent circuit, a schematic of which is inserted in Figure 3.4a. A series resistance, R_s, is used to represent the bulk electrolyte resistance, while a parallel resistor-capacitor element is used to represent the active material-electrolyte interface. The capacitance, C_{dl}, represents the charging of the surface double-layer that naturally arises at a working electrode, while R_{ct} is the resistance to charge or lithium transfer at the particle surface. A Warburg element, denoted as W in Figure 3.4a, is a type of constant phase element included to encapsulate the effects of diffusion.[99]
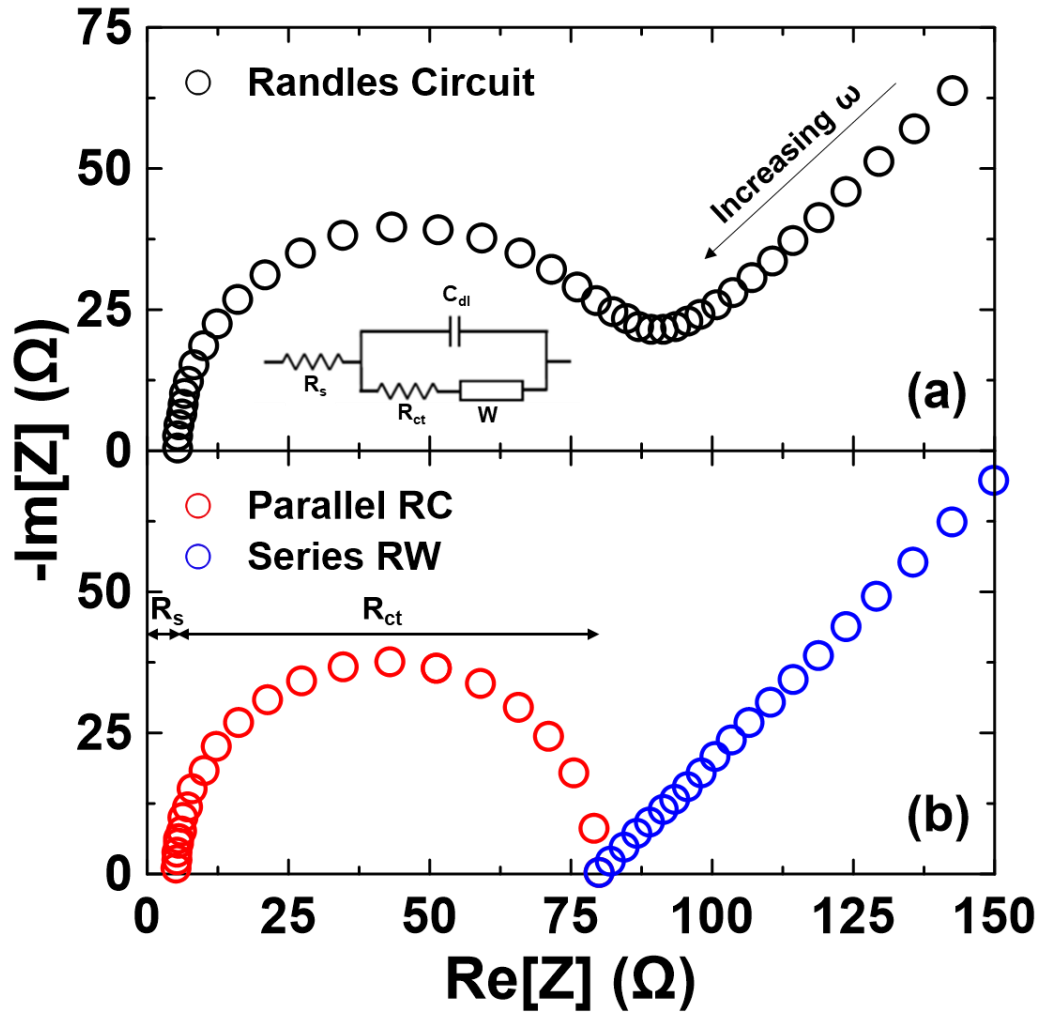
Figure 3.4. Nyquist plot of representative impedance spectra for (a) a Randles circuit and (b) separate RC and RW elements. While not noted in the legend for panel (b), the same series resistance, R_s, is assumed. The impedance of the series RW element is horizontally offset by an additional amount R_{ct} to obtain positioning that reflects panel (a).

Figure 3.4a shows the calculated impedance spectrum for the representative Randles circuit included in the figure. Figure 3.4b attempts to isolate the shapes observed in Figure 3.4a and highlight their origin. A series resistance, such as R_s, results in the entire spectrum shifting to the right. The impedance spectrum of a parallel RC element with resistor R_{ct} and capacitor C_{dl} is a semi-circle with diameter R_{ct}. The positioning of points, as a function of frequency, along the semi-circle is dependent on C_{dl}. The impedance of a

series RW element yields a 45° line that contributes to a "Warburg tail" observed at low frequency. Anecdotally, the spectra measured in real Li-ion cells can have a low frequency tail which deviates from 45°, and therefore cannot be convincingly described by a Warburg element. Generally, constant phase elements have questionable physical validity which leads to difficulty extracting meaningful information when they are used.

A simple and well accepted method of analyzing impedance spectra is to assign the high-frequency intercept with the real axis to the series electrolyte and electrode resistance, R_s, and the distance along the real axis between the high-frequency and low-frequency intercepts to the charge transfer resistance, R_{ct}. This method ignores many of the details of the spectra and is an idealized interpretation but has an acceptable physical basis. A real cell (and associated electrical connections) also can have an inductive contribution to the impedance. In practice, the high-frequency intercept is not just determined by a series resistance, R_s, but also the frequency at which the imaginary impedance contributions from capacitance and inductance add to zero. It has been shown that multiple semi-circular features can be measured, due to an interface with the electrolyte at each electrode, contact impedance, and more.[211] These can be fit with many RC elements, using a transmission line type of model,[212] but models with many parameters often struggle to establish a physical basis for all parameters and terms. When multiple features are present in a spectrum, the charge transfer resistance obtained as described previously is simply said to represent the combined resistance to charge transfer across many interfaces and processes.

One means of isolating the origin of features measured in full cell impedance spectra is the construction of symmetric cells, originally described by Petibon et al.[99] Symmetric cells are cells constructed with a pair of like electrodes. A positive symmetric

cell would contain a pair of positive electrodes, and no negative electrode, but otherwise assembled like any other Li-ion cell. A negative electrode symmetric cell would similarly contain two negative electrodes. When a full cell is disassembled, its electrodes are harvested and used to make symmetric cells, Petibon et al. found that the impedance of the full cell was equal to the average of the impedance of the resultant positive and negative symmetric cells. This apparent average comes about from the fact that cells are constructed with two electrodes in series. The measured impedance of a symmetric cell therefore contains the contribution from two identical electrodes connected in series and must be halved to account for each electrode individually. Comparison of the symmetric cell spectra indicates if the positive electrode or negative electrode is responsible for the majority of the full cell impedance. [99] For one pouch cell, discussed in Chapter 4, symmetric cells were made from its electrodes for the purpose of characterizing large impedance growth. The cell was charged to approximately 50% state-of-charge and transferred to an argon-filled glove box to avoid the reaction of moisture or oxygen with charged electrodes. Multiple circular punches, 0.95 cm^2 in area, were made from unwound pouch cell electrodes. Electrodes were assembled into coin-type symmetric cells with stainless steel hardware, a blown microfiber separator (0.275 mm, 3.2 mg/cm^2, 3M Co, St. Paul, USA) and fresh electrolyte, following the prescription of Petibon et al.[99] EIS measurement parameters were identical to those for pouch cells, mentioned above. Symmetric cell construction was completed thanks to collaboration with Alison Keefe.

3.6 Isothermal Microcalorimetry

Isothermal microcalorimetry has been shown to be a precise way of determining parasitic reaction rates and to compare how changes in cell chemistry may impact lifetime.[213] For microcalorimetry experiment, cells were prepared as described in Section 3.3 and tested in a TA Instruments (New Castle, DE, USA) TAM III microcalorimeter (stability $\pm$ 0.0001°C, accuracy $\pm$ 1 µW, precision $\pm$ 1 nW), following the methods of Glazier, et al.[51] Two sets of cells were tested: one at beginning-of-life, just after formation, and the other after 40 cycles of cycle-hold testing at a time when some cells were starting to reach end-of-life. Four-wire electrical connections were made using 32 AWG cryogenic polyimide coated wires inside the calorimeter. These wires connect to conventional insulated copper wire outside calorimeter and connect to a Maccor Series 4000 charger. Cells are inserted into 20 mL ampoules, sealed, and lowered into one of 12 calorimeter channels. The interior temperature of the calorimeter, maintained by a heated oil bath, was set to 40°C and cells were given 24 h to thermally equilibrate. Heat flow measurements were obtained from thermopiles, two of which are in contact with each ampoule, and generate an electrical signal in response to heat flow from the sample via the Seebeck effect. Cells were cycled, with a charge endpoint voltage limit of 4.4 V, at a rate of C/130, to carefully determine the parasitic heat flow as a function of the cell voltage. Parasitic heat flow was obtained by subtracting contributions for rate of work associated with current flow under an applied overpotential and the entropic heat flow associated with changes in electrode lithium concentrations, as described in the doctoral thesis of Stephen Glazier.[214] This work was completed thanks to collaboration with Eric Logan, who executed microcalorimetry experiments and raw data analysis.

3.7 Micro X-ray Fluorescence Spectroscopy

Transition metal dissolution from the positive electrode is among the various failure modes possible in Li-ion cells. This is thought to be due to oxidation reactions with electrolyte or attack by acidic electrolyte species.[147] This can affect the positive electrode crystal structure, but is also thought to cause damage to the negative electrode SEI. TM migration to the negative electrode through the electrolyte can occur, where reactions with the SEI disrupt the quality of passivation against lithium-consuming parasitic reactions. For this reason, examination of TM deposition on the negative electrode by X-ray fluorescence microscopy has been used as a means of assessing TM dissolution.[215,216]

Fluorescence is an atomic absorption-emission phenomenon where incident photons are absorbed, a core electron is promoted to a higher energy level leaving a hole in its original energy level, and an electron located in a higher energy level falls into the hole position, releasing energy in the form of an emitted photon. The electron energy levels are unique and characteristic to each element. If these energy levels are known *a priori*, the measured energy of emitted photons can be assigned to the transition between two energy levels of a particular atom. Measurement of characteristic radiation therefore allows for elemental identification. X-ray fluorescence (XRF) relies on excitations and emission involving photons in the X-ray section of the electromagnetic spectrum. These are well suited for detection of metals, because XRF is a competing process with Auger electron emission, which favors XRF at high atomic weight. Micro X-ray fluorescence (μXRF) or in this case, scanning μXRF, is the implementation of spatially resolved XRF spectroscopy

with micrometer spot size that can be rastered over the sample surface to collect a composition map.

Cells were usually analyzed using μXRF after some time cycling, as a means of failure analysis, although some cells were analyzed immediately after formation, for reference. The following procedure follows the methods of Thompson et al.[215] and Eldesoky et al.[216] Cells were discharged to 2.5 V to ensure safe handling in ambient atmosphere. Cells were disassembled, jellyroll unwound, and negative electrode allowed to dry in a fume hood. A section of negative electrode from each cell was mounted on an acrylic sample plate using double sided tape.

Measurements were made using a Bruker (Madison, Wisconsin, USA) M4 Tornado μXRF system located at either University of New Brunswick or Saint Mary's University, both of which have identical machines. The prepared sample plate was loaded onto a translation stage in the sample chamber, which was then evacuated to <20 mBar. A microfocus X-ray tube containing a rhodium target (maximum 50 kV, 600 μA) was used to generate a spot size of 25 μm. Emitted photons were detected, and energy resolved using a silicon drift detector. Energy spectra of K_α transitions (M to K transition) were collected as a function of position, which was scanned at a rate of 4.00 mm/s.[216]

Spectra obtained were compared to a blank sample (pristine graphite electrodes, never exposed to electrolyte or charged) and several calibrant samples. Calibrant samples used aluminum foil and a pristine graphite electrode as substrates, onto which a linearly varying wedge of Mn, Fe, Co, or Ni was sputter deposited. The known spatial variation in the sputtered TM mass was compared to the spatial variation in integrated area of the Mn, Fe, Co or Ni K_α peaks (at 5.900 keV, 6.405 keV, 6.931 keV and 7.480 keV respectively)

to construct a calibration curve from which mass per unit area of TM could be obtained. Integrated peak areas were obtained automatically via the data analysis functionality of the Bruker M4 control software, along with artificially colored maps. This work was completed thanks to collaboration with the University of New Brunswick, Saint Mary's University and Ahmed Eldesoky, who ran XRF experiments and raw data analysis. Calibrant samples were prepared by Mike Johnson.

3.8 Li-ion Differential Thermal Analysis

Changes in the electrolyte composition are often measured in an effort to describe how cells age and fail. Typical analytical methods are destructive tests in that they require electrolyte to be extracted from the cell so the analysis can be performed. Non-destructive tests are valuable because cells can be analyzed and continue testing. Day et al. demonstrated the method of Li-ion differential thermal analysis (DTA) where the melting temperature and phase diagram of electrolyte in a cell, measured *in situ*, was used to deduce details about the composition and quantity of electrolyte remaining.[217] Briefly, the Li-ion DTA apparatus contains a two-cell holder into which the sample cell and an inert reference cell, filled with a 1M $LiPF_6$ in methyl acetate (MA) electrolyte, were loaded, in contact with platinum resistance temperature detectors (RTD). The holder was lowered into a liquid nitrogen cooled cryostat and temperature is controlled using a resistive heater connected to a Lakeshore 340 temperature controller. The cells were cooled to -100°C at a rate of -3.0°C/min, cold soaked for 10 minutes, and heated to approximately room temperature at a rate of 1.0°C/min. The temperature of phase change events and magnitude

of features in the thermal signature, along with knowledge of the electrolyte phase diagram, allow for the deduction of electrolyte composition and relative quantities of those components.

Cells selected for DTA measurements were provided both after formation and after long-term cycling so changes to the thermal signature could be examined as a function of cell age. Cells were given at least one week after any current flow before DTA testing to allow any localized electrolyte concentration gradients to equilibrate and become homogeneous. DTA measurements were completed thanks to Michael Bauer.

3.9 Synchrotron X-ray Computed Tomography and Thickness Measurements

The accumulation of solid parasitic reaction products and/or electrode microstructure changes has been shown to yield measurable thickness change in wound 204035 pouch cells like those used in this thesis. This has been demonstrated using macroscopic measurements of cell thickness and X-ray computed tomography experiments that can probe the electrode microstructure at the micrometer scale.[218]

Part way through the work in this thesis, it was learned that thickness measurements of Li-ion pouch could be useful and correlate with electrochemical performance. A selection of NMC532 and LFP cells, discussed in Chapters 4 and 6 respectively, that were already under test had their thickness measured by a Mitutoyo linear gauge. A linear gauge, which is a plunger-type digital indicator or digital thickness gauge, uses a spring-loaded plunger to gently clamp a sample against a flat reference surface. The position of the

plunger is determined digitally to a resolution of 0.005 mm. Thickness measurements were made in the center of the jellyroll area of the pouch cell.

To complement cell thickness measurements, the same cells, at end-of-life, were sent for synchrotron X-ray computed tomography (CT) imaging at Canadian Light Source on the Biomedical Imaging and Therapy Insertion Device beamline, following the methods of Bond et al. for performing high resolution scans.[218] X-ray tomography is an imaging technique that relies on the material and distance dependent attenuation of X-ray transmission, and varied angle of incidence to produce structural and phase imagery of a sample. Synchrotron X-ray sources are generally more intense and more monochromatic than lab X-ray sources, yielding high resolution, high contrast imaging with short exposure time and low dose delivery to cells, even with large millimeter scale objects like 204035 pouch cells.[218] This enables imaging of whole cells without requiring disassembly and minimizes the risk of damage to cell under exposure of ionizing radiation. In this sense, synchrotron X-ray CT can be used as a non-destructive, *in situ* technique.

To achieve high resolution imaging, a corner of each cell was imaged under a collimated, coherent 50 keV X-ray beam. X-ray transmission was measured using a single-crystal $Lu_3Al_5O_{12}$:Ce scintillator element paired with a 5x magnification optical system and sCMOS camera. The effective pixel size using this beam energy and optical set up was 1.44 μm. Measurements consisted of 2500 projections, with an exposure time of 1.0 s. Selected scans for each cell were used to determine the thickness of the combined negative electrode and separator layers, as well as the positive electrode. The negative electrode, voids filled with electrolyte and separator have nearly the same appearance in resultant images due to similar density and/or elemental composition. This means the combined

thickness of the negative electrode and separator is defined by the edges of the positive electrode and copper current collector. Thickness was determined by manual pixel counting, using a portion of an image where the jellyroll is flat. This work was completed thanks to collaboration with Canadian Light Source and Toby Bond, who handled cell loading and beam line operation, along with some image analysis.

3.10   Nuclear Magnetic Resonance Spectroscopy

Nuclear magnetic resonance (NMR) spectroscopy was selected as an analytical technique for determining electrolyte composition, complementing other techniques, like Li-ion DTA. NMR spectroscopy utilizes the characteristic response of nuclei with half-integer spin to an applied magnetic field. Nuclear spins are aligned to a large, static applied magnetic field, and then perturbed by a pulsed, perpendicular radio-frequency field. The frequency of the RF pulse which excites resonance in a particular nucleus corresponds to the energy difference between parallel and anti-parallel alignment of the nuclear spin with the applied, static field. Small changes to this resonance frequency occur as the adjacent nuclei and electron density are varied. These changes, when measured, can be used to identify the nuclei, bonding environment, and neighboring atoms in a sample. In the case of Li-ion electrolytes, this can be used analyze and quantify electrolyte composition.[219–221]

In preparation for NMR experiments, cycled cells were discharged to 2.5 V and transferred to an argon-filled glovebox. Cells were cut open and 1 mL of MA was added to the cell before resealing. Cells were left for at least 24 h for the MA to mix fully with the electrolyte throughout the cell. The cell was opened, and a syringe was used to

withdraw a sample of the extraction solvent-electrolyte mixture, consistent with the methods of Taskovic et al.[220] The extracted sample was added to a glass NMR tube (Wilmad 506-PP-8) along with additional MA. A known quantity of 1,4-bis(trifluoromethyl)benzene was also added to act as an internal standard in spectra for both ^{1}H and ^{19}F nuclei, allowing quantitative analysis. Spectra were obtained using a Magitrek Spinsolve 60 MHz spectrometer, with ^{1}H spectra collected using 16 scans and ^{19}F spectra collected using 240 scans. Both spectra were collected using a 10 s pulse delay time.

3.11   Measurements of Pouch Cell Volume

Due to the pliant and flexible nature of pouch cell casing material, the generation of gases during formation or cycling can cause an increase in cell volume. This is due to the requirement that the system eliminate or minimize any pressure gradient between the cell interior and the atmosphere. The volume change in pouch cells can be determined by measuring the difference in apparent weight when the cell is submerged in a fluid and calculating the volume from Archimedes principle for the buoyant force.[222]

Cells were submerged in a beaker of water while suspended from the under-balance hook of a Shimadzu AUW-D analytical balance (Shimadzu Corp., Kyoto, Japan) and mass reading recorded. This procedure was done both before and after testing. According to Archimedes principle, the volume change, Δv, is equal to

$$\Delta v = \frac{\Delta m}{\rho_{water}} \tag{3.1}$$

where Δm is the difference in balance readings and ρ_{water} is 1 g/mL.

3.12 Lifetime Models from Literature

A multitude of models have been proposed to fit and predict the lifetime of Li-ion cells based on preliminary or incomplete data. This has become ever present with the growing interest in machine learning methods for data analysis.[223] The value of this work is that Li-ion cells have become increasingly long lived, to where reaching a predefined end-of-life, perhaps 80% remaining capacity, can take many years. Being able to predict lifetime from less data is useful in alleviating this difficulty. Three models will be briefly mentioned, and some discussion here will be revisited in Chapter 7.

During study of the growth of oxide passivation layers on metals, Lawless proposed many laws governing the rate of oxide growth, including the parabolic growth law.[117] This has been applied to SEI growth in Li-ion cells with some degree of success, where the SEI growth is considered to grow at a rate inversely proportional to the thickness.[115,224] This qualitatively agrees with the observation that the quality of passivation should improve as the SEI thickens. This is written as

$$\frac{dx}{dt} = \frac{k}{x} \tag{3.2}$$

where x is the film thickness, k is the growth rate constant and t is the time. This can be solved by separation of variables to yield

$$x = (2k)^{1/2}t^{1/2} \tag{3.3}$$

or when converted to describe the cell capacity as a function of time, including a contribution lost due to SEI formation

$$\frac{Q}{Q_0} = 1 - At^{1/2} \tag{3.4}$$

Here, Q is capacity as a function of time, Q_0 is the initial capacity and A is a constant which encapsulates the SEI thickness growth rate and the amount capacity consumed per unit thickness of SEI. This suggests that the SEI thickens at a rate proportional to the square root of time, and the capacity loss as a function of time should asymptotically reach a stable level in the limit of very long times. In most cases, this asymptote is below the common end-of-life thresholds used in the field, such as 80% capacity remaining. A well-produced but realistic cell would exhibit a very small value of A, such that the asymptote reached in the limit of long time is something like 90% capacity remaining. This model is very simple and has a physical basis that is easy to understand, hence why it remains favored at has seen use for over 20 years. Nevertheless, this model ignores many forms capacity loss, such as impedance growth, and oversimplifies the passivation mechanism and thickness growth of the SEI.

A second model is to assume that SEI production requires an electron from the negative electrode to reach a solvent molecule in the electrolyte, where reduction can occur and contribute to SEI growth. An ideal SEI is electronically insulating, therefore once any initial SEI is produced, an electron must tunnel through that insulating barrier to reach the

electrolyte. The rate of SEI thickness should therefore depend on the probability of tunneling through the barrier, according to

$$\frac{dx}{dt} = \alpha \exp(-\beta x) \tag{3.5}$$

where α and β are constants related to the tunneling attempt frequency and the barrier height respectively. This can be solved using separation of variables to yield

$$x = \frac{1}{\beta} \ln{(1 + \alpha\beta t)} \tag{3.6}$$

or when converted to describe the cell capacity as a function of time, including a contribution lost due to SEI formation

$$\frac{Q}{Q_0} = 1 - A \ln(1 + Bt) \tag{3.7}$$

Here, A and B are new constants, where A incorporates β and the amount of charge consumed per unit thickness of SEI, while B incorporates both α and β. This model remains simple to understand and has a physically sensible basis. It also tries to provide a mechanism behind SEI growth. Like the parabolic growth law, it ignores other forms of capacity loss, and ignores factors that change throughout the life of the cell, such as electrolyte formulation.

The final model presented here is referred to as the "sigmoidal model" due to the functional form of the final result that describes the capacity as a function of time. The model was proposed and developed by Gering, arriving at the form

$$\frac{Q}{Q_0} = 1 - 2A\left[\frac{1}{2} - \frac{1}{1 + \exp[(Bt)^D]}\right] \tag{3.8}$$

where A, B and D are all constants. Gering arrived at Equation 3.8 by considering the factors that would diminish available sites for Li intercalation and charge transfer, along with the available inventory of cyclable Li. Gering constructed mathematical definitions for amounts of Li and active sites but needed a functional form to express rates of change. Sigmoidal expressions were selected without any direct physical basis, but were noted for being differentiable, summed to account for multiple mechanisms, and suit the boundary behaviors reasonably.[225]
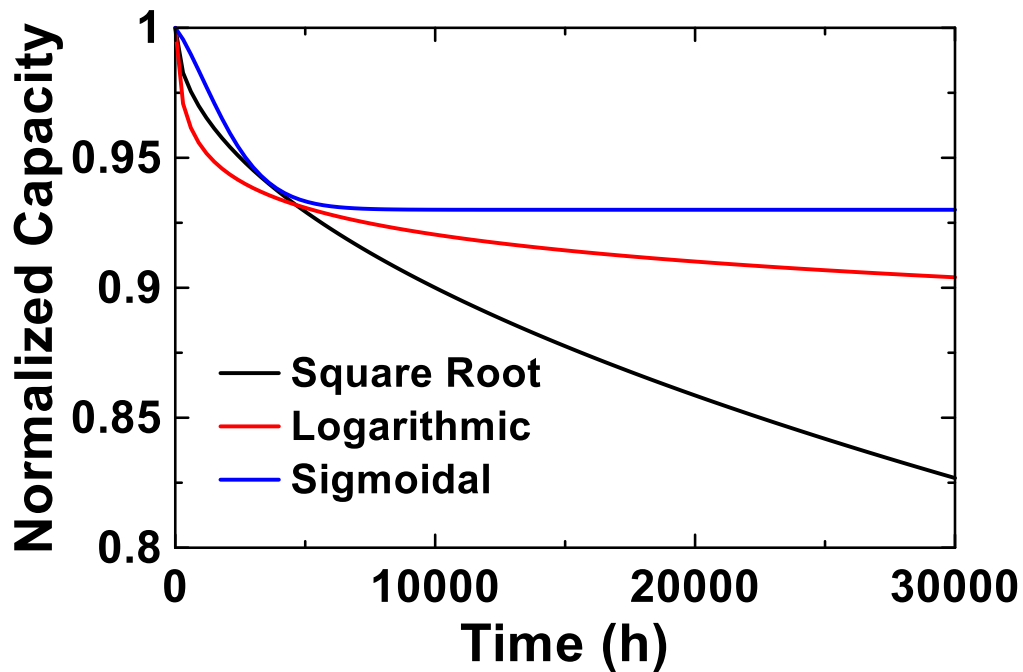
Figure 3.5. Calculated capacity versus time curves for lifetime models with square root (Eq. 3.4), logarithmic (Eq. 3.7) and sigmoidal (Eq. 3.8) time dependence. Capacity is normalized to 1 at 0 h. Curves shown serve as examples to illustrate simple behavior. Nuanced differences can arise as model parameters are changed.

Figure 3.5 shows capacity as a function of time for the models discussed in this section. The comparison made is not comprehensive, at the behaviors can change notably with vastly different parameters. Nevertheless, a few features are worth noting. The square root time dependence of the parabolic growth model shows the least change in curvature when the beginning and end of the curve are compared. A small time, the capacity decrease is gradual, and the decrease in fade rate as time increases is also gradual. The logarithmic time dependence of the electron tunneling model yields much more rapid capacity loss at small times, but quickly reaches much lower fade rates than the parabolic growth model. This is due to the exponential increase in passivation quality with thickness if SEI growth is believed to be governed by a tunnelling process. Finally, the sigmoidal time dependence of Gering's model can show more gradual capacity loss at small time, but rapidly transitions to asymptotic behavior with near zero fade at long times.

These models have improved utility and robustness when the fitted parameters can be linked to experimental parameters through well-established physical relationships. The simplest example of this is Arrhenius temperature dependence. The capacity loss rate parameter in the parabolic growth model, A in Equation 3.4, has been shown to follow Arrhenius' Law when the model is fit to data collected at different temperatures,[42,226,227] according to

$$A = \gamma \exp\left(-\frac{E_a}{k_B T}\right) \tag{3.9}$$

where γ is the attempt frequency and E_a is the activation energy for the reaction leading to capacity loss and SEI growth. The cycling temperature is given by T and k_B is Boltzmann's constant. Although it does not confirm model validity, it is reassuring that

there is some physical correctness when a model can be fit well, and the fit parameters are described well by Arrhenius Law.

It is not uncommon for complex models to be constructed where some combination of functions described here are combined, with a term each for many capacity loss modes. Models have been presented that have separate terms for calendar, or time-dependent aging, in both the short and long term, plus terms for cycle-dependent aging, also separated into short and long term.[223] As the number of model elements are added, the number of fitted parameters increases while the challenge of ascribing physical significance to each parameter also increases. Another common observation is the use of one of the models discussed here, with the addition of a term that has linear time dependence. This additional term is useful in improving the quality of fits at large time scales. For instance, modifying the parabolic growth model with a linear term would yield

$$\frac{Q}{Q_0} = 1 - At^{1/2} - Ct \tag{3.10}$$

where C is the coefficient of the linear term. The use of a linear term generally improves fit quality, but does not have robust physical justification behind it's use.[223] Anecdotally, the addition of a linear term to the parabolic growth model, such as in Equation 3.10, can also ruin the Arrhenius temperature dependence noted in the absence of a linear term. For the work in this thesis and particularly chapter 7, simple models with few parameters that have a sensible physical origin are preferred.

CHAPTER 4 THE ROLE OF SALT AND ELECTROLYTE FORMULATION IN HIGH VOLTAGE LI-ION CELLS

Some of the results presented in this Chapter have appeared in the peer-reviewed article *J. Electrochem. Soc.* **167**, 130451 (2020). Additionally, other results will appear in a manuscript that is presently under intellectual property review by the industrial sponsor of this work, Tesla Motors. The author of this thesis was responsible for planning of all experiments, construction of cells, initiating all electrochemical testing and all data analysis from electrochemical experiments in Sections 4.3. The author was responsible for all aspects of Section 4.4, from planning to experimental work and data analysis, except for a couple electrolyte additive suggestions from Jeff Dahn. Jeff Dahn was responsible for supervision throughout, including planning initial experiments in Section 4.2 that formed the foundation for the rest of this chapter, advising on electrolyte and testing parameters throughout and reviewing of all results. Toren Hynes and Julian Oxner assisted with some cell making. Eric Logan completed microcalorimetry measurements and processing of raw microcalorimetry data. Ahmed Eldesoky completed μXRF and NMR measurements and processing of raw data for these two methods. Toby Bond completed synchrotron X-ray CT measurements at Canadian Light Source and image processing. Michael Bauer completed Li-ion DTA measurements. Symmetric cells were constructed by Alison Keefe.

4.1 Introduction

Li-ion batteries have seen widespread commercial adoption because they tend to provide among the best combination of performance metrics of any battery technology, with very few compromises. One such example is the combination of energy density and lifetime. The maximum possible energy density inherent to the cell chemistry, assuming one lithium per formula unit of positive or negative electrode, is determined by the formula unit mass or density and the chemical potential of lithium as a function of composition in each electrode. One reason why the energy density obtained in practice is lower than the theoretical maximum is that conventional Li-ion cells tend to have charging restricted to 4.2 V, or 4.3 V vs Li^+/Li, which leaves approximately 20% of the capacity in the positive and even more of the energy unutilized (see Figure 1.3). Typically, when a certain positive electrode or cell assembly has the energy density specified, it is assumed to be within a certain operating voltage window that does not access all possible energy. Accessing additional lithium in the positive electrode necessitates charging to higher voltage, which is accompanied by a host of effects that can directly or indirectly negatively impact cell lifetime. In this sense, charging to 4.2 V is understood to be a compromise between high energy density and preserving long lifetime.

Nevertheless, charging to high voltage means that existing materials and cell chemistries can provide greater energy density, and to do so without much, if any, lifetime penalty would be a great accomplishment for the field. It would also be a significant socio-economic improvement as it means that the amount of energy stored per unit lithium and transition metal mined would be greater and help alleviate material constraints.

Conventional testing of cells at high voltage involves implementing CCCV methods, and raising the charge endpoint voltage beyond 4.2 V. While this does briefly expose cells to higher voltage, CCCV methods spend only a small fraction of the entire cycle near the charge endpoint voltage or 100% state-of-charge (SoC). This may not be representative of certain real-world applications where devices spend extended time connected to a charger, being maintained at 100% SoC. Simple examples of this include batteries in backup, uninterruptable power supplies, cell phones where the user charges for the entirety of the night while they sleep, laptop computers that remain plugged in most of the time and function effectively as desktop computers, or electric vehicles that are continuously charged to 100% capacity as owners attempt to relieve psychological pressure of range anxiety.

Nelson et al.[190] and Xia et al.[228] have previously studied NMC442 cells using cycling methods with long duration, high voltage holds, noting an increase in charge transfer resistance that varied when different electrolyte additives were used. Zhu et al. did similarly but in $Li_{1.2}Ni_{0.15}Mn_{0.55}Co_{0.1}O_2$ cells, noting electrolytes containing $LiB(C_2O_4)_2$ (LiBOB) and $LiBF_2(C_2O_4)$ LiDFOB could improve rates of capacity loss.[229] Petibon et al. studied the effect of $LiPF_6$ concentration at high voltage using CCCV methods in NMC442 cells, noting lower impedance when 2M salt concentrations were used, compared to 1M.[230] It has been shown that the use of cells with single crystal NMC532 positive electrodes, even at higher voltage, provide among the longest lifetimes reported in the academic literature using CCCV cycling methods.[28,231]

The work presented in this chapter aims to extend upon these works. At the time this work was started, the performance improvement seen in cells with increasing $LiPF_6$

concentration was expected, particularly when cells were charged to high voltage. Understanding of some of the mechanisms behind this performance improvement and using the understanding to accelerate testing was the goal at the outset of the experiments described in the following sections. Long duration, high potential cycling methods are applied to NMC532 cells. Experimental parameters explored to understand their impact on lifetime include electrolyte salt concentration, the use of conventional and contemporary electrolyte additives, alternate lithium salts, electrolyte solvent blend and test temperature. Investigation into the failure mechanisms is presented, using evidence from a collection of techniques. Finally, excellent cycle life is demonstrated from cells that have favorable construction or usage.

4.2 Study of Accelerated Failure using Long Duration, High Voltage Testing and Low Salt Concentration

Figure 3.2 in Chapter 3 showed a comparison of CCCV, cycle-hold and cycle-store electrochemical testing protocols. As has been asserted in Section 4.1, CCCV methods do not adequately allow the study of high voltage failure mechanisms because most of the test time is spent at low and moderate voltages. Longer times spent at high voltage should result increased rates of degradation. Cell performance metrics, such as the capacity or ΔV, the difference between the average charge and discharge voltage, are typically measured using a CCCV or just a constant-current cycle. Adherence to these conventional definitions for computing cycling metrics is why the cycle-hold and cycle-store methods still include conventional constant-current cycles every second cycle, rather than implementing a

constant voltage or a storage period every cycle. The storage or hold at high potential for

long duration every cycle would not enable the regular assessment of cell performance.
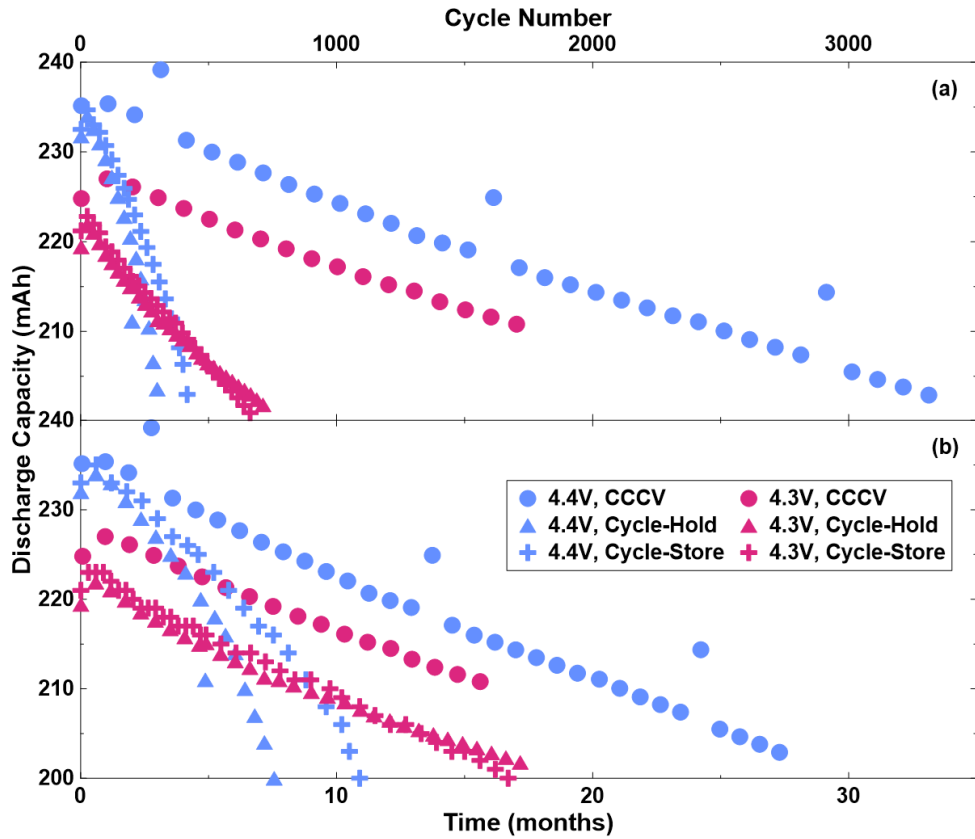
Figure 4.1. (a) Discharge capacity as a function of cycle number and (b) as a function of months for NMC532/AG pouch cells, containing 1.2M LiPF$_6$ with 2% FEC + 1% DTD electrolyte. Cells were charged to either 4.3 V or 4.4 V under CCCV, cycle-hold or cycle-store protocols, at C/3 and 40°C.

Figure 4.1 shows the discharge capacity a function of both cycle number and month

for NMC532 cells tested under conventional CCCV, with CV until the current diminishes

below C/20, cycle-hold, and cycle-store protocols, to charging upper cutoff voltages of

either 4.3 V or 4.4 V. The constant current segments of all protocols were completed at a

rate of C/3. All cells contained 1.2M LiPF$_6$ in EC/DMC electrolyte with 2% FEC + 1%

DTD electrolyte additives. In both Figures 4.1a and 4.1b, cells which are charged to higher

voltage show greater capacity fade when comparing identical cycling protocols. Additionally, cells which undergo cycle-hold protocols show greater capacity fade per cycle and per unit time than those which undergo cycle-store, which both show greater capacity fade than cells which undergo conventional CCCV charging. In the case of the cell which does cycle-hold testing at 4.4 V, it spends two-thirds of the test time at 4.4 V and sees an average voltage of 4.2 V. This results in the shortest time to failure, in under 8 months. Figure 4.1 shows data versus both cycle number and time to account for differences in average cycle time for each protocol. This is important to acknowledge, because when compared in terms of cycle number, the cell tested with CCCV charging to 4.4 V shows greater than 10 times the cycle life of the cell subjected to cycle-hold testing at 4.4 V, but the cell tested with cycle-hold only failed about 3.5 times faster, due to the longer time per cycle required to complete a 24 h constant voltage hold. From the view of rapid learning and experiment throughput, the faster failure rate is a considerable merit. It should not be forgotten that cycle-hold protocols also may resemble real device usage profiles.

Figure 4.2 shows the discharge capacity versus cycle number of cells made with a series of $LiPF_6$ concentrations, ranging from 0.2M to 1.2M. 0.2M is an extremely low salt concentration while 1.2M is a typical concentration. Salt concentrations less than or equal to conventional were selected to understand trends with salt concentration while also attempting to accelerate the rate of cell failure. This second aim was applied with cycle-hold and cycle-store methods to compound the rate of experiment throughput under high voltage conditions. The trends identified in Figure 4.1 also occur in Figure 4.2, in that cells cycled to higher potential show fewer cycles before showing accelerated rates of capacity

fade and ultimately failure. The same is true of cells subjected to cycle-hold testing, when compared to equivalently made cells subjected to cycle-store testing.
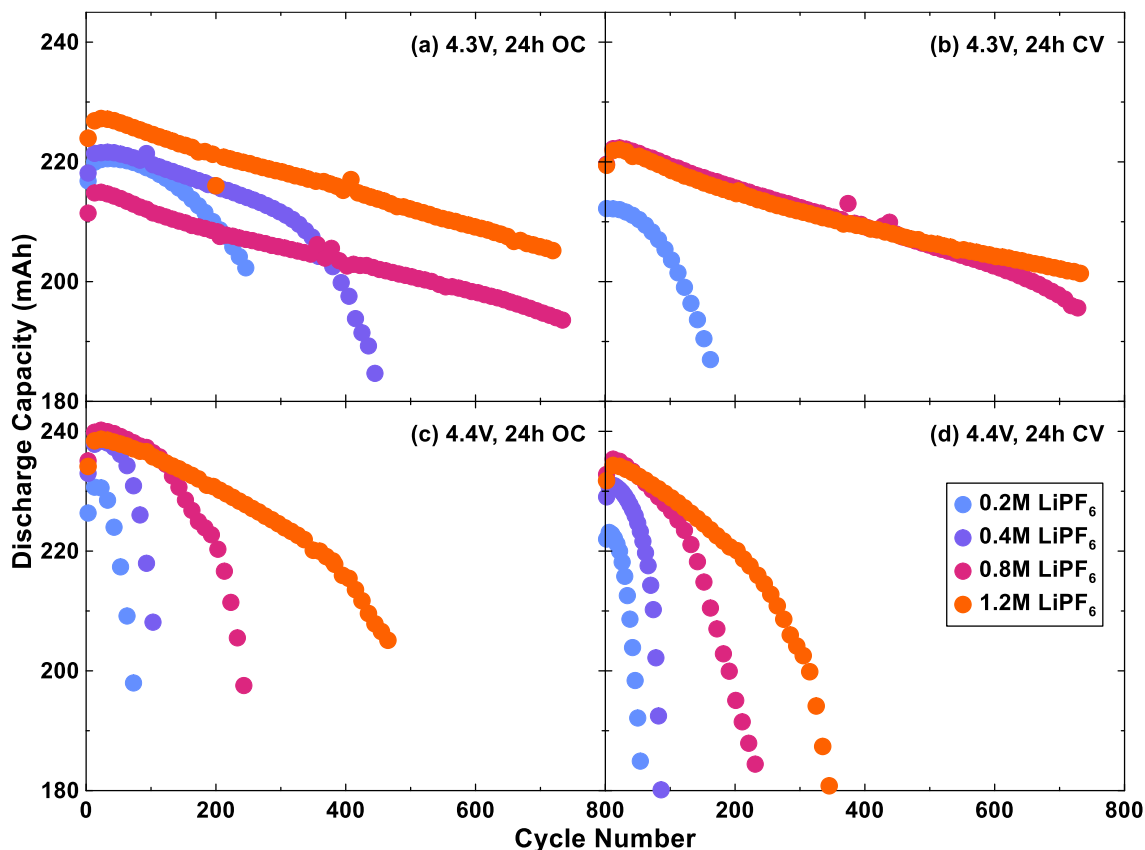
Figure 4.2. Discharge capacity versus cycle number for NMC532/AG cells, containing 2% FEC + 1% DTD electrolyte with various $LiPF_6$ concentrations. Cells followed (a,c) cycle-store or (b,d) cycle-hold protocols, with charging to (a,b) 4.3 V or (c,d) 4.4 V. Testing was performed at C/3 and 40°C.

Apparent throughout Figure 4.2, but most readily observed in Figures 4.2c and 4.2d, the cycle-life at high voltage is strongly dependent on the $LiPF_6$ concentration, with a positive correlation observed. The detailed description of how the capacity retention changes as cycle number accumulates is very similar for all cells, independent of test conditions or salt concentration. Initially, the capacity decreases at a constant rate for a number of cycles that is largely dependent on the $LiPF_6$ concentration. After some time,

the rate of capacity loss accelerates, and a relatively sudden failure occurs. It is regularly reported that increased electrolyte salt concentrations can increase the anodic stability of the electrolyte through improved solution structures[144,159,161,232,233] which would be consistent with the results here if the sudden failure is induced by electrolyte-electrode reactions at the positive electrode. If higher salt concentrations provide enhanced electrolyte stability, lower salt concentrations can result in inferior solution structures and greater numbers of solvent molecules not participating in solvation resulting in great susceptibility to oxidation.

Figure 4.3 shows ΔV, the difference between average charge and discharge voltages, as a function of cycle number for the cells introduced in Figure 4.2. Data is shown for cycles which do not contain 24 h holds or open circuit storage segments as those protocol steps disrupt the symmetry inherent to the typical understanding of ΔV. ΔV is a proxy for the internal resistance of the cell, or the polarization voltage drop from the open circuit when a current is drawn. The trends in ΔV mirror the capacity retention curves shown in Figure 4.2, in that they are vertically flipped. Initially, most cells display linear ΔV growth until sudden failure occurs and ΔV increases rapidly, in perfect correspondence with linear capacity loss that suddenly accelerates.
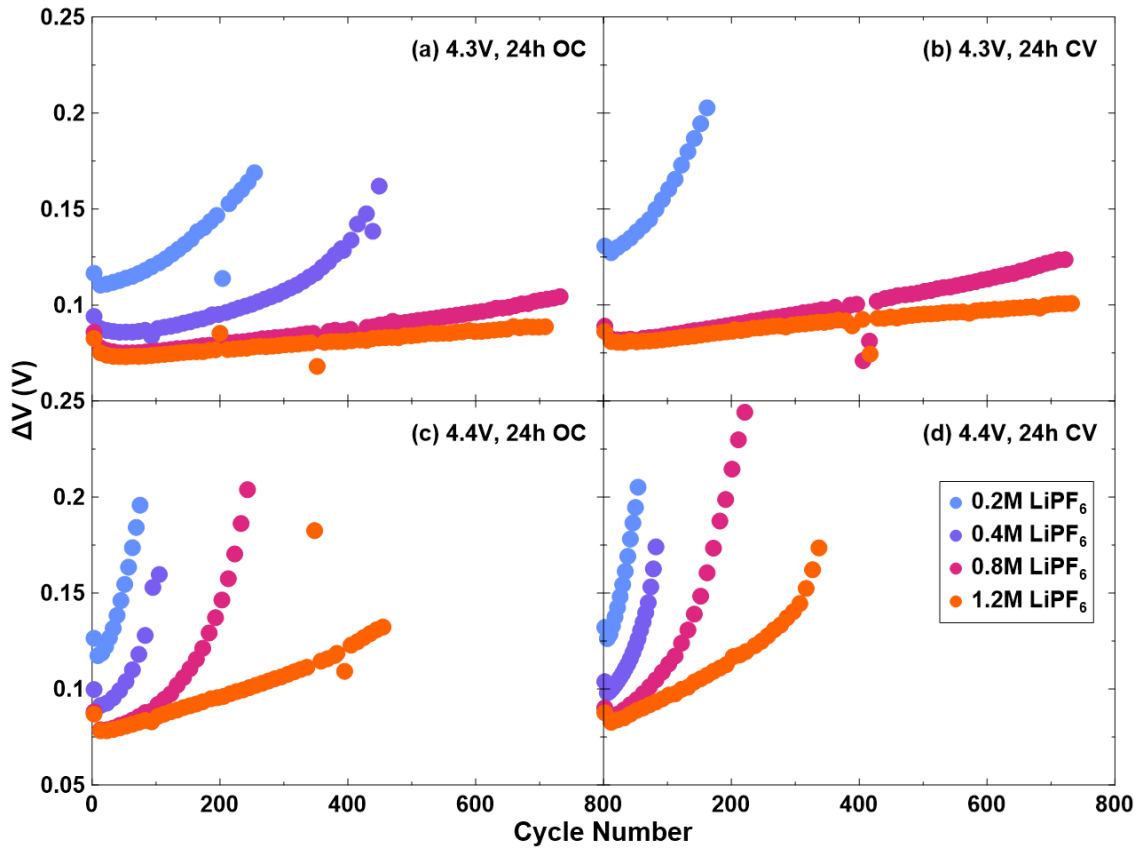
Figure 4.3. ΔV versus cycle number for NMC532/AG cells, containing 2% FEC + 1% DTD electrolyte with various $LiPF_6$ concentrations. Cells followed (a,c) cycle-store or (b,d) cycle-hold protocols, with charging to (a,b) 4.3 V or (c,d) 4.4 V. Testing was performed at C/3 and 40°C.

The ΔV growth that has occurred as most cells reach the point of failure is approximately 200 mV, which corresponds to about twice the beginning-of-life value. While failure is clearly defined by the rapid increase in ΔV, or internal resistance, some in industry consider a doubling of the cell internal resistance to be a defining metric for end-of-life. Increase in ΔV, or internal resistance contributed to failure through apparent capacity loss. Cycling, particularly the discharge where usable capacity in a device application is characterized, happens between fixed voltage limits. In this case, the discharge and any measurement of capacity associated with that discharge is terminated

when the voltage measured across the cell terminals is 3.0 V. A measurement of ΔV yielding 200 mV, when cycling with a particular current, can be interpreted as 100 mV of polarization voltage drop that will occur due to that current when the cell is discharging. This means that the cell voltage will read 3.0 V when the open-circuit potential difference of the cell is at 3.1 V. The amount of capacity available between 3.1 V and 3.0 V will therefore not be extracted and the discharge will be terminated. A similar effect occurs during charge, which limits the amount of charge stored, hence can be withdrawn, and measured during the following discharge. All of this can occur without consuming any of the active lithium in cell, and hence is not real capacity loss or depletion of the lithium inventory but is an apparent capacity loss that affects results obtained under appreciable current.

Figure 4.4a show Nyquist plots of electrochemical impedance spectra for the cells which completed 4.4 V cycle-hold testing, introduced originally in Figure 4.2d. EIS was collected both before and after testing, to so changes to the spectra could be compared. After formation, the general spectral size in a Nyquist plot and the charge transfer resistance orders with increasing size correlated with decreasing $LiPF_6$ concentration. This suggests $LiPF_6$ plays a role in the passivation film morphology or chemistry, and/or the dynamics of (de)solvation and charge transfer at either electrolyte-electrode interface are governed by salt concentration and accompanying solution structure. EIS measurements collected after testing show the reverse trend (save for the outlier with 0.8M $LiPF_6$), in that the size of spectra in a Nyquist plot and the charge transfer resistance increase with increasing $LiPF_6$ concentration and undergo the largest increase in impedance during testing. Cells with higher $LiPF_6$ concentrations spent more time under test, therefore the

impact of LiPF$_6$, suggested by Figure 4.4a, is to enable longer lifetime through the ability

to sustain or endure more impedance and charge transfer resistance increase.
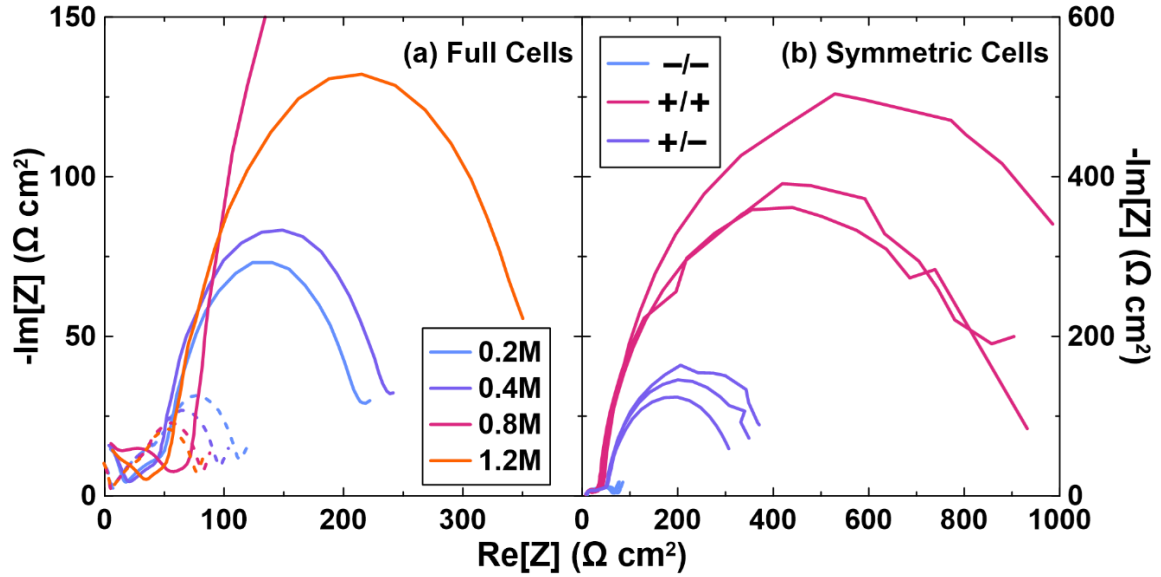
Figure 4.4. (a) Nyquist plot of impedance spectra collected from NMC532/AG pouch cells before (dashed) and after (solid) testing. Cells completed cycle-hold testing to 4.4 V and were originally introduced in Figure 4.2. (b) Nyquist plot of representative symmetric and full coin cells constructed at end of life, for the cell containing 0.4M LiPF$_6$. Impedance spectra collected at 10°C.

To determine the electrode of origin for large increases in impedance measurements, the construction of symmetric cells can be an invaluable tool.[99] Figure 4.4b shows a Nyquist plot of impedance measured on symmetric and full coin cells that were constructed from the cell containing 0.4M LiPF$_6$ in Figure 4.4a. Symmetric cells made from two negative electrode and two positive electrodes show very small and very large impedance respectively, while the impedance of the full coin cells is somewhat in between. This suggests that the cause of impedance growth in these cells is due to positive electrode impedance growth, which is a known failure mode in high voltage testing.[52,230] It should be noted that the results of Figure 4.4 and Figure 4.3 seem to have slight disagreement.

93

Figure 4.3 suggests that cell failure is at least partially due to an increase in internal resistance, which when measured under constant current conditions, can be thought of as a direct-current quantity. Even if the alternating application of charge and discharge currents at a rate of C/3 were considered as an alternating signal, the frequency of that signal is 93 µHz, whereas the lower limit of the measurements represented in Figure 4.4 is 10 mHz. This is to say that ∆V and the charge transfer resistance (or entire spectra) extracted from Figure 4.4 represent related, but not necessarily equivalent quantities. The former probes the entire cell response under direct-current use. while the latter is an analytical probe of the electrode surfaces where charge transfer processes occur. Figure 4.4 shows that positive electrode impedance and charge transfer resistance increases between beginning and end-of-life. When the duration of time under test is considered, Figure 4.4 may indicate that having more $LiPF_6$ present can slow the rate at which those quantities grow, and ultimately allows tolerance of more impedance before failure.

Figures 4.5a and 4.5b show the average end current, over the final 3 h of a 24h hold, as a function of the cycle number for cells completing cycle-hold testing to either 4.3 V or 4.4 V. Data presented in Figure 4.5 was obtained from the same experiment introduced in Figure 4.2. The quiescent current during a high potential hold is indicative of the rate of electrolyte oxidation happening at the positive electrode surface. The currents reported are very small, corresponding to C/8000, and there is a considerable amount of scatter to the data. Nevertheless, all cells, independent of $LiPF_6$ concentration, in Figure 4.5a have similar end currents when compared to each other. The same is true when comparing cells within Figure 4.5b. This indicates that by this metric, the amount of oxidation current is independent of $LiPF_6$ concentration, which suggests that increased rates of capacity loss

and ΔV growth which is $LiPF_6$ dependent may not be linked to oxidation processes. Figure 4.5c shows a representative current trace during a 24 h hold, to demonstrate that the current is generally well-behaved and decays to a steady-state value as might be expected.
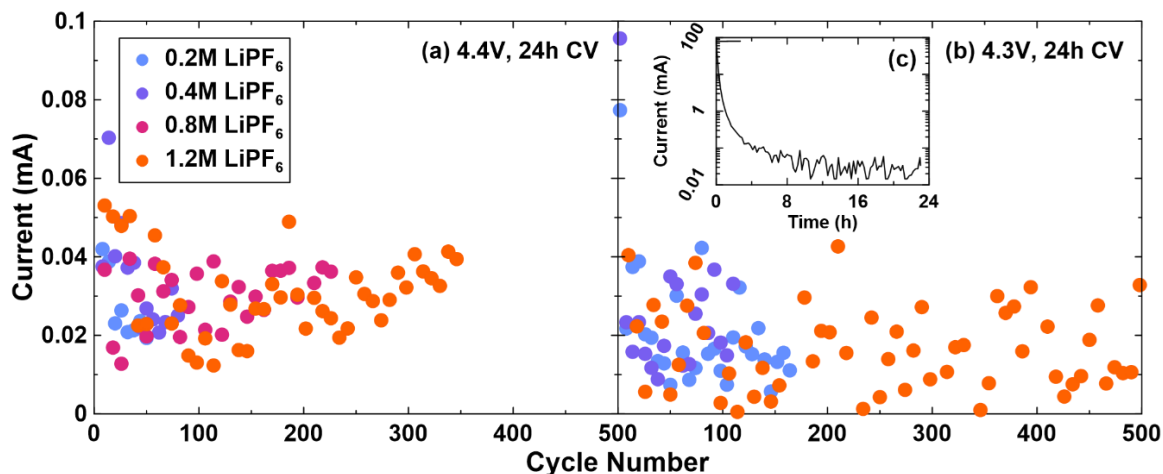
Figure 4.5. Average end current, measured during the final 3 h of 24 h constant voltage holds at (a) 4.4 V or (b) 4.3 V, as a function of cycle number. Data was obtained from NMC532/AG pouch subjected cycle-hold testing at 40°C and were originally introduced in Figure 4.2. (c) A representative current profile as a function of time during a single, 24 h hold. Measurements performed using a Keithley 2602B with current resolution 1 nA and accuracy 50 nA.

After experiments presented in Figure 4.2 were completed, cells were transferred to an ultra-high precision charger and were cycled at C/40 to carefully measure remaining capacity while minimizing the effects of impedance growth. As previously described, an increasing internal resistance can cause apparent capacity loss when cycling occurs between fixed voltage limits. The polarization voltage drop that causes the cell voltage measurement to differ from the open-circuit voltage is equal to the product of the applied current and internal resistance. Therefore, this voltage drop and the apparent loss of capacity due to internal resistance growth are minimized as the current is decreased.
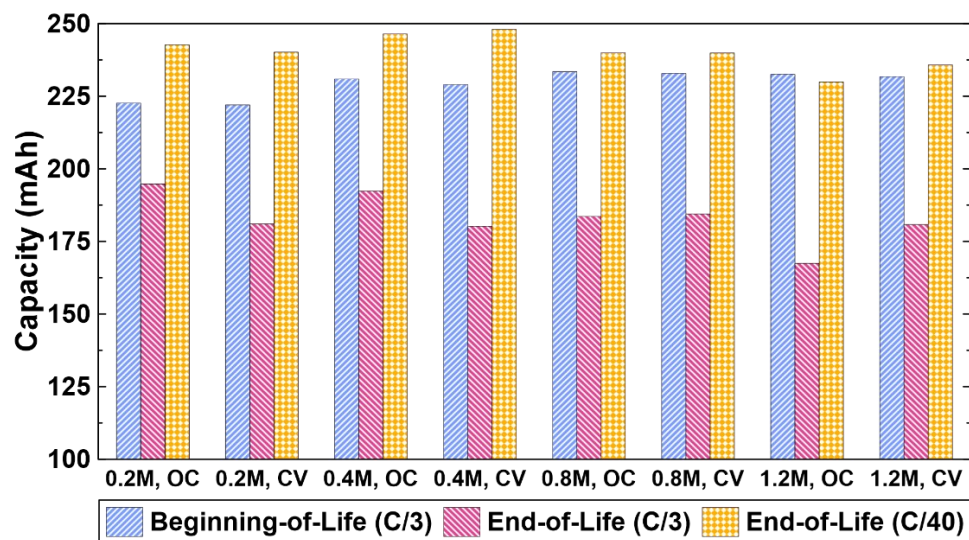
Figure 4.6. Discharge capacity of NMC532/AG pouch cells, cycled to 4.4 V using cycle-hold (denoted CV in figure) or cycle-store (denoted OC in figure) test methods. Capacities shown are grouped by $LiPF_6$ concentration in the electrolyte and end-of-charge procedure. For each grouping, capacity is shown at beginning and end-of-life, measured at C/3, as well as end of life, measured at C/40.

Figure 4.6 shows the capacity measured at the beginning and end of cycle-hold and cycle-store testing, using a C/3 rate, along with the capacity measured afterwards by UHPC using a C/40 rate. Cells selected for UHPC cycling were those that charged to 4.4 V. All capacity characterization was completed at 40°C. The capacity measured at the beginning-of-life was similar for all cells, at approximately 225 mAh. Cells were removed from testing and deemed to have reached the end-of-life when sudden, accelerating fade occurred and capacity reached or was close to 180 mAh. It is remarkable to see that all cells show capacities, when measured at the end-of-life using a C/40 rate, which are the same or exceed the beginning-of-life capacities measured using a C/3 rate. This implies that most of the lithium inventory in the cell is preserved and eliminates lithium plating as a major source of failure. It is possible for electrolyte oxidation to replenish the lithium inventory and counteract the effects of poor passivation at the negative electrode,[111] but

nevertheless, impedance growth of the positive electrode is firmly implicated as the primary source failure in these cells, subjected to both cycle-hold and cycle-store testing.
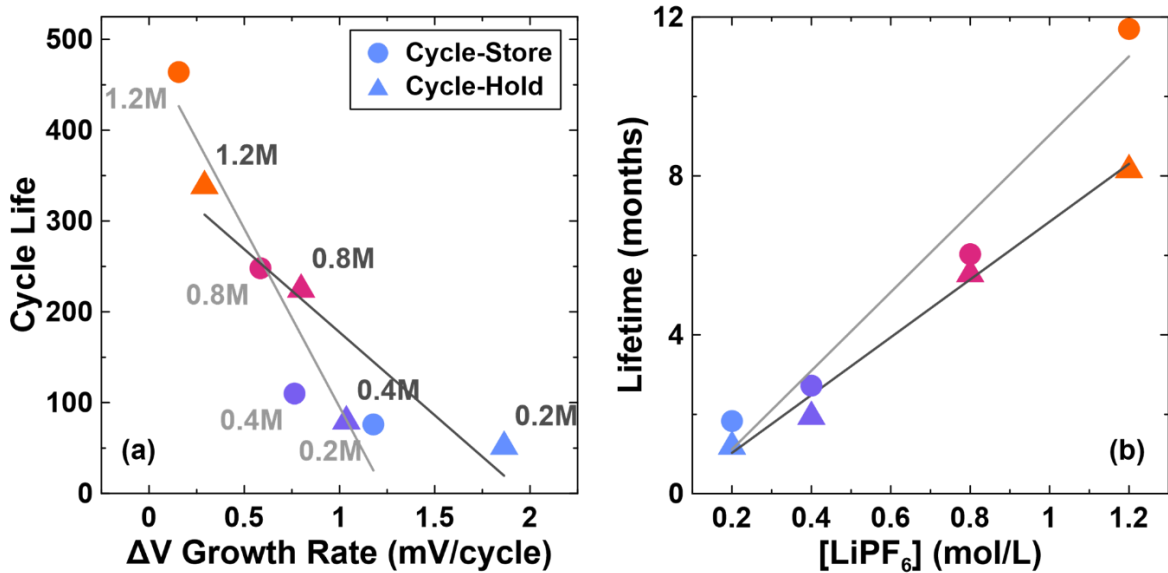
Figure 4.7. (a) Number of cycles to failure as a function of ΔV growth rate and (b) time to failure as a function of $LiPF_6$ concentration for NMC532/AG pouch cells, cycled to 4.4 V using cycle-hold or cycle-store test methods. Data was obtained from cells that were originally introduced in Figure 4.2. Lines of best fit are included for both cycle-hold (triangles, dark grey line) and cycle-store data (circles, light grey line)

Figure 4.7 summarizes the impact of salt concentration and internal resistance growth in the cycle and calendar life of cells tested with long duration, high voltage cycling protocols. It also gives a lens into leveraging the results here into an aggressive test method for accelerating failure and increasing experiment throughput. Figure 4.7a shows the number of cycles to failure plotted against the average ΔV growth rate. This is defined as the maximum and minimum ΔV values in Figure 4.3 for a given cell, which occur at the point of failure and in the first few cycles respectively, divided by the number of cycles between these two points. Cells containing low $LiPF_6$ concentrations experience faster ΔV

growth and lower cycle life. Cells undergoing cycle-hold testing experience faster ΔV growth and lower cycle life, compared to cells undergoing cycle-store testing.

Figure 4.7b shows the lifetime, or time to failure, plotted as a function of $LiPF_6$ concentration. Lifetime is important to consider because cells undergoing cycle-hold or cycle-store testing have an effective cycling rate of C/9, despite implementing constant current segments at a C/3 rate. The added time required for 24 h holds or open-circuit storage periods, and the fact that constant current segments get shorter as capacity is lost means cycle number can be misleading when comparing experimental throughput and cell lifetime. As mentioned throughout this section, the salt concentration is positively correlated with lifetime. Cycle-hold testing has been discussed as being more aggressive than cycle-store testing to the same voltage limit. Figure 4.7b shows that lifetimes are slightly improved in cycle-store experiments, compared to cycle-hold experiments with equivalent $LiPF_6$ concentrations.

For applications trying to achieve excellent high voltage cycle-life, this suggests using high salt concentration and minimizing time spent at 100% SoC. Alternately, to accelerate testing throughput and subject cells to aggressive conditions that push the limits of stability and performance, improvements to cell formulation could be tested using cycle-hold methods in cells that contain minimal salt concentrations. The results in this section show that internal resistance and positive electrode impedance growth result in measured capacity loss when a rate of C/3 is used. Improvements to cell chemistry such as improved electrolyte formulation that may help mitigate impedance growth can be rapidly screened when used in cells with low salt concentration electrolyte and will be demonstrated in subsequent sections. The fact that quiescent currents during holds and the general lithium

inventory is intact in all cells tested here, independent of salt concentration, suggests that rates of oxidation and parasitic reactions may not vary significantly as a function of salt concentration. This is particularly surprising and highlights the need for more investigation into the mechanisms of failure in these cells.

4.3 Analysis of Cells Subjected to Equal Times Under Cycle-Hold Testing

One main drawback of the work presented in the previous section is that cells were cycled to failure and then analyzed, despite often having vastly different time spent under test. This can lead to misleading conclusions about the rates of processes leading to failure. Figure 4.4a and the accompanying discussion is a good example of this. When considered alone, without other results, Figure 4.4a suggests that use of high salt concentrations produces greater positive electrode impedance growth. The duration of time under test and the rate of impedance growth is missed entirely. To begin to grasp these concepts, a group of NMC532 cells were made with a series of $LiPF_6$ concentrations and two electrolyte additive choices, and subjected to C/3 cycle-hold testing at 40°C with a charge endpoint voltage of 4.4 V. The $LiPF_6$ concentrations used were adapted from the series presented in Section 4.2 to be 0.2M, 0.4M, 1.2M and 1.8M. This differs in that a salt concentration considerably above what is typical is introduced, where in Section 4.2 only typical or less-than-typical concentrations were used. The electrolyte additives used were either the combination 2% FEC + 1% DTD, used previously in Section 4.2, or the single additive system 1% LFO. Introduction of different additives ensures that results and behaviors are not due to a unique interaction between the 2% FEC +1% DTD additive system and $LiPF_6$.

This group constitutes 8 unique cells, that were cycled for the purpose of providing samples for various forms of analysis. Identical batches of these cells were prepared and cycled to the same extent as certain analysis techniques are destructive and a single batch of cells cannot produce samples for all techniques used.
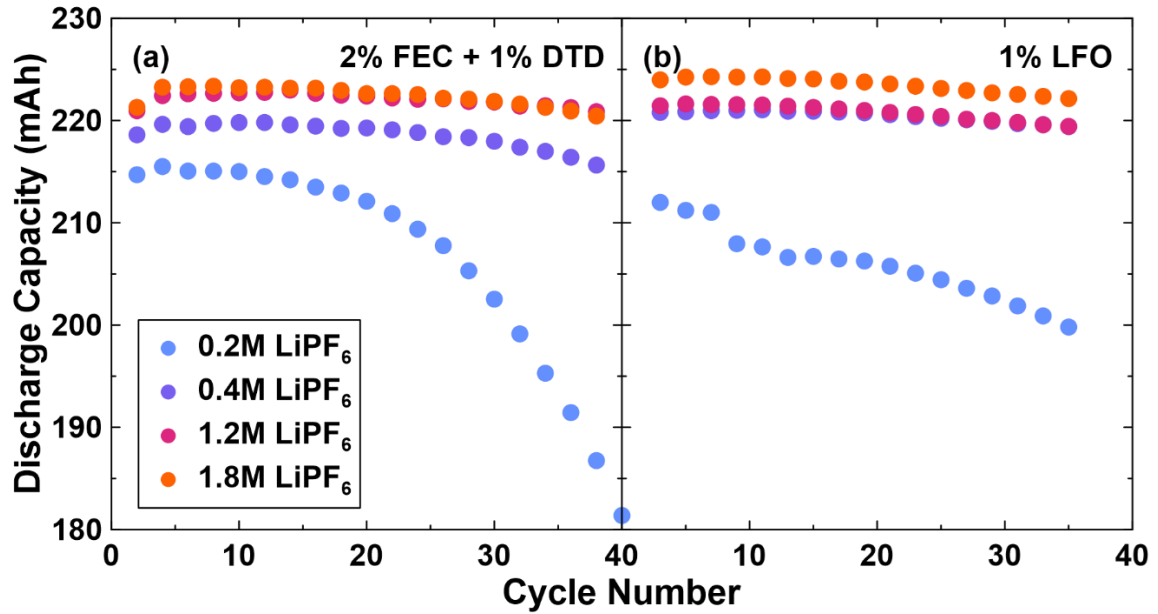
Figure 4.8. Discharge capacity versus cycle number for NMC532/AG cells, containing (a) 2% FEC + 1% DTD or (b) 1% LFO electrolyte additives with various $LiPF_6$ concentrations. Cells were charged to 4.4 V using C/3 cycle-hold testing at 40°C.

Figure 4.8 shows the discharge capacity as a function of cycle number for a group of cells prepared as described in the preceding paragraph. Figure 4.8a is very reminiscent of Figure 4.2d, except that cells are not cycled all the way to failure. The cycle-hold experiments that this group of 8 cells was subjected to were terminated and cells were removed from the charger when the cell containing 0.2M $LiPF_6$ and 2% FEC + 1% DTD electrolyte reached 180 mAh. This was the fastest cell to fail of this octet, and therefore its cycle life and lifetime were used to define the end of cycle-hold testing for all cells, so they could be analyzed on the basis of equal time under test. This cell reached failure in 40

cycles or approximately 650 h. All analysis results presented throughout this section that were measured in cells described as after testing are 650 h of cycle hold testing.

Comparison of data within Figure 4.8 shows that yet again, cells with lower LiPF$_6$ concentration show faster failure. In only 650 h of testing, most cells have capacity versus cycle number profiles that track parallel to each other, indicating they are still in the regime of slow, constant fade that precedes accelerating fade and failure. Only the two cells with 0.2M LiPF$_6$ and the cell containing 0.4M LiPF$_6$ with 2% FEC + 1% DTD show appreciable capacity loss that distinguishes them from other cells. Comparison of Figures 4.8a and 4.8b show that 1% LFO appears to be a superior high voltage additive selection compared to 2% FEC + 1% DTD. While cells containing these two additive choices that have 1.2M and 1.8M LiPF$_6$ do not have enough cycles accumulated to distinguish them, cells containing 1% LFO are superior to their 2% FEC + 1% DTD counterparts when 0.2M and 0.4M LiPF$_6$ cells are compared. The use of 1% LFO has shown excellent results in high voltage CCCV testing of NMC532, so it is reasonable that similar results are obtained here.[150] ΔV versus cycle number is not plotted in Figure 4.8 as it simply mirrors the capacity data for both additive options, as was the case with Figures 4.2 and 4.3. The facts that the cell containing 0.2M LiPF$_6$ is the cell approaching failure the fastest among all the cells containing 1% LFO, and ΔV growth mirrors capacity loss even for 1% LFO cells constitute limited evidence that suggest the trends reported in Section 4.2 for 2% FEC + 1% DTD containing cells may carry over to other electrolyte additive systems.

Figure 4.9 shows results from electrochemical impedance spectroscopy for the cells introduced in Figure 4.8. Figures 4.9a and 4.9b show that the general size of features in the impedance spectra increase with decreasing LiPF$_6$ concentrations when EIS is measured

after 650 h of cycle-hold testing. This is consistent with the trend of increasing internal resistance and ΔV growth rate with decreasing noted in Section 4.2. This also rectifies the small discrepancy between Figures 4.3 and 4.4 that seemed to suggest dissimilar trending between impedance spectra and ΔV growth but failed to account for equal time under test.
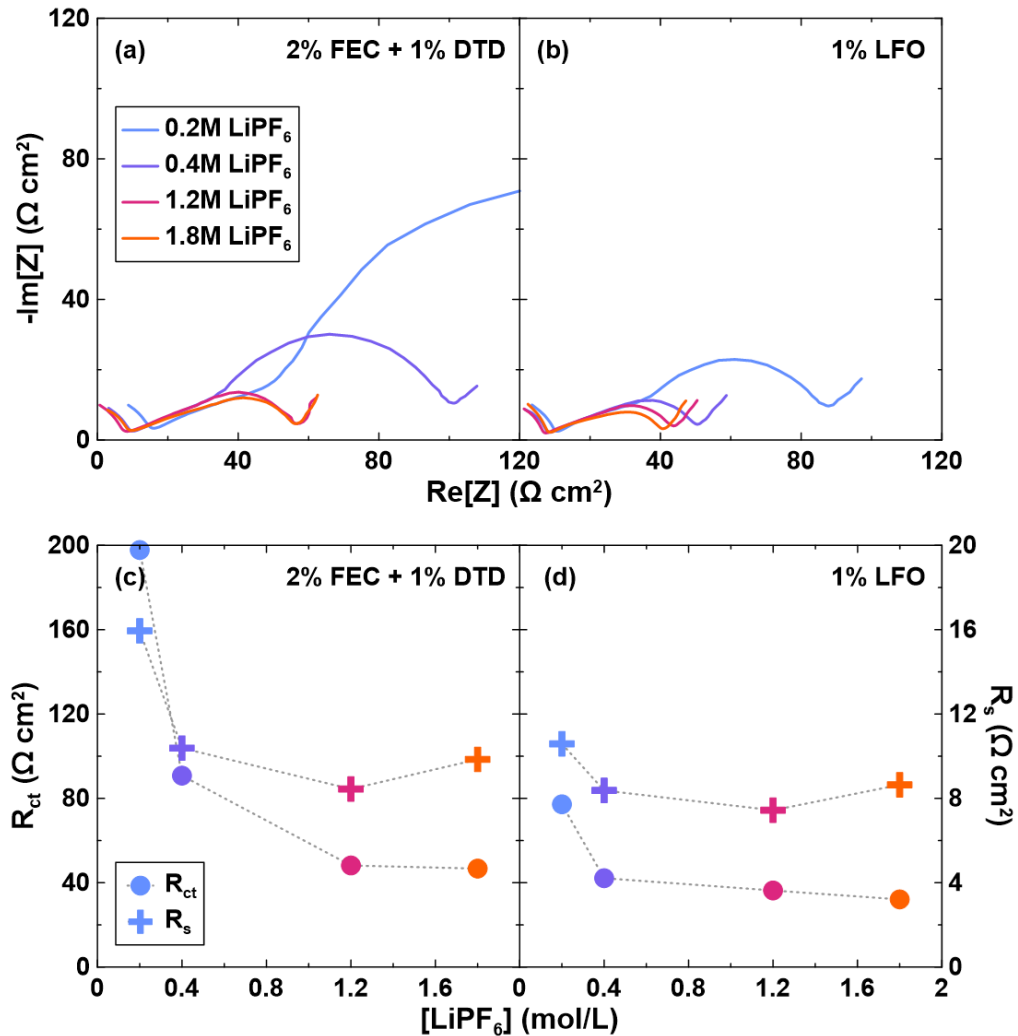
Figure 4.9. Summary of EIS results for NMC532/AG cells with varied $LiPF_6$ concentrations, collected after 650 h of testing. Nyquist plots are shown for cells containing (a) 2% FEC + 1% DTD, or (b) 1% LFO. Extracted charge transfer and series resistance, R_{ct} and R_s, are also shown for groups of cells containing (c) 2% FEC + 1% DTD, or (d) 1% LFO. The symbol color for R_{ct} and R_s data points match the line color for the spectrum from which the values were extracted. Lines in (c) and (d) are drawn to guide the eye only.

Figures 4.9c and 4.9d show the charge transfer and series resistance that can be extracted from the spectra in Figures 4.9 and 4.9b, as a function of salt concentration. The series resistance, which is typically attributed to the resistance of the bulk electrolyte and reciprocally related to the electrolyte conductivity, shows increases at low salt concentration for both electrolyte additive systems used. This is due to increased viscosity that occurs and causes reduced conductivity at high salt concentration, and low carrier count that causes reduced conductivity at low salt concentration. The cell which reached failure, containing 2% FEC + 1% DTD and 0.2M $LiPF_6$ shows much higher series resistance than all other cells. This implies that salt or solvents have been consumed in this cell as it has reached failure. Diminished salt concentrations would contribute to a reduced solution carrier count. Consumption of EC could result in reduced solution dielectric constant, while consumption of DMC could increase solution viscosity. All other cells show electrolyte resistance that are remarkably similar to each other, considering that salt concentration range spans nearly an order of magnitude. Logan et al., however, have shown that at 10°C, changing the $LiPF_6$ concentration in an EC/DMC (3:7) solvent blend from approximately 0.55M to 2.25 M in yields electrolyte conductivities that differ by no more than 15%[73] which is similar to the variation in R_s seen in Figure 4.9. Significant conductivity decreases were predicted for lower $LiPF_6$ concentrations, but not confirmed experimentally. The R_s data therefore suggests there is a change in the electrolyte composition, particularly apparent in cells with low $LiPF_6$ concentration as they approach failure, although without further evidence this cannot be attributed to salt or solvent consumption.

The charge transfer resistances shown in Figures 4.9c and 4.9d exhibit monotonic increase as $LiPF_6$ concentration decreases. Based on the results in Figure 4.4, this suggests the rate of charge transfer impedance growth at the positive electrode is inversely correlated with electrolyte salt concentration. Comparing Figure 4.9c to Figure 4.9d, the cells containing electrolyte with 1% LFO show less R_{ct} growth than cells that have the same $LiPF_6$ concentration and contain 2% FEC + 1% DTD. This correlates well superior capacity retention demonstrated by cells containing 1% LFO, shown in Figure 4.8, and is consistent with the idea that reduced rates of positive electrode impedance and R_{ct} growth prolongs cycle life. The differences in R_{ct}, due to both $LiPF_6$ concentration and additive selection could be due to either superior quality of the passivation films established during the formation cycle due to the unique electrochemistry of the entire electrolyte composition, or the inherent electrochemical stability that may be offered due to increased salt concentration and superior solution structure. This can involve different solvent species accompanying a solvated lithium to the electrode surfaces as salt concentration changes. The presence of species in the lithium solvation sphere dictates which electrolyte components participate in parasitic reactions.

Figure 4.10 shows parasitic heat flow measured using microcalorimetry for the cells introduced in Figure 4.8a, that contain 2% FEC + 1% DTD. Figure 4.10a shows data collected after formation, while Figure 10b shows data collected after approximately 650 h of testing. The main result is that among cells that contain different $LiPF_6$ concentrations, in either panel, there is no appreciable difference in the parasitic heat profiles as a function of voltage. All minor variation is well within the normal limits of cell-to-cell variation normally seen in microcalorimetry experiments.[185,234] The parasitic heat flow measured in

microcalorimetry experiments is a measure of the rate of parasitic reactions. In the data shown in Figure 4.10, the parasitic heat flow increases as the cell is charged beyond 4.2 V. This is due to increased rates of electrolyte oxidation at the positive electrode surface. The similarity of all curves in either Figures 4.10a or 4.10b there suggests that both before testing and after 650 h of testing, the rate of electrolyte oxidation has no significant salt concentration dependence. The decrease in the magnitude of the heat flows measured before testing, or just after formation, to after testing is indicative of the fact that with increasing time under test and exposure of electrolyte to the charged electrode surfaces, the positive and negative electrode passivation films continue to develop and increase in their passivation ability. One thing to note in the interpretation of Figure 4.10 is that while it does not appear that the parasitic reaction rates vary considerably with $LiPF_6$ concentration, the lifetime of cells in cycle-hold testing does.
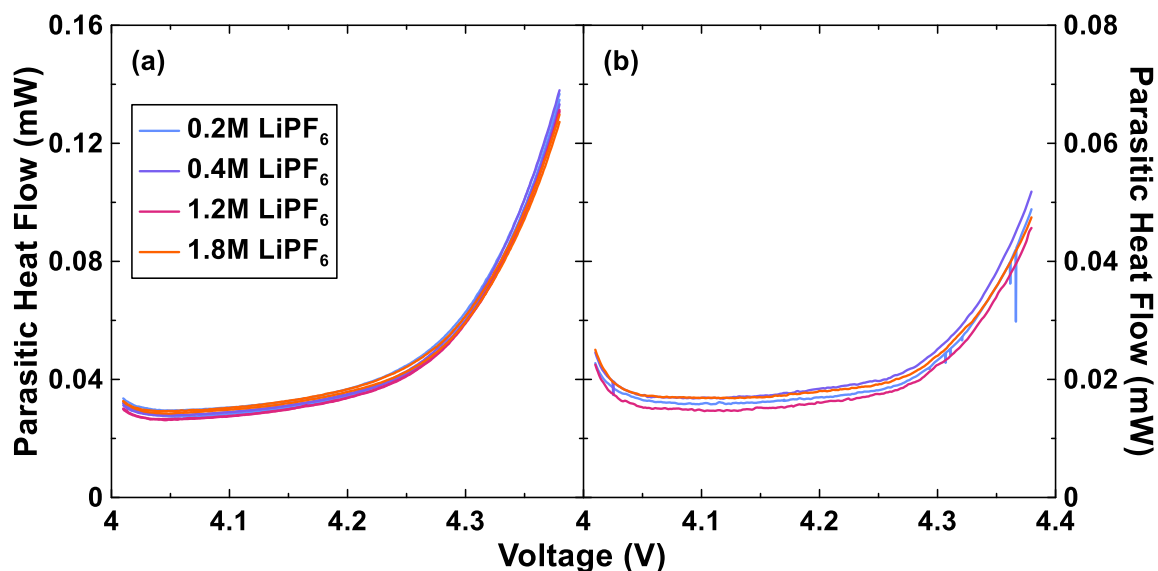
Figure 4.10. Parasitic heat flow as a function of voltage for NMC532/AG cells measured by isothermal microcalorimetry during a charge to 4.4 V, for cells at (a) beginning-of-life and (b) after cycling for approximately 650 h. Cells contained electrolytes with varied $LiPF_6$ concentrations. All cells contained 2% FEC + 1% DTD electrolyte additives.

Figure 4.11 shows a summary of the parameters obtained from differential voltage analysis, otherwise referred to as dV/dQ fitting. Cells were transferred to a UHPC after 650 h of cycle-hold testing to complete C/40 constant-current cycles from which dV/dQ analysis can be performed. The measured and fitted differential voltage curves can be found in Figures B.1 and B.2, in Appendix B, for cells with 2% FEC + 1% DTD or 1% LFO respectively. The fit for the cell containing 0.2M LiPF$_6$ with 2% FEC + 1% DTD, in Figure B.1a, is notably poor. It has anecdotally been noted that dV/dQ fitting can be quite challenging when cells have experienced significant degradation, as might be expected when a cell with low LiPF$_6$ concentration is cycled at elevated temperature to 4.4 V using cycle-hold methods. Some methods to improve the quality of data acquired for the purpose of dV/dQ fitting have been discovered after this data was collected, so partial solutions now exist. Fitting the left limit, the three consecutive bumps immediately to the right, and the fourth bump at approximately 50% SoC in a dV/dQ profile is achieved by varying the negative electrode active mass and slippage, or alignment to the positive electrode. In most cases, these three dV/dQ features are not entirely independent and can be fit well simply by adjusting the aforementioned two parameters. Here, this is not the case, meaning the fitted values for negative electrode mass loss and relative slippage for this cell are the result of fitting to the best of the author's ability with automated assistance, but ultimately are unreliable.

Figure 4.11 shows that both positive and negative electrode capacity (or active mass) are lost as salt concentration is decreased, independent of electrolyte additive. This may be due to the nature of electrolyte-electrode interactions that are modulated by salt concentration or just the proximity to failure after 650 hours of cycle-hold testing. The

amount of capacity lost from each electrode is not large, particularly when the negative electrode capacity of the cell containing 0.2M LiPF$_6$ with 2% FEC + 1% DTD is ignored, due to low quality fitting. Nevertheless, this suggests a small amount structural degradation of the electrodes, possibly due to electrochemical attack of the binder or fracture of the particles. With single crystal, low-to-moderate Ni positive electrodes and artificial graphite negative electrodes are used, the detection of active mass loss is exceedingly rare. This likely reflects the aggressive nature of cycle-hold testing and long times spent at high voltage.
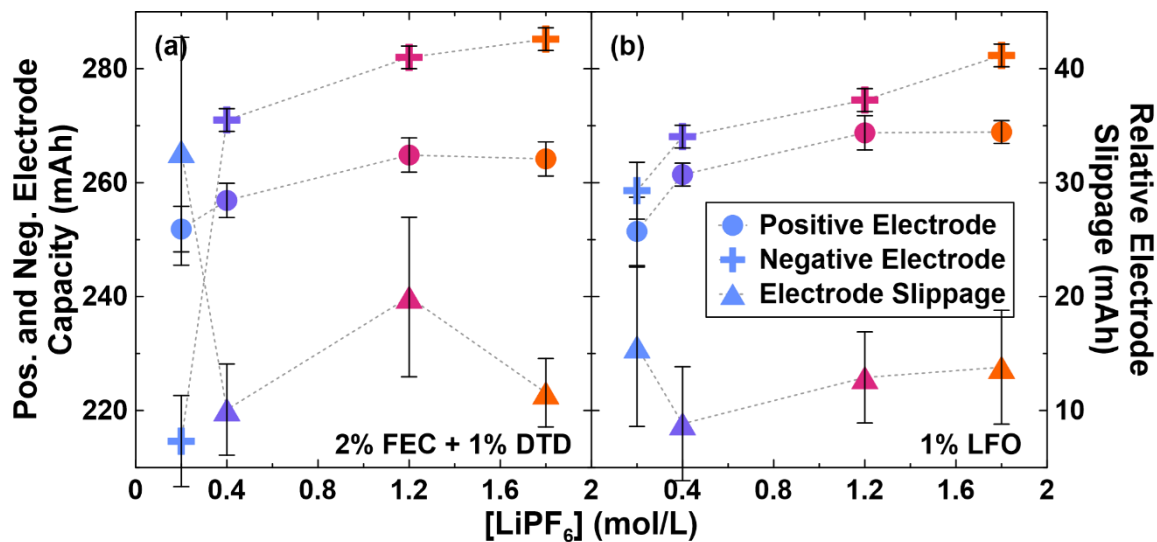
Figure 4.11. Differential voltage analysis fitting parameters for NMC532/AG cells measured after cycling for approximately 650 h. Cells contained electrolytes with varied LiPF$_6$ concentrations and either (a) 2% FEC + 1% DTD or (b) 1% LFO electrolyte additives. Differential voltage data and fits can be found in Figures B.1 and B.2. Colors are consistent with LiPF$_6$ concentration color scheme in Figure 4.8. Lines drawn to guide the eye.

The results for electrode slippage do not show a clear pattern, particularly when the cell containing 0.2M LiPF$_6$ and 2% FEC + 1% DTD is ignored. The result from this cell is easily discarded as a fitting error, as the lithium inventory was shown to be intact in Figure

4.6, after cycle-hold testing. This makes it unlikely that almost 40 mAh of true capacity is lost due to electrode slippage and therefore the result of poor fitting. It is normal for 10-15 mAh of electrode slippage to occur as part of the irreversible capacity loss associated with first cycle passivation film formation. Therefore, the slippage shown in Figure 4.11 for all other cells is within the expected first cycle losses. The results in Figure 4.11 as a whole show that the use of electrolytes with increasing salt concentrations can preserve the capacity of sites to store lithium in each electrode. This can be rephrased as preventing loss of the electrode active masses. The fact that the dV/dQ results didn't vary significantly between cells containing 2% FEC + 1% DTD and cells containing 1% LFO may imply that the active mass losses shown in Figure 4.11 are largely unrelated to the rate positive electrode impedance growth shown in Figure 4.9, which does depend somewhat on additive formulation. Data collected for performing dV/dQ analysis is collected at low rate, C/40, partly to assess the state of the material with minimal polarization caused by impedance growth. It is possible, particularly in the case of the cell containing 0.2M LiPF$_6$ and 2% FEC + 1% DTD, that the impedance increase is sufficiently large that it may lead to some undesirable contribution to the analysis that is not accounted for.

Figure 4.12 shows the results of μXRF analysis on the negative electrode of the cells introduced in Figure 4.8a, after approximately 650 h of testing, along with a set of identically prepared cells measured after formation. Specifically, the mass per unit area of Mn deposited on the negative electrode that was obtained from these cells is shown. In both Figures 4.12a and 4.12b, the amount of Mn present on the negative electrode after formation, before testing, increases as the LiPF$_6$ concentration increases. The mechanism behind transition metal dissolution from the positive electrode is often cited as acid attack,

particularly from HF which is known to be a product of $LiPF_6$ thermal decomposition. In practice, it has been suggested that this unlikely to occur once cycling commences as HF is eliminated during charging of the cell, and that the dissolution of TMs is due to electrolyte oxidation which in turn reduces TMs as part of their removal from the positive electrode.[147] Therefore, the increasing Mn dissolution with increasing $LiPF_6$ observed in cells that were measured just after formation may be due to the increased HF quantities that would be present in electrolytes with increased $LiPF_6$ concentrations. The exposure of the positive electrode to HF could occur during handling and wetting, prior to formation. It has also been shown that the concentration of $LiPF_6$ can yield different decomposition products on the positive electrode surface, indicating different oxidation reactions that can occur during formation,[230] which could be accompanied by TM dissolution.
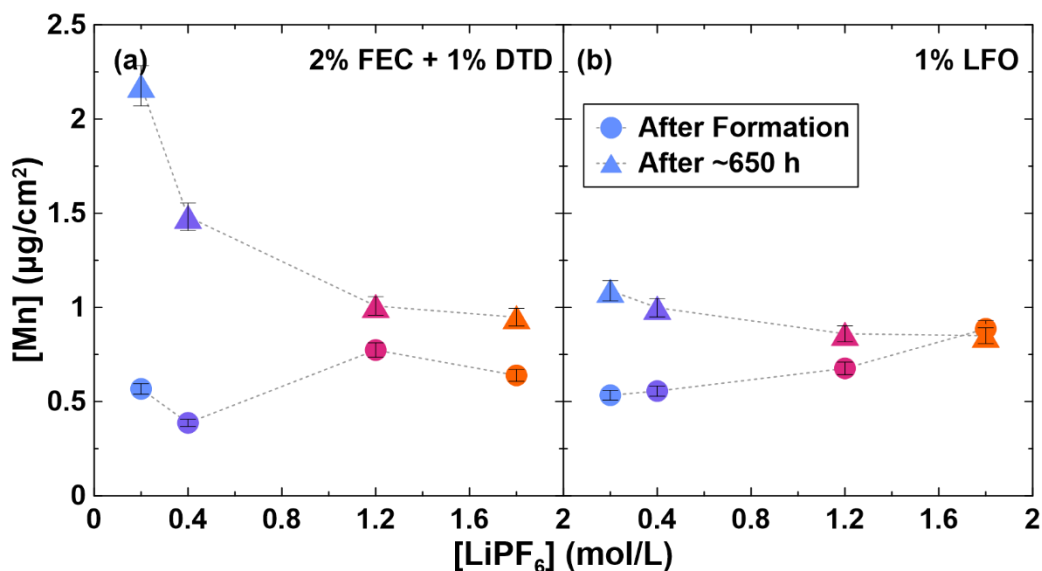
Figure 4.12. Manganese deposition on the negative electrode for NMC532/AG cells measured by μXRF after formation and after cycling for approximately 650 h using a cycle-hold protocol with charging to 4.4 V at 40°C. Cells contained electrolytes with varied $LiPF_6$ concentrations and either (a) 2% FEC + 1% DTD or (b) 1% LFO electrolyte additives. Representative μXRF spectra can be found in Appendix Figure B.3. Colors are consistent with $LiPF_6$ concentration color scheme in Figure 4.8. Lines drawn to guide the eye.

In addition to formation results, Figure 4.12 also shows that the rate of Mn dissolution during cycle-hold testing decreases as the $LiPF_6$ concentration in the electrolyte increases. This behavior is well correlated with results from Figures 4.8 and 4.9, in that the cells that have higher amounts of Mn deposited on the negative electrode also show increased the rates of capacity loss and positive electrode impedance growth. Similarly, cells containing 1% LFO, which showed better electrochemical performance during cycle-hold testing, show less Mn dissolution than cells containing 2% FEC + 1% DTD, with the same $LiPF_6$ concentrations.

Figure 4.12 does not show data for Ni and Co. Figure B.3 shows representative µXRF spectra from cells that were measured after testing, in Figure 4.12a. The peaks measured in the vicinity of the Mn K_α energy are readily visible and the trend from spectra-to-spectra is clear. There are small, almost indiscernible signals centered at the Ni and Co K_α energies that are beneath the analysis limit of the data analysis software to fit and integrate. Thus, the software reports no Ni or Co deposition. It is likely that small amounts of Ni and Co do indeed dissolve from the positive electrode but compared to Mn the amount is small. The amount of Mn measured is approximately 250 ppm relative to the total quantity of the Mn initially in the positive electrode. Also, the presence of an obvious peak relative to the baseline at the Ti K_α energy is due to the surface coating on the positive electrode particles and does not vary with electrolyte salt concentration.

It has been shown that a resistive rock salt surface phase can develop with layered positive electrodes that are charged to high voltage, likely of the form $Li_xM_{1-x}O$.[52,235] This implies transition metals in this phase exist in either the 2+ or 3+ oxidation state, dependent on the *x*, the concentration of Li. Ni and Co Rocksalt phases of $Ni_xCo_{1-x}O$ have been

reported,[236] where either Ni and Co readily exist as 2+ and 3+ ions, while Mn prefers to exist in the 3+ or 4+ state. All of these ions can therefore satisfy a Li-containing rock salt structure in the 2+ oxidation state. It is possible that the source of the fatal positive electrode impedance growth observed in cells undergoing cycle-hold testing and discussed with Figures 4.4 and 4.9, is due to a resistive rock salt surface phase growth. Because the impedance growth is positively correlated with Mn dissolution, this could suggest that rock salt phase growth and Mn dissolution may be mechanistically related. This is largely speculation, but conceivably may involve a mechanism that favors a rock salt phase consisting of Co and Ni rather than Mn, for some unknown reason. Mediation by salt concentration or other aspect of electrolyte composition may occur through electrolyte reactions at the surface, the chemistry and morphology of a positive electrode passivation film, or some other influence determined by the presence of certain solution structures. Verifying and validating such a mechanism requires means and equipment that are presently unavailable to the author and the author's institution, specifically access to atomic resolution transmission electron microscopy and many experiments to correlate with μXRF results.

Figure 4.13 shows cells thickness and combined negative electrode thickness of cells after approximately 650 h of cycle-hold testing with charging to 4.4 V at 40°C, as functions of the electrolyte $LiPF_6$ concentration. An external measurement of cell thickness was not taken after formation, or prior to commencing cycle-hold testing, therefore an exact reference for determining the thickness change during cycling for each cell does not exist. This was due to the implementation of thickness measurements as a part of regular cell handling after these cells had been constructed and started testing. As a proxy for this

beginning-of-life measurement, five cells that were identical to those that were tested had thickness measured as obtained from the manufacturer, without electrolyte. The average thickness and standard deviation of these are indicated graphically in Figure 4.13. In both Figures 4.13a and 4.13b, the cell thickness, measured externally using a linear gauge, increases with increasing electrolyte salt concentration. There is some non-monotonic increase in the cells containing 1% LFO, in Figure 4.13b, but nevertheless the overall trend is increasing as a function of $LiPF_6$ concentration. The thickness increase in a cell is typically attributed to thickening of the passivation films on either the positive or negative electrode, which can be interpreted as two possible ways. Increased film thickness can yield improved passivation, by providing a physically larger barrier between the electrode and electrolyte, but this can also result in increased internal resistance for the same reason. Increased film thickness could also indicate initially poor passivation or disrupted passivation through phenomena such as film or particle expansion due to material volume changes, which induce continuous film repair and an accumulation of decomposition products.
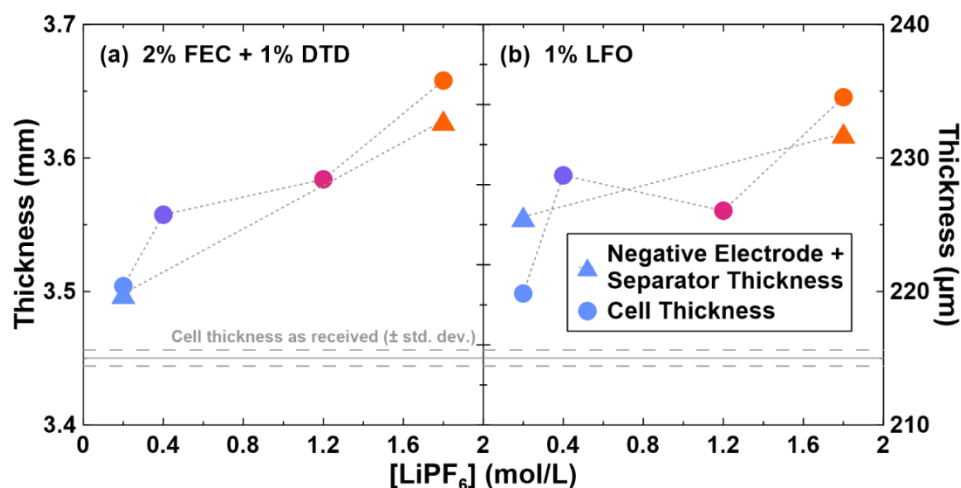
Figure 4.13. Thickness measurements made on NMC532/AG cells measured after cycling for approximately 650 h using a cycle-hold protocol with charging to 4.4 V at 40°C. Cells contained electrolytes with varied $LiPF_6$ concentrations and either (a) 2% FEC + 1% DTD or (b) 1% LFO electrolyte additives. Cell thickness (circles, left axis) was measured in the jellyroll vicinity using a linear gauge. The thickness of identical cells, as received is indicated with a horizontal grey line, with dash line representing uncertainty. Electrode + separator thickness (triangles, right axis) was measured using synchrotron X-ray computed tomography. X-ray images from which thickness values were obtained can be found in Figure B.4. Symbol colors are consistent with $LiPF_6$ concentration color scheme in Figure 4.8.

Figure 4.13 also shows the combined thickness of the negative electrode and separator, as a function of $LiPF_6$, as determined by analysis of synchrotron X-ray CT images. Due to beamtime constraints, only cells containing 0.2M and 1.8M $LiPF_6$ could be analyzed for each electrolyte additive system. Fortunately, these are endpoint electrolyte concentrations and therefore should represent the average trend. The thickness of the negative electrode and the separator are measured together because similar atomic number and densities make these two components nearly indistinguishable in X-ray images. Interpretation of this data assumes that the separator thickness is unchanging, and therefore any differences between cells is due to differences at the negative electrode. When both 2% FEC + 1% DTD or 1% LFO are used, the thickness of the negative electrode and separator increase as the $LiPF_6$ concentration increases. The thickness of the positive

electrode was also measured but changes from cell-to-cell were negligible. This indicates that the increase in cell thickness that occurs in cells with increasing salt concentration, measured externally using a linear gauge, trends identically to the negative electrode thickness measured using X-ray CT. This is due to increased thickness of the negative electrode, presumably caused by increased SEI thickness. This is a surprising result from a certain perspective, as high voltage testing leads to greater amounts of electrolyte oxidation at the surface of the positive electrode and presumably the solid decomposition products of that electrolyte oxidation accumulate on the positive electrode. Alternately, no increase in the rate of electrolyte oxidation was detected as a function of $LiPF_6$ concentration in microcalorimetry experiments and therefore there should be no change in the positive electrode passivation film thickness. This increase in thickness is not detected when EIS measurements are made, as cells with high $LiPF_6$ concentrations show smaller charge transfer resistances and lower rates of impedance growth. It was shown via measurements on symmetric cells that impedance spectra are largely dominated by positive electrode impedance. The contribution of negative electrode thickness to impedance may be too small in comparison to resolve in comparison. Altogether, this suggests that the use of higher $LiPF_6$ concentrations can produce a thicker SEI with perhaps greater passivation ability. The use of higher $LiPF_6$ concentrations also results in an SEI that does not have a significant decrease in Li-ion conductivity associated with increasing thickness, or outright has improved conductivity to Li-ions.
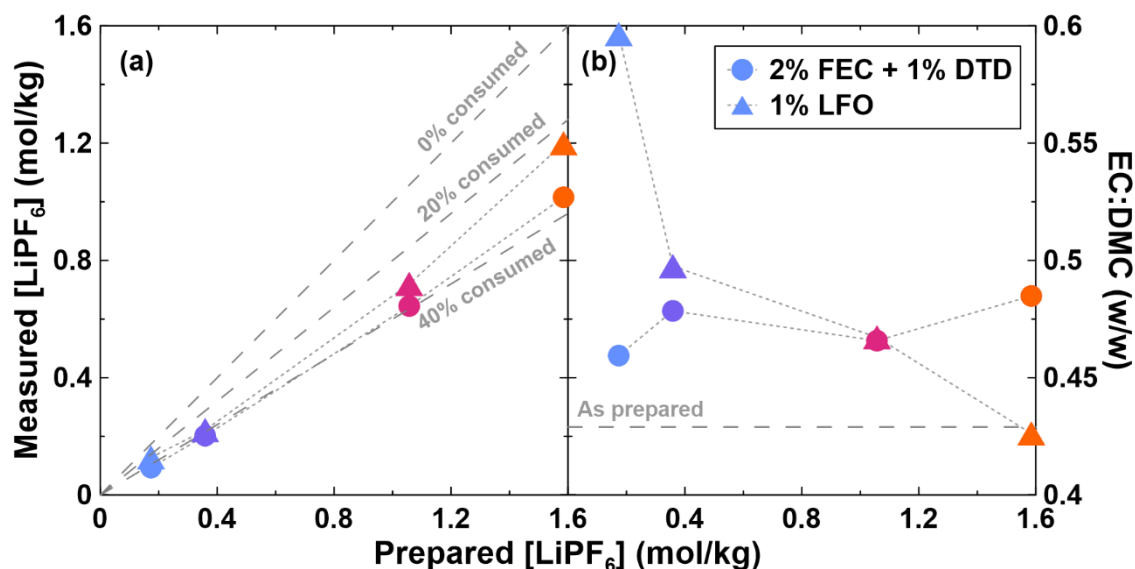
Figure 4.14. (a) LiPF$_6$ concentration and (b) EC:DMC ratio as a function of electrolyte LiPF$_6$ concentration as prepared, as determined by NMR spectroscopy on electrolyte extracted from NMC532/AG cells after cycling for approximately 650 h using a cycle-hold protocol with charging to 4.4 V at 40°C. Cells contained electrolytes with varied LiPF$_6$ concentrations and either 2% FEC + 1% DTD or 1% LFO electrolyte additives. Symbol colors are consistent with LiPF$_6$ concentration color scheme in Figure 4.8. A diagonal dashed line in (a) indicates relationship between measured and prepared concentrations if there is 0, 20 and 40% salt consumption during testing. A horizontal dashed line in (b) indicates the EC:DMC ratio of as prepared electrolyte. Dotted lines connecting data points are to guide the eye only.

Figure 4.14 shows results of electrolyte analysis by NMR spectroscopy on electrolytes extracted from cells that completed 650 h of cycle-hold testing with charging to 4.4 V at 40°C. Figures 4.14a and 4.14b show the LiPF$_6$ concentration and the solvent blend measured as functions of the LiPF$_6$ concentration of electrolyte originally injected into cells. The salt concentrations, for reasons of convention, are reported in Figure 4.14 with units of molality, or moles per kilogram of solvent. The reader should note that conversion between molarity and molality is governed by the density of the solvent mixture, which in this case is approximately 1.13 g/mL. Concentrations will be referred to using molarity to remain consistent with the rest of this document.

Figure 4.14a shows that all cells experienced significant amounts of salt consumption, approaching 40% of the initial concentration. It has been noted previously that significant decreases in conductivity do not occur a as a function of salt concentration until very low salt concentration, well below 0.5M.[73] These two pieces of evidence are consistent with the increase in series electrolyte resistance noted in the discussion of Figure 4.9 and the consumption of salt in cells containing higher initial concentrations is not noticed in the measured series resistance due to little change in the conductivity. The measured salt consumption in cells containing 2% FEC + 1% DTD is slightly more than in cells containing 1% LFO. This agrees well with 1% LFO providing better capacity retention, impedance control and mitigation of Mn dissolution, but overall, the differences between the two additive systems are small.

Figure 4.14b shows considerable variation in solvent ratio as a function of both salt concentration and electrolyte additive system. Cells containing 2% FEC + 1% DTD show nearly no difference to the EC:DMC ratio when different salt concentrations are used, but a small amount of DMC consumption in all cells. Considerably different behavior is noted in cells that contain 1% LFO. In such cells, Figure 4.14b suggests that the EC:DMC ratio increases, meaning greater relative amounts of DMC consumption, as the $LiPF_6$ concentration decreases. The amount of electrolyte consumed in the most extreme case, 0.2M $LiPF_6$ with 1% LFO, is equal to approximately 20% of the original solvent volume added to the cell. Consumption of such a large fraction of electrolyte is certainly possible, without necessarily altering cell performance as these cells contain approximately 4 g of electrolyte per Ah of capacity and are considered to have quite a bit of excess electrolyte compared to commercial cell making standards.

The consumption of electrolyte via parasitic reactions can result in thickening of the SEI which should show a measurable increase in electrode and cell thickness. The relative solvent consumption shown in Figure 4.14b does not agree well with the thickness measurements shown Figure 4.13. This may suggest spurious results obtained from the NMR experiments, shown in Figure 4.14. This is possible, due to the nature of extraction-based electrolyte analysis techniques and the susceptibility to handling or preparation errors, which will be discussed further in this section. It is also possible to have electrolyte decomposition products that are similar in density to the electrolyte itself, which could result in electrolyte consumption without changes to the jellyroll volume. This is generally not observed, as SEI thickening can happen uniformly over the entire surface of all electrode particles, causing them to increase in effective diameter (when considered ideally as spheres) and hence increasing the volume of the electrode coating. Therefore, it would be expected that cells which showed greater thickness, specifically those with higher $LiPF_6$ concentrations, should show higher amounts of solvent consumption, which disagrees with results shown in Figure 4.14b.

The fact that there is increasing DMC consumption with decreasing $LiPF_6$ concentration does seem to agree with the typical suggestion that increased salt concentration provides greater anodic and cathodic electrolyte stability. This amount of DMC consumption corresponds to approximately 60 mAh of capacity if the consumption reactions are a one-electron process. This amount of true capacity loss from the lithium inventory is not measured in these cells, therefore the solvent consumption is likely not due to reduction at the negative electrode surface. This process could occur via oxidation at the positive electrode, as oxidative process do not consume active lithium and can even

replenish lost capacity from the lithium inventory.[111] In practical sense, the amount of measured DMC consumption diminishes to negligible amounts when higher $LiPF_6$ concentrations are used, suggesting this consumption would be a non-issue in real cells that are designed to achieve long lifetimes. Again, it should be mentioned that there are indications that the NMR results presented here are spurious but are shown for completeness. This will be discussed below in comparison to complementary electrolyte analysis in the form of Li-ion differential thermal analysis.

Figure 4.15 shows Li-ion DTA profiles for cells containing 2% FEC + 1% DTD and a series of $LiPF_6$ concentrations, measured before and after 650 h of cycle-hold testing with charging to 4.4 V at 40°C. Measurements were made on different, but identically prepared cells after formation and after testing. Li-ion DTA interpretation is presently very simple and rudimentary despite the complex and detailed nature of the measured profiles, as the technique is mostly still in its infancy and models to calculate the profiles do not yet exist. Generally, the change in temperature of the negative feature associated with the liquidus is reported and profile shapes can be compared to previously measured compositions.[215,217] Here, there is very little change in the liquidus temperature, which indicates a mostly unchanged electrolyte composition and little if any $LiPF_6$ consumption. Comparing to the NMR results presented in Figure 4.14, the DTA profiles do not capture the small amount of DMC consumption that occurs with cells containing 2% FEC + 1% DTD additives that is invariant with $LiPF_6$ concentration, nor does it capture the nearly 40% $LiPF_6$ consumption indicated by the NMR.
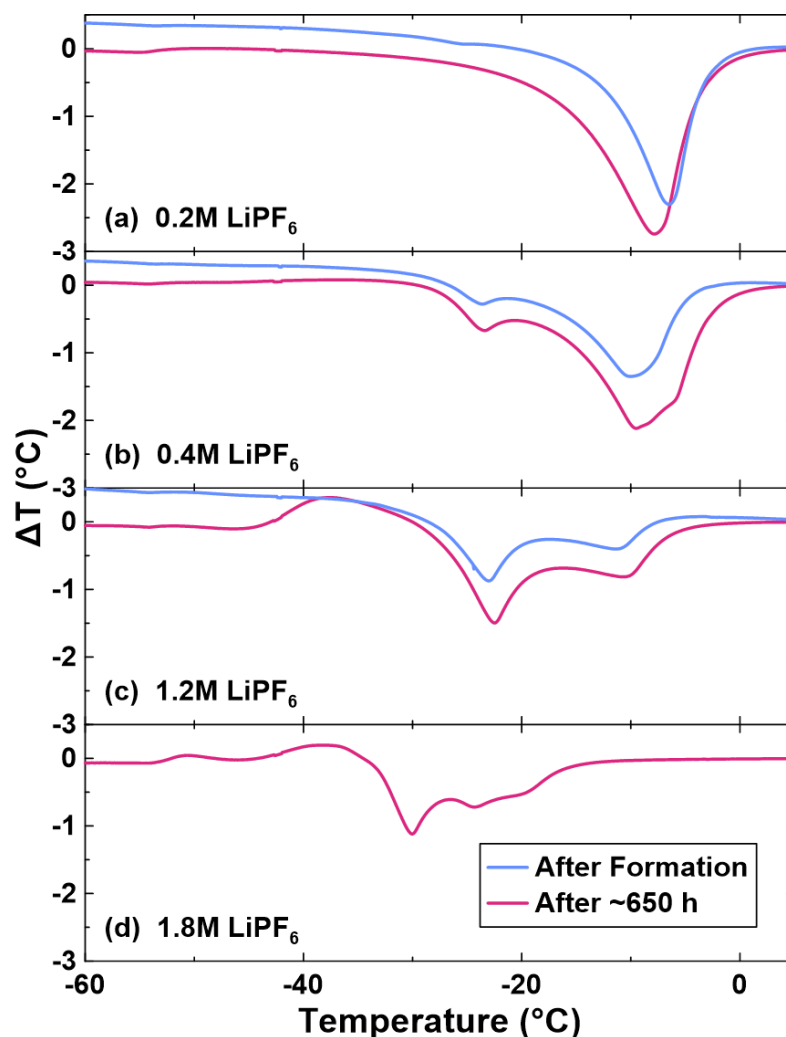
Figure 4.15. Li-ion differential thermal analysis traces for NMC532/AG cells collected at 3.8 V, after formation or after approximately 650 h of testing using a cycle-hold protocol with charging to 4.4 V at 40°C. ΔT refers to the difference between the sample temperature and the temperature of a reference cell, while the temperature on the horizontal axis is the sample temperature. Cells contained electrolytes with (a) 0.2M, (b) 0.4M, (c) 1.2M or (d) 1.8M $LiPF_6$ concentrations. Cells contained 2% FEC + 1% DTD electrolyte additives.

As an example, the DTA profiles of cells that were constructed with 1.2M $LiPF_6$ electrolyte look nearly the same after formation and after testing. This generally suggests little change in electrolyte formulation during testing. The similar is true of cells constructed with 0.4M $LiPF_6$ electrolyte. The difference between the DTA profiles of cells at these two concentrations is the relative size of the features at approximately -10°C and -

23°C, with the latter showing a stronger signal as the salt concentration is increased. If, as the NMR results shown in Figure 4.14 suggest, up to 40% $LiPF_6$, the cell which was constructed with 1.2M $LiPF_6$, should have approximately 0.7M $LiPF_6$ after 650 h of testing. This would show a DTA profile somewhat between those for the 0.4M and 1.2M cells measured after formation. This is not the case and highlights the discrepancy between the NMR and DTA experiments.

The difference in the DTA and NMR results could be attributed to several factors. It has been reported that in the $EC/EMC/LiPF_6$ electrolyte system, simultaneous consumption of solvent and $LiPF_6$ can result in offsetting effects that result in little discernable change to DTA profiles and specifically liquidus temperature.[215] At the time of preparing this thesis, compositions in the $EC/DMC/LiPF_6$ system have not yet been carefully measured by DTA and published. NMR and DTA experiments were made on identically prepared but different cells, which allows the opportunity for undocumented differences and handling errors to occur. NMR is an extraction-based technique which requires care and expertise during extraction but is well established and provides a relatively simple interpretation. Li-ion DTA is an *in situ* technique that requires minimal handling care but is immature and can be challenging to interpret. Nevertheless, it is a simple measurement and is undeniably representative of the contents of the cell at the time of measurement. Other evidence presented in this chapter, such as changes in the series electrolyte resistance, as measured by EIS, agrees with the picture of salt consumption presented by NMR. The NMR and DTA results are contradictory but serve as a good example of the need for both repeated testing and use of varied experimental techniques when elucidating the chemical and structural changes associated with Li-ion failure. In

addition to repetition, introducing other electrolyte analysis techniques such as gas chromatography/mass spectrometry and inductively coupled plasma/optical emission spectroscopy would be highly instructive and beneficial.

In summary, the work presented in this section further explores the mechanisms of failure in cells constructed with different $LiPF_6$ concentrations subjected to cycle-hold testing. Capacity loss and positive electrode impedance growth that are controlled and slowed by increasing $LiPF_6$ concentration coincided with Mn dissolution from the positive electrode and active mass loss from both the positive and negative electrodes that are similarly controlled and mitigated with increasing salt concentration. Electrolyte analysis resulted in inconclusive findings. More experimentation is needed to rectify this and to explore a proposed mechanism relating positive electrode impedance growth and Mn dissolution to the growth of a resistive positive electrode surface phase, likely of the disorder rock salt structure.

4.4 Study of the Role of Electrolyte Formulation and Temperature on Lifetime During Cycle-Hold Testing

Sections 4.2 and 4.3 showed that high voltage performance of NMC532/AG cells was strongly dependent on the concentration of $LiPF_6$ used in the electrolyte. Section 4.3 also showed that selecting improved electrolyte additives, such as 1% LFO, could make a positive contribution to the high voltage performance as well, in a similar manner to adding more $LiPF_6$ in many metrics. The following results and discussion aim to explore the

121

possible improvements that can be obtained by variations of more aspects of electrolyte chemistry than two additive systems and four LiPF$_6$ concentrations.

Previous study has shown that the removal of EC from electrolytes for high voltage cells can improve cycle life.[168,169] The use of fluorinated solvents rather than alkyl carbonates has led to the use of FEC which is expected to have superior anodic resistance and high voltage performance due to the electron withdrawing nature of fluorine.[169,174] Figure 4.16 shows the discharge capacity versus cycle number for cells undergoing cycle-hold testing at 40°C with charging to 4.4 V, with electrolytes containing different solvent blends, four different LiPF$_6$ concentrations and two different additive systems. The experiments represented by Figure 4.16 can be thought of as an extension of the basic cycle-hold experiments introduced in Section 4.3, with altered solvent systems. Either EC/DMC or FEC/DMC with 1:9, 3:7 or 5:5 ratio by weight, were used. Either 2% FEC + 1% DTD or 1% LFO, consistent with Section 4.3, were used. In the case of cells already containing FEC as a co-solvent and were assigned to be made with 2% FEC + 1% DTD, only 1% DTD was added due to the abundance of FEC already in the electrolyte.
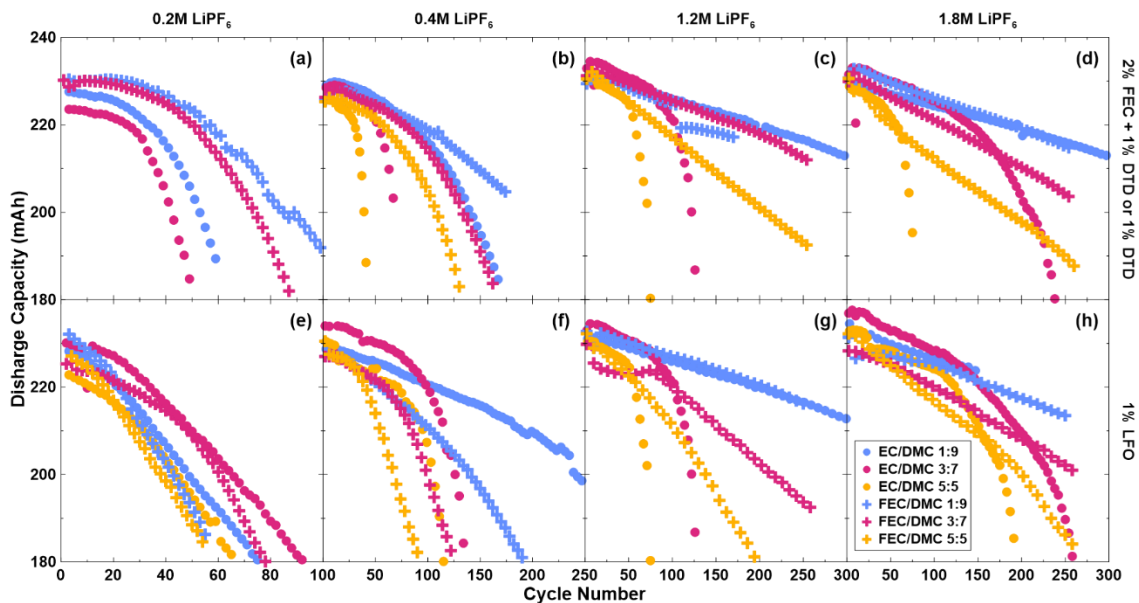
Figure 4.16. Discharge capacity as a function of cycle number for NMC532/AG cells subjected to cycle-hold testing at 4.4 V and 40°C. Cells contained electrolytes with various solvent blends, as indicated in the legend. Cells also contained (a,e) 0.2M, (b,f) 0.4M, (c,g) 1.2M or (d,h) 1.8M LiPF$_6$ concentrations and either (a-d) 2% FEC + 1% DTD in the case of EC co-solvent, or 1% DTD in the case of FEC co-solvent, or (e-h) 1% LFO electrolyte additives.

When Figure 4.16 is viewed as a whole, better cycle-life is demonstrated as the concentration of cyclic carbonate in the electrode is decreased. This is generally true independent of salt concentration, the choice of FEC or EC, or the choice of additive system, with a few exceptions. In Figure 10e, cells with electrolyte containing EC/DMC (1:9) and FEC/DMC (1:9) both show among the worst performance. When low concentrations of salt and cyclic carbonates are used, the solution dielectric constant and resulting dissociation and conductivity are low.[73] This may affect the solution structures and interaction of the electrolyte with the charged electrode surfaces when 1% LFO is used. To achieve a long-lived Li-ion cell that operates well at high voltage, it has been demonstrated the higher salt concentrations are warranted, so this issue would never arise in practical applications, but in tests such as these, it demonstrates that in fringe cases or

compositions, behaviour of certain additives and the overall electrolyte chemistry can become unpredictable. This suggests that a minimum solution dielectric constant is required for effective use of certain additives, like LFO.

When 0.2M or 0.4M LiPF$_6$ concentrations and/or cyclic carbonate concentrations of 30% or 50% are used with the 2% FEC + 1% DTD (or 1% DTD) combination, cells that have FEC as a co-solvent show superior cycle-life compared to cells containing EC instead. Electrolytes with low salt concentration should present solution structures with low anodic stability. The above observation may be a case of a fluorinated solvent contributing anodic stability that might otherwise be conferred by salt if a higher concentration were used. It could also be simply due to the quality of the passivation films formed in the presence of this additive system in combination with FEC and the absence of EC. Examining the same case, but with electrolytes that contain 1% LFO, the opposite is found: cells containing EC show superior lifetime than those containing FEC when lower salt concentrations are considered. The difference in solvent preference is an example of how significantly the inclusion of a small amount of carefully selected additive can dramatically alter cell performance, presumably through *in situ* passivation film engineering. When 1.2M and 1.8M LiPF$_6$ are used, FEC appears to provide better lifetime than EC, in the presence of both 2% FEC + 1% DTD and 1% LFO when solvent ratios of 3:7 or 5:5 are used. The best cycle-lives are obtained with the most salt (1.8M LiPF$_6$) and the lowest cyclic carbonate ratio solvent blends (1:9) for both additive systems. In these cases, the difference between the performance of EC-based and FEC-based electrolytes is very minimal. The improved electrolyte chemistry afforded by reduced cyclic carbonate concentration and increased salt concentration makes the choice of cyclic carbonate less important. This is a favorable result

for practical applications and cell makers seeking high voltage capable cells because the use of fluorinated solvents comes with associated cost increases and safety/handling difficulties.

The best electrolyte composition being high salt concentration, low cyclic carbonate is also very fortuitous from a transport perspective. Cyclic carbonates are typically responsible for providing the solvent blend with a high dielectric constant to enable salt dissociation and excellent ion transport properties. Low cyclic carbonate solvent blends have lower dielectric constants prior to adding salt, but as the amount of salt in solution increases, the dielectric constant increases, enabling the dissolution of yet more salt and improvement of transport properties to a level that is comparable to higher cyclic carbonate concentration blends once sufficient concentrations are reached.[137]

Figure 4.17 shows the discharge capacity and ΔV as a function of cycle number for cells containing electrolytes comprised of EC/DMC (3:7), four different $LiPF_6$ concentrations, and seven different electrolyte additive systems, tested using cycle-hold methods at 40°C with charging to 4.4 V. ΔV growth in Figures 4.16e-4.16h is noted to increase in a manner that mirrors the capacity loss for corresponding cells in Figures 4.16a-4.16d, indicating impedance growth, likely from the positive electrode, is the primary cause of failure. Increased cycle-life and lower rates of ΔV growth are observed among individual additive systems as the $LiPF_6$ concentration is increased. Cells containing 2% LiDFDOP and 2% LiDFDOP + 1% LFO show among the longest cycle-life at every salt concentration, and vastly outperform the additive systems discussed thus far, 2% FEC + 1% DTD and 1% LFO. LiDFDOP is considered to be a modern electrolyte additive and

shows progress in additive development, as 2% FEC + 1% DTD and 1% LFO have both previously been reported as excellent additives for high voltage use.[150,231]
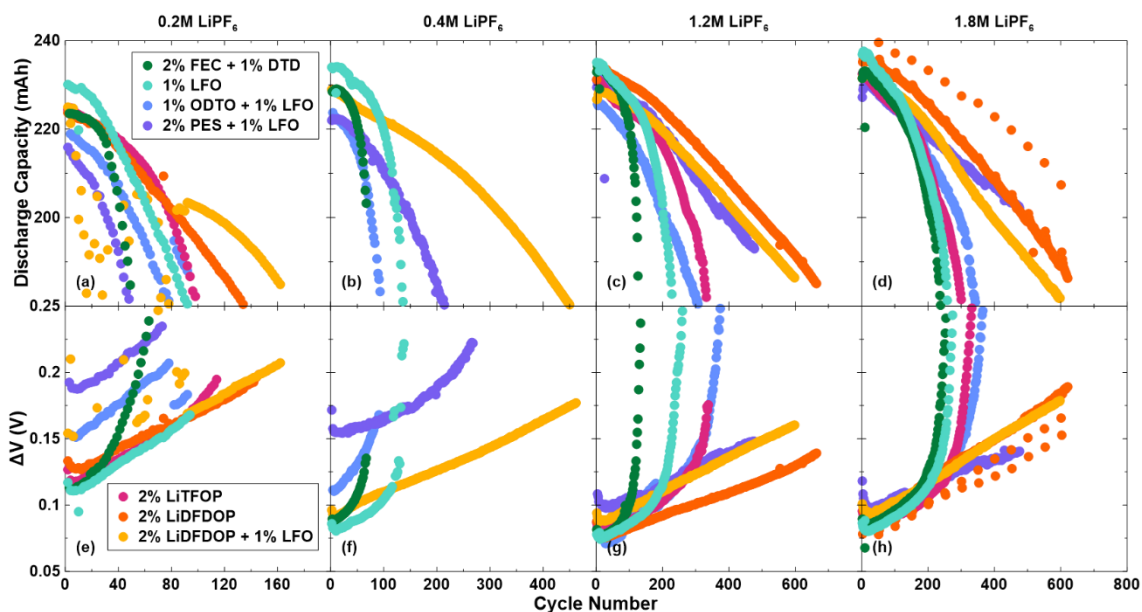
Figure 4.17. (a-d) Discharge capacity and (e-h) ΔV as a function of cycle number for NMC532/AG cells subjected to cycle-hold testing at 40°C with charging to 4.4 V. Cells contained electrolytes with (a,e) 0.2M, (b,f) 0.4M, (c,g) 1.2M or (d,h) 1.8M LiPF$_6$. Cells also contained electrolytes with one of seven electrolyte additive blends, as indicated in the legend. The reader should note the x-axis scales vary column-wise.

Cells containing 2% PES + 1% LFO are of note for showing performance relative to other additive blends that depends strongly on the LiPF$_6$ concentration. In Figures 4.16a and 4.16b, when low LiPF$_6$ concentrations are used, the cells containing this additive blend show among the shortest cycle-life. Performance is improved relative to other blends with the use of 1.2M LiPF$_6$, in Figure 4.16c, as the cell containing 2% PES + 1% LFO is nearly as good as the best cells, containing LiDFDOP. Finally, when electrolytes with 1.8M LiPF$_6$ are used, 2% PES + 1% LFO appears to be the best electrolyte, showing superior ΔV control and providing better capacity retention than 2% LiDFDOP when compared after 500 cycles. This demonstrates the need for considerable testing of electrolytes subjected to

small variations in formulation. The interaction between electrolyte components is not presently well understood, and it is not uncommon to find that changing one aspect of an electrolyte formulation slightly leads to a completely different set of results and behaviours. It is possible that if the experiments shown in Figure 4.16 were repeated with the best base electrolyte formulation from Figure 4.15, namely EC/DMC (1:9), it is entirely possible longer cycle-life is found but with a different additive system performing the best.

Figure 4.18 shows the effect of replacing $LiPF_6$ with an alternate salt, $LiBF_4$. $LiBF_4$ has been shown to have merit over $LiPF_6$ in UHPC studies conducted with CCCV methods, subject to the condition that the cell voltage remains limited to 4.4 V or below,[237] which is perfectly suited for cycle-hold test methods being implemented throughout this chapter. Again, Figure 4.17 shows ΔV growth that mirrors capacity loss, which indicates impedance growth as a main mode of failure. The capacity and ΔV data for cells containing $LiBF_4$ show a more gradual rate of capacity loss and less accelerated failure and ΔV growth than cells containing $LiPF_6$, indicating at least somewhat different failure processes. Detailed investigation and description of the failure in $LiBF_4$ cells as a function of salt concentration, like that presented for $LiPF_6$ cells, is not performed here and could be an element of future work.

When 0.2M salt concentrations are used with either additive system, cells containing $LiBF_4$ are worse the cells containing $LiPF_6$. This is possibly due to poor transport properties inherent to $LiBF_4$ and low carrier count at low concentration. When higher salt concentrations are used, the combination of $LiBF_4$ and the 2% FEC + 1% DTD additive system in cells is no better than or is worse than otherwise identical cells containing $LiPF_6$. When $LiBF_4$ is combined with 1% LFO however, cells containing salt

concentrations of 0.4M, 1.2M and 1.8M all show superior cycle-life to their $LiPF_6$ counterparts, despite initially lower capacity. It is unclear the origin of this improved cycle-life, but thermal decomposition of the PF_6^- anion to PF_5 radicals is known and deleterious to cell performance,[79,238] but does not occur when $LiBF_4$ is used. $LiPF_6$ is nearly ubiquitous as the preferred salt for Li-ion cells in nearly all applications. At the very least Figure 4.18 suggests that the use of $LiBF_4$ can provide superior high voltage performance when sufficient concentrations are used and should be considered in experimental matrices aimed at optimizing high voltage cycle-life.
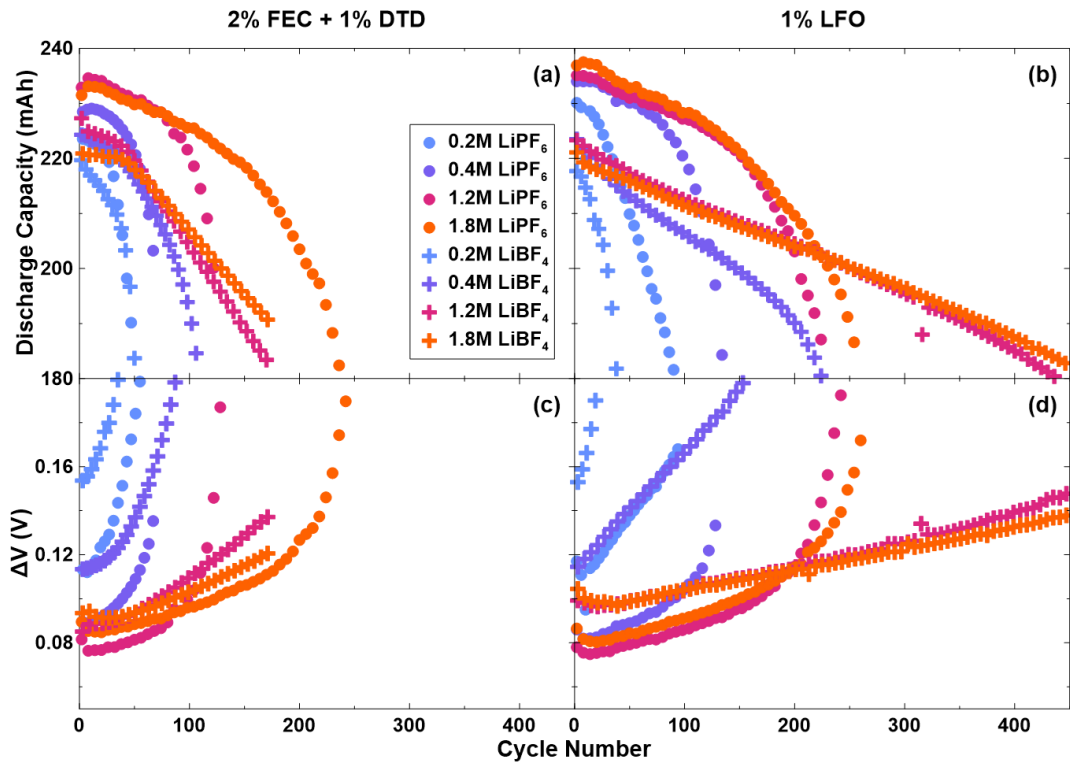
Figure 4.18. (a,b) Discharge capacity and (c,d) ΔV as a function of cycle number for NMC532/AG cells subjected to cycle-hold testing at 40°C with charging to 4.4 V. Cells contained electrolytes with two types of salts, used at four concentrations, as indicated in the legend. Cells also contained either (a,c) 2% FEC + 1% DTD or (b,d) 1% LFO electrolyte additives.
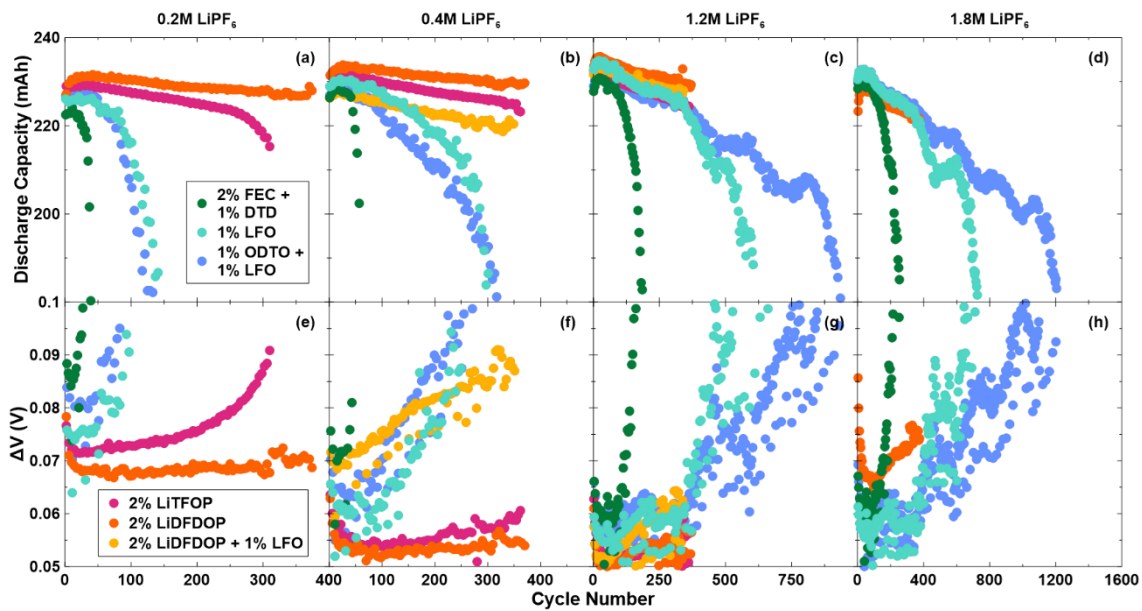
Figure 4.19. (a-d) Discharge capacity and (e-h) ΔV as a function of cycle number for NMC532/AG cells subjected to cycle-hold testing at room temperature (approximately 20°C) with charging to 4.4 V. Cells contained electrolytes with (a,e) 0.2M, (b,f) 0.4M, (c,g) 1.2M or (d,h) 1.8M LiPF₆. Cells also contained electrolytes with one of six electrolyte additive blends, as indicated in the legend. Symbol colors are consistent with Figure 11. The reader should note the x-axis scales vary column-wise.

Figure 4.19 shows the discharge capacity and ΔV for a large group of cells that is equivalent (save for the absence of 2% PES + 1% LFO) to the group discussed in relation to Figure 4.16. The difference is that the cells for which data is shown in Figure 4.18 were tested using a C/10 cycle-hold protocol with charging to 4.4 V at room temperature, in a room climate controlled to approximately 20°C. The slower C/10 rate was selected rather than a C/3 rate to reduce the possibility of localized electrolyte depletion due to concentration gradients that occur in cells proportional to the magnitude of the applied current.[239] Testing of cells at ambient or room temperatures is likely more representative of many common applications, but is less aggressive and requires more time to reach failure due to reduced thermal activation of parasitic reactions. Comparing Figure 4.19 to Figure

4.17, the longest-lived cells in the former last for 1200 cycles, while the longest-lived cells shown in the latter last for 600 cycles.

Like Figure 4.17, inspection of Figure 4.19 shows cells with electrolytes containing LiDFDOP have among the least capacity fade when comparing to other cells of equal LiPF$_6$ concentration. Unfortunately, at the time of writing, more cycles are required to determine if 2% LiDFDOP and 2% LiDFDOP + 1% LFO electrolytes will show the longest cycle-lives among cells with 1.2M or 1.8M LiPF$_6$, but early trends suggest they will. Also similar to Figure 4.16, cells containing 2% FEC + 1% DTD and 1% LFO have among the shortest lifetimes, indicating some of the newer additives tested do come with merit and represents progress for the research community.

The behaviour of cells containing 1% ODTO + 1% LFO, in terms of relative cycle-life, is another example of an additive system that benefits more from the addition of LiPF$_6$ compared to other additives. Relative to 1% LFO, when 0.2M and 0.4M LiPF$_6$ is used, 1% ODTO + 1% LFO, shows slightly worse or comparable cycle-life. When the LiPF$_6$ concentration is increased to 1.2M and 1.8M, the number of cycles to reach failure for the cells containing 1% ODTO + 1% LFO are nearly double those of the cells containing 1% LFO alone. The cell containing 1% ODTO + 1% LFO with 1.8M LiPF$_6$ shows the longest cycle-life, 1200 cycles, of cells reported in this chapter. The corresponds to reaching 80% of the nominal cell capacity after 4.5 years of testing, where that testing involved 40% of the time spent at 4.4 V. Even more remarkable is that the performance of cells containing 2% LiDFDOP and 1.8M LiPF$_6$ in Figure 4.19 implies a longer cycle-life would be achieved, with more time under test.

4.5 Conclusions

NMC532/AG cells that spend more time at higher potentials were shown to reach failure in fewer cycles and less time. Specifically, when cycle-hold and cycle-store methods were applied to cells with electrolytes containing varying concentrations of $LiPF_6$, cells were shown to fail due to positive electrode impedance growth. This resulted in apparent capacity loss under appreciable current rather loss of the cyclable lithium inventory, and the rate of impedance growth and failure inversely associated with $LiPF_6$ concentration.

Analysis of cells the underwent cycle-hold testing with charging to 4.4 V, at an elevated temperature of 40°C showed no difference in rates of parasitic reactions at high voltage, or the thickness of a CEI passivating layer on the positive electrode as a function of $LiPF_6$ concentration, suggesting that the increasing positive electrode interface was not due to build up of solid reaction products on the electrode surface. Increased Mn dissolution from the positive electrode during testing along with detection of increased positive electrode active mass loss with decreased $LiPF_6$ concentration suggest possible structural problems at the positive electrode relating to the associated increase in impedance. One speculated mechanism is the growth of a resistive surface phase, such as a disordered rock salt.

In addition to using electrolyte salt concentration to control the rate of cell failure and impedance growth during cycle-hold experiments, further exploration of electrolyte formulation showed that reduced cyclic carbonate concentrations, alternate salts and the use of modern electrolyte additives were all shown to be beneficial to improving cycle-life. Cells containing 2% LiDFDOP showed the best overall electrochemical performance

regardless of the salt concentration. Certain additive combinations, such as 2% PES + 1% LFO and 1% ODTO + 1% LFO, showed additional dependence on $LiPF_6$ concentration, where increasing concentrations improved overall cell performance while also unlocking better additive performance relative to other additive systems. Finding additives that respond synergistically to increased $LiPF_6$ concentrations represents one means of achieving vastly improved electrolytes for high voltage applications.

It should be apparent, particularly in reading Section 4.4, that small or individual changes to electrolyte formulation can result in an entirely different electrochemical environment. Electrolyte additives that once worked with a particular salt concentration and solvent blend may not be suitable when one of those parameters changes and a new optimization is required. To build a broad and deep knowledge base, combinatorial style testing could be used to properly elucidate relationships between electrolyte components and optimize electrolyte formulations in a particular cell type for use in a certain application. Models do not yet exist that allow one to project the lifetime, *in operando* electrochemical stability and surface chemistry at an electrode interface associated with electrolyte formulation. This needs to be tested not just for lifetime or cycle life in cells but coupled with careful analysis and characterization. The necessary amount of work and dimensionality of the phase space is truly staggering. If all the independent results presented in this chapter hold true, the best electrolyte formulation for use at high voltage would be 1.8 M $LiBF_4$ in EC/DMC (1:9 w/w) with 2% PES + 1% LFO. Due to the unique nature of every electrolyte formulation however, it is unlikely that this would end up being a solution to the optimization of all variables and possibilities presented here. The discussion in this chapter has mostly centered on changes to electrolyte formulation in a

single cell type, mostly using a single mode of testing. While many results carryover, it should also be noted that if one changes one of the electrode materials or the test type, the optimum electrolyte and certain behaviors likely change as well. This will be demonstrated in subsequent chapters.

CHAPTER 5 SURVEY OF ELECTROLYTE ADDITIVES, TEMPERATURE AND CHARGE LIMIT IN CO-FREE CELLS

The author of this thesis was responsible for most of the experiment planning including electrolyte additive selection and testing parameters, executing all experiments and data analysis. Jeff Dahn was responsible for facilitating the relationship with the industrial sponsor of this work, who encouraged research towards improving high voltage, low cobalt cells, selecting the cell type for this work, supervision of experiments throughout and review of data at each step. Julian Oxner helped with cell making for many of the cells in this section, with Saad Azam and Wentao Song also making a small fraction.

5.1 Introduction

The positive electrode is a major driver of cell energy density and cost, while also being a significant contributor to electrochemical performance and the determination of acceptable operating parameters (e.g., voltage window). The historic chronology of NMC-type positive electrode materials used in known commercial cells and academic research publications on commercial quality cells roughly follows the order: $LiCoO_2$, $Li[Ni_{1/3}Mn_{1/3}Co_{1/3}]O_2$ (NMC111), $Li[Ni_{0.4}Mn_{0.4}Co_{0.2}]O_2$ (NMC442), $Li[Ni_{0.5}Mn_{0.3}Co_{0.2}]O_2$ (NMC532), $Li[Ni_{0.6}Mn_{0.2}Co_{0.2}]O_2$ (NMC622), and $Li[Ni_{0.8}Mn_{0.1}Co_{0.1}]O_2$ (NMC811). The trend over time has been to decrease Co and increase Ni concentrations. Co is particularly expensive and is distributed geographically in countries that often implement unethical mining and labor practices[240] but offers improved stability and solid-state kinetics when used in NMC-type materials.[240,241] Ni is

more economical than Co and depresses the voltage curve so that more capacity can be extracted without necessitating charging to higher voltage, but particularly high Ni positive electrodes have a structural contraction that occurs between 4.0 V and 4.1 V[43], inferior safety and lower electrochemical stability[39].
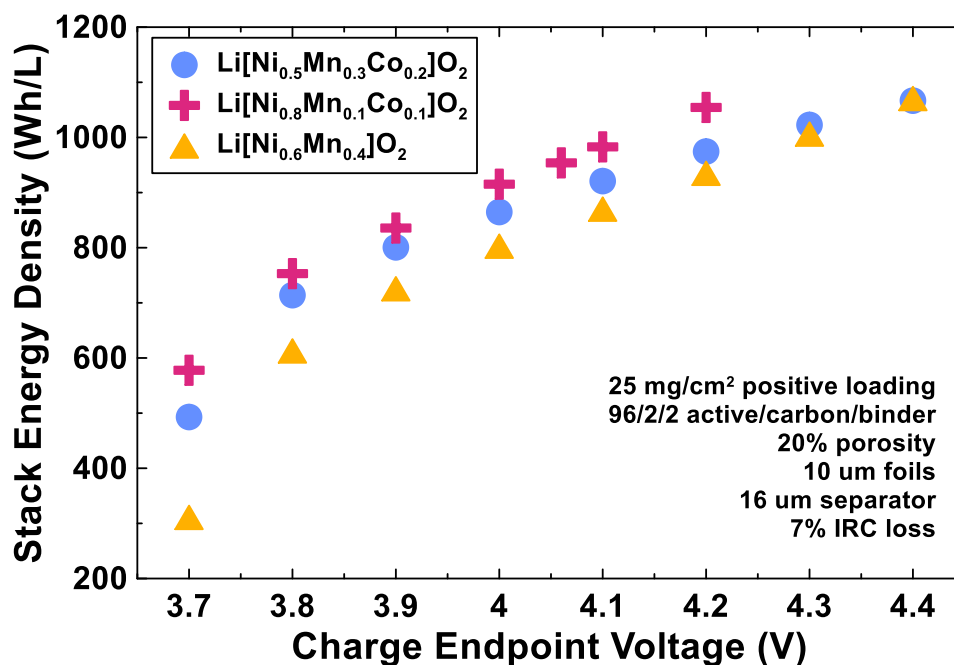
Figure 5.1. Calculated volumetric stack energy density as function of charge endpoint voltage for NMC532, NMC811 and NMC640. Stack energy density considers the active material coatings, current collectors and separators, but ignores the cell geometry and casing. Calculation assumptions are listed in the text insert.

Figure 5.1 shows the calculated volumetric stack energy density as a function of the voltage to which charging is limited for cell constructions with various layered positive electrodes, paired with graphite negative electrodes. Stack energy density calculations only include the electrode coatings, current collectors and separators, without considering cell casing or arrangement into a pack. The specific capacities for each electrode are used to determine a theoretical negative electrode mass loadings with an assumed 25 mg/cm^2 positive electrode loading and an N/P capacity ratio of 1.05. The electrodes are assumed to

be 20% porous, which along with the thickness of the separator and current collectors, allows for the determination of the stack volume Of the materials considered, $Li[Ni_{0.8}Mn_{0.1}Co_{0.1}]O_2$ or NMC811 shows the highest energy density at any given charge endpoint voltage. Data is not shown past 4.2 V for this material because usage at higher voltage yields poor lifetime and diminishing energy density returns when compared to other materials,[43] and is not done in a commercial setting. The energy density of a cell containing $Li[Ni_{0.5}Mn_{0.3}Co_{0.2}]O_2$ or NMC532 is competitive with NMC811 once charged to 4.3 V or 4.4 V. The energy density of $Li[Ni_{0.6}Mn_{0.4}]O_2$ (NMC640) is the lowest in Figure 5.1, but converges with that of NMC532 when charged to 4.4 V, and is comparable to the energy density of NMC811 that is charged to 4.2 V. Positive electrodes materials that are free of Co and not Ni-rich generally require charging to high voltage to achieve energy density that makes it commercially appealing to replace Ni-rich materials like NMC811.
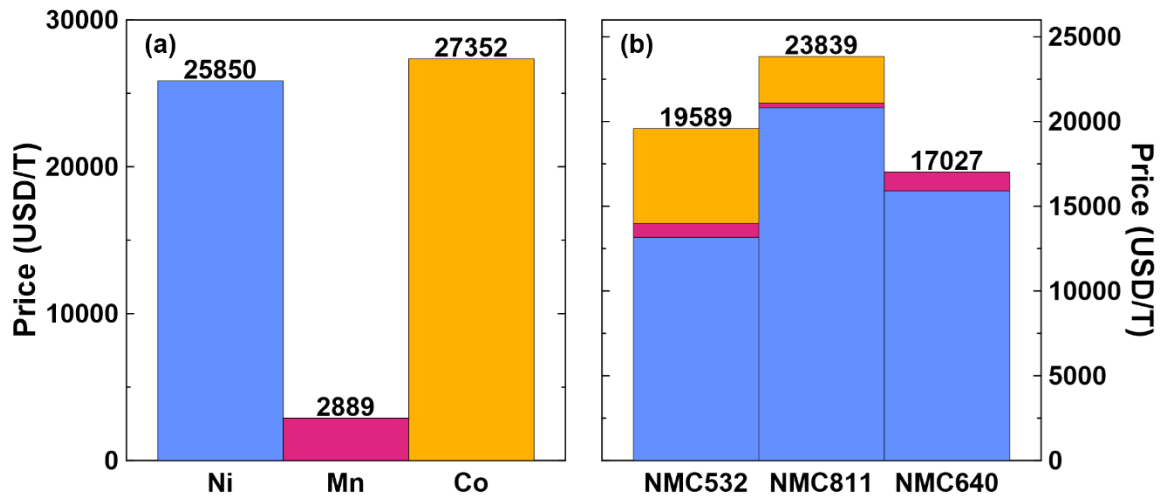
Figure 5.2. (a) Market price for Ni, Mn and Co in US dollars per ton as of March 1, 2023, plotted on a logarithmic axis. Prices are based on sulfate materials, sourced from Shanghai Metals Market spot pricing. Prices are adjusted per ton of metal. The mass of sulfates or hydrate constituents has been removed from this comparison. (b) Cost per ton of transition metals required to make $Li[Ni_{0.5}Mn_{0.3}Co_{0.2}]O_2$ (NMC532), $Li[Ni_{0.8}Mn_{0.1}Co_{0.1}]O_2$ (NMC811) and $Li[Ni_{0.6}Mn_{0.4}]O_2$ (NMC640) calculated from values in (a). Colors that comprise each bar in (b) match the transition metals labeled in (a).

The main merit of removing Co from the positive electrode of a Li-ion cell has conventionally been reducing cost. Figure 5.2a shows the price per unit weight of the three primary transition metals required to produce NMC materials, as of March 1, 2023, according to Shanghai Metals Market.[242] The prices shown are originally sourced from transition metal sulfates, which are common positive electrode precursors. The prices shown in Figure 5.2a are adjusted to show the cost per unit weight of each transition metal only, with the masses of any sulfate and hydrate constituents removed. Co is the most expensive metal used in NMC materials, although the price of Ni rivals it after a significant price increase in the last year. The price of Mn is nearly an order of magnitude smaller than the price of either Ni or Co. Figure 5.2b shows the cost per unit weight of the transition metals required to make the three positive electrodes introduced in Figure 5.1. Because NMC532 contains more Mn than NMC811, the cost of transition metals to make NMC532 is cheaper despite having slightly more Co. Due to the similar price of Ni and Co, along with the much lower price of Mn, NMC materials can essentially be ranked on cost by comparing the amount of Mn they have. Having no Co and the most Mn means NMC640 has the lowest price of the three materials compared in Figure 5.2b.

When assessing the economic viability of a material, cell and device makers typically assess the cost per unit energy a cell can store, typically denoted as $/Wh. If NMC640 can charge to 4.4 V without extremely deleterious effects, it can provide energy density competitive with NMC811 and NMC532, while being less expensive from a raw material perspective. This implies that in this case, it should demonstrate superior $/Wh and be a viable candidate as a sustainable and economical replacement for existing positive electrode materials. The assessment in this introduction does not account for other factors

that contribute to the final cost of a material, such as synthesis complexity, handling concerns, or energy expenditures. It should be noted that the cost of lithium, specifically lithium carbonate, is among the highest cost in cathode material production based on today's markets, with a price of approximately 53 300 USD/T or approximately 284 000 USD per ton of lithium.[242] Typically, optimal synthesis of positive electrode materials requires some excess lithium, rather than a stoichiometric formulation. Anecdotally, excellent NMC532, NMC811 and NMC640 materials are synthesized as $Li_{1.02}[Ni_{0.5}Mn_{0.3}Co_{0.2}]_{0.98}O_2$, $Li_{1.02}[Ni_{0.8}Mn_{0.1}Co_{0.1}]_{0.98}O_2$, and $Li_{1.07}[Ni_{0.6}Mn_{0.4}]_{0.93}O_2$ respectively. The reader should carefully note that NMC640 has more excess lithium than the other two materials. The total material costs are approximately \$32 600, \$35 000 and \$32 500 respectively. Based on current prices, which are of course subject to change, the cost benefit of NMC640 is small. Nevertheless, development of cells containing Co-free materials stands to have both economic and ethical benefits. It may also be possible to use improved synthesis methods to reduce the amount of excess lithium required to make NMC640 with less excess lithium and hence lower costs in the future.

The work presented in this chapter covers the use of electrolyte additives to improve the lifetime of Co-free, NMC640 cells that are charged to high voltages. Many of the electrolyte formulations used were shown to have merit in NMC532 cells in Chapter 4, and this chapter therefore demonstrates application of previous excellent results to a cell chemistry that has more commercial relevance. The results presented in Chapter 4 are from a cell type that is too expensive, using cycling methods that are enlightening and useful, but unconventional compared to the cycling methods that are typical of the field. With the goal of demonstrating improved performance in a language familiar and convincing to the

academic and industrial research communities, conventional testing methods are implemented rather than cycle-hold or similar test methods. The test methods include charging to high voltage and leverage some of the results of Chapter 4, as NMC640 cells must charge to high voltage without suffering degradation in order to deliver competitive energy density to cells made with contemporary positive electrode materials (e.g. NMC811).

5.2 Experimental

NMC640, or alternately NM64, cells were selected for use in this chapter and prepared in the general manner described in Chapter 3. Cells were balanced for charging to a limit of 4.5 V to enable exploration of high voltage performance and cycle life, and provide nominally 200 mAh, 215 mAh and 230 mAh when charged to 4.3 V, 4.4 V and 4.5 V respectively.

Electrolytes were prepared with 1.5M $LiPF_6$, as this corresponds to longer lifetimes obtained with higher-than-conventional $LiPF_6$ concentrations described in Chapter 4. Multiple additive formulations were used, based on the structures found in Table 3.2. Some combinations were selected to match electrolytes used in Chapter 4, in the hope that excellent additives and understanding developed in NMC532 cells carried over to NMC640. Other combinations were selected from literature and anecdotal reports. All formulations used in this chapter are listed in Table 5.1. For improved readability and minimal visual clutter in figures and the text, a shorthand designation for each additive formulation is provided. Additives are categorized based on approximate date of

appearance in the literature. Generation 1 are additives that are well studied and have been reported in the literature five or more years ago. Generation 2 additives are considered to be modern, or more recent additives and were provided as part of a collaboration with Zhuhai Smoothway Electronic Materials. Generally, these additives are oxalato-phosphate lithium salts. Generation 3 only contains one additive but represents a future or cutting-edge group of additives. The one additive, LiTFMP, is an *in situ* synthesized additive, introduced to the author as part of a collaboration with Argonne National Laboratory and has been described by Azam et al.[219] These categories and additive selections are not all inclusive, and many more additive types, concentrations and combinations are possible.

Table 5.1. Electrolyte additive formulations used in this chapter, shorthand used to simplify identification in the text and figures, and the category based on generation or chronology.

Full Description	Shorthand	Category
2% FEC + 1% DTD	2F1D	Gen 1
1% LFO	1L	Gen 1
2% PES + 1% LFO	2P1L	Gen 1
1% ODTO + 1% LFO	1O1L	Gen 1
2% FEC + 1% TAP + 1% LFO	2F1T1L	Gen 1
2% PES + 1% TAP + 1% LFO	2P1T1L	Gen 1
1% TAP + 1% LFO	1T1L	Gen 1
5% DiFEC	5DiF	Gen 1
5% DiFEC + 1% LFO	5DiF1L	Gen 1
2% LiDFDOP	2LDF	Gen 2
5% LiDFDOP	5LDF	Gen 2
2% LiDFDOP + 1% LFO	2LDF1L	Gen 2
2% LiTFOP	2LTF	Gen 2
5% LiTFOP	5LTF	Gen 2
5% LiTFOP + 1% LFO	2LTF1L	Gen 2
2% FEC + 2% LiDFOP	2F2LDF	Gen 2
2% LiTFMP	2LTFM	Gen 3

Multiple cells were made with each electrolyte additive and directed into one of four test protocols: UHPC cycling at 40°C, CCCV cycling at a rate of 1C at 20°C, CCCV cycling at a rate of C/3 at 40°C and CCCV cycling at a rate of C/3 at 55°C. Identical cells were made so each of the above tests could be applied with charge endpoint voltage limits of 4.3 V, 4.4 V and 4.5 V. Cells underwent formation with charging to a voltage limit that matched the cycling conditions. After formation, the volume of gas generated was measured and EIS was conducted. The group of cells that completed CCCV cycling at 40°C, with charging to 4.4 V was transferred to a UHPC to complete C/40 constant-current cycles to provide data which dV/dQ analysis can be performed on. This testing condition most closely matches the cycle-hold conditions described in Chapter 4.

5.3 Summary of Formation Metrics

Formation is simply the first cycle a cell completes and is normally associated with the establishment of passivation layers. It is also highly relevant to cell manufacturers because cells complete the formation cycle and any conditioning processes prior to release to customers. The performance and behavior of a cell during the formation process can affect manufacturer processes and the quality of cell delivered to a customer.

Figure 5.3 shows ordered bar graphs of the first cycle inefficiency, volume of gas produced, and the charge transfer resistance measured after completing formation. Results for each metric are separated by the charge endpoint voltage limit the cells were charged to during formation, and later during cycling experiments. The first cycle inefficiency is defined as the capacity lost per unit capacity stored during the first cycle. Excessive lithium

inventory loss due to the reactions that establish electrode passivation can result in a high first cycle inefficiency and a reversible cell capacity that is much lower than the theoretical capacity, as constructed. Cells that have low first cycle inefficiency therefore have higher energy density. The volume of gas produced during formation can affect the decision to use an electrolyte in a particular cell format and may add steps to the formation procedure. Excessive volumes of gas produced in formation can deform the casing and electrodes in flexible casing pouch cells that are not constrained or burst pressure interrupt devices in hard casing prismatic or cylindrical cells. This can require rigid constraints for forming pouch cells or moisture-free environments for forming unsealed hard cased cells. This can increase the operating costs associated with forming a cell. Manufacturers often try to find electrolytes that produce no gas during formation because they can eliminate an otherwise necessary degas step as a way of lowering the processing costs of building cells. Finally, low charge transfer resistance is often representative of overall low cell internal resistance, which enables greater fractions of energy delivery under high power draw. All three of the metrics reported in Figure 5.3 are better when minimized. Therefore, each panel in Figure 5.3 is sorted from highest to lowest (viewing from left-to-right) and better electrolytes for a given metric and charge endpoint voltage can be found towards the right side of each panel.

Figures 5.3 shows that first cycle inefficiency changes very little when comparing cells charged to 4.3 V, 4.4 V and 4.5 V. This is mostly because the inefficiency is due to SEI forming reactions on the negative electrode that occur immediately as the first charge commences and is largely independent of charging to higher voltage. The electrolytes that result in the lower first cycle inefficiency, at all three charge endpoint voltage limits, are

those that contain 2% PES + 1% LFO + 1% TAP, 2% PES + 1% LFO and 1% ODTO. The latter two are among the best electrolytes discussed in Chapter 4 and the former is one of those combinations with the addition of TAP, which has been shown to be excellent when used at in high voltage cells.[190] All of the Generation 2 additives have inefficiency greater than 10%, with electrolytes containing LiTFOP having higher inefficiency than those containing LiDFDOP. It should be noted that cells containing just 2% and 5% LiDFDOP and LiTFOP were all formed to 4.5 V, hence no data for these is seen in Figures 5.3d and 5.3g. Electrolytes containing DiFEC have the highest inefficiencies of all of 4.3 V, 4.4 V and 4.5 V.
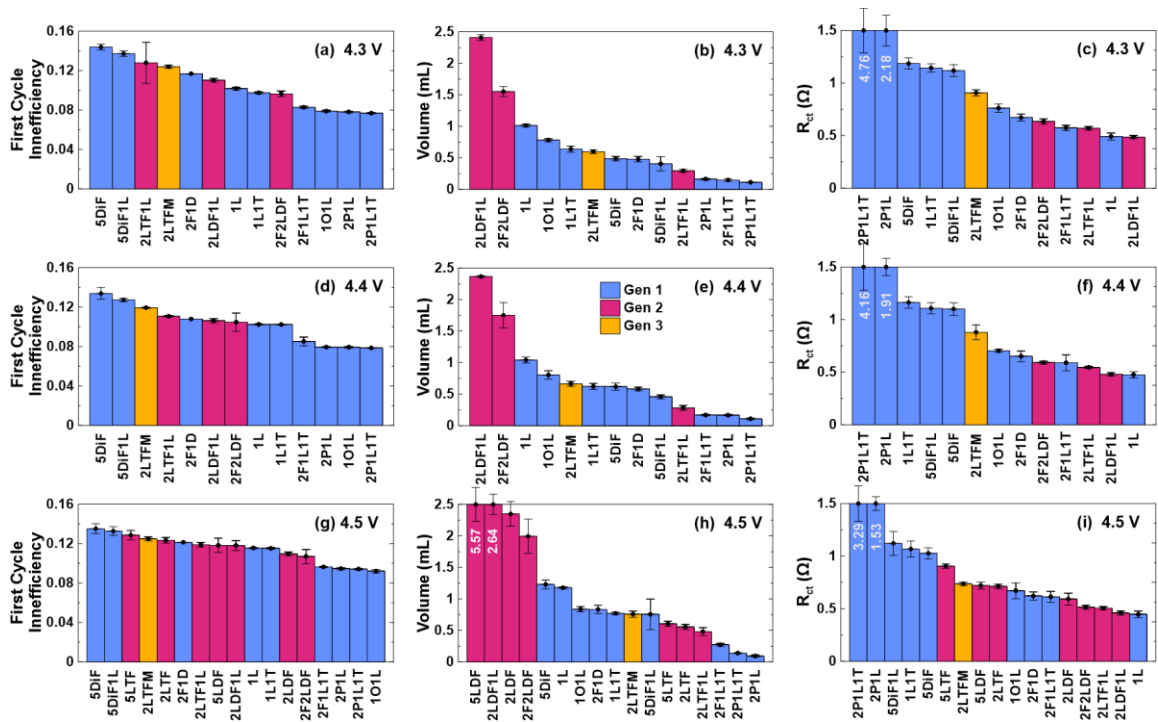
Figure 5.3. Summary of formation metrics obtained from NMC640 pouch cells. (a,d,g) First cycle inefficiency, (b,e,h) formation gas volume, and (c,f,i) charge transfer resistance obtained from EIS measurements made after formation are reported a function of the electrolyte additive formulation used in each cell. Cells were charged to (a-c) 4.3 V, (d-f) 4.4 V or (g-i) 4.5 V during formation.

Figures 5.3b, 5.3e and 5.3h show the volume of gas produced when each electrolyte is used. The nominal volume of the cell jellyroll is 2.8 mL, therefore 1 mL of gas produced is approximately a 35% increase. Cells containing PES consistently produce among the least gas, less than 0.25 mL of gas at all charge endpoint voltages. Even though these are the smallest volumes measured, this likely still warrants a degas step during commercial manufacturing. Cells containing LiDFDOP show the highest volumes of gas produced, even when co-additives are used. LiDFDOP contains two C_2O_4 groups, which conceivably can react to form two CO_2 molecules each. The fact that co-additives, at least FEC and LFO tested here, cannot reduce the excessive gassing associated with the use of LiDFDOP may suggest the use of LiDFDOP in commercial applications may be problematic. The action of additives is complex, and it is unclear without careful investigation into mechanistic details whether excessive gas production is due to lack of passivation and reaction of the electrolyte solvents, or gas associated with the reaction of additive molecules themselves. The amount of gas produced is not necessarily indicative of additive performance in other areas such as cycle-life but may be prohibitive for use by cell manufacturers that cannot tolerate a degas step in their cell preparation.

Figures 5.3c, 5.3f and 5.3i show the charge transfer resistance extracted from EIS measurements performed after formation. Cells containing PES, TAP and DiFEC often show high charge transfer resistance, while cells containing LiDFDOP and LFO often show lower charge transfer resistance. It is worth noting that the *in situ* synthesized additive, LiTFMP is middle of the field for all three metrics at all three charge endpoint voltage limits. Generation 2 additives are excellent for achieving low charge transfer resistance but can have high gas production and moderate first cycle efficiencies. In this sense, the older,

Generation 1 additives do not seem to be outclassed by newer additives. It is difficult to rank a single additive relative to the field across many metrics, particularly based on the data presented in Figure 5.3. An attempt is made later in this chapter to quantitatively rank many of these additives considering many metrics.

5.4 Ultra-High Precision Testing Results

UHPC testing is useful for obtaining information about the parasitic reactions occurring in cells without requiring long-term testing where cells must cycle for many hundreds or thousands of cycles. Because UHPC cycles are performed at low rates, results obtained are independent of impedance growth. Figure 5.4 shows the coulombic inefficiency (CIE) per hour and the fractional charge endpoint capacity slippage as a function of cycle number for NMC640 cells containing 2% FEC + 1% DTD, as representative UHPC results. It is desirable for UHPC metrics like CIE and fractional charge slippage to reach nearly constant values before estimating each quantity as a single value. Figure 5.4 shows that neither quantity has reached a constant or asymptotically constant value, but it is normal that approximately 20 cycles can still provide meaningful comparisons.[94,243] Both CIE and fractional charge slippage decrease with cycle number, as electrode passivation improves as cycles accumulate at the beginning of life.

Figure 5.4a shows that after 20 cycles, the CIE per hour is higher as the charge voltage is increased from 4.3 V to 4.5 V. This is expected and due to the increased rate of parasitic reactions experienced at higher voltage. The charge endpoint capacity slippage is the rate of change of the final capacity at the end of each cycle, per cycle, and usually

interpreted as the rate of electrolyte oxidation,[111] which contributes to determining CIE. Unexpectedly, the fractional charge endpoint capacity slippage does not increase monotonically with increasing charge endpoint voltage limit. Increased charge voltage is thought to increase the rate of electrolyte oxidation. The difference shown at cycle 20 in Figure 5.4b is very small between all three cells shown, but charge endpoint capacity slippage increases from the cell charged to 4.3 V, to 4.5 V to 4.4 V. It is possible that with more cycles under test, the charge endpoint capacity slippage would order based on charge endpoint voltage, as the values reach an asymptotic value. In general, this demonstrates the need for more time under test with future UHPC experiments, even though channel time on UHPC systems is very expensive.
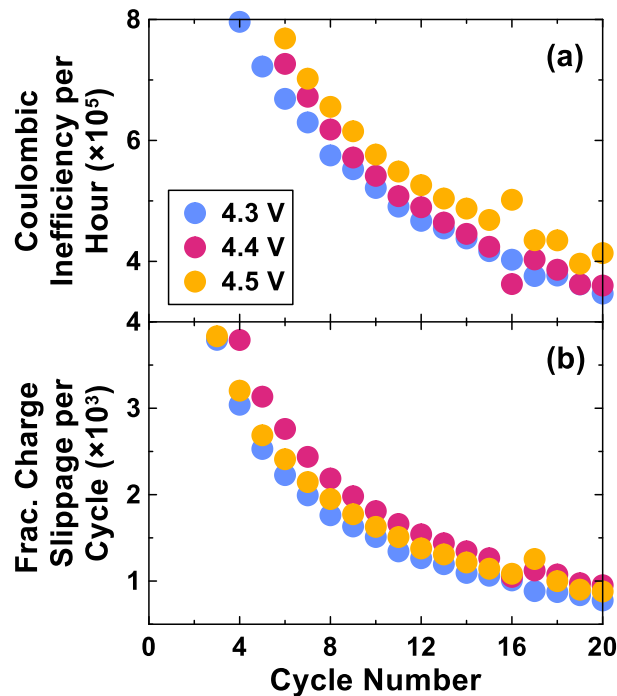
Figure 5.4. Representative data from a UHPC experiment on NMC640 cells containing 2% FEC + 1% DTD electrolyte additives, charged to 4.3 V, 4.4 V and 4.5 V. (a) Coulombic inefficiency per hour and (b) fractional charge endpoint capacity slippage per cycle plotted as a function of cycle number.

The data in Figure 5.4 is representative of a typical UHPC experiment. Similar experiments were conducted on not only cells containing 2% FEC + 1% DTD, but also cells containing many of the other electrolytes in Table 5.1. To facilitate easy comparison of different cells, rather than plotting many graphs as a function of cycle number, the CIE per hour and the fractional charge endpoint capacity slippage are reported as a single quantity per cell. This value is obtained through the conventional process of fitting a straight line through the three data points between cycles 15 and 17 and calculating the value of this line at cycle 16. This is intended to obtain contributions from multiple cycles to avoid any noise or fluctuation that may occur on a single cycle at the end of the test. Figure 5.5 shows the CIE per hour and fractional charge endpoint capacity slippage as a function of electrolyte additive formulation and charge endpoint voltage, as measured by UHPC. Comparing Figures 5.5a, 5.5c, 5.5e show that CIE per hour increases as the charge voltage limit increases, like Figure 5.4a. Also similar to Figure 5.4, Figures 5.5b, 5.5d and 5.5f, charge endpoint capacity slippage is higher at 4.4 V than 4.5 V for most electrolytes. This may be because superior positive electrode passivation is achieved at 4.5 V during formation and prevents greater amounts of electrolyte oxidation in further electrolyte chemical testing. It is also conceivable that positive electrode mass loss could occur at an increasing rate during charging to higher voltage, which in turn can contribute to the charge endpoint moving to lower capacity. This may be best described as charge endpoint capacity slippage in the decreasing direction and may contribute simultaneously to other processes that cause an increase in the charge endpoint capacity. The competition of these factors may result in less net slippage at 4.5 V, compared to 4.4 V.

The best cells in terms of CIE per hour are those that contain the Generation 2 additive LiDFDOP at 2 wt% (not 5 wt%) and the Generation 1 additive FEC. Cells that contain 2% LiDFDOP, 2% LiTFOP or 2% FEC also have the lowest charge endpoint capacity slippage when all charge voltages are considered. When electrolyte with the Generation 3, *in situ* synthesized additive LiTFMP is used, the CIE per hour and the charge endpoint capacity slippage are middle of the pack, except when charging to 4.5 V is implemented, and the CIE per hour ranks third best. Cells with 5% DiFEC and 5% DiFEC + 1% LFO have surprisingly low charge endpoint capacity slippage with charging to 4.5 V, compared to lower charge voltages. This suggests that the rates of electrolyte oxidation decrease and performance improvements relative to other electrolytes are dramatically better at 4.5 V. DiFEC may not be among the best additives for 4.3 V or 4.4 V charging, but if charging to 4.5 V is required for a particular application, it may be an excellent choice for an additive blend. Cells with LFO are consistently among the worst CIE per hour and charge endpoint capacity slippage. The use of LFO has shown to yield long lived cells in high rate cycling, due to excellent impedance control, but generally shows modest UHPC metrics compared to other excellent electrolyte blends.[150]
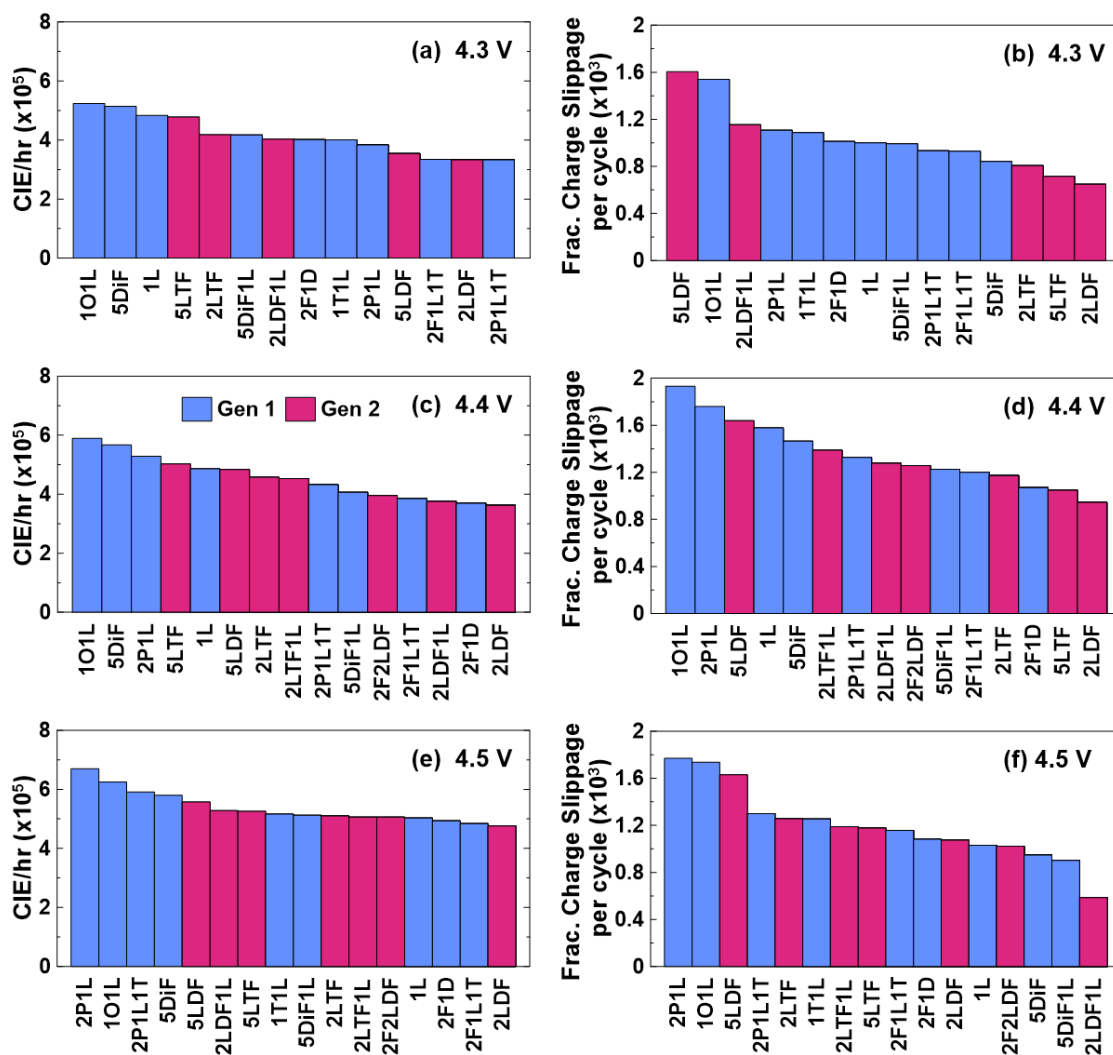
Figure 5.5. Summary of ultra-high precision coulometry (UHPC) metrics obtained from high-voltage NMC640 pouch cells, after ~16 cycles of testing at 40°C. (a,c,e) Coulombic inefficiency per hour and (b,d,f) fractional charge endpoint capacity slippage per cycle are reported a function of the electrolyte additive formulation used in each cell. Cells were charged to (a,b) 4.3 V, (d,e) 4.4 V or (e,f) 4.5 V during UHPC testing.

It should be noted that UHPC testing is done at 40°C, as is convention. Certain additives can perform well at ambient temperature while worse at elevated temperature. Cells with 1% ODTO + 1% LFO had excellent cycle life in cells cycled at 20°C and only good cycle life in cells cycled at 40°C. Cells with 1% ODTO + 1% LFO are consistently among the two worst electrolytes in every panel in Figure 5.5. UHPC testing at other

149

temperatures would certainly yield different values for CIE per hour and charge endpoint capacity slippage but may also change the ranking of electrolytes and relative performance. Finally, it should be noted that UHPC results do not necessarily translate to similar relative performance in long-term cycling at higher currents because it does not capture the apparent capacity loss due to increased internal resistance. Again, capturing the impact of each electrolyte on two UHPC metrics, with three charge endpoint voltages and determining the best electrolyte formulation for an application is challenging. An attempt is made later in this chapter to quantitatively rank many of these additives considering many metrics, including those present in Figure 5.5.

5.5 Long-Term Electrochemical Testing

Long-term electrochemical testing with a CCCV protocol is perhaps the most compelling and well-understood evidence to academic and industrial researchers alike when describing the lifetime capability of a particular cell chemistry. Anecdotally, predictive methods that project when end-of-life will occur are often met with some distrust until validated with cycling that achieves failure. This remains true even though CCCV cycling protocols do not accurately mimic real-world use.

Figure 5.6 shows the discharge capacity as a function of cycle number for NMC640 cells containing the electrolytes listed in Table 5.1, charged at different temperatures and to different charge endpoint voltages. Cycling at 20°C was conducted with a 1C charge and 1C discharge rate to particularly stress the rate capability of the cells, while cycling at 40°C and 55°C cycling was conducted with a C/3 rate on charge and discharge. Due to the high

number of data series in Figure 5.6 (18 electrolytes × 3 temperatures × 3 voltages = 162), background data are all plotted in gray and certain data is highlighted in color to differentiate it from the "pack" of other data. In the case of Figure 5.6, data from cells containing electrolytes previously presented in Chapter 4 are highlighted. The reader is asked to note the different x-axis scales when interpreting Figure 5.6.

Testing at lower temperature and to lower charge endpoint voltage results in longer cycle-life. This is due to lower rates of thermally and electrochemically activated parasitic reactions and impedance growth. The staggering drop in cycle-life seen from Figure 5.6a to 5.6d to 5.6e shows that as the charge endpoint voltage is increased, the cycle-life under high-rate testing dramatically drops. This suggests that charging to high voltage in NMC640 cells is accompanied by impedance growth, likely similar to the positive electrode impedance growth identified in NMC532 cells in Chapter 4. Other than results shown in Figure 5.6a, the data shown in the remainder of Figure 5.6 and particularly the number of cycles to failure shows low variation as a function of electrolyte additive formulation. This is not to say that certain additives do not enable longer cycling but does suggest that if electrolyte variations cannot enact significant improvements, there may be structural problems at one of the electrodes, likely the positive, that are largely independent of electrolyte chemistry. In these cases, improvements to electrode material synthesis, microstructure and electrode assembly are necessary before optimized electrolyte formulations can truly enable maximum lifetimes. It is also possible that there are reactions between the solvents or salt and the electrodes, for which additives cannot provide sufficient passivation at sufficiently high voltage. This would indicate a situation where the thermodynamics are energetic enough that the kinetic barrier provided by typical

passivation films is insufficient. In this case major changes to the cell chemistry or restriction of the charging voltage may be necessary to achieve an adequate lifetime.
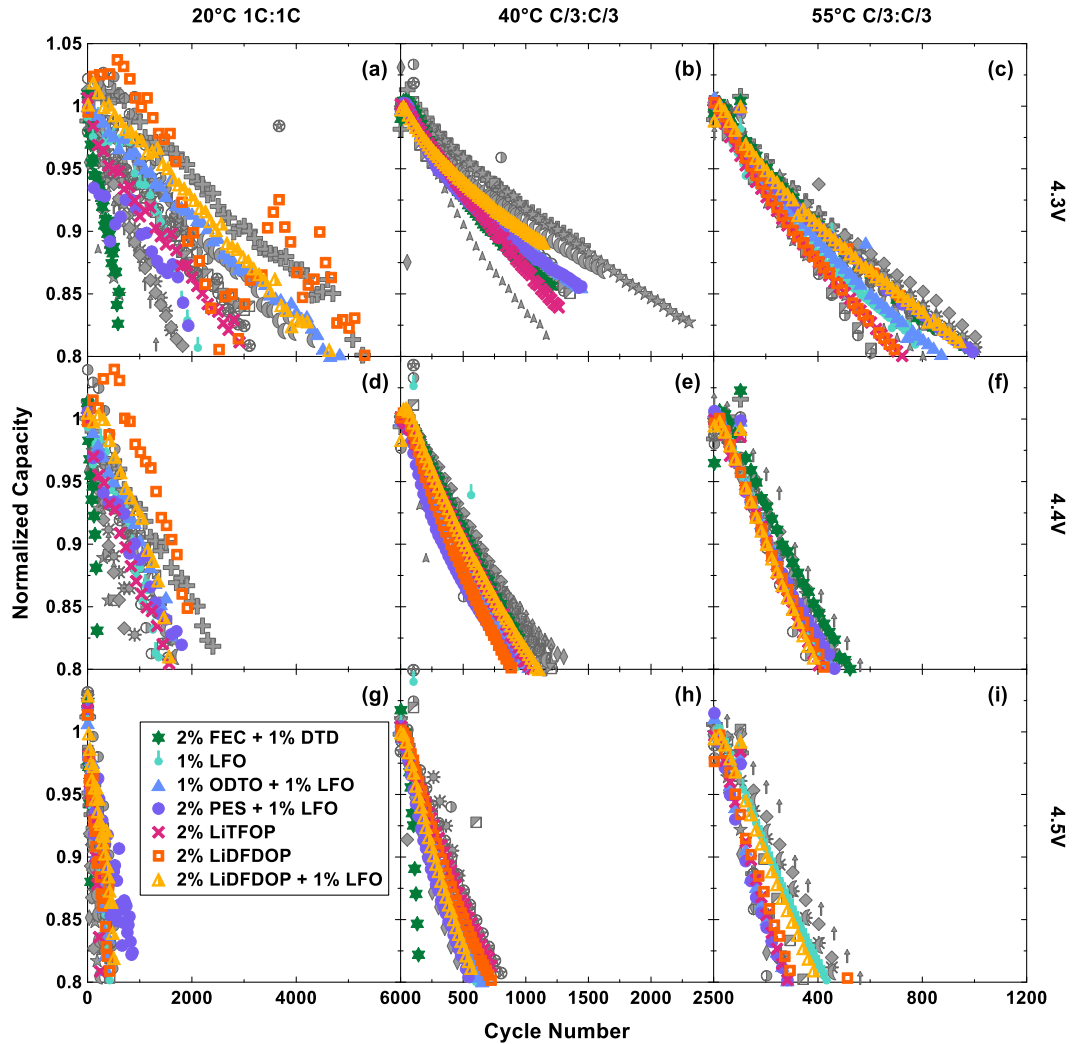
Figure 5.6. Long-term electrochemical cycling results for NMC640 cells subjected to CCCV test methods. Discharge capacity normalized to a value of 1 at cycle 10 is plotted as a function of cycle number. Cells were charged to (a-c) 4.3 V, (d-f) 4.4 V or (g-i) 4.5 V. Cycling was conducted at (a,d,g) 20°C at a 1C rate, (b,e,h) 40°C at a C/3 rate or (c,f,i) 55°C at a C/3 rate. There are 18 or more data series plotted per panel, therefore the majority are identically colored grey to avoid unnecessary visual clutter. Electrolytes additives of interest in relation to Chapter 5 are plotted with colored symbols.

In Chapter 4, NMC532 cells containing LiDFDOP and tested with cycle-hold methods were shown to have among the best overall lifetime potential. Cells containing 2% LiDFDOP and 2% LiDFDOP + 1% LFO show among the best capacity retention in

Figure 5.6 at charge endpoint voltages of 4.4 V or lower, or temperatures of 40°C or lower. Testing at even higher temperature and voltage may introduce new decomposition pathways or prove to be too strenuous for the passivation offered by LiDFDOP-containing electrolytes. Cells containing 2% LiTFOP consistently have worse capacity retention than those containing 2% LiDFDOP. Cells containing 2% FEC + 1% DTD have been referenced somewhat as a baseline electrolyte chemistry throughout Chapters 4 and 5. Figure 5.6 shows that with 20°C testing at 1C rate, 2% FEC + 1% DTD shows the most rapid failure, likely indicating impedance growth or other rate capability problems when used in NMC640 at high voltage. Cells containing 1% LFO provide middling performance relative to other electrolytes in Chapter 4 in NMC532 cells. Most panels in Figure 5.6 show similar relative performance for cells containing 1% LFO, although the data curves are difficult to discern due to the number of other series plotted. It is however the best of the additives colored in Figure 5.6i, where testing was completed at 55°C with charging to 4.5 V, which is the most abusive test condition in this set of experiments. This highlights that optimization of Li-ion cell chemistries is application dependent, and that increasing the charge voltage by 100 mV or changing the temperature represent new applications for which new parasitic reactions may occur. This is also observable throughout Figure 5.6 among relative rankings of electrolyte additives that vary somewhat as test conditions change.

Like with previous figures, the discussion of Figure 5.6 is challenging due to multidimensional experimental design and the quantity of results being compared. To add to that, as has been discussed, most of the capacity retention profiles shown in Figure 5.6 appear very similar. The differences in many panels of Figure 5.6 appear small, however,

represent improvements to cycle-life of a couple hundred cycles, which is a significant improvement to battery powered device manufacturers and users. The similar capacity retention of the various cells containing different electrolyte additives still implies that problems exist beyond the capability of additives to control. These may be structural instability of the electrode assemblies or incompatibility of the major electrolyte components against the electrodes at very high voltage. Combining improved NMC640 electrode materials with the better electrolytes demonstrated here is likely to result in cells with high voltage lifetime that can rival NMC532 cells. To simplify the comparison of cells for which data is shown in Figure 5.6, selected results will be simplified to bar charts, reminiscent of Figures 5.3 and 5.5.

Further analysis of cells presented in Figure 5.6 will be restricted to the cells in Figure 5.6e, which were cycled at 40°C with charging to 4.4 V. This is the same temperature and voltage limit which was used in Chapter 4. Most cells from this section of the experimental matrix were removed from testing when they reached 80% capacity and were transferred to a UHPC system to complete cycling for dV/dQ analysis. Figure 5.7 shows a representative dV/dQ fit and accompanying results for a cell containing 2% FEC + 1% DTD. Cycling data for this cell can be found in Figure 5.6e. Differential voltage, or dV/dQ, curves can be calculated for a full cell by fitting a linear combination of dV/dQ curves for the individual positive and negative electrode, where the adjustable parameters are the electrode masses and relative alignment of the voltage curves in the full cell. Figure 5.7a and 5.7b show that both measured and calculated dV/dQ and dQ/dV profiles show a reasonable agreement throughout nearly the entire capacity and voltage ranges respectively. There is some minor disagreement in the high capacity or high voltage range.

Through experience it is common that aged positive electrodes cannot be well fit with reference curves from unaged positive electrodes in this region.
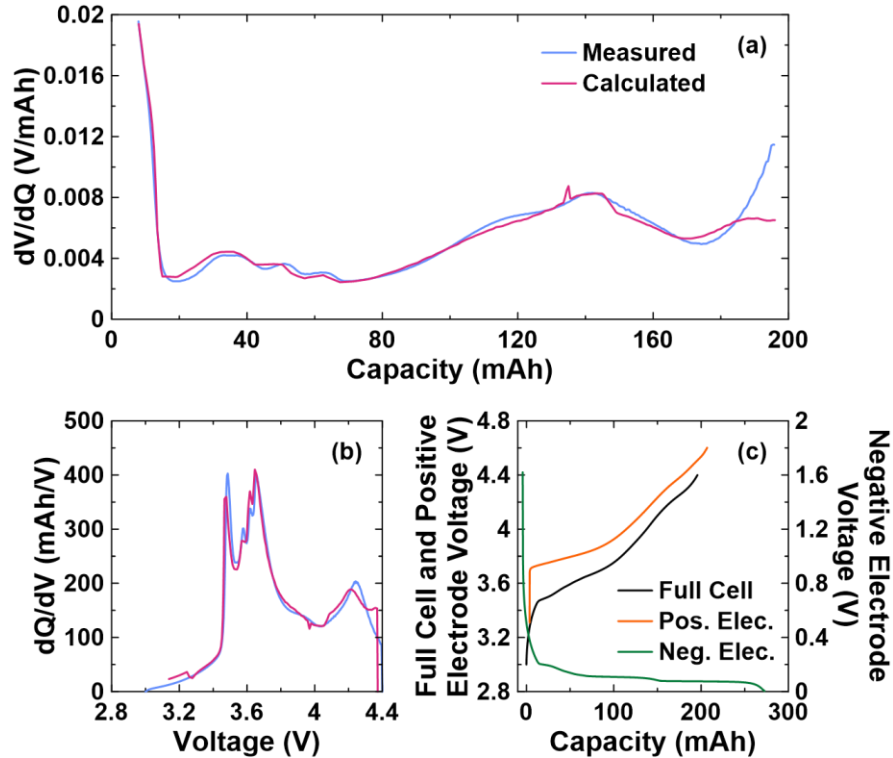
Figure 5.7. Representative dV/dQ analysis data and results for an NMC640 cell containing 2% FEC + 1% DTD, that cycled at 40°C with charging to 4.4 V. Analysis was performed on a C/40 charge completed on a UHPC at 40°C. (a) Measured and calculated dV/dQ versus capacity, (b) measured and calculated dQ/dV versus voltage and (c) resultant electrode and full cell voltage curves.

Examination of Figure 5.7c shows that nearly no relative shift has occurred between the positive and negative electrode. The positive electrode capacity is greatly diminished to where it can only provide approximately 200 mAh of capacity. As obtained, these cells should have approximately 245 mAh of positive electrode capacity. In comparison, the full negative electrode capacity from beginning of life remains. It is typical that imperfect passivation of the negative electrode causes the negative electrode voltage curve to shift or slip to the right as lithium inventory is consumed on the negative electrode, accompanied

by electrolyte reduction, during cycling.[111] If there is no shift between the positive and negative electrode voltage curves, this suggests that there are absolutely no electrolyte reactions happening, which is unlikely, or there is also electrolyte oxidation happening at the positive electrode which could cause the positive electrode voltage curve to slip to the right at the same rate as the negative electrode.[111] In this event, there is no capacity loss due to electrode shift or misalignment of the electrode curves. The results shown in Figure 5.7 suggest that electrolyte oxidation occurs while significant positive electrode active mass loss is happening. It is unclear if the mass loss is a consequence of electrolyte oxidation or is simply happening simultaneously. Positive electrode mass loss can be due to particle fracture caused by volume changes during cycling although this problem is thought to plague single-crystal positive electrode materials much less,[244] like the NMC640 cells used here. Twelve other cells shown in Figure 5.6e were analyzed by dV/dQ fitting, similar to the cell containing 2% FEC + 1% DTD discussed here. The results were very consistent in that no relative electrode shift and considerable positive electrode mass loss were observed. The fits for these cells can be found in Figure B.5, in Appendix B. Some cells from Figure 5.6e did not complete dV/dQ analysis after cycling due to being diverted into other experiments, or handling errors that resulted in accidental and fatal over-discharge.
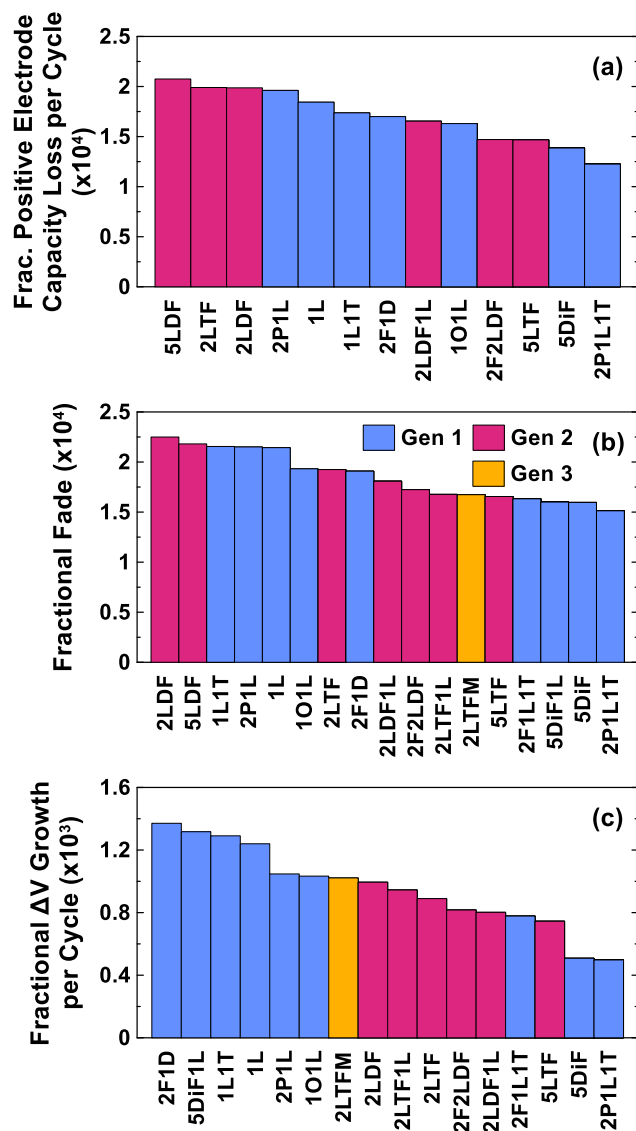
Figure 5.8. Summary of long-term cycling data and analysis for NMC640 cells cycled at 40°C with charging to 4.4 V. The per cycle rates of (a) average fractional positive electrode capacity loss, (b) average fractional fade and (c) average fractional ΔV growth are plotted versus electrolyte additive composition.

Figure 5.8 summarizes and ranks the long-term cycling performance of cells that were tested at 40°C with charging to 4.4 V. Figure 5.8a shows the average fractional positive electrode capacity loss per cycle as a function of electrolyte additive formulation as determined by dV/dQ fitting and the total number of cycles completed, for each cell. Among the best additive combinations among those reported are 2% PES + 1% LFO + 1%

TAP, 5% DiFEC and 5% LiTFOP. 2% PES + 1% LFO and 1% LFO + 1% TAP both rank much worse than 2% PES + 1% LFO + 1% TAP, which suggests a particular compatibility of TAP when used with PES and LFO for protecting the positive electrode integrity. 5% LiTFOP ranks third best 2% LiTFOP ranks second worst. The selection to make these cells with 2% and 5% was somewhat arbitrary and based on successful typical loadings with other additives. LiTFOP may be an additive that benefits from much larger loadings, particularly for protecting an NMC640 positive electrode. The use of LiDFDOP without co-additives ranks among the worst additive formulations.

Figure 5.8b shows the average fractional fade, alternately referred to as the average fractional capacity loss per cycle for various electrolyte formulations. Figure 5.8b is essentially a single point summary of the capacity retention curves in Figure 5.6e. The ordering in Figures 5.8a and 5.8b are very similar with few differences. Because both the quantities in Figures 5.8a and 5.8b are determined in part by the number of cycles to reach 80% capacity, it makes sense that there is quite a bit of similarity in the rank ordering. Figure 5.8b includes some cells which did not undergo dV/dQ analysis, so the largest difference is the insertion of these cells not in Figure 5.8a. Again, 2% PES + 1% LFO + 1% TAP ranks the best, while the use of LiDFDOP without co-additives ranks the worst. The use of DiFEC results in low fade and again ranks among the very best. 2% FEC + 1% LFO + 1% TAP is compositionally very similar to 2% PES + 1% LFO + 1% TAP, and similarly ranks very high in terms of average fade, while 2% PES + 1% LFO and 1% LFO + 1% TAP are the fourth and third worst rank for fade respectively. This against suggests a compatibility of a passivation film forming additive such as PES or FEC, with LFO and

TAP. The *in situ* formed additive, LiTFMP shows above median ranking, but is not among the best, as one might hope for an additive that is introduced as new or even "cutting edge".

Figure 5.8c shows the fractional growth of ΔV per cycle for various electrolyte formulations. The values in Figure 5.8c are derived from fractional ΔV versus cycle number data, which is not shown, but akin to the capacity retention data presented in Figure 5.6e. The approximate ordering shown in Figures 5.8a and 5.8b is not preserved here. Again, the cells containing 2% PES + 1% LFO + 1% TAP, 5% DiFEC and 5% LiTFOP rank the best, but the next group of cells are essentially all the Generation 2 lithium salt additives, followed by all Generation 1 additives blends that contain LFO and finally 2% FEC + 1% DTD. The Generation 2 additives have been discussed previously as providing low impedance and excellent rate capability. It is therefore consistent that they should rank among the better half in limiting the rate of ΔV growth. The highest rate of ΔV growth demonstrated by the cell containing 2% FEC + 1% DTD is consistent with the abysmal performance in 20°C cycling at a 1C rate in Figure 5.6, where rate capability is tested most aggressively.

Finally, Figure 5.9 attempts to summarize many of the results presented throughout this chapter. Figure 5.9 shows a figure of merit, plotted versus electrolyte additive formulation. This figure of merit is simply the average rank in first cycle efficiency, formation gas production, charge transfer resistance measured after formation, coulombic inefficiency per hour, fractional charge endpoint capacity slippage, average fractional positive electrode capacity loss per cycle in long-term cycling, average fractional fade in long-term cycling and average fractional ΔV growth per cycle in long-term cycling. Formation and UHPC metrics were only considered for cases with charging to 4.4 V, to

remain consistent with the long-term cycling parameters being considered. Each of these factors is given an equal weight of 1. It would be easy to argue that long-term cycling metrics are more important than other metrics, or vice versa, however relative weighting is likely application dependent and largely subjective. A cell which ranked first in all these metrics would have a figure of merit of 1. A cell which ranked fourth in half the metrics and sixth in the other half, would have a figure of merit of 5. Only cells for which results for all necessary metrics existed to calculate the figure of merit are included in Figure 5.9.
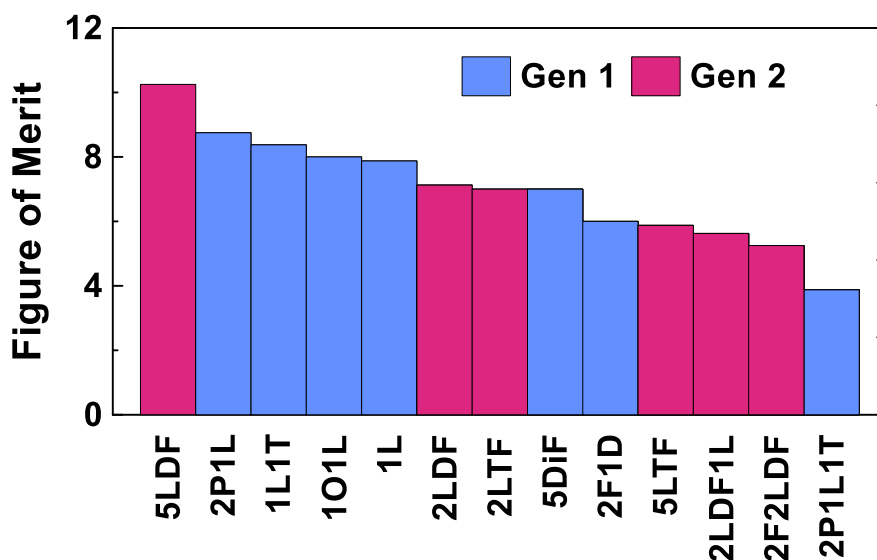
Figure 5.9. Figure of merit calculated for various electrolytes that cycled and were formed at 40°C with charging to 4.4 V. The figure of merit is the average ranking of metrics shown in Figures 5.3, 5.5 and 5.8 for 4.4 V and 40°C sections of the experimental matrices. Only electrolyte additives with a full set of parameters to complete the figure of merit calculation are shown.

The electrolyte additive formulation with the lowest and therefore best figure of merit is 2% PES + 1% LFO + 1% DTD. Cells that used this combination showed among the best long-term cycling results, formation gas production and inefficiency, is middling in UHPC metrics and ranks poorly in formation charge transfer resistance. This would be

an excellent additive choice with NMC640 cells for applications that do not operate near room temperature and are not subjected to high power demands. It is often the case that highly passivating and electrochemically stable SEI and CEI films can unfortunately be accompanied by higher resistance, which seems to be the case with 2% PES + 1% LFO + 1% TAP. 2% FEC + 2% LiDFDOP and 2% LiDFDOP + 1% LFO are next highest ranked in Figure 5.9 and all show good long-term cycling metrics, middling UHPC metrics, excellent charge transfer resistance measured after impedance, but poor first cycle efficiency and large amounts of gas production. 5% LiTFOP is the fourth ranked electrolyte in Figure 5.9, based on excellent long-term cycling results, excellent charge endpoint capacity slippage, below median in all of CIE per hour, formation charge transfer resistance and first cycle efficiency. Even among the four highest ranked electrolytes in Figure 5.9, there is no single electrolyte that satisfies all metrics exceptionally, and the requirements of a cell will vary from application to application.
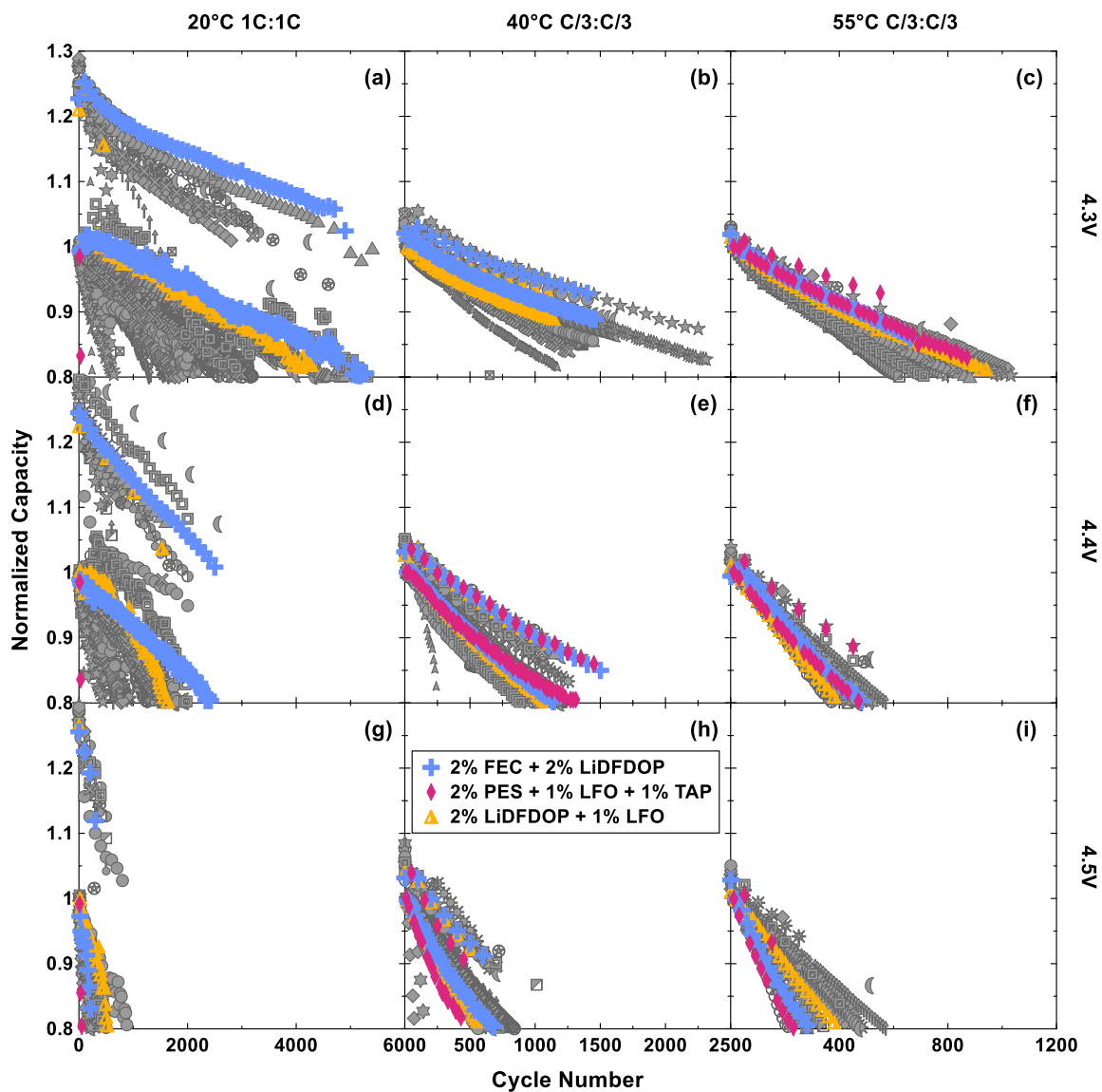
Figure 5.10. Long-term electrochemical cycling results for NMC640 cells subjected to CCCV test methods. Discharge capacity normalized to a value of 1 at cycle 10 is plotted as a function of cycle number. Cells were charged to (a-c) 4.3 V, (d-f) 4.4 V or (g-i) 4.5 V. Cycling was conducted at (a,d,g) 20°C at a 1C rate, (b,e,h) 40°C at a C/3 rate or (c,f,i) 55°C at a C/3 rate. There are 18 or more data series plotted per panel, therefore the majority are identically colored grey to avoid unnecessary visual clutter. The three highest ranked electrolyte additive combinations in Figure 5.9 are colored.

With the electrolytes that were covered in Chapter 4, for use in NMC532 cells tested with cycle-hold protocols, only 2% FEC + 1% DTD has a figure of merit that ranks in the top half, and yet showed the worst lifetime in cycle-hold testing in Chapter 4. This

highlights many complexities of research in the Li-ion field and the difficulty of hoping to carry over results from one experiment to another that is thought to be similar. NMC640 and NMC532 are similar but ultimately different materials that can perform and fail differently. The NMC532 cells used in Chapter 4 have a Ti-based surface coating while it is presently unknown if a similar coating exists on the NMC640 cells used in this chapter. The use of CCCV testing is preferred by both academic and industrial researchers because it is convention and easy to interpret. It does not anodically stress electrolyte and electrodes to the same degree as cycle-hold testing, so failure modes can be different even when identical cells are used. Lastly, the results presented here in Chapter 5 do not provide a particularly detailed insight in the failure mechanisms of these NMC640 cells, like was done in Chapter 4 for NMC532, but there are far more results that describe cell performance beyond simply cycle-life.

Figure 5.10 shows a replotting of Figure 5.6, except the colored symbols are only for the three highest ranked electrolytes in terms of the figure of merit shown in Figure 5.9. All of 2% FEC + 2% LiDFDOP, 2% PES + 1% LFO + 1% TAP and 2% LiDFDOP + 1% LFO show excellent capacity retention in all panels of Figure 5.10 where charge endpoint voltage is limited to 4.4 V or less and temperatures are limited to 40°C or less. This aligns with the fact that the analysis which leads to the figure of merit, by which ranking was done, was based on data collected at 40°C and with the charge endpoint voltage limited to 4.4 V. It is particularly clear from Figure 5.10i, which shows data collected at 55°C with charging to 4.5 V, that the three best electrolytes based on Figure 5.9 are unsuitable at such extreme temperature and voltage. It is possible that new means of failure are introduced and require different additives and surface chemistry.

5.6 Conclusions

A survey of electrolyte additives for use in high voltage NMC640 cells was completed. For use at 40°C with charging to 4.4 V, the electrolyte additive combinations 2% PES + 1% LFO + 1% TAP, 2% FEC + 2% LiDFDOP and 2% LiDFDOP + 1% LFO were found to rank the best, in that order, by a figure of merit that includes formation, UHPC, and long-term cycling data. Data for cycling at temperatures of 20°C and 55°C with charging to 4.3 V and 4.5 V was also collected but were not carried forward to a figure of merit analysis for brevity.

Analysis of cells showed that electrolyte additive formulation does alter the rate of parasitic reactions and electrolyte oxidation at high voltage slightly, but capacity loss in long-term cycling for all electrolyte additives is primarily due to positive electrode active mass loss and secondarily due to impedance growth that is speculated to be attributed to the positive electrode. The rate of positive electrode mass loss and impedance growth can decrease with the selection of good electrolyte additives, like those listed above, but the consistent prevalence of large amounts of positive electrode mass loss and impedance growth regardless of additive formulation suggests problems with the positive electrode that need to be resolved before optimizing cycle-life and other parameters with electrolyte improvements. Strategies such as surface coatings, optimizing synthesis conditions for particle size, microstructure and stoichiometries, along with improving the electrode coating through improved binders and conductive additives are all viable strategies that may improve the performance of the positive electrode.

For cells charged to 4.3 V, cycle-lives exceeding 5000 cycles were demonstrated at room temperature, and exceeding 2000 cycles at 40°C. For cells charged to 4.4 V, cycle-lives exceeding 2000 cycles were demonstrated at room temperature, and exceeding 1000 cycles at 40°C. These are likely long-lived enough to be suitable for many applications, particularly given that Figure 5.1 shows charging to 4.3 V and 4.4 V with NMC640 cells is sufficient to provide competitive energy density to NMC532 and NMC811 cells. When the cost savings of a Co-free material are accounted for, these cells presumably demonstrate excellent $/Wh and adequate lifetime. Cells of this type should therefore receive commercial consideration for having excellent economic and ethical value. Cycle-life seems to greatly diminish when cells are charged to 4.5 V or test temperatures are raised to 55°C, but these could be considered outside the realm of regular use, especially given that charging to 4.5 V is not necessary to achieve energy density parity.

It was discussed throughout this chapter that cycling with different charge endpoint voltages and at different temperatures can almost constitute different applications. This is because new reactions can be electrochemically or thermally activated as the energetics of the system increase and may change the performance of a particular electrolyte additive combination depending on how it participates in such new reactions. A simple example of this is how cells charged to 4.5 V showed less charge endpoint capacity slippage than cells charged to 4.4 V, as measured by UHPC, shown in Figure 4.5. This suggests greater rates of positive electrode mass loss occur at 4.5 V, although the mechanisms behind this are not clear, particularly as they relate to electrode additive content. This really draws attention to the need to test and optimize electrolytes and overall cell chemistry for each application or use-case based on required rate, temperature window, lifetime and charging profiles.

This requires a great research effort and will produce many more null or poor results than exemplary results but are still valuable. The current collective understanding of the field does not allow the *a priori* prediction of mechanisms and cell performance that come about with the use of any electrolyte additive with sufficient accuracy and ease. It is essential to pursue the development of theoretical understanding and model development from which calculations and predictions can be made. Given the goal of rapid development and electrification of global energy systems, high-throughput survey-style testing and a pseudo-brute force approach in parallel to model development is equally important.

CHAPTER 6 THE ROLE OF SALT IN LITHIUM IRON PHOSPHATE CELLS OPERATED AT HIGH STATE OF CHARGE

The author of this thesis was responsible for experiment planning, including the usage of LiFePO$_4$ cells as a contrasting example to the cells described in Chapter 4. The author was also responsible for cell construction and execution of electrochemical experiments and subsequent data analysis. Supervision throughout was provided by Jeff Dahn, along with review of data and feedback on results at each step. Michael Bauer completed Li-ion DTA measurements. Ahmed Eldesoky performed µXRF measurements at facilities graciously provided by Saint Mary's University and completed analysis of raw data collected.

6.1 Introduction

Cells containing LiFePO$_4$, or LFP, have gained significant commercial interest at the time of writing as a low-cost, higher safety alternative to NMC-type positive electrode materials.[37] LFP is a lower voltage and lower specific capacity material than all NMC positive electrodes,[37] but the cost per unit weight of Fe as mined is approximately 150 times cheaper than Ni and 300 times cheaper than Co,[242] such that the final \$/Wh of LFP cells are becoming attractive to cell and device makers alike. It should be noted that the cost of Li$_2$CO$_3$, the lithium source used in positive electrode synthesis, currently exceeds the cost of positive electrode transition metals, per unit weight and per mole. This relative savings of 150 times or 300 times with the use of Fe rather than Ni or Co translates to a non-negligible but much smaller savings at the level of a fully synthesized positive electrode material, due to the cost of lithium, anions, and processing. Modern LFP cells have lower

cycle-life, particularly at elevated temperature, than NMC cells[196] and as such, compromise on both energy density and longevity compared to NMC cells. Longer lived LFP cells will improve their value proposition and enable increased rollout of battery powered devices through more affordable batteries.

As has been discussed in the previous chapters, laboratory electrochemical testing usually involves CCCV electrochemical cycling, that isn't particularly representative of real-world use-cases and is often not as stressful a test as alternates such as cycle-hold testing. The voltage-capacity curve of LFP is shown in Figure 1.4. It is a two-phase material that has a flat voltage profile except for vertical segments when the material is completely lithiated or delithiated. On discharge, LFP/graphite cells have a voltage plateau at 3.2 V. This means that four series connected LFP cells have a flat voltage profile of 12.8 V. This makes LFP cells an excellent alternate for battery applications that operate nominally as 12 V, 24 V or 48 V architectures and conventionally utilize lead-acid batteries. Many of these applications, such as vehicle starter batteries or uninterruptable power supply backup batteries, have the cell spend most of its life being held at full state-of-charge. Such use-cases are much better studied using cycle-hold testing, rather than CCCV testing, particularly for LFP cells.

The work discussed in this chapter was inspired by the results of Chapter 4 and the challenges in further investigating the high voltage failure in NMC532 cells. In those cells, cycle-hold testing resulted in fatal positive electrode impedance growth. The origin of this was speculated as possibly being due to $LiPF_6$ concentration mediated growth of a resistive surface rock salt phase on the positive electrode particles. To test for this requires access to atomic resolution scanning transmission electron microscopy (STEM). Due to the

micron size of the NMC532 particles and the relatively small size of STEM samples, samples made from NMC532 electrodes may only have a few particles. This is after tedious lift-out focused ion beam and thinning/polishing steps. The NMC532 particles must be oriented so correct facets can be examined, and with an ensemble of a few particles per sample, the likelihood of obtaining the correct orientation is low. This results in considerable equipment and technician time, resulting in prohibitive costs if a STEM and sample preparation facilities are not freely available for extended use. This is the case for the author and therefore an alternative experiment was required.

The crystal structure of $LiFePO_4$ is orthorhombic and based on PO_4 tetrahedra. There is not a simple, low energy pathway by which a disordered rock salt phase can form on the material surface. If, when LFP is cycled with cycle-hold test methods, the failure is similar to NMC532 cells, in that there is fatal impedance growth that occurs at a faster rate with decreasing $LiPF_6$ concentrations, it is possible that the source of failure in NMC532 cells is not due to a resistive rock salt layer on the positive electrode. If the LFP cells show different failure modes and a different performance dependence on the salt concentration, then the hypothesis of rock salt formation in NMC532 cells is not disproven. The original motivation behind the work in this section was to generate data from LFP cells that could be compared and contrasted to the results presented in NMC532 cells in Chapter 4. The results were intriguing enough, that in addition to fulfilling this comparison, they can stand alone to form their own narrative. The work presented in this chapter serves as both insight into the failure of cells tested with cycle-hold methods and into the performance of LFP cells under unconventional testing schemes.

6.2 Initial Studies of LiPF₆ Concentration in LiFePO₄ Cells

Li$_x$FePO$_4$ is a two-phase material that exists as discrete domains of xLiFePO$_4$ + FePO$_4$. As such, the entirety of an LFP/graphite cell's capacity is essentially stored or delivered along a voltage plateau, and when the cell is fully charged, the voltage-capacity curve is vertical. A voltage curve of an LFP/graphite cell can be found in Figure 1.4. Conventionally, LFP cells are charged to 3.65 V, but charging to higher voltages can be achieved with negligible additional current flow and will not provide additional stored capacity. Therefore, charging an LFP cell to 4.4 V will not result in lithium plating or any greater material utilization, but does duplicate the anodic stress experienced by electrolyte in NMC532 cells that are charged to 4.4 V.
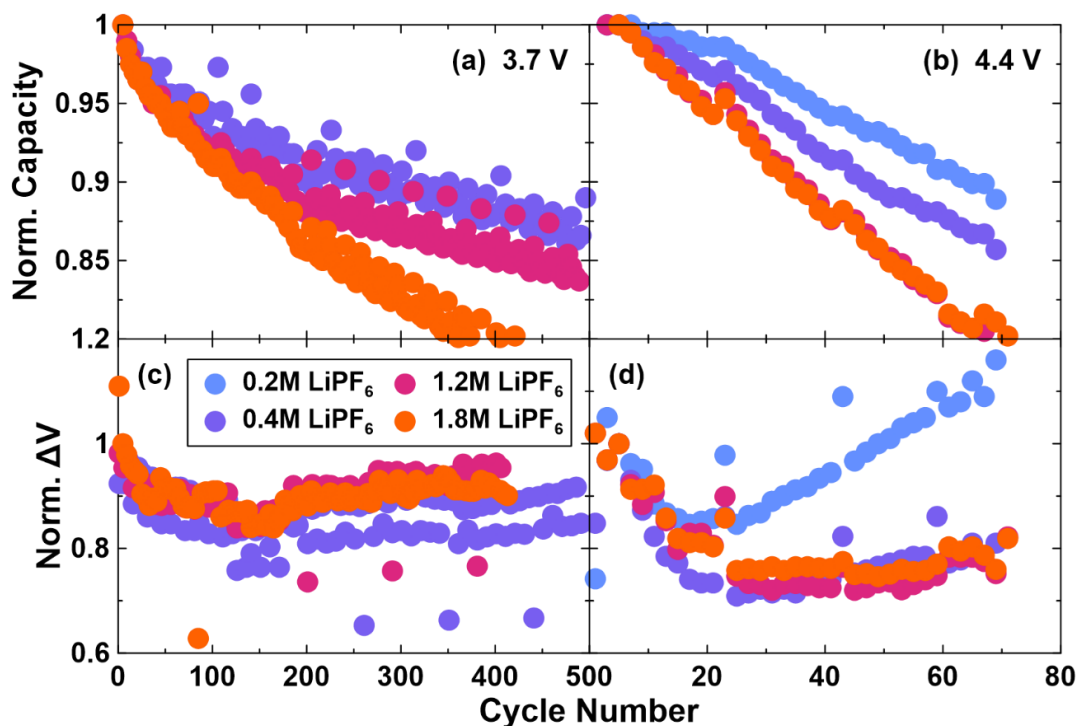
Figure 6.1. (a,b) Discharge capacity and (c,d) ΔV, normalized to 1 at cycle 5, versus cycle number for LFP/AG cells, containing the 2% FEC + 1% DTD electrolyte additive system with various LiPF₆ concentrations. Cells were charged to either (a,c) 3.7 V or (b,d) 4.4 V using the C/3 cycle-hold test protocol shown in Figure 3.2c at 40°C.

LFP cells were constructed with electrolytes containing 2% FEC + 1% DTD and various $LiPF_6$ concentrations, following the methods of Section 3.3, and completed formation with charging limited to 3.65 V. Following this, cells completed electrochemical cycling at 40°C using cycle-hold protocols, originally introduced in Figure 3.2c, with the charge endpoint voltage and the constant voltage limit set at with 3.7 V or 4.4 V. There is no practical difference between the conventional charge limit of 3.65 V used for LFP cells and 3.7 V which is used here. Initially, 3.7 V was used due to a test protocol programming error and simply carried forward to future experiments for consistency.

Figure 6.1 shows the normalized discharge capacity and ΔV as a function of cycle number for LFP cells undergoing cycle-hold testing with charging to 3.7 V or 4.4 V. The discharge capacity in both Figures 6.1a and 6.1b is mostly linear, implying a constant fade rate. During charging to 3.7 V or 4.4 V, the capacity fade rate increases with increasing $LiPF_6$ concentration, but the fade rate is much higher in cells charged to 4.4 V compared to 3.7 V. This suggests the rate of parasitic reactions increases with increasing charge endpoint voltage in LFP cells subjected to cycle-hold testing. In nearly all cells, ΔV decreases or remains constant over the duration of testing. In the cell with 0.2M $LiPF_6$ that was charged to 4.4 V, there is an increase in ΔV of approximately 20%, which is not negligible, but small and not the primary cause of the measured capacity loss.

The results in Figure 6.1 suggest that there is $LiPF_6$ mediated failure occurring, which suggests that conventional salt concentrations are incompatible with long cycle-life, at least when $LiPF_6$ is used. Logan et al. showed that identical LFP cells can contain significant amounts of water, but explained that the use of electrolyte additives generally

mitigated any deleterious effects of water contamination.[196] The following reaction mechanism was also suggested and simplified here:

$$\text{LiPF}_6 + 2\,\text{H}_2\text{O} \rightarrow 3\,\text{HF} + \text{LiF} + \text{HPO}_2\text{F}_2 \qquad\qquad (6.1)$$
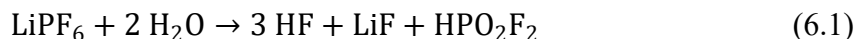
Stich et al. showed that electrolytes containing LiPF_6 dissolved in carbonate solvents, with water contamination had increasing HPO_2F_2 and HF concentrations, along with decreasing H_2O concentrations as a function of time.[245] Additionally, Liu et al. showed that the rate of LiPF_6 hydrolysis and corresponding HF production increases as the cell is charged to higher voltage.[246] This, along with the results shown in Figure 6.1, suggests that LFP cells containing more LiPF_6 and are charged to higher voltage should produce more HF, which may help explain the increased rate of capacity fade with increasing LiPF_6 concentrations. NMC532 cells tested in a similar manner in Chapter 4 did not show decreasing cycle-life as LiPF_6 concentration was increased. It has also been reported that during cycling, NMC cells do not suffer significant acid attack from HF.[147] This suggests a fundamental difference in the parasitic reactions and passivation films in NMC and LFP cells, and may suggest that NMC cells have a means to mitigate the effects of HF while LFP does not.

Cycle-hold testing is generally uncommon in the literature for all types of cells but is especially uncommon for cells that do not charge to high voltage as it is viewed as an aggressive probe into high voltage failure. LFP cells are counted among these cells that do not charge to high voltage, typically, but as mentioned in the introduction to this chapter, there are practical applications where LFP cells remain fully charged for extended periods of time. Figure 6.2 shows the normalized discharge capacity as a function of time under test for three LFP/graphite cells completing cycle-hold testing, at 40°C with charging to 3.7 V, and one LFP/graphite cell tested using CCCV cycling, also at 40°C but with

charging to 3.65 V. All cells contain 2% FEC + 1% DTD electrolyte additives. The cell containing 1.5M $LiPF_6$ electrolyte, undergoing CCCV cycling, shows capacity retention better than the cells containing 1.2M $LiPF_6$ and 1.8M $LiPF_6$ that are undergoing cycle-hold testing. It is unfortunate that a direct comparison of cells undergoing CCCV and cycle-hold testing with identical salt concentrations does not exist. It can be inferred that a cell made with 1.5M $LiPF_6$ and subjected to cycle-hold testing would yield capacity retention somewhere between the data for cells containing 1.2M and 1.8M in Figure 6.2. This suggests that LFP cells undergoing cycle-hold testing experience greater rates of capacity loss than those which are tested with CCCV cycling. This may be due to longer time spent at full state-of-charge and higher average voltage per unit time, which may increase the rate of HF production[246] or could simply be due to prolonged time with the negative electrode spent at very low voltage, which is highly reducing. It is assumed the difference between 3.65 V and 3.7 V is negligible in these cells.
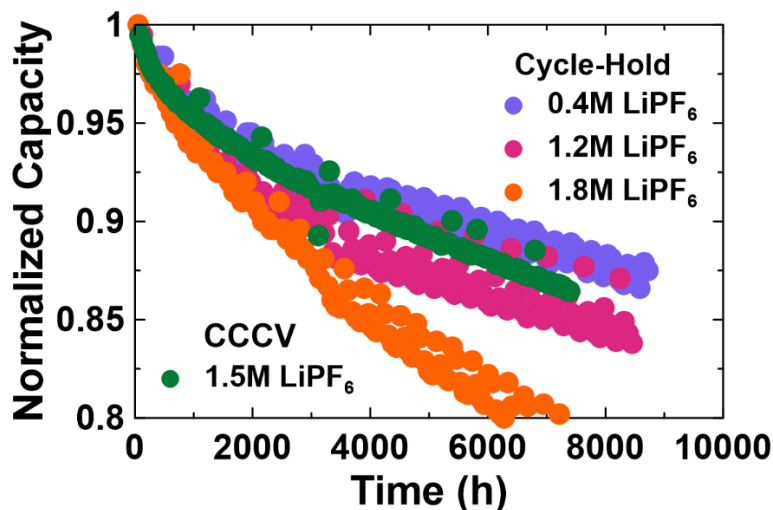
Figure 6.2. Discharge capacity, normalized to 1 at cycle 5, versus time under test for LFP/AG cells, containing 2% FEC + 1% DTD electrolyte additive system with various $LiPF_6$ concentrations. Cells were tested using either CCCV or cycle-hold protocols at 40°C.

The cell that contains 0.4M LiPF$_6$ and is tested using a cycle-hold protocol shows slightly better capacity retention than the cell containing 1.5M LiPF$_6$, undergoing CCCV cycling. This suggests that lower LiPF$_6$ concentrations are particularly useful in applications where LFP cells remain at full state-of-charge for extended periods of time. It is also possible that low LiPF$_6$ concentrations would improve the lifetime of LFP cells subjected to CCCV testing, but this remains speculation at this point.
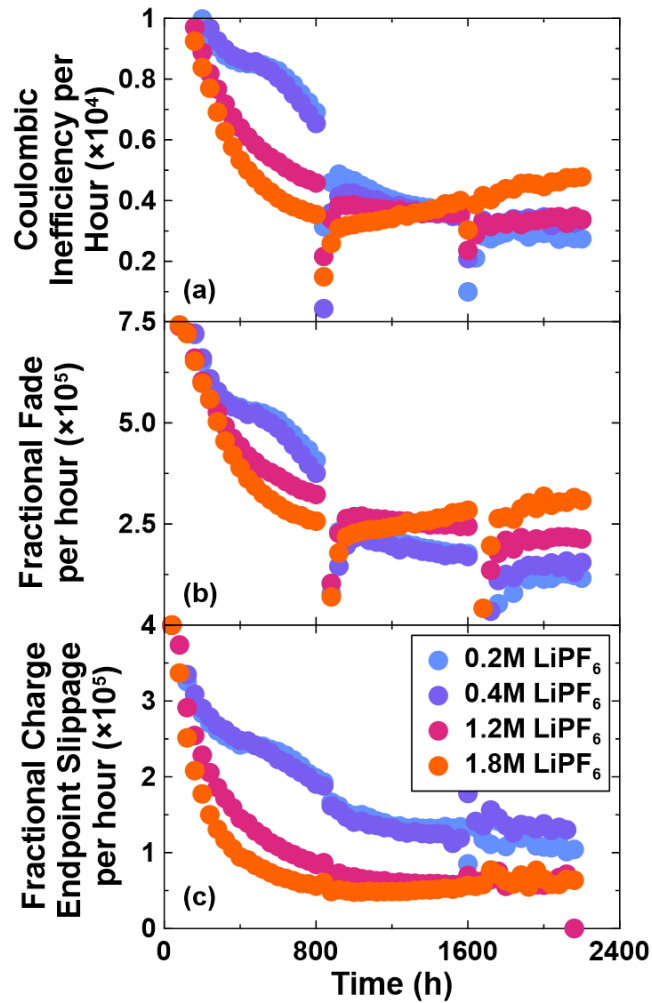
Figure 6.3. (a) Coulombic inefficiency per hour, (b) fraction capacity fade per hour and (c) fractional charge endpoint capacity slippage per hour as a function of test time for LFP/AG cells, containing 2% FEC + 1% DTD electrolyte additive system with various LiPF$_6$ concentrations. Cells were cycled on a UHPC system at 40°C, with a C/20 rate and charging to 3.65 V.

The trends shown in Figures 6.1 and 6.2 are opposite what is normally observed in NMC cells, particularly those that charge to high voltage. To investigate the role of $LiPF_6$ in LFP cells further, UHPC testing was conducted on identically prepared cells to those shown in Figure 6.1. UHPC cycling, adhering to convention, consisted of C/20 constant current or galvanostatic cycling and charging was limited to 3.65 V. Figure 6.3 shows the coulombic inefficiency per hour, fractional capacity fade per cycle and fractional charge endpoint capacity slippage per cycle as a function of cycle number. Each of these quantities are better when lower. A typical UHPC experiment is completed after 800 hours or 20 cycles, due to the value of equipment time and the assumption that comparisons and predictions made after 20 cycles will remain true over more cycles. Figure 6.3 shows that cells containing electrolytes with lower $LiPF_6$ concentrations had higher coulombic inefficiency, greater capacity fade and greater charge endpoint slippage than cells containing electrolytes with higher $LiPF_6$ concentrations after 800 h. Despite this, the slopes at 800 hours or 20 cycles suggest that cells containing lower $LiPF_6$ concentrations would eventually reach similar or better values to cells containing higher $LiPF_6$ concentrations, and therefore UHPC testing was continued for additional rounds.

The coulombic inefficiency can be thought of as containing contributions from both capacity fade, commonly attributed to parasitic reactions at the negative electrode, and charge endpoint slippage, commonly attributed to parasitic reactions at the positive electrode.[111] The coulombic inefficiency in Figure 6.3a and the capacity fade in Figure 6.3b show nearly identical shapes, while the charge endpoint capacity slippage in Figure 6.3c is somewhat different. After approximately 1400 h or 35 cycles, the cells containing low $LiPF_6$ concentrations cross over the cells containing high $LiPF_6$ concentrations to have both

lower capacity fade and coulombic inefficiency. This suggests that capacity fade and reactions at the negative electrode are the primary contributor to the coulombic inefficiency. By the end of the UHPC experiments, around 2200 h or cycle 55, both the coulombic inefficiency and capacity fade are ordered from highest to lowest following decreasing $LiPF_6$ concentration. Charge endpoint capacity slippage is lower for cells with higher $LiPF_6$ concentrations, but this does not make a meaningful contribution to lowering coulombic inefficiency, because the values are much smaller.

In all, this suggests that parasitic reactions at the negative electrode, which increase in rate with increasing $LiPF_6$ concentration are the major contributor to increased capacity fade and rates of cell failure. If HF is produced at the positive electrode, as suggested by Liu et al.,[246] it may be possible for that HF to migrate to the negative electrode and damage the SEI or to react at the positive electrode, producing a subsequent species that will then migrate to the negative electrode. An example of the latter would be acid attack of the positive electrode, resulting in transition metal dissolution into the electrolyte which can deposit on the graphite, necessitating lithium inventory consumption to repair the SEI. It has been shown by Boulanger et al. than shuttle mechanisms involving reaction products migrating between both electrodes can occur with certain electrolyte formulations in LFP/graphite cells.[247] Logan et al. also showed that most of the parasitic reactions in LFP/graphite cells occur at the negative electrode using so-called "pouch bag" experiments, which corroborates the results in Figure 6.3.

It is worth noting that the graphite electrodes used in these LFP cells are identical except for geometry (thinner electrodes used here) to the graphite electrodes used in Chapter 4. The NMC532/graphite cells discussed in Chapter 4 do not appear to have

parasitic reactions at the negative electrode as the predominant source of failure, and they do not increase in rate as the concentration of $LiPF_6$ increases. This suggests that certain reactions in NMC532 cells can either eliminate harmful species that would otherwise attack the negative electrode SEI or produce beneficial species that will migrate to the negative electrode and provide superior passivation. The discussion here suggests that such mechanisms do not exist in LFP cells.

It took approximately 40 cycles or 1600 h of UHPC testing to clearly resolve long-term differences between LFP cells with different $LiPF_6$ concentrations. This indicates that the SEI and electrolyte-electrode interfaces are dynamic and evolving for a number of cycles. It has been speculated by Logan et al. that trapped moisture in the LFP electrode may be liberated slowly[196] which might connect the hydrolysis of $LiPF_6$ and the fact that many UHPC cycles were required here to resolve the true behavior as a function of $LiPF_6$ concentration. It also impresses the need for more time under test for UHPC experiments, despite the relatively expensive cost for channel-time on such equipment, and patience to determine long-term behavior of many UHPC quantities. Finally, the ranking of cells with respect to $LiPF_6$ concentration agrees between Figures 6.1 and 6.3, even though the former utilizes cycle-hold testing while the latter utilizes constant-current cycling. This indicates that increased capacity fade as a function of increasing $LiPF_6$ concentration is not a unique failure mode that only occurs when cycle-hold or similar protocols are implemented.

6.3 Analysis of Cells Subjected to Equal Times Under Cycle-Hold Testing

As was discussed in Section 4.3, failure analysis of a group of cells that have all reached end-of-life, but after a different number of cycles or times under test can be misleading if all cells show similar signs of failure. Following the approach in Section 4.3, LFP cells identical to those presented in Figure 6.1 were constructed and tested until the point of failure for the worst cells. In addition to cells that were originally presented in Figure 6.1 that contained 2% FEC + 1% DTD, otherwise identical cells were made but contained 1% LFO, to provide more degrees of comparison with the NMC532 cells discussed in Chapter 4. LFP cells were again cycled at 40°C using a cycle-hold protocol with charging to 3.7 V and 4.4 V.
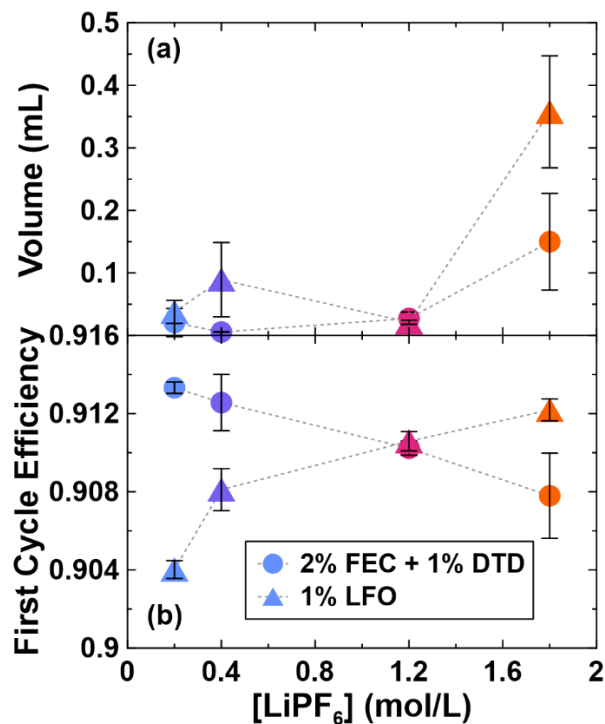
Figure 6.4. Mean (a) volume of gas produced during formation and (b) first cycle efficiency versus electrolyte LiPF$_6$ concentration for LFP/AG cells, containing either 2% FEC + 1% DTD or 1% LFO electrolyte additives. The formation cycle was completed at 40°C with a C/20 rate and charging to 3.65 V.

Figure 6.4 shows the role of LiPF$_6$ in formation of LFP cells containing 2% FEC + 1% DTD and 1% LFO, that were constructed for failure analysis testing. Figure 6.4a shows that the volume of gas produced is relatively low for both electrolyte additive systems, under 0.1 mL except for when 1.8M LiPF$_6$ is used. This suggest LiPF$_6$ or LiPF$_6$ decomposition products participate directly in SEI-forming reactions, or the altered solution structures that occur when increased salt concentrations are used result in different solvent or additive molecules participating in SEI-forming reactions. Figure 6.4b shows that first cycle efficiency decreases with increasing LiPF$_6$ concentration, when 2% FEC + 1% DTD is used and increases with LiPF$_6$ concentration when 1% LFO is used. This shows that aspects of mechanisms behind how additives act involve reaction with other electrolyte components, including the salt. The discussion in Section 6.2 established that lower LiPF$_6$ concentration can result in improved lifetime, but this may be incompatible with achieving maximal energy density with certain additives. In the case of 1% LFO, using less LiPF$_6$ to achieve a better lifetime causes significantly more capacity loss on the first cycle than 2% FEC + 1% DTD. This, in general, highlights the need for optimization of the entire electrolyte formulation with the details of an application carefully considered.

Figure 6.5 shows the discharge capacity and ΔV as a function of cycle number, for LFP cells containing 2% FEC + 1% DTD or 1% LFO. Cells were only cycled until the approximate time that the first cell failed. In this case this was the cell containing 2% FEC + 1% DTD and 1.8 M LiPF$_6$ which performed cycle-hold with charging to 4.4 V. This cell stopped testing after just under 65 cycles. The remaining cells were removed before reaching 80 cycles. For future discussion, cells analyzed after cycling will be referred to as having completed approximately 80 cycles, for convenience. The trends observed in Figure

6.1 are present in Figure 6.5 and will not be repeated. It is worth noting that cells which were charged to 3.7 V, shown in Figure 6.5a, are very tightly grouped and difficult to distinguish from each other. In Figure 6.1a, approximately 150 cycles were required to distinguish the performance of cells with $LiPF_6$ concentrations when charged to 3.7 V.
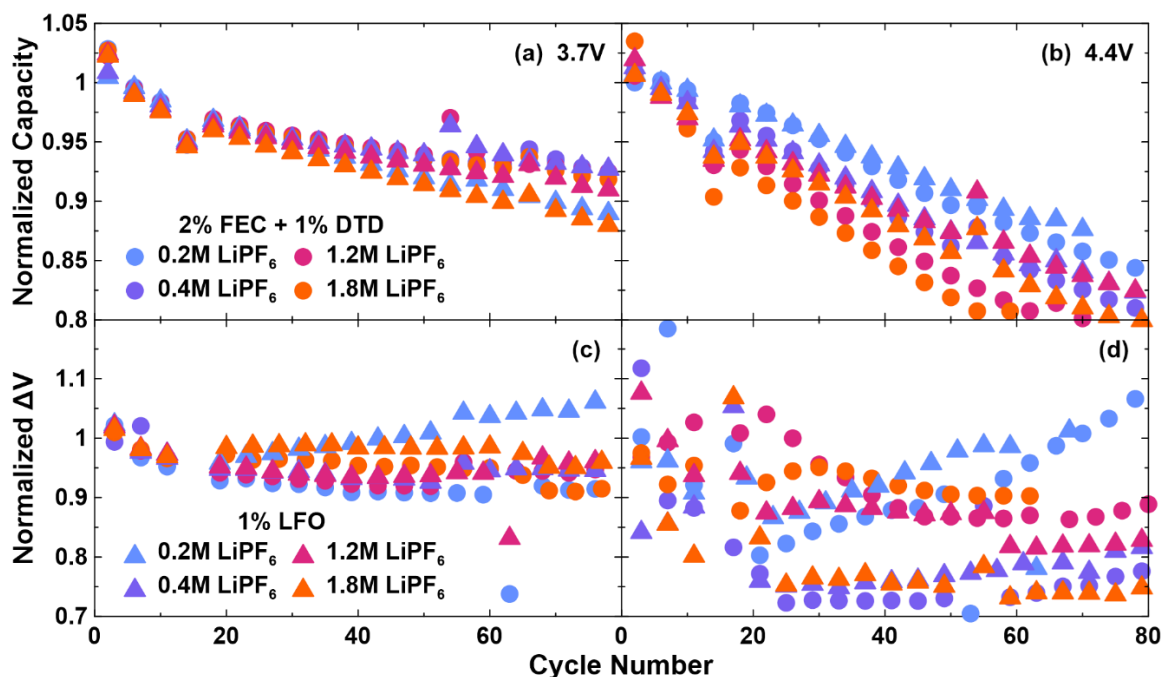
Figure 6.5. (a,b) Discharge capacity and (c,d) ΔV, normalized to 1 at cycle 5, versus cycle number for LFP/AG cells, containing either 2% FEC + 1% DTD or 1% LFO electrolyte additives, with various $LiPF_6$ concentrations. Cells were charged to either (a,c) 3.7 V or (b,d) 4.4 V using C/3 cycle-hold testing at 40°C.

The largest difference between Figures 6.1 and 6.5 is the addition of cells containing 1% LFO rather than only 2% FEC + 1% DTD. In cells charged to 4.4 V, cells containing 1% LFO show slightly lower capacity fade than cells containing 2% FEC + 1% DTD, and clear ordering is present with lower $LiPF_6$ concentrations resulting in lower fade. It has previously been shown that 1% LFO can improve high voltage cycle-life, both in the literature[150] and in Chapter 4. When charging is limited to 3.7 V, there is no clear ordering

among cells that contain 1% LFO and different $LiPF_6$ concentrations, in terms of both capacity retention and ΔV. This is largely due to the point that was previously mentioned, where approximately 150 cycles seem to be required to clearly elucidate trends in LFP cells subjected to cycle-hold testing, when charging is limited to 3.7 V.

Both cells with 2% FEC + 1% DTD and 1% LFO, that contain 0.2M $LiPF_6$ and are charged to 4.4 V show slight increase in ΔV with increasing cycle number, whereas all other cells with higher $LiPF_6$ concentrations show constant or decreasing ΔV. This suggests that at high voltage, the use of very low $LiPF_6$ concentrations in carbonate solutions in LFP cells may introduce new reactions which can increase the internal resistance of the cells. This could be salt consumption or the development of a resistive passivation film on either electrode. In practical applications, LFP cells are neither charged to 4.4 V nor contain such low concentrations of $LiPF_6$ due to low electrolyte conductivity.

Figure 6.6 shows Nyquist plots of impedance measurements made before and after cycling for cells for which cycling results are shown in Figure 6.5. Apart from the cell containing 1% LFO and 0.2M $LiPF_6$, all cells that were cycled with charging to 3.7 V show little difference in impedance spectra collected before and after cycling. This is consistent with no increase in ΔV observed for these cells in Figure 6.5c. This again suggests that the capacity loss observed in Figure 6.5a is largely due to lithium inventory loss, rather than apparent loss of measured capacity due to impedance growth. The increase in impedance noted in Figure 6.6a for the cell containing 1% LFO and 0.2M $LiPF_6$ is both an increase in the width of the Nyquist plot, or an increase in the overall charge transfer resistance of the cell along with a shift to the right, implying an increase in either electrode or electrolyte series resistance. Symmetric cells were not constructed from these full cells, to determine

the electrode responsible for the increase in charge transfer resistance. An increase in the electrolyte contribution to the series resistance could occur because of salt consumption. It could also occur with solvent consumption that results in lowered dielectric constant or increased viscosity. It is again possible that the use of very low salt concentrations may introduce new failure modes in LFP cells and this increase in impedance does not manifest as vastly worse cycling performance in Figure 6.5.
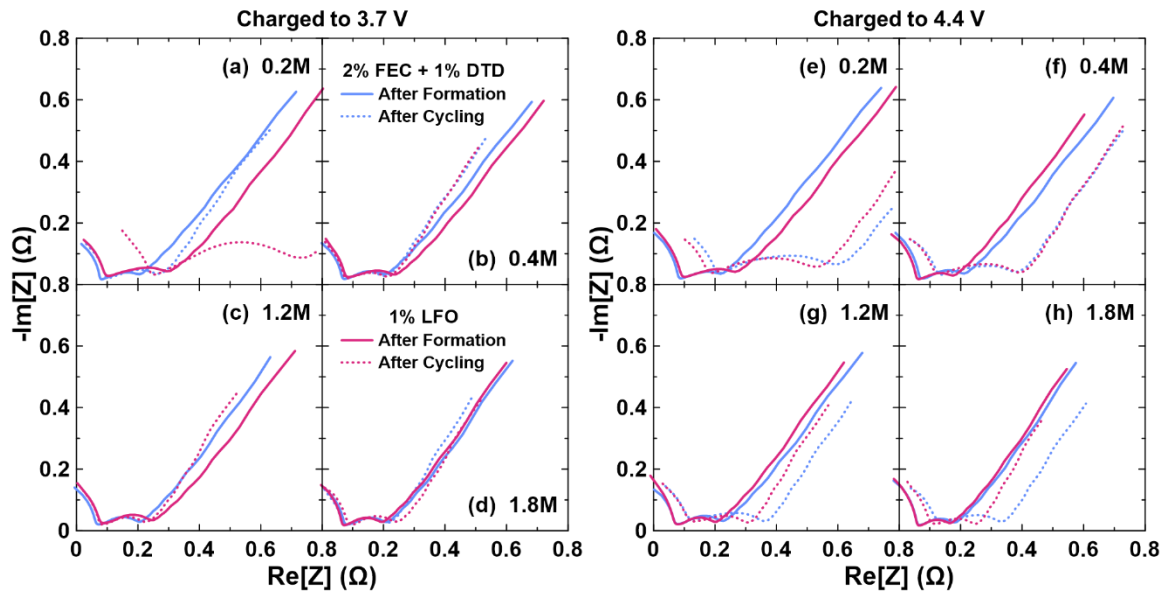
Figure 6.6. Nyquist plots of impedance spectra collected from LFP/AG cells before and after cycling for approximately 80 cycles. Cells contained either 2% FEC + 1% DTD or 1% LFO electrolyte additives and $LiPF_6$ concentrations (a,e) 0.2M, (b,f) 0.4M, (c,g) 1.2M or (d,h) 1.8M. Cells were charged to either (a-d) 3.7 V or (e-h) 4.4 V using C/3 cycle-hold testing at 40°C. Impedance was measured at 10°C with cells charged to 50% state-of-charge.

Cells that were charged to 4.4 V all show increases the width of the spectra and a shift to the right, which both decrease in magnitude as the concentration of $LiPF_6$ in the electrolyte increases. This indicates that overcharged LFP cells undergo both increases in charge transfer resistance and series resistance but the rate of increase of these parameters

is slowed by increasing LiPF$_6$ concentration. In this regard, the impedance behavior of LFP cells subjected to cycle-hold testing is similar to NMC532 cells subjected to cycle-hold testing, particularly the increase in charge transfer resistance as a function of LiPF$_6$ concentration. The increases shown in Figure 6.6 appear large in measurements conducted at 10°C, where ion kinetics are slow. In cycling tests at 40°C, shown in Figure 6.5, the differences are much smaller, to the point where cells with larger LiPF$_6$ concentration show greater rates of fade, despite having better impedance control. This implies the effects of lithium inventory loss outweigh the effects of impedance growth in determining cycle life.
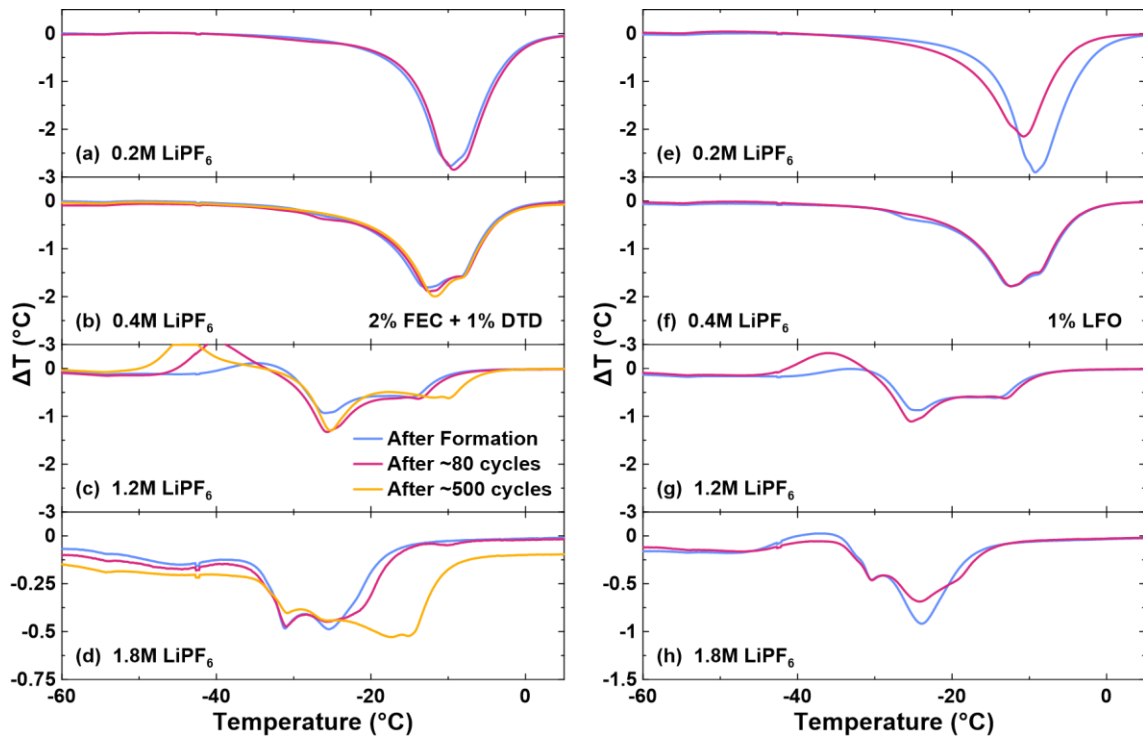
Figure 6.7. Li-ion DTA profiles collected on LFP/AG cells before, after cycling for approximately 80 cycles, and after cycling for approximately 500 cycles in a few cases. Cells contained either (a-d) 2% FEC + 1% DTD or (e-h) 1% LFO electrolyte additives and LiPF$_6$ concentrations (a,e) 0.2M, (b,f) 0.4M, (c,g) 1.2M or (d,h) 1.8M. Cells were charged to either 3.7 V using C/3 cycle-hold testing at 40°C.

Figure 6.7 shows Li-ion DTA profiles for cells for which cycling results are shown in Figures 6.5a and 6.5c, measured after formation and after being removed from cycling after approximately 80 cycles. DTA measurements were also made on the cells for which cycling results are shown in Figures 6.1a and 6.1c after they were removed from test. These cells were removed between 450 and 500 cycles but are referred to as having completed approximately 500 cycles, for convenience. All of these cells were tested after charging to 3.7 V. When 2% FEC + 1% DTD is used, Figure 6.7a shows little change in the DTA profile after 80 cycles, suggesting the electrolyte composition remains relatively constant. The same is true when the salt concentration is increased to 0.4M, shown in Figure 6.7b. When the $LiPF_6$ concentrations are increased to 1.2M and 1.8M, the DTA profiles shows a liquidus feature that moves to higher temperature with more time under test and greater concentration of $LiPF_6$. This suggests that $LiPF_6$ consumption is occurring at an increasing rate as cells are made with increasing amounts of $LiPF_6$.

Similar trends are observed in cells that contain 1.2M $LiPF_6$ and 1.8M $LiPF_6$ and 1% LFO, although not having data collected after ~500 cycles makes the comparison and the visual effect less striking. The cell containing 0.4M $LiPF_6$ and 1% LFO shows essentially no change in electrolyte composition. The cell containing 0.2M $LiPF_6$ and 1% LFO shows a decrease in liquidus temperature, which implies solvent consumption. This same cell showed anomalously high impedance increase in Figure 6.6a and is likely related to the solvent consumption shown in Figure 6.7. These combined results suggest that either low salt concentration electrolytes that contain 1% LFO introduce different degradation modes in LFP cells, or this cell is an outlier in terms of poor construction or handling. It is possible that solvent decomposition products could accumulate on either electrode surface,

resulting in increased charge transfer resistance, while either decreasing dielectric constant (via EC consumption) or decreasing viscosity (via DMC consumption) could result in increased solution resistance.
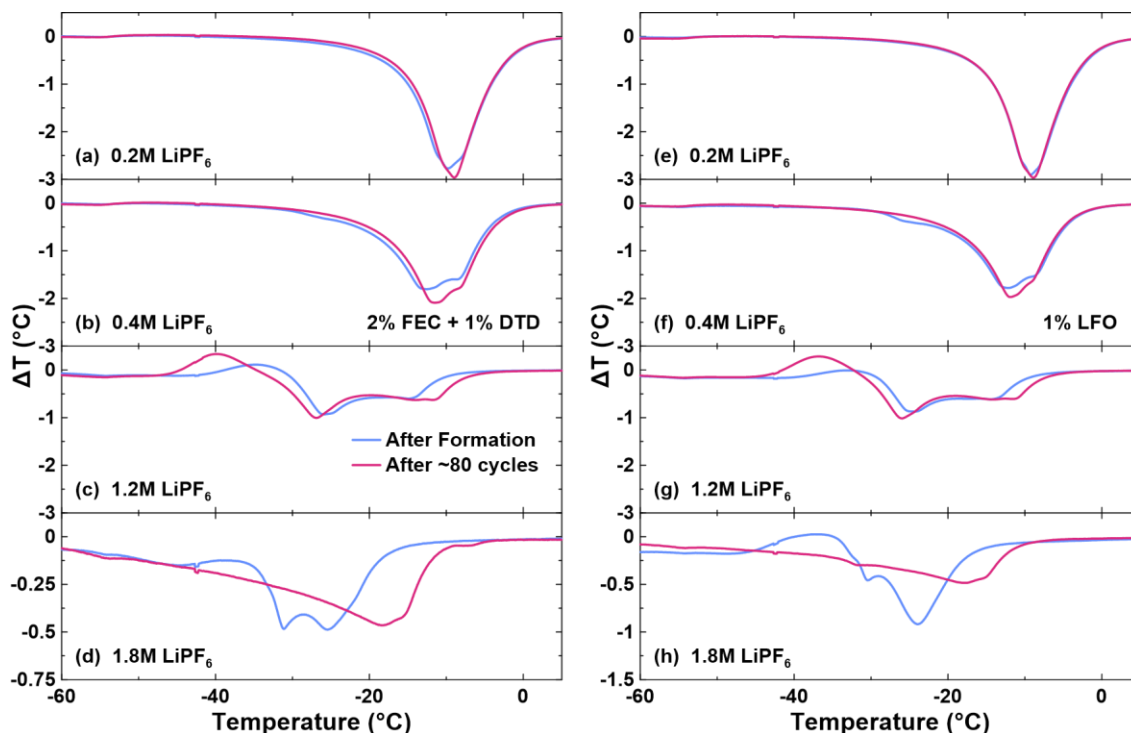
Figure 6.8. Li-ion DTA profiles collected on LFP/AG cells before and after cycling for approximately 80 cycles. Cells contained either (a-d) 2% FEC + 1% DTD or (e-h) 1% LFO electrolyte additives and LiPF$_6$ concentrations (a,e) 0.2M, (b,f) 0.4M, (c,g) 1.2M or (d,h) 1.8M. Cells were charged to either 4.4 V using C/3 cycle-hold testing at 40°C.

Figure 6.8 shows Li-ion DTA profiles, similar to Figure 6.7, except for cells that were charged to 4.4 V during cycling. In Figure 6.8, the trends exhibited by cells containing 2% FEC + 1% DTD and cells containing 1% LFO are both very similar and will be discussed without consideration for the different additives. The liquidus temperature feature remains mostly unchanged after approximately 80 cycles when 0.2M and 0.4M LiPF$_6$ concentrations are used. Meanwhile, when 1.2M and 1.8M are used, the liquidus feature moves to lower temperature when comparing measurements made before and after

cycling, indicating salt consumption during cycling. The temperature difference of the liquidus feature, comparing before and after approximately 80 cycles, is higher in Figure 6.8 than in Figure 6.7. Taken together, the results of these two figures suggests that $LiPF_6$ consumption occurs in LFP cells tested at 40°C using cycle hold methods, with increasing rate when higher $LiPF_6$ concentrations are used, and higher charge endpoint voltage limits are implemented. This agrees with Liu et al. who found that the rate of $LiPF_6$ hydrolysis increased as cells are charged to high voltage.
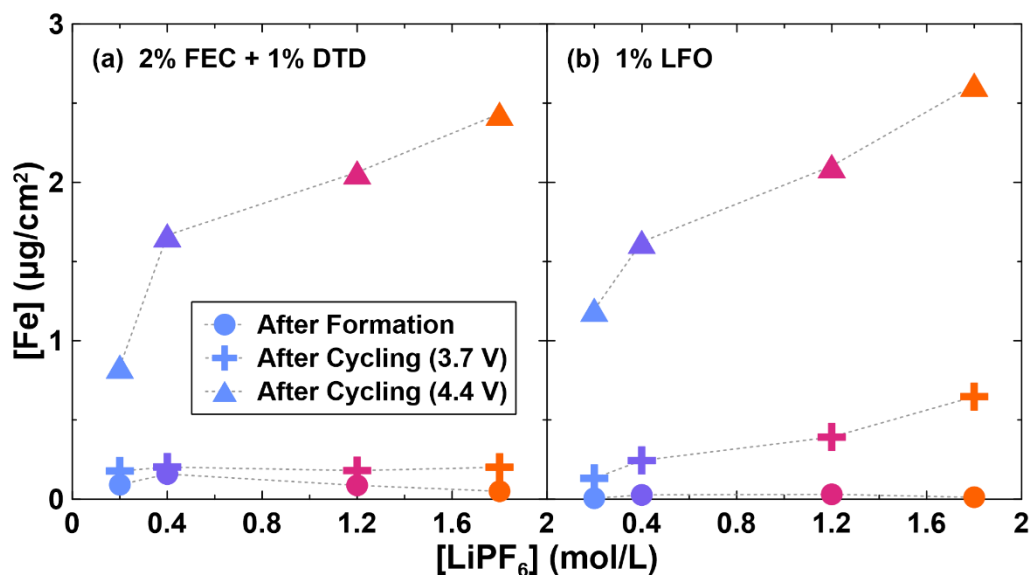
Figure 6.9. Iron deposition on the negative electrode for LFP/AG cells measured by μXRF after formation and after cycling for approximately 80 cycles. Cells contained electrolytes with varied $LiPF_6$ concentrations and either (a) 2% FEC + 1% DTD or (b) 1% LFO electrolyte additives. Colors are consistent with $LiPF_6$ concentration color scheme in Figure 6.1. Lines drawn to guide the eye.

Figure 6.9 shows the areal loading of iron deposited on the negative electrode, as determined by μXRF spectroscopy, as a function of $LiPF_6$ concentration for LFP cells containing either 2% FEC + 1% DTD or 1% LFO. Measurements were completed on cells after formation and after cycling with charging to either 3.7 V or 4.4 V. Previous work by

Logan et al. has shown that LFP cells that are longer lived show lower rates of Fe dissolution from the positive electrode.[89,196] Figure 6.9 shows that the amount of Fe deposited during cycling, relative to the amount measured after formation, increases with increasing $LiPF_6$ concentration and with increasing charge endpoint voltage. It has been discussed that the presence of acid can result in transition metal dissolution from the positive electrode[147] and that $LiPF_6$ hydrolysis can occur more rapidly at high voltage.[246] Figure 6.8 suggested that $LiPF_6$ consumption occurs at greater rates in LFP cells charged to 4.4 V. If such increased salt consumption resulted in HF production or otherwise resulted in dissolved Fe from the positive electrode, that would explain the increased Fe dissolution shown in Figure 4.9 in cells charged to 4.4 V.

Comparing cells that cycled with a charge endpoint voltage of 3.7 V, the amount of Fe dissolution, particularly when higher $LiPF_6$ concentrations are used, is much greater for cells containing 1% LFO than those containing 2% FEC + 1% DTD. Comparing to literature results, Fe deposition in similar cells with reported excellent electrolyte systems tend to show around 0.5 $\mu g/cm^2$ or less, after 1400 hours of testing at 40°C.[89] The time required for 80 cycles of cycle-hold testing is also approximately 1400 hours, and cycle-hold testing performed in this work was also done at 40°C. Therefore, the increase in Fe dissolution observed with the use of 1% LFO compared to 2% FEC + 1% DTD in cells charged to 3.7 V likely suggests that 1% LFO is an inferior additive system for LFP cells and may result in worse long-term cycle life, but Fe dissolution quantities are comparable to other excellent cells. The significantly lower rates of Fe dissolution observed in cells charged only to 3.7 V again suggests that applications which use LFP cells should be

careful to avoid regular overcharge situations or voltage spikes during charging, although momentary increases in voltage beyond 3.65 V or 3.7 V are likely fine.

Taken as a whole, the results presented in this section clearly show that by many metrics conventionally used to describe cell performance and degradation, the use of lower $LiPF_6$ concentrations is beneficial to achieving long-lived LFP cells that spend considerable amounts of time at full state-of-charge, or even in overcharge conditions. Cells fail due to lithium inventory loss at the negative electrode. While not definitive, there is evidence and literature that would support a failure mechanism where $LiPF_6$ could decompose in the presence of trace water contamination to yield HF, which in turn causes Fe dissolution from the positive electrode and migration to the negative electrode. The deposition of the Fe at the negative electrode may cause damage to the SEI which consumes lithium as a means of self-repair. If the initiation of this mechanism, namely the decomposition of $LiPF_6$, occurs with a rate dependent on the concentration of $LiPF_6$, this mechanism would be consistent with all the results presented this far in this chapter.

6.4 Comparison with NMC Cells and the Use of an Alternate Salt

The preceding sections in this chapter establish that the use of $LiPF_6$ in high concentrations is harmful to the lifetime of LFP cells. The use of low $LiPF_6$ concentration electrolyte to achieve longer lifetime is unfortunately accompanied by poor electrolyte physical properties such as low conductivity which results in cells with poor rate capability.[73]

Therefore, the use of an alternate salt which can be used at high concentration without negatively affecting the lifetime, or better yet can improve lifetime as a function of increasing concentration, like $LiPF_6$ does in NMC cells, is desirable. It has recently been shown that replacement of $LiPF_6$ by LiFSI in LFP results in higher lifetime, particularly at high temperature.[89]

Additionally, to explore the effect of salt concentration in LFP cells, comparison can be made with NMC cells that can operate at similar voltages to LFP cells. Rather than comparing to a conventional NMC cell which is designed to be charged to 4.2 V, or beyond, NMC cells can be constructed with only enough graphite to support charging to an upper cutoff voltage limit similar to LFP cells. Such cells are the topic of Chapter 7, and are also discussed in recent publications,[15,42,248] but are briefly introduced here for a relevant comparison with LFP cells when tested using cycle-hold methods. Such cells contain an NMC532 positive electrode and an artificial graphite negative electrode identical in composition to the negative electrodes used thus far in this thesis and specifically the LFP cells discussed in this chapter. These NMC532 cells are constructed so that operation without plating lithium requires charging be limited to 3.80 V or lower voltages. These are referred to as low voltage NMC cells here.

Figure 6.10 shows cycling results for both LFP and low voltage NMC cells, subjected to cycle-hold testing at 40°C with a C/3 rate. LFP cells were charged to 3.7 V while the low voltage NMC cells were charged to 3.8 V. The data for LFP cells containing $LiPF_6$, shown in Figures 6.10a and 6.10c, is the exact same data introduced in Figure 6.1. Cells that produced this data contain 2% FEC + 1% DTD as electrolyte additives. The remaining cells for which data is shown in Figure 6.10 contain 2% VC to better compare

to other experiments that are not mentioned here. The structure of FEC and VC are somewhat similar, and anecdotally, both additives offer similar performance improvements. It is possible that any comparisons made in Figure 6.10 could be influenced by slightly different additive formulations, but this is not believed to be the case.
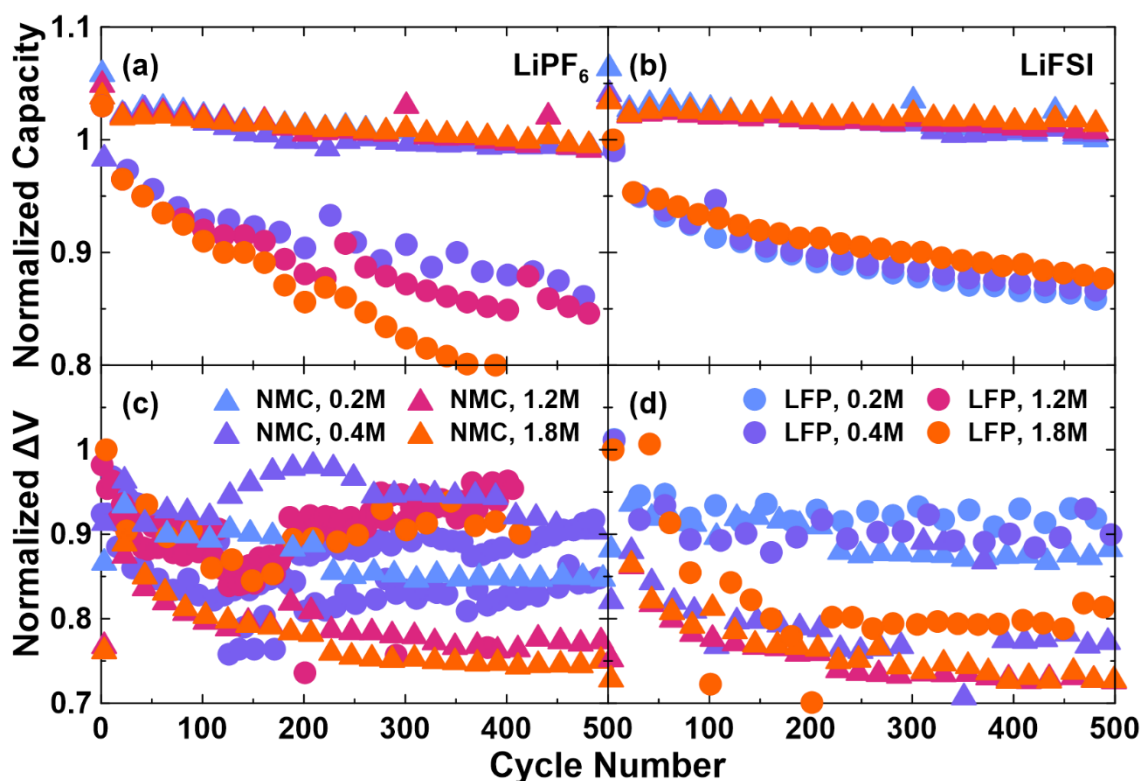
Figure 6.10. (a,b) Discharge capacity and (c,d) ΔV, normalized to 1 at cycle 5, versus cycle number for LFP/AG and low voltage NMC532/AG cells, containing either (a,c) LiPF$_6$ or (b,d) LiFSI at one of four concentrations. LFP cells were charged to 3.7 V while low voltage NMC cells were charged to 3.8 V, both using C/3 cycle-hold testing at 40°C. This represents over 1 year of testing.

Figures 6.10a and 6.10c show that low voltage NMC cells have much better capacity retention than LFP cells both when either LiPF$_6$ or LiFSI are used as electrolyte salts. Low voltage NMC cells do not show different amounts of capacity fade that depend on the electrolyte salt concentration with either LiPF$_6$ or LiFSI. As has been thoroughly

190

discussed, LFP cells containing $LiPF_6$ show increasing capacity fade as the $LiPF_6$ concentration increases. LFP cells containing LiFSI show improved cycle-life compared to LFP cells containing $LiPF_6$ and show decreasing capacity fade as the LiFSI concentration is increased, although the trend is very subtle. Figures 6.10c and 6.10d show that there is no ΔV growth whatsoever for any of the cells tested. When comparing cells with identical salt type and concentration, NMC cells tend to have lower ΔV than LFP cells. This is largely due to a period at the beginning-of-life, where ΔV decreases during the first approximately 100 cycles, which is characteristic of cells with NMC positive electrodes, but not those with LFP positive electrodes. These first 100 cycles aside, the main result from Figures 6.10c and 6.10d is that both cell types experience no ΔV growth, or equivalently, no impedance growth.

The use of lithium imide salts has been proposed as an alternate to $LiPF_6$ due to greater stability against thermal and hydrolytic decomposition.[87] The improved performance and the reversal of the salt concentration dependence of capacity fade when LiFSI is used in LFP cells is consistent with the results and discussion of the previous section. If the replacement of $LiPF_6$ by LiFSI eliminates a pathway for salt consumption and the resulting production of HF, then much of the failure described in Section 6.3 should not happen. The fact that NMC cells do not suffer increase rates of capacity loss with increasing salt concentration when $LiPF_6$ is used suggests that NMC cells may prevent continuous salt consumption or have a means of clearing harmful byproducts such as HF, that is not present in LFP cells. Figure 6.10b shows that LFP cells containing LiFSI are still considerably worse than NMC cells with identical electrolytes. Despite eliminating the problems associated with the use of $LiPF_6$, a large performance gap remains to NMC cells.

This suggests an inherent disadvantage of LFP as a material when combined with graphite and conventional Li-ion electrolyte systems, when compared to otherwise identical cells that contain NMC materials. Reactions between the positive electrode and the electrolyte can result in byproducts that migrate to the negative electrode and may have beneficial or harmful effects.[249] It is therefore possible that researchers may need to understand and artificially create the benefits associated with using an NMC positive electrode, in LFP cells to achieve comparable lifetimes.

6.5 Conclusions

LFP cells that were cycled with protocols that included 24 h constant voltage holds at either 3.7 V or 4.4 V were shown to have a greater rates of capacity loss as higher $LiPF_6$ concentrations were used. UHPC testing suggested that this $LiPF_6$ mediated failure is due to increased parasitic reactions at the negative electrode and accompanying lithium inventory loss. Electrolyte analysis by Li-ion DTA and quantification of transition metal dissolution from the positive electrode noted $LiPF_6$ consumption and Fe dissolution that increase in rate as the $LiPF_6$ concentration is increased. These results are consistent with evidence from the literature that together suggest the following mechanism: $LiPF_6$ decomposition can result in the production of HF, which in turn reacts with the LFP electrode, causing transition metal dissolution. Dissolved Fe migrates to the negative electrode where SEI damage occurs. Lithium inventory is consumed in repairing the SEI. This occurs at a greater rate when the charge endpoint voltage is raised from 3.7 V to 4.4

V. The increased rate of capacity loss with increased salt concentration is eliminated when LiFSI, a salt which is not thought to react to produce HF, replaces LiPF$_6$.

The use of LiFSI salt is highly recommended, over LiPF$_6$, if lifetime is a priority. There are certain manufacturers that may need to build LFP cells that contain LiPF$_6$ for reasons such as an existing inventory of LiPF$_6$ or desirable physical properties obtained with LiPF$_6$ electrolytes. In these cases, especially if the LFP cells may spend considerable times are full state-of-charge, utilizing lower LiPF$_6$ concentrations, such as 0.4M will yield improved lifetime. Additionally, research into classes of additives that can scavenge trace water or acid, or otherwise prevent LiPF$_6$ decomposition may enable the use of LiPF$_6$ in LFP cells and mitigate the failure described here.

The implications of the test parameters used in this chapter should also be noted. Cells were tested with cycle-hold protocols at 40°C. It is possible that the deleterious effects of LiPF$_6$ would not occur appreciably if the temperature were around room temperature, and perhaps the concerns raised in this chapter are not relevant in applications where battery temperature is carefully controlled. It has been suggested that time spent at high voltage can increase the rate of failure of LFP cells, particularly those with high LFP concentrations. Most of the charge and energy that can be stored in an LFP cell exists along the two-phase plateau of the voltage curve, around 3.4 V. Charging the cell from 3.45 V to 3.65 V, the conventional charge endpoint voltage, does not store appreciably more energy. In cases where LFP cells are used and must achieve the longest possible lifetimes, it may be prudent to limit charging to 3.45 V rather than a slightly higher value.

Finally, the original purpose of the experiments described in this chapter was to form a comparison with the experiments described in Chapter 4, on NMC532 cells. LFP

cells discussed in this chapter showed increased rates of capacity loss with increased salt concentration and failure due to lithium inventory loss, not impedance growth. This large and opposite difference, along with the difference shown in other tests, such as transition metal deposition, suggest that the failure observed here is notably different than the NMC532 discussed in Chapter 4. It was previously hypothesized that the fatal impedance growth observed in NMC532 cells in Chapter 4 could be due to the growth of a disordered rock salt surface layer on the positive electrode particles. LFP cells cannot form such a surface layer. When tested similarly, LFP cells show vastly different behaviors and failure modes compared to NMC cells. This strengthens the case for rock salt growth as the primary cause of failure in the NMC532 cells described in Chapter 4, while adding to the understanding of the operational differences between LFP and NMC cells.

CHAPTER 7 STUDY AND USAGE OF NOVEL LOW VOLTAGE LI-ION CELLS FOR ULTRA-LONG LIFETIME

Many of the results presented in this Chapter have appeared in the peer-reviewed articles *J. Electrochem. Soc.* **169**, 050512 (2022) and *J. Electrochem. Soc.* **169**, 090523 (2022). The author of this thesis was responsible for experiment planning, including the repurpose of cells originally unintended for the purposes described herein and the design of constant capacity charging methods described in Section 7.5, the majority of cell construction, all electrochemical testing and resulting data analysis. Supervision throughout, review of results and feedback on experiments was provided by Jeff Dahn. Jeff Dahn also helped select and design follow up cell types mentioned in Sections 7.4.2 and 7.4.3. Eric Logan made a small number of LiFePO₄ cells that are used for comparison. Ahmed Eldesoky performed μXRF measurements at facilities graciously provided by Saint Mary's University. Julian Oxner and Helena Hebecker assisted in some cell making.

7.1 Introduction

Cells containing NMC-type and LFP positive electrodes, paired with a graphite negative electrode, when counted together, comprise the vast majority of commercial Li-ion cells produced. NMC cells typically provide higher energy density, owing to both a relatively high positive electrode specific capacity and high average voltage of $\geq$ 200 mAh/g and $\geq$ 3.6 V respectively.[21,34,41] These benefits come at the expense of safety[50,55,155,250] and expensive materials.[47,251] LFP cells have lower energy density, due to both a lower positive

electrode specific capacity (170 mAh/g) and average voltage (3.2 V),[45] but offer improved safety[50] and use a cheaper transition metal compared to NMC cells.

Accessing most of the capacity in an NMC type positive electrode necessitates charging to higher voltages, especially considering a large fraction is available beyond 4.0 V vs Li$^+$/Li.[21,41,252] In addition to the failure modes noted in the discussion of Chapters 4 and 5, high voltage charging can be associated with particle cracking,[253–255] phase transitions[41,52,256,257] and electrolyte oxidation,[258–260] which can all reduce lifetime. Alternately, charging to high voltage can also introduce reactions at the positive that consume or produce certain species that result in improved performance and/or lifetime.[261,262] Selecting a voltage limit for charging NMC cells can be viewed as a compromise between the harmful and beneficial effects, and the voltages at which those effects occur at appreciable rate, along with achieving sufficient energy density. Conventional NMC cells are generally charged to a limit between 4.0 V and 4.2 V, which has historically been seen as a good compromise of the above.

In Chapters 4 and 6, NMC cells and LFP cells charged to high voltage were demonstrated and compared. The two cell types were shown to have different failure mechanisms, particularly at high voltage. To compare NMC and LFP cells as they are traditionally used has merit but does not exactly help identify mechanistic differences and facilitate a comparison on mostly even terms. To compare NMC and LFP cells by implementing low, LFP-like, charge endpoint voltages with conventional NMC cells would result in excess graphite capacity that would be largely unused. This comparison would result in similar levels of electrochemical stress between the two cells but yield NMC cells with lower energy density than is necessary to achieve the desired charge

endpoint voltage, or balance, and may introduce unrepresentative or outright negatives effects due to excess graphite that requires additional passivation.

The direct comparison of NMC532 and LFP cells was briefly mentioned and introduced in Chapter 6, in Figure 6.11. In that example and under typical testing conditions, NMC cells showed improved lifetime compared to LFP cells, despite being charged to much higher voltages.[196] The work in this chapter aims to compare NMC cells to LFP cells when they are charged to voltage limits similar to LFP cells, using a novel NMC cell design with only enough graphite to enable charging to 3.8 V. This enables a comparison between NMC and LFP cells operated in a similar electrochemical window, along with similar graphite utilization, which is a first as far as the author is aware of. The goal, at the outset of this work, was to probe why NMC cells typically show better lifetime than LFP cells and if this performance difference was changed when NMC cells were charged to lower-than-conventional voltages.

7.2 Low Voltage NMC Cell Design

The usage and design of the cells in this chapter is rather novel, although the concept of utilizing lower charge voltage limits to achieve longer lifetime is not. The cells utilized here are repurposed from an original implementation, described by Martin et al.[263] In that work, cells were designed to charge only to approximately 3.8 V with lithium intercalating into graphite. At higher voltages, with all available intercalation sites full and the graphite capacity fully utilized, additional charging results in plating of metallic lithium on the surface of the graphite particles. This lithium metal can be plated and stripped with modest

reversibility. In this mode of operation with utilization of both a graphite intercalation and metallic negative electrodes, Martin et al. described these cells as hybrid lithium-ion/lithium metal cells.[263] Here the cells are used without charging to voltages beyond 3.8 V, where lithium plating would occur, and operate only as lithium ion cells with a graphite negative electrode.
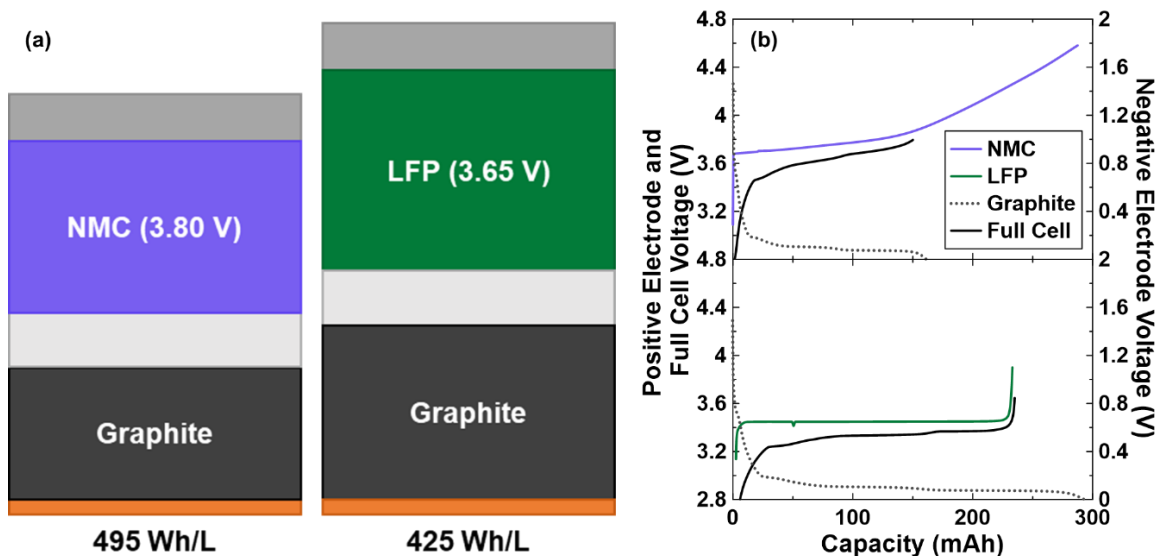
Figure 7.1. (a) Schematic representation of volumetric stack energy density of low voltage NMC532/graphite cells, when charged to 3.80 V, and LFP/graphite cells, when charged to 3.65 V. The major jellyroll components are included in the schematic, specifically the aluminum foil (light grey), positive electrode (purple or green), separator (off-white), negative electrode (dark grey) and copper foil (orange). (b) Voltage curves showing the electrode alignment for NMC and LFP cells at the beginning-of-life, based on differential voltage analysis and build specifications.

Figure 7.1a shows a schematic which is representative of the volumetric "stack" energy density of the low voltage NMC532 cells used in this chapter, and the LFP cells they will be compared to throughout. Figure 7.1a shows the volume of "stack" material required for a given amount of energy, based on the two cell types, and accounts for the electrode coatings, current collectors, and separator. The "stack" energy density does not

account for materials outside the stack, such as the cell casing, and tries to facilitate a comparison at the electrode level, rather than the cell level. A smaller depiction represents less material required to achieve the same amount of energy, therefore higher volumetric energy density. Despite charging to a much lower than conventional voltage limit and leaving so much unutilized capacity in the positive electrode, the low voltage NMC cells have a greater stack energy density than LFP cells, of 495 Wh/L compared to 425 Wh/L. It should be noted that neither of these cell designs is optimized for energy density, such as implementing very thin current collectors and separator, along with thick electrode coatings. It is unclear which cells would have a higher energy density if cells were redesigned with this quantity in mind, however, the fact that they are similar here suggests that optimized energy densities for revised low voltage NMC and LFP cells wouldn't be significantly different from each other. A key takeaway is that LFP cells are presently considered to be a viable commercial option, despite having low energy density because of the other merits they provide. The low voltage NMC cells presented here should therefore not be disqualified from commercial viability on the basis of energy density.

Figure 7.1b shows the cell and electrode voltage curves for the low voltage NMC cells and LFP cells respectively. The voltage curves in Figure 7.1b, along with the energy densities in Figure 7.1a, are based on electrochemical measurements performed at beginning-of-life, but after formation, and therefore account for any irreversible capacity losses in the first cycle. The low voltage NMC cells can charge to 3.80 V with an N/P ratio of approximately 1.1. The LFP cells used in this work have an excess of graphite, yielding an N/P ratio of 1.2, which is both higher than the NMC cells and higher than conventional commercial quality cells. It is possible that this excess graphite presents greater reactive

surface area for parasitic reactions and higher passivation demands per unit capacity in the LFP cells compared to the NMC, causing worse relative performance. It has been shown that excess graphite is electrochemically active,[264] however it is believed that the difference in relative graphite amount is far too small to explain the large differences that will be shown later in this chapter. If this excess graphite was eliminated, and the N/P ratio for LFP was approximately 1.1 like the low voltage NMC cells, the energy density would change by 3%, to approximately 440 Wh/L which is still less than the NMC cells. Volumetric energy density is prioritized here as a metric of energy content, as most applications of commercial relevance experience space constraints that are more demanding than weight constraints. When compared on the basis of gravimetric stack energy density, both cell types yield approximately 210 Wh/kg.

7.3 Conventional Testing of Low Voltage NMC Cells

The cells used in this chapter were prepared following the methods of Chapter 3. Electrolytes were mixed with either 1.5M $LiPF_6$ or 1.5M LiFSI and 2% VC was included as an additive. This salt concentration was selected as it is in a conventional range that typically delivers excellent physical properties and lifetime. It was shown in Chapter 6 that such high concentrations of $LiPF_6$ are not a good choice for LFP cells, but nevertheless, 1.5M is used here in all cells for comparison and adherence to convention. The selection of 2% VC was made to ensure good passivation on the negative electrode, but to avoid complicating the system with multi-species additive blend.

Cells underwent a typical formation cycle, during which they were charged to the same voltage that they would be charged to during electrochemical cycling experiments. For NMC cells, the charge endpoint voltages were either 3.65 V, to exactly match LFP cells, or 3.80 V, to fully utilize the graphite while still restricting charging to a low voltage. For LFP cells, the charge endpoint voltage was 3.65 V. Figure 7.2 shows the volume change due to gas production and the first cycle efficiency measured during the formation cycle for NMC and LFP cells, based on electrolyte salt type and charge endpoint voltage. Among the NMC cells, there is little difference between the gas production between cells that charged to 3.65 V and 3.80 V, but more gas was produced when LiFSI was used, compared to $LiPF_6$. Gas production often accompanies SEI formation, particularly at the very beginning of the very first charge.[222] This suggests gas production occurs almost entirely on the negative electrode and the salt either directly participates in SEI forming reactions or indirectly affects other species that participate in SEI forming reactions. The LFP cells show more gas production than all the NMC cells, and similarly LFP cells with LiFSI produce more gas than with $LiPF_6$. The former can be explained by some combination of the small amount of excess graphite in the LFP cells, excess residual water content often found in LFP electrodes which can react with active lithium to form LiOH and H_2, and fundamentally different electrochemistry, even at the negative electrode, in the presence of a different positive electrode.
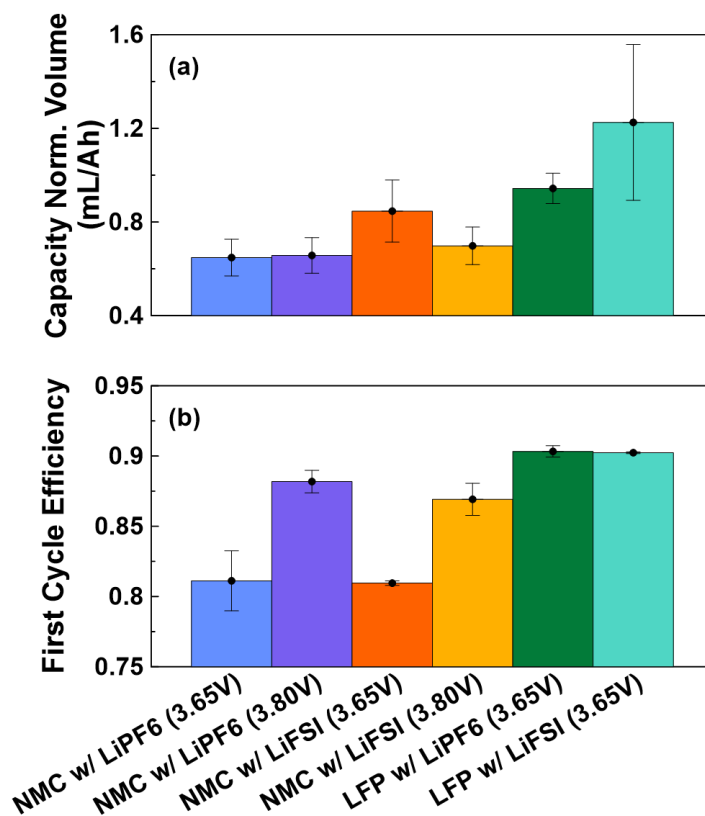
Figure 7.2. (a) Volume of gas per unit capacity generated and (b) the first cycle efficiency measured during the first, or formation cycle, measured at C/20 and 40°C. NMC/graphite and LFP graphite cells were both measured, with charging to the limit specified in the horizontal axis labels. All cells contained electrolyte with 2% VC. The color association with cell type, electrolyte salt and charge endpoint voltage presented here is carrier forward in most of the figures in the section.

Figure 7.2b shows that the first cycle efficiency of NMC cells increases as the charge endpoint voltage increases, and within error there is no significant difference between the use of $LiPF_6$ or LiFSI. Because a large fraction of the capacity lost on the first cycle is due to SEI formation at the very beginning of the first charge, charging NMC cells to higher voltage, within reason, results in more reversible capacity storage. This in turn lessens the relative amount of capacity irreversibly lost to SEI formation as the charge endpoint voltage is raised.[265] The LFP cells show higher first cycle efficiency than any of the NMC cells, and again, the first cycle efficiency does not significantly differ in LFP

cells that use LiPF$_6$ compared to LiFSI. LFP cells show higher first cycle efficiency primarily since LFP itself has no irreversible capacity loss, and any inefficiency of an LFP/graphite cell is due to reactions on the graphite surface.[266] NMC has an irreversible capacity loss that contributes along with the graphite electrode to the overall cell inefficiency.[265] Overall, the selection of the charge endpoint voltage when specifying an NMC cell build is a compromise between energy density, first cycle efficiency and longevity.
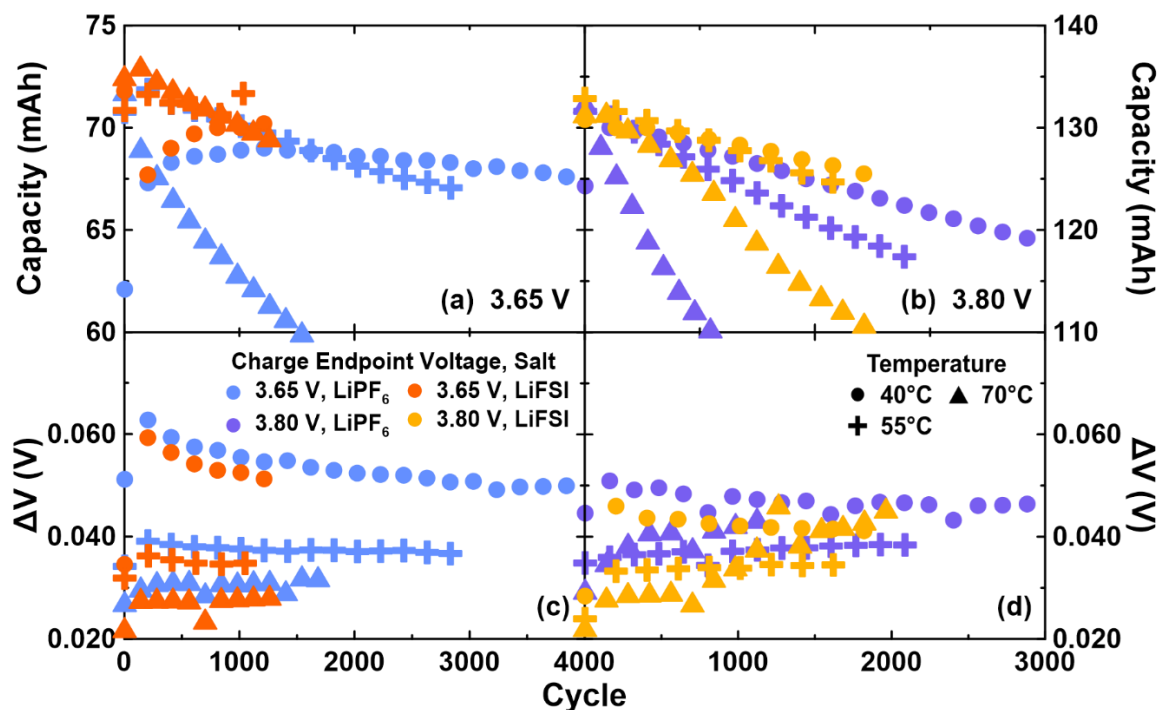
Figure 7.3. (a,b) Discharge capacity and (c,d) ΔV versus cycle number for low voltage NMC532 cells. Cells were cycled at 40°C, 55°C or 70°C, contained either LiPF$_6$ or LiFSI electrolyte salt, and were charged to either (a,c) 3.65 V or (b,d) 3.80 V. Cells charged to 3.65 were cycled at C/2 and cells charged to 3.80 V were cycled at C/3.

Figure 7.3 shows electrochemical cycling results for the low voltage NMC cells. Figures 7.3a and 7.3b show that more capacity is obtained, as expected, by charging to 3.80 V compared to 3.65 V, but the relative rate of capacity loss, based on the initial capacity,

is greater for cells charged to 3.80 V. This is again a compromise between storing energy more densely and longevity. Figures 7.3a and 7.3b also show that the rate of capacity loss increases as the test temperature increases, which is again an expected result and indicates parasitic reactions that occur at increasing rate at higher temperature. Figures 7.3c and 7.3d show that all cells tested have very little discernable ΔV or equivalently, impedance growth. The cells tested at 70°C, with charging to 3.80 V show a small amount of impedance growth relative to the other cells, but this increase is not of a magnitude typically associated with a problem delivering full capacity.

Finally, the use of LiFSI appears to yield superior capacity retention compared to $LiPF_6$ under all test conditions, but the improvement is more noticeable as the test temperature increases. This is suggestive of a thermally activated $LiPF_6$ decomposition mechanism or other deleterious reaction pathway that $LiPF_6$ participates in which is eliminated or diminished when $LiPF_6$ is replaced with LiFSI. It has been shown that graphite electrodes perform better in cells which use LiFSI electrolytes, rather than $LiPF_6$ electrolytes due to thinner, more thermally stable SEI films.[267] Because the charge endpoint voltages used are relatively low, undesirable effects from the positive electrode, such as electrolyte oxidation or transition metal dissolution are thought not to occur. It is likely that the performance of the graphite negative electrodes is also the primary factor in determining overall cell performance.

Although not shown, duplicate cells of those shown in Figure 7.3 were cycled simultaneously. After approximately 3000 h of cycling, one of each pair was removed and directed into further testing to determine cell condition. This included UHPC cycling, EIS analysis and quantification of transition metal dissolution by μXRF spectroscopy. From

the UHPC cycling, data of sufficient quality was collected to perform differential voltage analysis. Figure 7.4 shows the relative positioning of the positive and negative electrode voltage curves, obtained by this analysis. The positive electrode voltage curves shown in Figure 7.4 are all aligned at 0 mAh along the capacity axis. The negative electrodes are aligned relative to this positive electrode curve, indicating slippage or shift loss. Negative electrodes positioned further to the right come from measurements on cells that have experienced greater amounts of lithium inventory loss due to parasitic reactions on the negative electrode. There is little active mass loss in most cells over 3000 h of testing, and the primary mode of capacity loss was determined to be lithium inventory loss, so Figure 7.4 illustrates shift loss without consideration of active mass loss. Negative electrode voltage curves that move further to the right in each panel indicate cells that have lost larger amounts of lithium inventory.
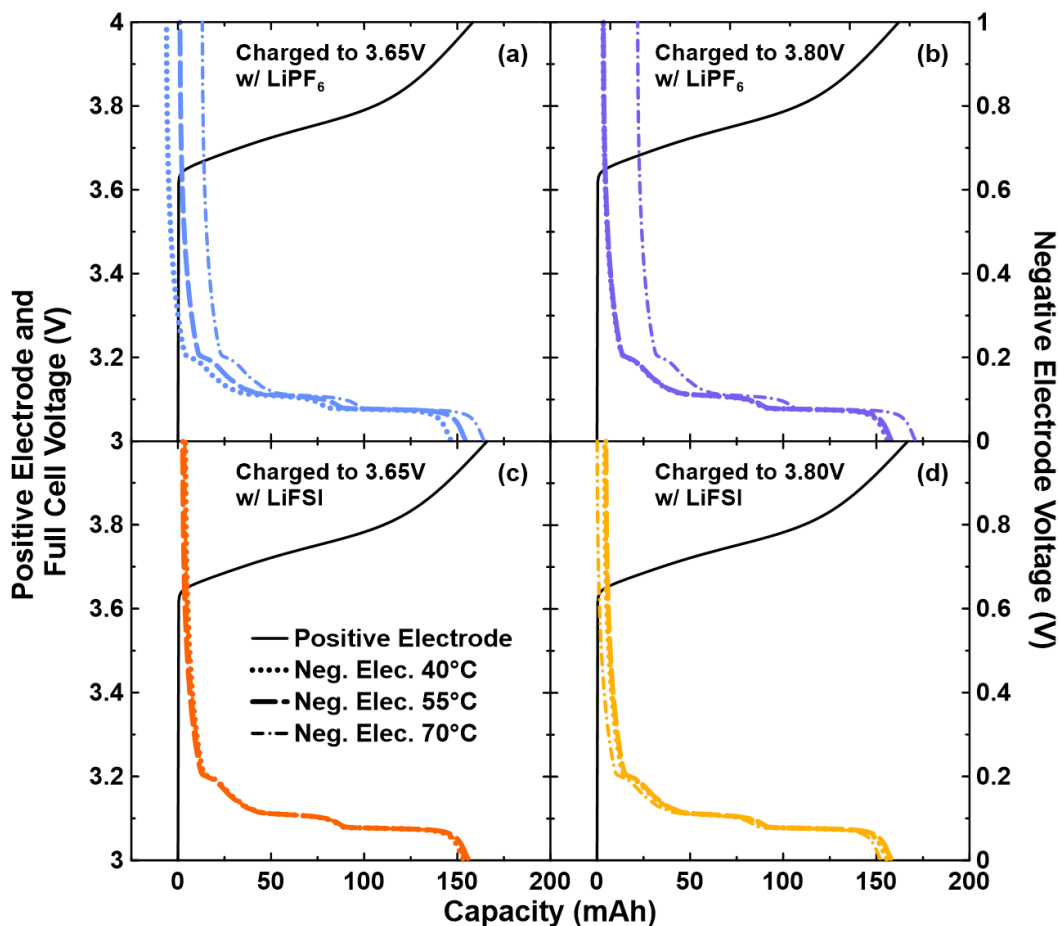
Figure 7.4. Voltage curves showing electrode alignment after 3000 h of cycling, as determined by differential voltage analysis, for low voltage NMC532 cells. Cells were charged to either (a,c) 3.65 V, or (b,d) 3.80 V and contained either (a,b) $LiPF_6$ or (c,d) LiFSI electrolyte salt. Each panel contains data for cells tested at 40°C, 55°C or 70°C. A representative positive electrode voltage curve is included in each panel.

Figures 7.4a and 7.4b show that in cells containing $LiPF_6$, shift loss occurs more as the charge endpoint voltage and the test temperature are increased. Cells containing LiFSI show far less shift loss than those containing $LiPF_6$. These observations collectively agree with the capacity retention presented in Figure 7.3, where higher charge endpoint voltage and higher test temperature resulted in faster rates of capacity loss. Agreement between shift loss and capacity fade typically implies a causal relation. The detailed behavior of cells containing LiFSI is considerably different than cells containing $LiPF_6$ and somewhat

unexpected. Cells that were charged to 3.65 V and containing LiFSI, all show identical voltage curve positioning and nearly no shift loss. It should be noted that 3000 h of cycling is approximately 500 cycles, and the cells containing LiFSI that charge to 3.65 V show very little difference after 500 cycles in Figure 7.3. It is expected that with the accumulation of more time under test, larger differences would unfold in differential voltage analysis, as they do in long-term cycling. Cells charged to 3.80 V that contained LiFSI also have very little shift loss, and an unexpected ordering of the negative electrode voltage curves. The cell which was tested at 70°C yielded a negative electrode which is positioned furthest to the left, indicating less shift loss. It has been mentioned that LiFSI electrolytes result in greater thermal stability than $LiPF_6$ electrolytes, and again, very little difference is observed between cells containing LiFSI and charged to 3.80 V in Figure 7.3. Nevertheless, the unexpected ordering could be explained by a process occurring at the positive electrode, activated at high temperature that causes the positive electrode to shift at the same rate as the negative electrode. This requires more careful investigation and could possibly indicate problems which may become apparent after longer time under test.

Figure 7.5 shows a summary of UHPC metrics measured after 3000 h of cycling for low voltage NMC cells which cycled at 40°C. Data for LFP cells with identical electrolytes was sourced from separate experiments[89] and is included in Figure 7.5 for comparison. These LFP cells cycled for 2000 h at 40°C before UHPC testing. The time difference is thought to be insignificant to the comparison as the SEI in all cells is sufficiently mature and most UHPC metrics are therefore relatively constant as a function of time. Of the cells tested, one NMC cell, containing LiFSI and having charged to 3.65 V is believed to have given erroneous or somehow spurious results. Data for this cell in Figure

7.5 is shown, for completeness, but is overlaid with a white 'X' and won't be discussed further and mention of any trends in the following text are assumed to not include data for this cell. It is believed this cell may have been damaged during transfer between experiments or have been a cell with inferior assembly which was not detected until high precision testing.
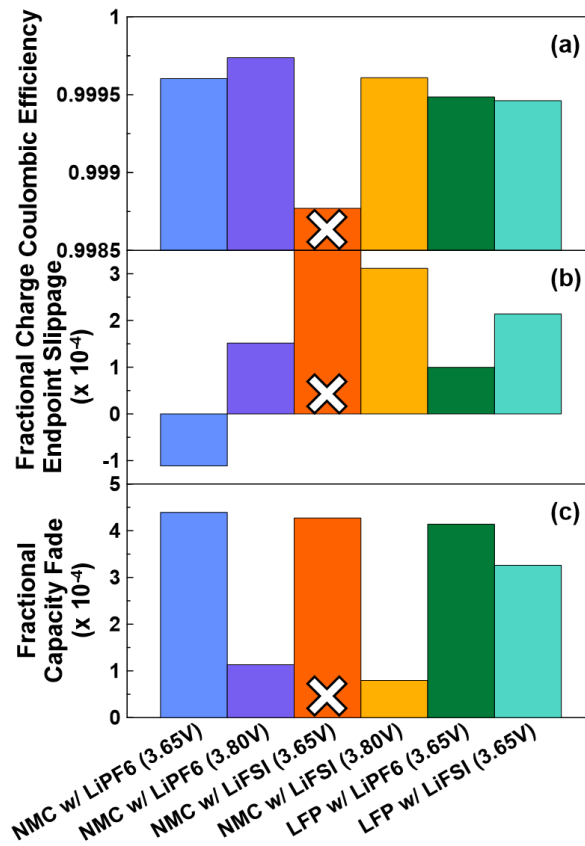
Figure 7.5. (a) Coulombic efficiency, (b) fractional charge endpoint capacity slippage (per cycle), and (c) fractional capacity fade (per cycle) of low voltage NMC and LFP cells, as measured by UHPC. UHPC measurements were conducted after 3000 h of cycling at 40°C for NMC cells and 2000 h of cycling at 40°C for LFP cells. An 'X' is placed over the data for a cell of questionable reliability, as mentioned in the text.

Figure 7.5a shows that the coulombic efficiency is higher for NMC cells than LFP cells, which translates to longer expected lifetime in situations where lithium inventory loss is the primary failure mode. For NMC cells that contain $LiPF_6$, charging to higher voltage

appears to yield higher CE. This is an unintuitive result, as parasitic reactions are expected to occur at a greater rate at higher voltage and the results of Figure 7.3 have suggested inferior lifetime in NMC cells charged to 3.80 V rather than 3.65 V. Figure 7.3c shows that the NMC532 cell with LiPF$_6$ which was charged to 3.65V at 40°C still has decreasing impedance. This suggests that at such low voltage and modest temperature, the SEI is in fact not fully mature in these cells. The use of LiFSI in NMC cells seems to result in lower CE, which is largely due to higher charge endpoint capacity slippage. This is typically interpreted as higher amounts of electrolyte oxidation on the positive electrode[111] and is consistent with the discussion of Figure 7.4 where it was suggested that the use of LiFSI may introduce an effect at the positive electrode that may cause shift of the positive electrode in parallel to shift of the negative electrode. An alternate interpretation that would be consistent with this is a shuttle mechanism where reaction products are cyclically reduced and oxidized as they migrate between electrodes.[247,268,269] Shuttle processes are more common in low voltage cells, because charging to higher voltage can irreversibly oxidize shuttle molecules[247] and shuttle processes have been speculated in LFP cells when LiFSI electrolytes are used, based on microcalorimetry results.[185] Similarly for LFP cells, the use of LiFSI results in greater charge endpoint capacity slippage.

Figure 7.5c shows that in both NMC and LFP cells, the use of LiFSI results in a slight decrease in capacity fade, where capacity fade is interpreted as the rate of lithium inventory loss due to parasitic reactions occurring at the negative electrode.[111] Both NMC and LFP cells that are charged to 3.65 V show similar amounts of capacity fade, but NMC cells that are charged to 3.80 V show much lower fade in these UHPC experiments. This implies that reactions occurring at slightly higher voltage, presumably on the positive

electrode surface, result in less lithium inventory loss at the negative electrode. This could be due to the production of a beneficial species that produces a robust SEI, or the elimination of a harmful species that causes SEI damage. Previous work has shown that NMC positive electrodes can participate in beneficial "cross-talk" reactions that improve the performance of negative electrode materials.[249,261,262] The UHPC metrics shown in Figure 7.5 are all excellent and the variations are small compared to typical measurements.
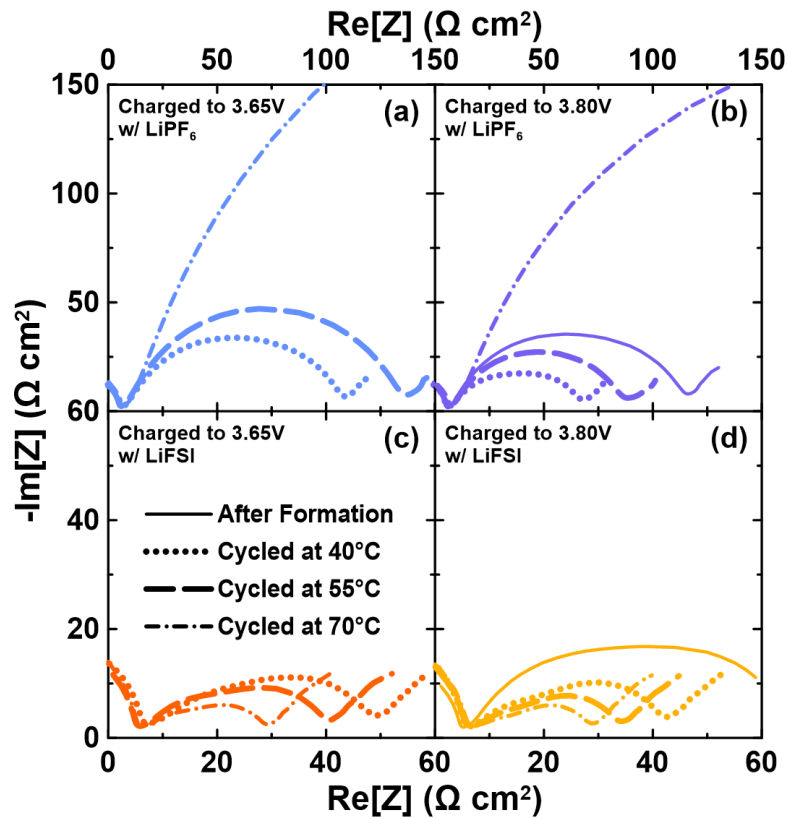
Figure 7.6. Nyquist plots of electrochemical impedance spectra collected from low voltage NMC cells after 3000 h of cycling. Cells were charged to either (a,c) 3.65 V or (b,d) 3.80 V and contained either (a,b) $LiPF_6$ or (c,d) LiFSI electrolyte salt. Each panel contains data for cells tested at 40°C, 55°C or 70°C. Impedance measurements were made at 10°C. All cells were charged to 3.80 V for impedance measurements. Spectra collected after formation are only included for cells that were charged to 3.80 V during cycling.

Figure 7.6 shows the area specific impedance of low voltage NMC cells after 3000 h of testing. These measurements were performed immediately after the UHPC characterization shown in Figure 7.5. Measurements were performed on all cells at 3.80 V. This corresponds to essentially 100% state-of-charge for these cells, based on their unique construction and the limits of operation without lithium plating, but only approximately 50% state-of-charge based on the capacity of the positive electrode. Impedance measurements in conventional cells are typically conducted at 50% positive electrode state-of-charge, so measurements made at 3.80 V achieve greater adherence to convention and can be used for comparison by other researchers. Cells which were charged to 3.65 V during long-term cycling were not charged to 3.80 V after formation to conduct impedance measurements to avoid introducing the effects of a higher voltage before cycling, and therefore do not have data after formation to compare to in Figure 7.6. Figure 7.3 showed all cells had nearly no changes in ΔV during the first 3000 h or 500 cycles of testing, and most differences were due to the temperature at which ΔV was collected. This is largely due to the difference in ion kinetics as a function of temperature, not necessarily due to differences in inherent conductivity in the cell. As has been mentioned earlier in this thesis, ΔV is determined by measurements with an effective frequency far smaller (~5 μHz) than the lower limit of frequencies implemented during impedance measurements (10 mHz). A direct translation between trends in ΔV and the measurements shown in Figure 7.6 are not clear without further testing and elucidation.

Figure 7.6 shows that the width and height of Nyquist plots are both smaller for cells containing LiFSI, compared to LiPF$_6$, indicating LiFSI results in thinner or ionically more conductive passivation films than LiPF$_6$, consistent with the findings of Kang et al.[267]

Cells which contained LiPF$_6$ resulted in impedance features and charge transfer resistances that increased as the cycling temperature increased. This suggested that the thermally activated process which LiPF$_6$ participates in and contributes to capacity loss plays a role in thicker or more resistive electrode interfaces in low voltage NMC cells. Cells containing LiFSI show the reverse trend, where increased cycling temperature results in smaller impedance after 3000 h of testing. This implies greater thermal stability and that the reactions involving LiFSI-containing electrolyte are markedly different than those containing LiPF$_6$-containing electrolyte, in low voltage NMC532 cells.
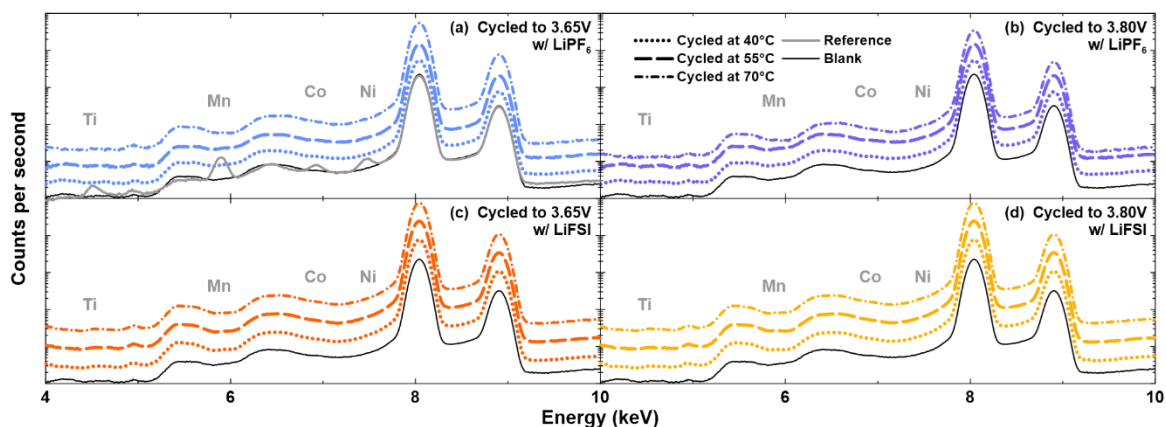
Figure 7.7. X-ray fluorescence spectra obtained from measurements on the negative electrodes of low voltage NMC cells after 3000 h of electrochemical cycling. Cells were charged to either (a,c) 3.65 V or (b,d) 3.80 V and contained either (a,b) LiPF$_6$ or (c,d) LiFSI electrolyte salt. Each panel contains data for cells test at 40°C, 55°C or 70°C. Blank (pristine negative electrode) and reference (negative electrode from a cell with notable transition metal dissolution) spectra are included for comparison.

Figure 7.7 shows the results of X-ray fluorescence spectroscopy measurements performed on negative electrodes that were harvested from the low voltage NMC cells after 3000 h of testing. Cell disassembly and μXRF measurements were performed following the EIS measurements shown in Figure 7.6 and a complete discharge to ensure safe handling in air. A blank spectrum obtained from a graphite electrode that was never

charged or exposed to electrolyte is shown in each panel. Figure 7.7a also includes a reference spectrum that was obtained from a separate experiment which shows typical signals in cells which suffer from notable transition metal dissolution, in the amount of 1-3 $\mu g/cm^2$ per each of Ni, Mn and Co. All cells from this work show identical spectra, which are also identical to the blank spectra. This indicates no detectable transition metal dissolution in these cells after 3000 h of testing, regardless of salt type, test temperature and charge endpoint voltage. This result is unsurprising as damage to the positive electrode is typically associated with high voltage charging and operation to voltages of 3.80 V and below should largely preclude positive electrode damage. It is possible that with different electrolyte formulations, longer temperatures or even simply greater time under test that limiting charging to 3.80 V would not be sufficient to prevent transition metal dissolution or other positive electrode degradation.
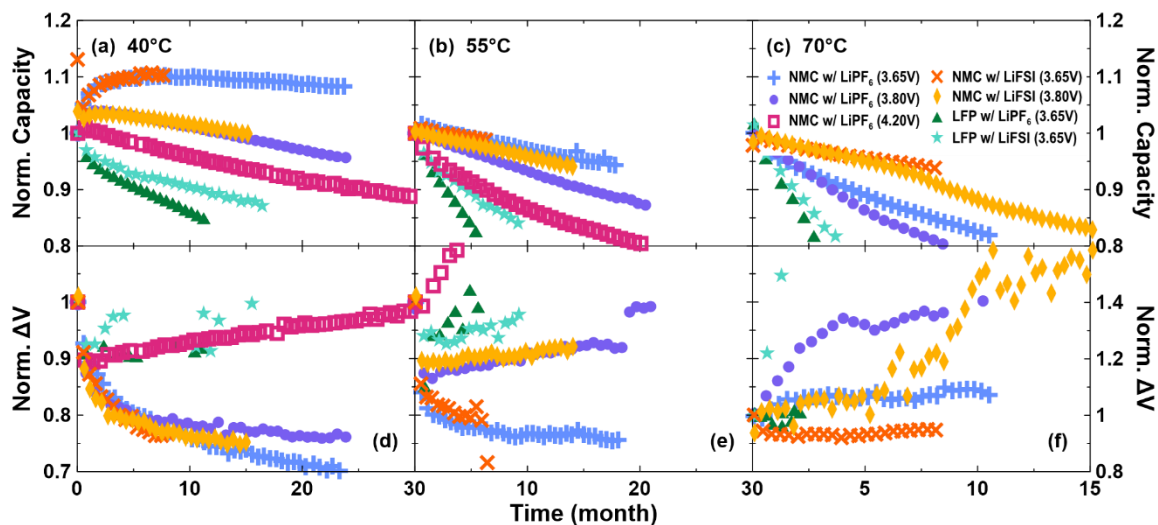
Figure 7.8. (a-c) Discharge capacity and (d-f) ΔV, normalized to respective cycle 5 values, as a function of time for NMC532 and LFP pouch cells. Cycling was performed at a rate of C/3 (except C/2 for low voltage NMC cells that were charged to 3.65 V) with charge endpoint voltage indicated in the legend. Cycling was performed at (a,d) 40°C, (b,e) 55°C or (c,f) 70°C.

Based on the evidence presented thus far, electrolyte containing LiFSI rather than LiPF$_6$ appears to be superior in low voltage NMC cells based on lithium inventory preservation, impedance characteristics and thermal stability. The use of LiFSI does result in higher charge endpoint capacity slippage in UHPC testing as the only possible demerit to its use. This may indicate oxidation or shuttle reactions that may impact long-term performance, but it is unclear if and after how many cycles this will become problematic.

Figure 7.8 shows a comparison of cycling results for low voltage NMC532 cells that charge to 3.65 V and 3.80 V, LFP cells that charge to 3.65 V and conventional built NMC532 cells that charge to 4.20 V. Data is shown for all cell types and charge endpoint voltages with both LiPF$_6$ and LiFSI electrolytes, except for the conventional NMC532 cells that charge to 4.20 V. These cells cannot use an LiFSI electrolyte as they will be susceptible to aluminum corrosion and fatal deterioration of the positive electrode current collector.[140] Data for conventional NMC532 cells does not exist for comparison at 70°C. The capacity and ΔV are plotted as a function of time to account for small differences in cycling rate between cells and because the materials used typically show time dependent capacity loss, not cycle dependent capacity loss. Figure 7.8 shows, at all three test temperatures, NMC cells, regardless of charge endpoint voltage or electrolyte salt show superior capacity retention compared to LFP cells. At both 40°C and 55°C, charging NMC cells to lower voltage limits results in lower rates of capacity fade and impedance growth. This is an expected result as parasitic reactions resulting in inventory loss and/or impedance growth often increase in rate as charge voltage limits increase. The large difference between the NMC cell that charges to 4.20 V and the low voltage NMC cells is that ΔV increase in the cell charged to 4.20 V is considerably larger and likely contributes significantly to the

measured capacity loss. The low voltage cells show no increase, or even up to 20 months of testing, a ΔV decrease, indicating lithium inventory loss as the primary means of capacity fade.

Like the discussion which accompanied Figure 7.3, a comparison of the low voltage NMC cells that contain either $LiPF_6$ or LiFSI, shown in Figure 7.8, shows that capacity retention and ΔV control are super for cells containing LiFSI in all test conditions. This superiority is much more apparent as the charge endpoint voltage increases from 3.65 V to 3.80 V and the test temperature is increased to 70°C. Again, this indicates thermal instability in $LiPF_6$ and/or instability of byproducts of reactions that involve $LiPF_6$, such as the SEI. Nearly all the low voltage NMC cells that charged to 3.65 V, shown in Figure 7.8, have been removed from test before reaching 80% capacity remaining, also denoted as end-of-life. This is due to the belief that trends among cells charged to 3.80 V will be similar and results will be obtained faster due to the higher charge endpoint voltage, and the lower energy density obtained by charging NMC cells to only 3.65 V did not warrant the channel usage. With that in mind, the low voltage NMC cell containing LiFSI electrolyte, charging to 3.80 V at 70°C is the longest-lived Li-ion cell under continuous test at this temperature at the author's institution, at the time of writing. It is likely the cell charged to 3.65 V also containing LiFSI would have exceeded that record eventually had it continued under test. Nevertheless, the results, particularly at high temperatures, demonstrate a particularly impressive lifetime. It should be noted that the cell containing LiFSI and charged to 3.80 V at 70°C shows a distinct change in slope of both capacity retention and ΔV data around 6 months. The source of this change is currently unknown but will be investigated when this cell reaches end-of-life. There has been speculation

throughout that the use of LiFSI may introduce oxidation or shuttling reactions. This observed change in capacity retention and ΔV slopes may signify those reactions finally amounting to a discernable effect.

Figure 7.8 shows that LFP cells experience little-to-no ΔV increase (with the exception of the LFP cell containing LiFSI electrolyte, tested at 70°C, which shows anomalous ΔV due to electrical connection noise) but suffer greater rates of capacity loss than all NMC cells. The use of LiFSI in LFP cells, similar to low voltage NMC cells, shows improved performance, likely due to improved thermal stability and SEI chemistry on the negative electrode.[89] Given that the trends in the lifetime of LFP cells with $LiPF_6$ versus LiFSI salt, along with increasing test temperature align with the trends in lifetime as a function of the same quantities in low voltage NMC cells, suggest a similarity in many of the mechanisms controlling failure in both cells. For instance, both are afflicted to some degree by thermal instability of $LiPF_6$ causing increased capacity fade. This is sensible because lithium inventory loss generally occurs due parasitic reactions at the negative electrode, and these cells have nearly identical negative electrode formulations, down to the same type of artificial graphite sourced from the same supplier. Despite this, the low voltage NMC cells show clear lifetime improvements and lower rates of capacity fade compared to the LFP cells, with the only real difference being the positive electrode. This suggests certain crosstalk, beneficial effects due to NMC usage or harmful effects associated with LFP usage. This chapter is primarily intended to motivate the use of low voltage NMC cells, therefore, the whole of Figure 7.8 and the accompanying discussion to this point should illustrate that they offer both superior lifetime and energy density

compared to LFP cells, and superior lifetime to even conventional NMC cells when tested at high temperatures.

The testing shown in Figure 7.8 is restricted to elevated temperatures relative to ambient. This is largely due to the desire to obtain results in a timely manner and testing at room temperature can often yield cells that take unreasonable amounts of time to resolve differences in lifetime, particularly when excellent Li-ion cells can test continuously for many years.[28] Extrapolating results to ambient temperatures is desirable, due to the number of applications that inherently have devices that operate around ambient, or have thermal controls to maintain the battery temperature close to ambient. As was introduced in Section 3.11, in the absence of impedance growth and cycle-dependent fade mechanisms, a simple equation for modeling the capacity as a function of time can be obtained from assuming a parabolic growth law governs the SEI thickness. This model, given by Equation 3.4, has a physical meaning that is easy to understand and does not introduce large numbers of parameters, particularly those with no physical grounding. Fitting a model to capacity retention data becomes particularly valuable when the model parameters are found to have a physically meaningful connection. In this case, the parameter A, which is the capacity loss rate constant, can follow an Arrhenius temperature dependance if no new failure mechanisms are introduced as the test temperature changes. In this case, it is assumed the same mechanisms are present and occur with rates that increase exponentially as the test temperature increases, as described by Equation 3.9. From the discussion in this paragraph alone, it is hopefully clear that this model has limited applicability and is not tolerant to changing failure mechanisms. The failure of Li-ion cells can be complex and the model in Equation 3.4 has a single adjustable parameter with which to fit data.

Not mentioned in the discussion of Figure 7.8, and not visible due to the number of data points plotted, it is conventional during CCCV cycling to perform occasional cycles at a slower rate, usually C/20. These lower rate cycles are useful to characterize capacity without the influence of impedance. Because the model represented by Equation 3.4 is not intended to handle contributions from increasing impedance during cycling, fitting with just these C/20 cycles is advantageous and well suited for the model. Figure 7.9 shows the adjustable parameter, *A*, obtained from fitting Equation 3.4 to the C/20 cycles from cells for which data is shown in Figure 7.8. This data and the fits are shown in Figures B.7, B.8, B.9 and B.10 in Appendix B. To generally remark on the quality of the fits, most are very reasonable fits, particularly when matching a single parameter model to many thousands of hours of data. That being said, the fits are not perfect, particularly the cell containing LiFSI and charged to 3.80 V at 70°C, which indicates the introduction of some new capacity loss mechanism. This cell was mentioned previously as it contains a slope change to the capacity retention data as a function of time which cannot be treated by this simple model.

It should be mentioned that the fits, shown in Appendix B, could all be improved with the inclusion of a linear term to the model, such as Equation 3.10, as most curves show a considerable amount of linearity, particularly cells containing LiFSI and as the test time becomes long. This suggests a capacity loss mechanism beyond that which is involved with SEI growth. Equation 3.4 shows that the rate of capacity loss due to SEI growth alone eventually asymptotes to zero as test time becomes long. As was discussed in Section 3.11, most justification for a linear term, such as impedance growth and cycle-dependent fade mechanisms, are not relevant to most of the cells shown in Figure 7.9, which predominantly

charge to low voltage and do not experience impedance growth. Without a compelling physical connection to the cells tested, it is difficult to justify the use of Equation 3.10 despite the fact the quality of the fits would certainly improve. For these reasons, the analysis performed here was done with slightly inferior fits of the understandable model in Equation 3.4. Uncertainties on adjustable parameters that come about from mismatches between the model and data at long time were computed as part of the non-linear fitting process and represented graphically in Figures 7.9 and 7.10.
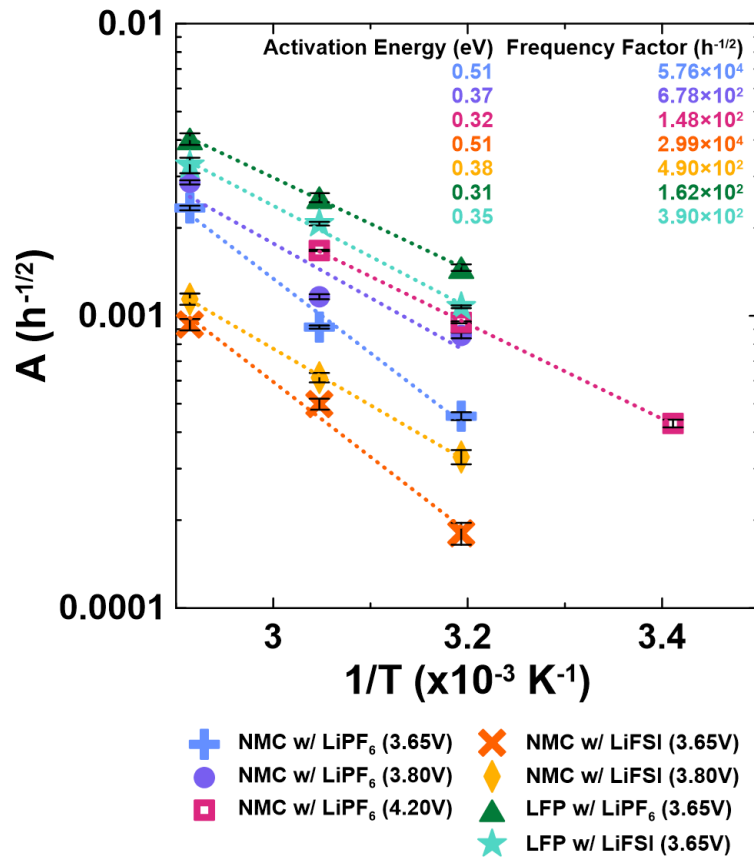
Figure 7.9. Capacity loss rate parameter versus reciprocal temperature obtained for fitting Equation 3.4 to the data shown in Figure 7.8, along with best fit lines. The slope and intercept obtained from the best fit lines are used with Equation 3.9 to ascribe Arrhenius temperature dependence to the capacity loss of each cell type, charge endpoint voltage and electrolyte salt.

Figure 7.9 shows that nearly all cells show approximate linear behavior in the *A* parameter that comes about from fitting Equation 3.4, when plotted on a logarithmic axis versus reciprocal temperature, indicating Arrhenius temperature dependence. Fitting of Equation 3.9 to the data series in Figure 7.9 yields associated frequency factors, also referred to as attempt frequencies and activation energies for the thermally activated capacity loss rates. These two parameters are listed, inset in Figure 7.9. Cells which are near the bottom of Figure 7.9 yield the best lifetime. It is unsurprising therefore that NMC cells are lower than LFP cells in Figure 7.9, cells containing LiFSI are lower than those containing $LiPF_6$ in Figure 7.9 and cells that charge to lower voltage limits, in the case of NMC, are all lower in Figure 7.9. The representation in Figure 7.9 contains no new information over Figure 7.8 and should simply be thought of as a different representation to obtain the activation energies and attempt frequencies listed. The longer-lived cells in Figure 7.9 tend to have a combination of high activation energy and lower attempt frequency. This is interpreted as requiring a large amount of energy to exceed the barrier for a capacity consuming reaction to occur, and fewer attempts to cross this barrier. Some weak ordering is seen in these two parameters in Figure 7.9, but it should be noted that consideration of the parameters together with Equation 3.9 is required to form a comparison of lifetime.

Table 7.1. Values and uncertainties for adjustable parameters obtained by fitting Equation 3.9 to data in Figure 7.9.

Positive Electrode	Charge Endpoint Voltage (V)	Salt	Activation Energy (eV)	Frequency Factor (h^{-1})
NMC532	3.65	$LiPF_6$	0.51 ± 0.04	60000 ± 10000
NMC532	3.80	$LiPF_6$	0.37 ± 0.05	700 ± 200
NMC532	4.20	$LiPF_6$	0.32 ± 0.01	150 ± 40
NMC532	3.65	LiFSI	0.51 ± 0.04	30000 ± 3000
NMC532	3.80	LiFSI	0.38 ± 0.04	500 ± 300
LFP	3.65	$LiPF_6$	0.31 ± 0.02	160 ± 80
LFP	3.65	LiFSI	0.35 ± 0.02	390 ± 90

Combining Equations 3.4 and 3.9 and solving for time yields an equation for the lifetime as a function of the fraction of capacity remaining defined as end of life, activation energy, frequency factor and operating temperature. Inserting the activation energy and frequency factor for each cell type in Figure 7.9 allows the calculation of lifetime as a function of temperature. Figure 7.10 shows the results of this calculation when end-of-life is defined as 80% capacity remaining. The trends discussed throughout remain true here and are demonstrated in Figure 7.10. The cells that have the longest projected lifetime at most temperatures are the low voltage NMC cells that only charge to 3.65 V, then those that charge to 3.80 V. LFP cells are near the bottom of Figure 7.10 and are projected to have the shortest lifetime. Cells containing LiFSI project to have higher lifetime than those that contain $LiPF_6$. Perhaps unexpectedly, Figure 7.10 shows that NMC cells, charged to 4.20 V have slightly better high temperature lifetime than NMC cells that charge to only 3.80 V, when cells containing $LiPF_6$ electrolyte are considered. This can be explained by

the fact that the model used does not capture impedance growth, but NMC cells charged to

4.2 V, operating at 55°C or above would certainly show impedance growth and resulting

loss of measured capacity, as was demonstrated in Figure 7.8. As mentioned previously,

uncertainties from the fitting process were captured and carried forward to the results

shown in Figure 7.10. An upper and lower bound on the lifetime is included in a dashed

line for each cell type. The reader is reminded that Figure 7.10 is plotted on a logarithmic

vertical scale, so the uncertainty range in most cases is quite large. For instance, despite

looking tightly bounded relative to the calculated lifetime, the uncertainty in the prediction

for the cells containing LiFSI that charge to 3.65 V is approximately 300 years at 20°C, or

about 15%. The largest percent uncertainty at 20°C comes about for the cells containing

LiFSI that charge to 3.80 V. The calculated lifetime is approximately 220 years, with an

uncertainty of approximately 160 years, or about 70%.
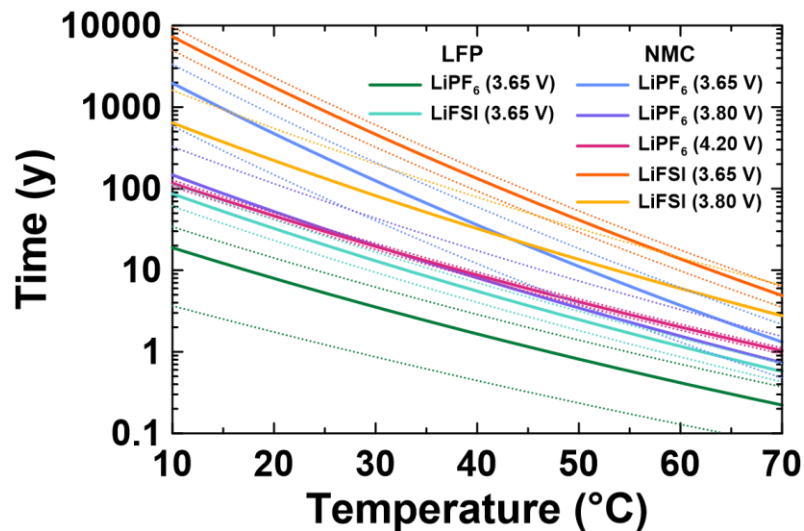
Figure 7.10. Projected lifetime to 80% capacity retention as a function of operating
temperature, in the absence of impedance growth. Projections are made by fitting data in
Figure 7.8 with Equation 3.4 and assuming the capacity loss mechanisms adhere to
Arrhenius temperature dependence. Projections are made for cells based on positive
electrode, charge endpoint voltage and salt type. Dashed lines in matching color indicate
the uncertainty bounds for each lifetime prediction, based on propagating errors on fitted
Arrhenius Law parameters in Equation 3.9.

The most striking result from Figure 7.10 is that low voltage NMC cells that contain LiFSI electrolyte when operated at 20°C and charge to 3.80 V project to live more than 200 years, while LFP cells with LiFSI may last a few decades. These low voltage NMC cells provide higher energy density than LFP cells and can offer 5x lifetime. This represents the possibility for significant improvement to costs over the course of a battery's lifetime via lower levelized cost of energy with a battery that does not require replacement. It also begins to satisfy the lifetime requirements that were discussed in the introduction, that will enable development of a sustainable fleet of global energy storage. It is not a particularly surprising result that lowering the charge endpoint voltage of NMC cells can result in longer lifetime. It is however important to acknowledge how the use of lower voltage cells allows for the use of LiFSI as an electrolyte salt, that enables an even longer lifetime.

7.4 Application of Low Voltage Cells to Alternate Chemistries

Low voltage NMC cells offer an electrochemical window that is compatible with LiFSI, which can experience corrosion problems at high voltage,[140] thereby unlocking the lifetime and impedance control benefits it brings to cells. There are other materials of interest in Li-ion cells that are susceptible to high voltage degradation, and therefore seem natural to use in the low voltage NMC cells demonstrated in this chapter. Additionally, there are results from Section 7.3 than could be leveraged to enable cells superior to conventional designs. This brief section consists of three independent experiments that demonstrate the utility of low voltage NMC cells and proof of concept of topics that warrant much further investigation.

7.4.1 Methyl Acetate in Low Voltage Cells

Methyl acetate (MA) is desirable for use as an electrolyte solvent do to its desirable physical properties that result in electrolytes with high conductivity and low viscosity.[73,184] The use of MA is typically investigated for low temperature or fast charging applications. The use of MA is somewhat problematic in applications that also value lifetime, because it has been shown to be anodically unstable, and its use results in lower lifetime.[75,186] The low voltage NMC cells discussed in this chapter are long-lived compared to conventional NMC cells, plus can receive a larger lifetime enhancement through the use of LiFSI. Lower charge endpoint voltages should reduce the rate of electrolyte oxidation when MA is introduced. Additionally, if the use of MA in low voltage NMC cells is accompanied by a decrease in lifetime, the lifetime of low voltage NMC cells is already so long that some decrease may be tolerable to enable the use of MA.

Low voltage NMC cells and LFP cells were made with electrolytes containing either 1.5M LiPF$_6$ or 1.5M LiFSI, a solvent blend of 20% MA with 80% EC/DMC (3:7), mixed by weight percent of total mixture, and 2% VC electrolyte additive. Cells were prepared and formed following the methods in Chapter 3. Low voltage NMC cells were only charged to 3.80 V, not 3.65 V. Cells were tested at either 20°C, 40°C or 55°C with 1C, C/3 and C/3 cycling rate respectively. Figure 7.11 shows the cycling results from these experiments and includes comparison data from Figure 7.8 for identically constructed cells that do not contain MA. Duplicate cells were constructed but not shown to avoid excessive visual clutter in Figure 7.11.

Figure 7.11. (a-c) Discharge capacity and (d-f) ΔV, normalized to respective cycle 5 values, as a function of cycle number for NMC532 charged to 3.80 V and LFP pouch cells charged to 3.65 V. Cycling was performed at (a,d) a rate of 1C at 20°C, (b,e) a rate of C/3 at 40°C, or (c,f) C/3 at 55°C. Cell type, electrolyte salt, and inclusion of 20% MA indicated in the legend.

Figure 7.11 shows that at 20°C, under high rate 1C charging, the use of MA with LiPF$_6$ in low voltage NMC cells results in sudden failure just before 1000 cycles which is accompanied by symmetric impedance growth. This could simply be impedance growth causing reduced measured capacity, or the precipitous rate of failure might suggest accompaniment by some lithium plating. This is possibly the case given that this sudden failure is only present at 20°C, where ion kinetics are slow. Conversely, the identical low voltage NMC cells that contains LiFSI with MA shows no capacity loss or ΔV growth over the first 2000 cycles of testing at 20°C. This suggests better impedance control properties

and compatibility of LiFSI with MA, compared to $LiPF_6$. The LFP cells containing MA, tested at 20°C show similar performance and no impedance growth, but slightly better capacity retention is obtained using LiFSI rather than $LiPF_6$. These cells show notably worse capacity retention than the low voltage NMC cell that contains LiFSI.

Results at higher temperatures are similar and can generally be discussed together. The trends observed at 55°C are consistent with but more obvious than the trends observed at 40°C. NMC cells show better capacity retention than LFP cells; cells with LiFSI show better capacity retention than those with $LiPF_6$; and cells containing no MA show better capacity retention than those containing MA. In all cases there is little impedance growth. The most remarkable observation however is how similar the capacity retention is, even at 55°C between low voltage NMC cells with and without MA, when they also contain LiFSI. This implies that the electrode passivation in which LiFSI plays role is capable of passivating reactions that involve MA and seems to be problematic when $LiPF_6$ is used. In the same way that low voltage NMC cells enable the use of LiFSI and can achieve long lifetimes, the use of LiFSI in turn seems to enable the use of MA, a solvent with increased reactivity, with far less of a lifetime penalty. The use of MA is just one example of an anodically unstable solvent that seems to be compatible with low voltage NMC cells and LiFSI electrolyte salt. Other examples that could be explored in the future are other alkyl acetates, such as ethyl acetate, or propionates.

7.4.2 Low Voltage Cells with a High Nickel Positive Electrode

Conventional Li-ion cells have seen a trend of using NMC-type positive electrodes with increasing nickel content. Increased nickel content depresses the positive electrode voltage

curve and enables more capacity to be delivered without raising the charge endpoint voltage, and correspondingly increasing the likelihood of effects such as electrolyte oxidation. To optimize cell usage for lifetime however, cells with high nickel NMC-type positive electrodes cannot be charged beyond 4.06 V. This is due to a lattice volume collapse that occurs every cycle when 4.06 V is exceeded, and results in rapid impedance growth and measured capacity loss.[43] When charging is restricted to 4.06 V in NMC811 cells for instance, cycle life is greatly improved.[270] High nickel positive electrodes are naturally compatible with the low voltage cell design presented in this chapter as they will offer more capacity than materials like NMC532, while also operating in an electrochemical window that avoids volume collapse.
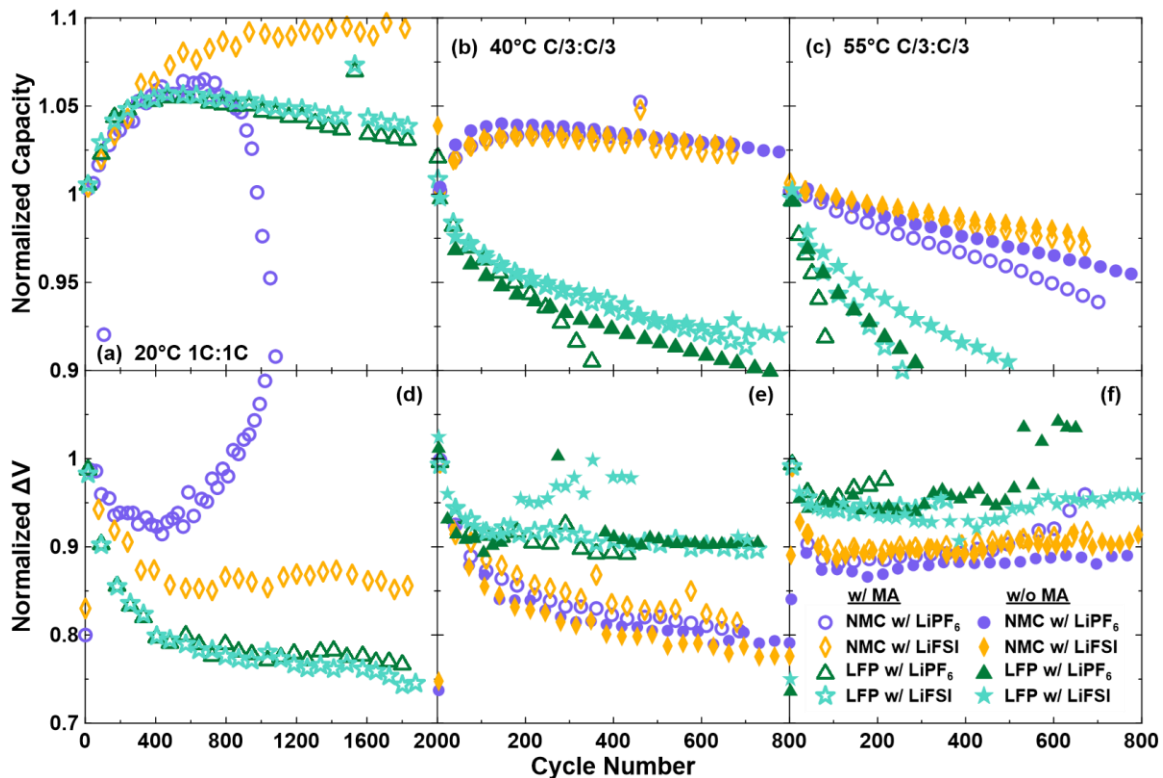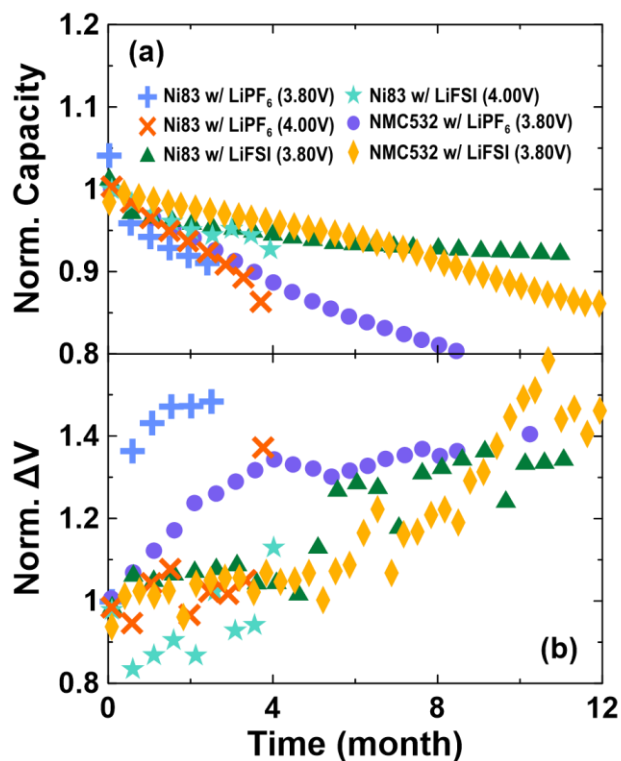

Figure 7.12. (a) Discharge capacity and (b) ΔV, normalized to respective cycle 5 values, as a function of time for NMC532 cells charged to 3.80 V and Ni83 (nominally NMC811) cells charged to either 3.80 V or 4.00V. Cycling was performed at C/3 at 70°C. Cell type, electrolyte salt, and charge endpoint voltage are indicated in the legend.

After the success of the low voltage NMC cells discussed in this chapter, a follow up cell build was requested from LiFUN Technology. The details of these cells are listed in Appendix A, but the most relevant details are a high nickel positive electrode was used and only enough graphite was included to allow for charging to 4.06 V without lithium plating. The increased charging limit of the cells was designed to increase the energy density even further while still restricting operation to voltages below conventional cells to enable long lifetime and the usage of LiFSI. The positive electrode material is nominally considered to be an NMC811, although the composition is slightly different from perfect NMC811, as it contains 83% Ni, rather than exactly 80%, by atomic percent of transition metals. These cells are referred to as Ni83 cells. Cells were prepared following the methods in Chapter 3, identically to the low voltage NMC532 cells mentioned previously in Sections 7.2 and 7.3. They contained electrolytes with either 1.5M $LiPF_6$ or 1.5M LiFSI, dissolved in EC/DMC (3:7) with 2% VC. Experiments were conducted at 40°C, 55°C and 70°C, but for brevity, only results from testing at 70°C are shown and discussed here.

Figure 7.12 shows a summary of the cycling results from these low voltage Ni83 cells, with data from NMC532 cells found in Figure 7.8 shown for comparison. Again, charging to higher voltage results in worse capacity retention and cells containing $LiPF_6$ show greater fade than cells containing LiFSI. The Ni83 cell that charges to 3.80 V and contains $LiPF_6$ shows anomalously low capacity and high ΔV growth and performs worse than its counterpart that charges to 4.00 V. Results for this cell are included for completeness but are believed to be unreliable. It appears that Ni83 cells have greater fade earlier in testing than NMC532 cells, but this eventually levels off. After 11 months of testing the Ni83 cell that charged to 3.80 V and contains LiFSI has the most capacity

remaining of all cells tested and is showing much more stable cycling than the equivalent NMC532 cell. Other than the cell mentioned with anomalous results, all cells show a similar ΔV increase and there are no clear advantages to a particular test condition or cell formulation. This result shows that the benefits of low voltage charging and LiFSI electrolyte carry over to high nickel systems and can produce longevity that exceeds NMC532 cells.

7.4.3 Blended Positive Electrode Cells

The comparison of low voltage NMC cells to LFP throughout Section 7.3 is particularly well made due to the fact that both cell types contain nearly identical negative electrode materials from the same manufacturer. The majority of the capacity loss was thought to be due to lithium inventory loss on the negative electrode, yet the choice of positive electrode, specifically NMC versus LFP, resulted in vastly different high temperature lifetime. It is logical to conclude that the graphite negative electrode receives a performance boost by being paired with an NMC positive electrode, compared to an LFP positive electrode. If this is true, it stands to reason a cell constructed with a blended positive electrode made mostly from LFP could retain the low cost and excellent safety of LFP, with a small amount of NMC to improve the performance of the graphite negative electrode and the cell as a whole.
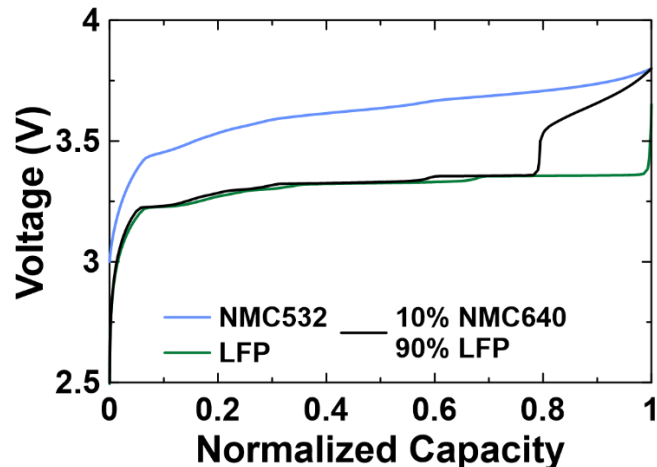
Figure 7.13. Charge voltage-capacity curves of low voltage NMC532, LFP and blended 10% NMC640 + 90% LFP (by weight) cells.

After the success of the low voltage NMC cells discussed in this chapter, another follow-up cell build was requested from LiFUN Technology. These cells contained positive electrodes where the active material was 90% LFP and 10% NMC640, by weight. NMC640 was selected as a material that has modest amounts of nickel and no cobalt and is therefore low cost as far as NMC-type materials are concerned. This was chosen to be complementary to the already low cost of LFP positive electrodes, while hopefully providing similar performance to NMC532. Cells were balanced for charging to 3.80 V. Cells were prepared following the methods in Chapter 3, identically to the low voltage NMC532 cells mentioned previously in Sections 7.2 and 7.3. They contained electrolytes with either 1.5M $LiPF_6$ or 1.5M LiFSI, dissolved in EC/DMC (3:7) with 2% VC. Experiments were conducted at 70°C and a cycling rate of C/3. Figure 7.13 shows a representative voltage curve from these cells, with a low voltage NMC532 cell and an LFP cell curve for comparison. The positive electrode materials in the blended cell are uniformly physically mixed. The materials are delithiated in entirely separate voltage

ranges, and therefore the voltage profile and accompanying capacity are easily distinguishable. Because NMC materials are more energy dense than LFP, 10% NMC640 by weight is responsible for approximately 20% of the capacity when charging is limited to 3.80 V.

Figure 7.14 shows cycling results for these cells with NMC532 and LFP cells from Figure 7.8 included for comparison. Figure 7.14a shows capacity as a function of time for the full electrochemical cycling window of each cell. The LFP cells show the fastest rate of capacity loss, followed by the NMC532 cell that contained $LiPF_6$. The NMC640 + LFP cell containing $LiPF_6$ shows better capacity retention than the NMC532 cell. It is difficult to confirm concepts like synergy between NMC and LFP when used together in the same cell in the presence of $LiPF_6$ electrolyte, largely due to the difference in NMC materials used. Nevertheless, it is an incredible result that a cell with a positive electrode that is predominantly LFP can have better capacity retention than a cell with an NMC positive electrode, at 70°C using an $LiPF_6$ electrolyte. The NMC640 + LFP cell containing LiFSI electrolyte shows slightly better capacity retention than its $LiPF_6$ counterpart. The NMC532 cell containing LiFSI still shows vastly superior capacity retention to all other cells at 70°C.
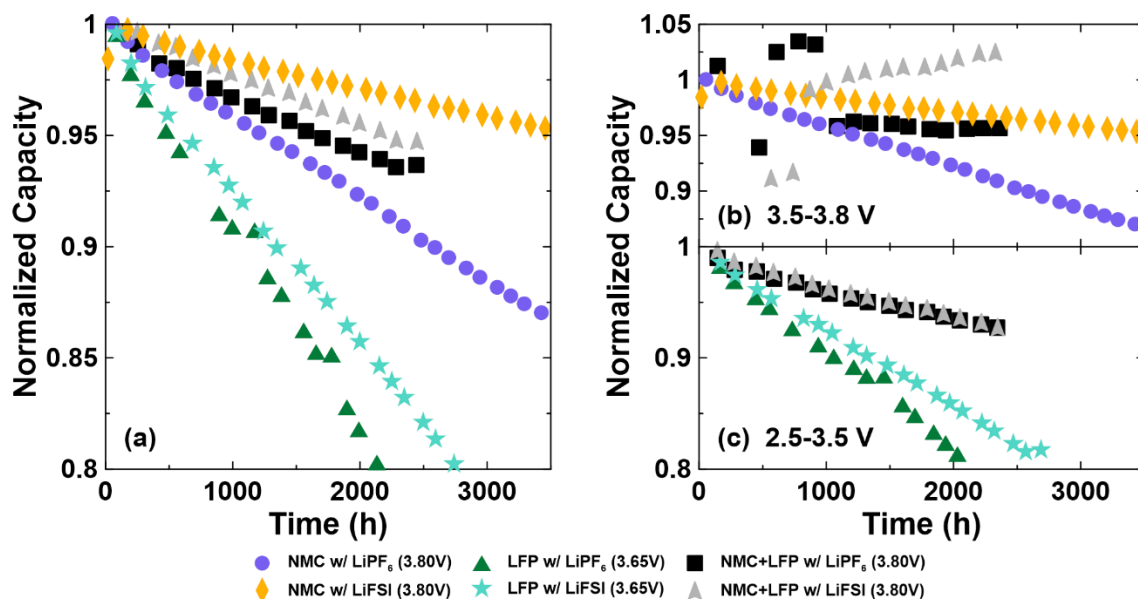
Figure 7.14. Discharge capacity, normalized to 1 at its cycle 5 value, as a function of time for NMC532 charged to 3.80 V, LFP cells charged to 3.65 V and blended positive electrode NMC640 + LFP cells charged to 3.80 V. Cycling was performed at C/3 at 70°C. Cell type, electrolyte salt, and charge endpoint voltage are indicated in the legend. (a) Capacity characterized over the full electrochemical window. Capacity delivered (a) below and (b) above 3.5 V, respectively indicating capacity exclusively from LFP and NMC materials.

Figures 7.14b and 7.14c show the discharge capacity sorted by the contributions above and below 3.5 V, indicating capacity from NMC and LFP respectively. The results from the NMC640 in the blended positive electrode cells, in Figure 7.14b have considerable noise, particularly at the beginning of life, but show very low rates of capacity fade after 1000 h, once the data stabilizes. More impressively, Figure 7.14c shows that the inclusion of NMC640 in the blended positive electrode cells cause the LFP to cycle much more reversibly, with much less fractional fade compared to cells that just contain LFP. The LFP in the blended positive electrode cells also shows excellent performance when LiPF$_6$ is used. The details of the interaction between a heterogeneously blended positive electrode and electrolyte are likely very complex. The results in Figure 7.14 show there is

some credibility to the idea that NMC improves graphite performance and inclusion of some NMC in LFP cells may provide enhanced cycle life. This warrants considerable future work to explore and optimize.

7.5 Constant Capacity Charging for Usage Beyond End of Life

The low voltage NMC cells presented in Section 7.3 and particularly those undergoing long-term testing demonstrated extremely long lifetime potential, with nearly all cells currently still cycling at the time of writing. Re-examining Figure 7.8 shows one cell reached the threshold of 80% capacity remaining, which is deemed end-of-life. This cell contained $LiPF_6$, was charged to 3.80 V and tested at 70°C. All subsequent discussion pertains to this single cell. To characterize the cell at the end-of-life, it was transferred to a UHPC system to complete a cycle at C/40 cycle at 40°C. Data from this cycle was used to complete differential voltage or dV/dQ analysis, which was compared to dV/dQ analysis performed on similar cells at earlier points in life.

Figure 7.15 shows differential voltage analysis results for cells containing $LiPF_6$ electrolyte, charging to 3.80 V and testing at 70°C, after different amounts of time under test. Figures 7.15a, 7.15 b and 7.15c show voltage curves indicating alignment between the positive and negative electrode. The most obvious feature of these three panels is the increasing amount of shift loss and the positive and negative electrode become increasingly misaligned as the amount of time under test increases. This indicates continuous lithium inventory loss which was previously mentioned in Section 7.3. Figure 7.15d shows a

summary of dV/dQ fitting parameters as a function of time and captures details that are not immediately obvious in the voltage curves but become clear when cross referenced with Figure 7.15d. There is a small but measurable amount of positive electrode active mass loss in the first 3000 h of cycling, but very little further after that time. This would have a small contribution to the capacity loss measured in a constant voltage window, such as for this cell in Figure 7.8 when undergoing CCCV cycling, but the predominant mode of capacity loss is still shift loss, also referred to as slippage.

Figure 7.15d also shows a nearly constant rate of negative electrode mass loss. Negative electrode mass loss is practically unheard of in cells that use a high-quality artificial graphite negative electrode, such as those used in the cells discussed throughout this thesis. This may be an effect of cycling at 70°C for long duration, which is a relatively unstudied topic. It is possible that graphite particles undergo damage during high temperature lithium insertion and extraction, or the binder degrades at high temperature. The origin of this negative electrode mass loss is speculation without further work to elucidate it. This mass loss does not immediately contribute to capacity loss, but if the cell were to continue cycling, eventually there would be insufficient graphite to store the desired amount of capacity. This would result in the excess capacity unable to be stored by the graphite being plated as metallic lithium, which typically results in accelerated cell failure.
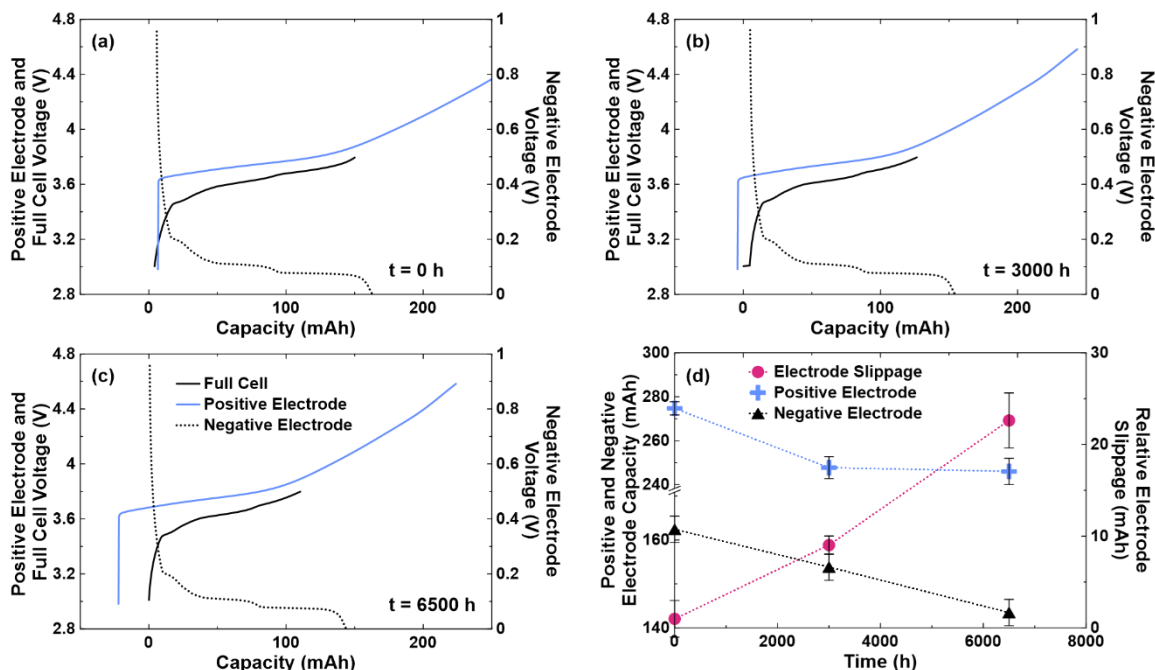
Figure 7.15. Electrode and full cell voltage curves for low voltage NMC cells cycling at C/3 and 70°C, with charging to 3.80 V. Voltage curves are shown for a cell at (a) beginning of life, (b) 3000 h under test and (c) 6500 h under test, as determined by dV/dQ analysis. (d) Summary of electrode capacities and relative electrode slippage, or shift loss, obtained through the previously mentioned dV/dQ analysis. dV/dQ analysis was performed on data for a C/40 cycle that was completed at 40 °C.

A final observation that can be made from examination of Figure 7.15c is that after 6500 h of testing, when the cell has reached 80% of its original capacity, charging to a voltage limit of 3.80 V results in nearly 40% of the capacity in the positive electrode remaining unused. The full cell voltage curve sweeps out a capacity of 105 mAh, however, there is accessible capacity in the positive electrode all the way to 225 mAh. To access this would necessitate charging beyond 3.9 V vs Li$^+$/Li. It is expected if the cell were returned to the charger to continue undergoing CCCV cycling, with charging limited to 3.80 V, shift loss, or slippage, would continue to occur and the measured capacity would continue to decrease. If the limit on charging was removed, the extra capacity in the positive electrode could be accessed as a lithium reservoir, by charging to higher voltage, as a means of

counteracting the ongoing capacity loss to electrode slippage. To achieve this with programmed voltage limits would require knowledge of the rate of slippage and continually adjusting the voltage limit based on the shape of the voltage curve. This is cumbersome and impractical to implement. A simple alternative is to program the cell to charge until a constant capacity (CQ) is stored, regardless of the voltage required to reach that capacity. In this mode, the rate of shift loss and the shape of the voltage curve at the end of charge control how much the charge endpoint voltage increases each cycle without any *a priori* knowledge of this information or continuous intervention with charger programming. Implementing testing with CQ charging in this manner can be thought of as a means of extending the service life of a low voltage NMC cell beyond the traditional definition of end-of-life.

Consistent with the previous discussion, after reaching 80% capacity retention and completing UHPC cycling for differential voltage analysis, the cell was returned to testing at 70°C. The cycling protocol implemented utilized constant capacity charging, with the charge capacity programmed to be 80% of the beginning of life capacity, or the final capacity measured during CCCV testing (105 mAh). NMC532 cells have been shown in this thesis to operate with acceptable performance even when charged to 4.4 V. A more conventional limit, particularly suited for excellent lifetime at high temperature would be 4.3 V[28]. In the implementation of testing with CQ charging, it is therefore reasonable to expect the low voltage NMC cells to perform acceptably until the charge endpoint voltage reaches 4.3 V. This limit was chosen to define end of life when using CQ charging.
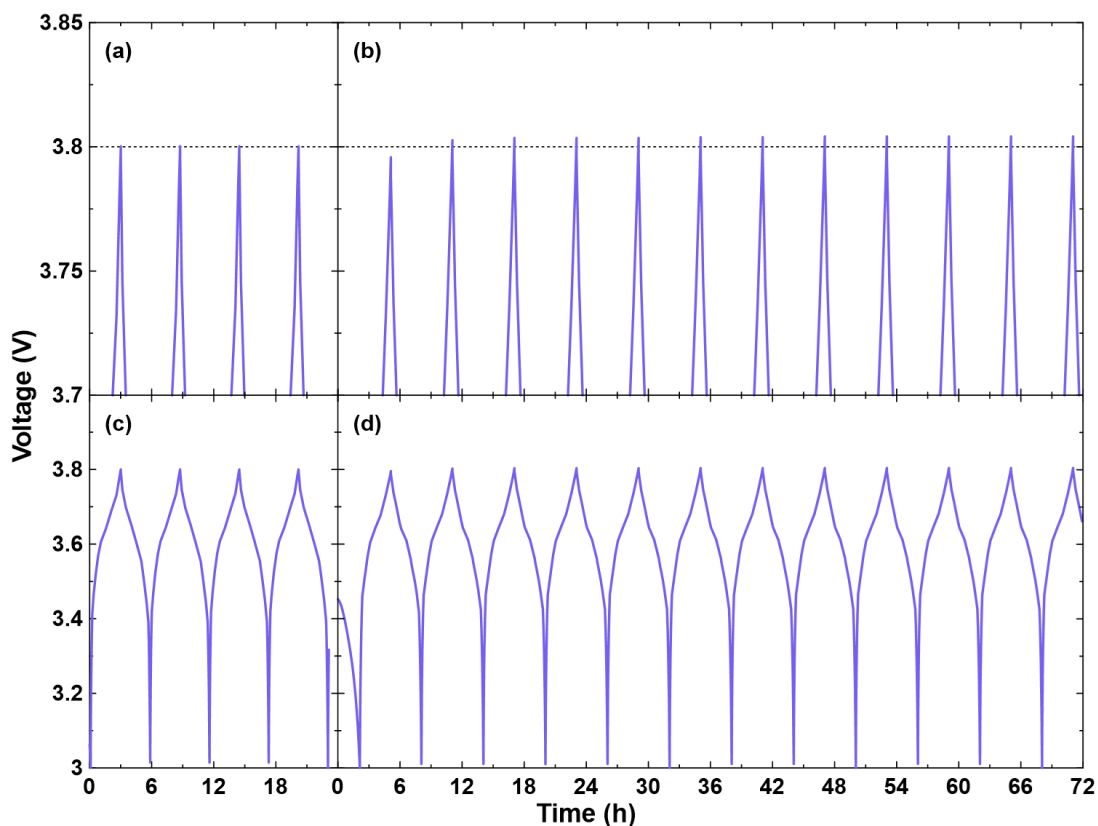
Figure 7.16. Representative cycling profiles for a low voltage NMC cell cycling at C/3 and 70°C with (a, c) charging and discharging between constant voltage limits of 3.0 V and 3.80 V respectively, or (b, d) charging with a constant capacity limit of 105 mAh and discharging with to a constant voltage limit of 3.0 V. Panels (a) and (b) show the same data as panels (c) and (d), but have an expanded y-axis scale. A horizontal dashed line is set at 3.8 V in panels (a) and (b) to assist the reader in resolving small changes in charge endpoint voltage.

Figure 7.16 shows the voltage profiles as a function of time for both CCCV cycling and cycling with CQ charging. Figures 7.16a and 7.16b highlight data between 3.70 V and 3.85 V, and show that during CCCV cycling, charging is terminated when the voltage reaches 3.80 V. During cycling with CQ charging, the charge terminates at a voltage higher than 3.80 V and this value increases by a tiny amount every cycle as the positive electrode reservoir is accessed to counteract shift loss. The increase in charge endpoint voltage beyond 3.80 V also has a small contribution from polarization because there is no constant

voltage step with CQ charging, like there is with a CCCV charge. It is expected that as the cell is exposed to increasingly higher charge endpoint voltage, the rate of parasitic reactions and impedance growth will increase. This will increase the rate of slippage and the effects of polarization, causing the rate of charge endpoint voltage increase to accelerate.

Figure 7.17 shows the discharge capacity, charge endpoint voltage and ΔV as a function of time for the cell during both CCCV and CQ testing regimes. While the cell is charged to a limit of 3.80 V, during CCCV cycling, capacity fade is observed due to lithium inventory loss. This capacity fade is not observed once the switch to CQ charging occurs, as the positive electrode lithium reservoir is accessed to offset the inventory loss. The discharge capacity is the product of the charge capacity and coulombic efficiency. Because the cell is sufficiently mature, both quantities are constant, and therefore a constant discharge capacity is delivered. This is appealing from the perspective of a device manager because the capacity delivery of a cell extending its useful life using CQ charging is more reliable than an aging cell experiencing diminishing capacity operating with conventional CCCV charging. A small number of points offset from the main group of points in Figure 7.17a indicate capacity measured during a low rate, C/20 cycle between constant voltage limits. The cycles were conducted periodically during CCCV and CQ cycling and follow a consistent trajectory in Figure 7.17a. This shows that after the switch to CQ charging is made, shift loss continues to occur at approximately the same rate.
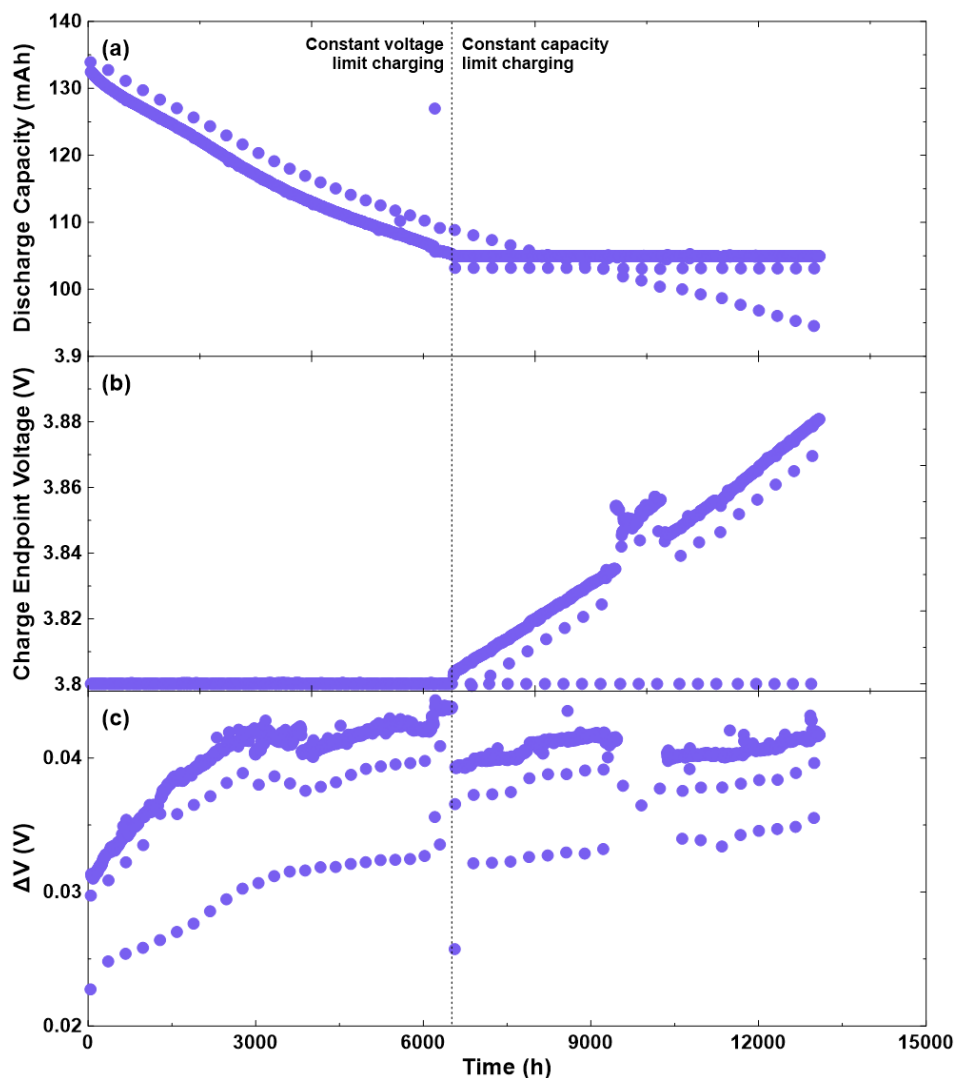
Figure 7.17. (a) Discharge capacity, (b) charge endpoint voltage, and (c) ΔV as a function of time for a low voltage NMC cell cycling at C/3 at 70°C. Cycling protocol transitions from charging between constant voltage limits, or CCCV charging, to constant capacity charging after 6500 h of testing.

Figure 7.17b shows the charge endpoint voltage as a function of time. Once CQ charging starts, the charge endpoint voltage increases as the positive electrode lithium reservoir is continually accessed to a greater amount. The increase is initially very linear, however after approximately 11000 h of total test time, the charge endpoint voltage trajectory does begin to accelerate upward as was previously expected. Finally, Figure 7.17c shows that after an initial increase during the CCCV charging regime, ΔV remains

relatively constant and stable. This is not expected to persist, as higher charging voltages will eventually cause impedance growth.

The charge endpoint voltage increase shown in Figure 7.17b shows largely linear behaviour as a function of time, with some indication of the beginning of deviation from linear behaviour. With a novel charging mode and no knowledge of the failure mechanisms, it is only possible to make naïve predictions about when this cell will reach end-of-life, or when the charge endpoint voltage of reaches 4.3 V. Two possible approaches are to apply either a linear fit or an exponential fit. The former matches the qualitative behaviour of the data for most of the CQ charging regime, while the former matches simple understanding common to many processes. It is expected that as the charge endpoint voltage increases, the rate of parasitic reactions and impedance growth will increase. This will necessitate greater access of capacity from the positive electrode lithium reservoir and increase the contribution of polarization, both in turn increasing the charge endpoint voltage. It is qualitatively reasonable to therefore consider the case where the rate of increase is proportional to charge endpoint voltage itself, given by

$$\frac{dV_{ch}}{dt} = AV_{ch}$$

(7.1)

where V_{ch} is the charge endpoint voltage, A is a constant, and t is the time. The solution to Equation 7.1 is an exponential growth function in time and is common to many processes with positive feedback. Neither this model nor the linear one is claimed to have any basis in first principles or the mechanistic processes governing the cell performance.
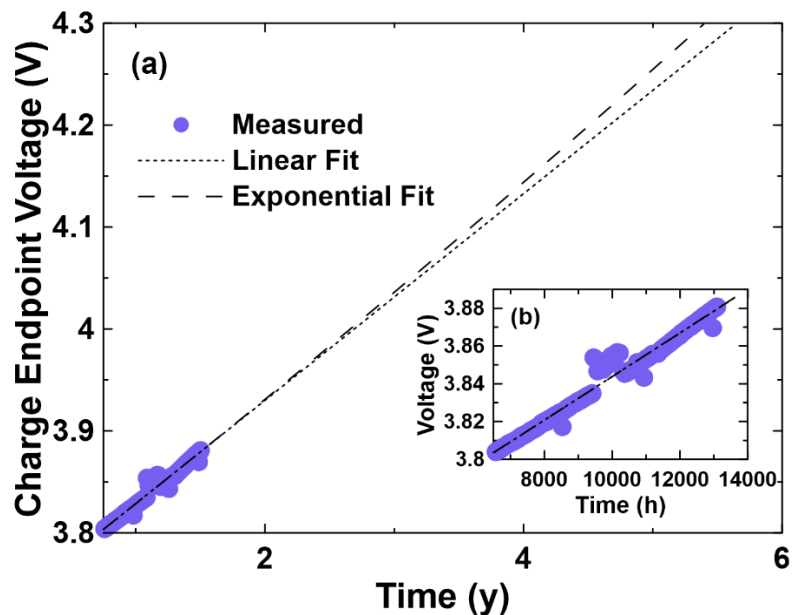
Figure 7.18. (a) Lifetime projection based on the data presented in Figure 7.17. Simple, naïve linear and exponential growth models are fit to the charge endpoint voltage measured during constant capacity charging. It is assumed that NMC532 cells can operate reasonably until the charge endpoint voltage reaches 4.3 V. (b) The insert panel shows a comparison of the fits to the measured data on expanded scales.

Figure 7.18 replots the charge endpoint voltage data in Figure 7.17b an includes both a simple linear and an exponential growth fit to the CQ data. It is clear from the representation in Figure 7.18b that the charge endpoint voltage data is initially rather linear and then starts to accelerate upward. Therefore, neither a linear nor an exponential function alone capture the behaviour perfectly. As more data is collected, it may be useful to fit with the sum of linear and exponential functions. Nevertheless, the projections imply a total lifetime at 70°C of beyond 5 years, and the data collected thus far has shown that CQ charging has already doubled the lifetime of this cell beyond traditional definition of end-of-life in CCCV testing. It is expected that the charge endpoint voltage trajectory will continue to accelerate upward, therefore the predictions here should be thought of as upper bounds on lifetime that will almost certainly not be achieved.

There are other reasons to expect the predictions made in Figure 7.18 are upper bounds on lifetime that may not be achieved in practice. Reexamining Figure 7.15, the average rate of slippage or shift loss is 3.75 mAh per 1000 h of cycling. Figure 7.15 also shows that after 6500 h of testing, the positive electrode has a lithium reservoir of 82 mAh up to a voltage limit of 4.4 V vs Li^+/Li. Assuming the average rate of shift loss, the positive electrode reservoir should be consumed during CQ charging after 22000 h. When including 6500 h of CCCV testing, this would result in a total lifetime of approximately 3.3 years, less than the ~5 years predicted in Figure 7.18. Figure 7.15d shows that the negative electrode capacity decreased by 20 mAh in 6500 h due to active mass loss. The negative electrode must be able to accommodate the constant capacity setpoint of 105 mAh, otherwise lithium plating will occur. Assuming the average rate of negative electrode capacity loss, lithium plating is projected to occur in a total time under test of 19500 h, or failure due to lithium plating after 2.2 years. Finally, it is normally assumed that consumption of lithium inventory on the negative electrode is due to reactions of the charged electrode and electrolyte. These cells contain approximately 0.5 g or 5.5 mol of electrolyte solvent, where an average solvent molar mass of 90 g/mol is assumed. In a one electron process, the rate of shift loss of 3.75 mAh per 1000 h corresponds to 0.14 mmol of solvent consumed per 1000 h. This is equivalent to almost 25% of the electrolyte in the cell annually. It is possible for cells to experience "dry-out", where there is insufficient electrolyte to make electrochemical contact with all active particles.[271] It is unclear at which threshold "dry-out" causes capacity loss, but it is quite possible it may be a limiting factor in the lifetime of these cells. Implementation in real cells may require adjusted electrolyte volumes to avoid this failure mode.

7.6 Conclusions

A novel cell design, with NMC532 cells balanced for low voltage operation with only enough graphite for charging to 3.80 V, was demonstrated to have volumetric energy density superior to LFP cells and extremely long lifetime potential, particularly at high voltage. These cells were shown to lose capacity due to lithium inventory loss due to reactions and the negative electrode, and yet outperform LFP cells with nearly identical negative electrodes, indicating a confounding role of the positive electrode, even at low voltage operation. In addition to improved lifetime due to a smaller electrochemical window, the low charging limits are compatible with the use of LiFSI as an electrolyte salt which reduces rates of lithium inventory loss and impedance growth even more and is an advantage unavailable to conventionally balanced NMC cells. This combination of low voltage NMC cells utilizing LiFSI electrolyte has demonstrated 1.25 years of continuous testing at 70°C at the time of writing and is continuing to cycle.

The low electrochemical window inherent to these cells and the extra stability offered by LiFSI show excellent compatibility with MA-containing electrolytes. The use of LiFSI electrolytes containing 20% MA results in performance far better than equivalent electrolytes with $LiPF_6$ and diminishes the lifetime penalty associated with the use of MA, compared to MA-free electrolytes. In general, this identifies opportunity for these cells in fast charge applications and as a cell design that can enable anodically unstable electrolyte materials.

This cell design was also shown to be compatible with high nickel positive electrodes that suffer high voltage degradation and offer more energy in a low voltage

electrochemical window than low voltage cells with an NMC532. An NMC811 cell, containing LiFSI electrolyte that was charged to 3.80 V was shown to have superior cycle life to the original low voltage NMC532 cells at 70°C. This represents a demonstration that material improvements optimizations can be made to these cells that both increase energy density and lifetime, which should inspire future work.

The vastly superior performance of NMC cells to LFP cells, even when charged to similar voltages, with similar graphite utilization and nearly identical negative electrodes strongly suggests that the positive electrode contributes to the parasitic reactions occurring at the negative electrode in some way. When 10% NMC640 was mixed into an LFP electrode, the cycling of capacity in the lower voltage, LFP electrochemical window was significantly improved compared to cells with pure LFP electrodes. This is a very important benefit of NMC positive electrodes and opens the door for considerable amounts of work on new olivine electrodes with the inclusion of small amounts of NMC, almost as performance enhancing dopants.

Lastly, a novel charging mode was described that utilizes low voltage cells and allows them to operate beyond traditional definitions of end-of-life. Once reaching traditional end-of-life, a cell was charged with constant capacity in a method that self-regulates the increase of the charge endpoint voltage to access additional capacity in the positive reservoir. In this constant capacity charging mode, the positive electrode was shown to have excess capacity that can serve as a lithium reservoir which can be accessed at increasing charge endpoint voltage to counteract the effects of lithium inventory loss. This method was shown to already double the lifetime of a cell tested at 70°C, and projects to continue for at least another year.

The true merit of the work in this chapter is that these cells enable the use of LiFSI and that it provides a host of benefits. Much of Li-ion research, particularly electrolyte development, involves taking an existing cell design and testing electrolytes until one is found that works well. This chapter perhaps identifies a necessary paradigm shift for some applications where a cell design is altered to accommodate the use of an incredible electrolyte component. The use of LiFSI can likely offer lifetime benefits in many systems, but requires measures, such as sacrificing some energy density, to avoid corrosion problems. Finally, all of the work discussed came about from cells that were originally designed for an entirely different purpose, where cells were designed to charge 3.80 V during which graphite was lithiated, and intentionally charging further resulted in plated lithium on top of the lithiated graphite.[263] These cells had been abandoned after that original study was completed. The content of this chapter is entirely different from that original purpose, and hopefully shows that sometimes the genesis of interesting results and experiments isn't thorough and detailed planning.

CHAPTER 8 CONCLUSIONS

8.1 Conclusion

The work presented in this thesis was introduced and motivated in Chapter 1 by connecting

increasing the lifetime of batteries with the necessity of increasing deployed energy storage

to serve various renewable energy generation technologies. A variety of Li-ion cells were

studied, with NMC532 and NMC640 cells at high voltage, LFP at both relatively low and

high voltage, and finally novel, low voltage NMC532 cells at low voltages. Among all

these cells, electrolyte variations, principally salt and additive types, and concentrations,

were studied in an effort to achieve improved lifetime.
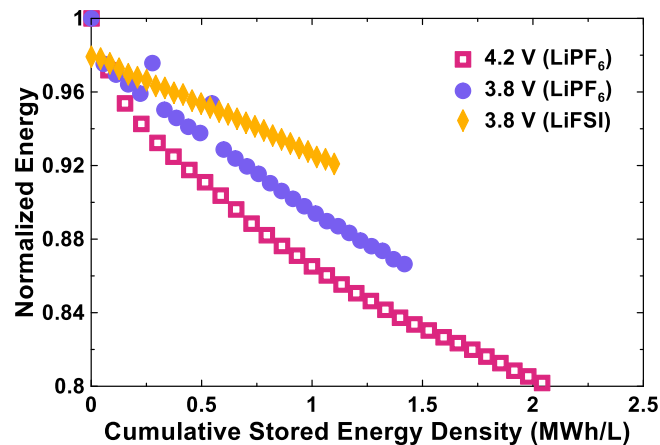
Figure 8.1. The energy, normalized to 1 at beginning-of-life, as a function of the cumulative stored energy density for NMC532 cells, cycled at a rate of C/3 at 55°C. Charge endpoint voltage and electrolyte salt are indicated in the legend.

Figure 8.1 shows the energy retention as a function of the cumulative stored energy

density for a selection of NMC 532 cells, with data taken from Figure 7.8. Note that these

results do not capture extended lifetime by way of constant capacity charging methods.

The horizontal axis quantity is a proxy for the cycle number that attempts to account for difference in cell energy density. The position on the horizontal axis when energy retention reaches 80% is a measure of the energy cumulatively stored, per unit volume, over the life of a cell. Figure 8.1 shows that cells that charge to lower voltage and use LiFSI project to store vastly more lifetime energy by the time they reach greater energy retention. In other words, making cell design choices that increase the lifetime of cells can yield greater energy throughput over the lifetime of the cell, compared to a more energy dense cell that fails faster, and hopefully illustrates the merit of long-lived cells which guided this entire thesis.

In Chapter 4, a description was given of the cycling of NMC532/graphite cells, utilizing protocols that included extended duration at high voltage, using both 24 h open-circuit or constant voltage (referred to as cycle-hold testing) periods that were implemented every second charge. The latter was shown to increase the rate of capacity loss and ΔV growth compared to the former, along with increasing the charge endpoint voltage. Cells tested in the manner with different electrolyte concentrations of $LiPF_6$ showed a negative correlation of the rates of both measured capacity loss and ΔV growth with the $LiPF_6$ concentration. Symmetric cell analysis showed capacity loss was largely due to positive electrode impedance growth, which was accompanied with Mn dissolution from the positive electrode, which both occur with increasing average rate as the $LiPF_6$ concentration in the electrolyte is decreased. Microcalorimetry and UHPC techniques showed very little evidence of parasitic reactions that vary as a function of $LiPF_6$ concentration and a lithium inventory that is mostly intact after cells reach approximately 80% of their original capacity. The use of electrolyte with lower cyclic carbonate

concentration and LiBF$_4$ rather than LiPF$_6$ was shown to yield extended cycle-life in cells subjected to cycle-hold testing. Certain additives combinations, particularly those containing PES, LFO and LiDFDOP showed excellent cycle life as well. Finally testing at lower temperature was shown to yield significantly longer cycle-life. Electrolyte mediated Mn dissolution and growth of a resistive, rock salt surface phase on the positive electrode particles was proposed as a possible mechanism for the behavior of cells described in Chapter 4.

Chapter 5 presented a survey of different electrolyte additives in NMC640/graphite cells that were charged to 4.3 V, 4.4 V or 4.5 V, at 20°C, 40°C, or 55°C. The work in Chapter 5 was designed to implement some of the better additive combinations from Chapter 4 in Co-free cells that require charging to high voltage to achieve competitive energy density to contemporary Li-ion cells. The cycling experiments in this chapter were implemented with conventional CCCV methods and cells containing typical electrolyte salt concentrations. The hope is that the experimental design is familiar to the broader Li-ion research community, easy to interpret and the results are a useful piece in encouraging the widespread adoption of Co-free positive electrodes. It was shown that cell failure was primarily due to a combination of positive electrode mass loss and impedance growth, which suggests that cycle life could be improved through more structurally robust electrode materials. This may come about from improved particle morphology via optimized synthesis conditions or dopants to the bulk material. These rates of failure increased as the charge endpoint voltage and the testing temperature were increased. Electrolyte additives were shown to have a role in improving cycle-life, despite the cell failure predominantly being due to positive electrode material issues. Different additive formulations resulted in

superior cycle-life depending on test condition, but in an analysis of cells cycled at 40°C and charged to 4.4 V (similar to the conditions in Chapter 4), cells containing 2% FEC + 2% LiDFDOP, 2% PES + 1% LFO + 1% TAP and 2% LiDFDOP + 1% LFO were considered to rank the best according to an eight-factor figure of merit. Cells that were charged to only 4.3 V and tested at 20°C showed cycle-life in excess of 5000 cycles, which indicates that these cells could very well be suitable for use in ambient temperature applications which require long lifetime and low-cost cells, that offer good but not ultra-high energy density.

In Chapter 6, experiments and results analogous to Chapter 4 were described. LFP/graphite cells were tested using cycle-hold methods with charging to 3.7 V, which is conventional for LFP cells, and to 4.4 V, which is extremely high for LFP cells, but comparable to the NMC532 cells described in Chapter 4. Cells with different $LiPF_6$ concentrations were constructed but showed positive correlation between the rate of capacity loss with $LiPF_6$ concentration. Little-to-no impedance growth was measured, and the rate of Fe dissolution was correlated with increasing $LiPF_6$ concentration. UHPC techniques indicated lithium inventory consumption at the negative electrode as the primary failure mode. A mechanism of capacity loss was suggested which involved the hydrolysis of $LiPF_6$ to form HF, which could attack the positive electrode, yielding dissolved iron which migrates the negative electrode and causes SEI damage. The behavior of LFP cells tested with cycle-hold methods as a function of $LiPF_6$ concentration is distinctly different than NMC cells tested similarly and suggest entirely different failure mechanisms. The use of LiFSI rather than $LiPF_6$ appears to eliminate the positive correlation between the rate of capacity loss and salt concentration. Despite improved

performance with LiFSI, LFP cells containing LiPF$_6$ or LiFSI show much worse cycle-life than low voltage NMC532 similarly tested with cycle-hold methods. The use of low LiPF$_6$ concentrations or alternate salts like LiFSI is encouraged in all LFP cells that require long lifetime, particularly those that spend considerable time at full state-of-charge or are at risk of regular overcharge, but considerable work remains until NMC-like lifetime is obtained.

Finally, Chapter 7 details the use of a novel cell design, where NMC532 cells are constructed with only enough graphite to enable charging to only 3.8 V, which is comparable to LFP cells. Cells were tested at elevated temperatures of 40°C, 55°C and 70°C. Such cells were shown to have vastly superior lifetime to both LFP cells and conventionally designed NMC532 cells that charge to higher voltage. Like in Chapter 6, the use of LiFSI, enabled by cells that limit charging below 4 V, resulted in cells with longer lifetime than those that used LiPF$_6$, primarily through reduced consumption of the lithium inventory at the negative electrode. Unlike NMC532 charged to higher voltages, little or no ΔV growth was measured. Temperature was shown to be a dominant factor in cell lifetime, and low voltage NMC532 cells with LiFSI were predicted to have lifetimes exceeding many decades when used in applications at ambient temperature. This is likely beyond the lifetime of any conventional, commercial cell.

Also in Chapter 7, a usage scheme was presented to extend the service life of low voltage NMC532 cells beyond traditional definitions of end-of-life, thereby enhancing their already incredible lifetime potential. It was shown that unutilized positive electrode capacity can be used as a lithium reservoir to offset lithium inventory loss at the negative electrode. Accessing this reservoir requires charging to increasingly higher charge endpoint voltage, which was reliably shown to be possible through the implementation of

a constant capacity charging mode. At the time of writing, the extra lifetime enabled by constant capacity charging projects to have an upper limit of approximately 5 years at 70°C. Proof of concept is demonstrated of the compatibility of this cell design with solvents, specifically MA, that are anodically unstable at higher voltages, high nickel positive electrodes that suffer from unique high voltage degradation modes, and heterogeneously blended olivine-layered positive electrode cells.
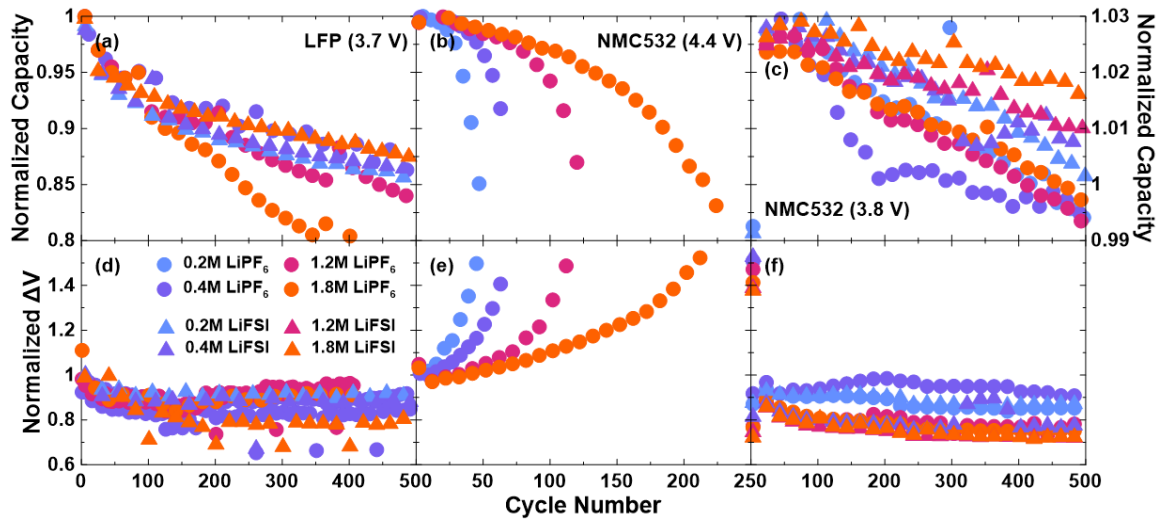
Figure 8.2. (a-c) Discharge capacity and (d-f) ΔV, normalized to 1 at cycle 5 values, as a function of cycle number for cells undergoing cycle-hold testing at 40°C. Cells include (a,d) LFP cells charged to 3.70 V, (b,e) NMC532 cells charged to 4.40 V, and (c,f) NMC532 cells charged to 3.80 V. Salt content is indicated in the legend.

The results of Chapters 4, 6 and 7 when considered together highlight the operational differences between NMC and LFP cells, along with high and low voltage usage. Figure 8.2 shows a summary of results from cycle-hold testing on LFP cells and NMC cells charged to high or low voltage. LFP cells show capacity fade that is positively correlated with the concentration of $LiPF_6$ and negatively correlated with the concentration of LiFSI, accompanied by no impedance growth. NMC532 cells charged to 4.4 V show

capacity fade and impedance growth that is negatively correlated with $LiPF_6$ concentration. NMC532 cells charged to 3.8 V show capacity fade that is largely uncorrelated with the concentration of $LiPF_6$, but is negatively correlated with the concentration of LiFSI, and accompanied by no impedance growth.

The narrative of this thesis implies some larger conclusions about the state of the field and some best practices that may be relevant for certain applications. In the author's opinion, the most important detail is on the use of LiFSI in layered positive electrode, low voltage cells. Chapter 4 showed that improvements to electrolyte can be made to considerably improve the lifetime of cells that are aggressively tested at high voltage, but that those cells fail sooner than those which are not tested at higher voltage. All things being equal, lower charge endpoint voltage should enable longer lifetime at the expense of energy density. All things are not equal however, because, as shown in Chapter 7, when cells are constructed to charge below 4 V or less, LiFSI can be used, which results in greater lifetime than $LiPF_6$. This not only enables greater lifetime overall, but greater cumulative energy throughput over the life of the cell, compared to a higher energy density cell, at the expense of needing more cycles.

Generally, the Li-ion field has favored cells along a trend of increasing energy density over the last decade, which shows preference to reducing the input resources and the battery footprint per single cycle or single discharge worth of energy. A paradigm shift may be required, due to finite mineral resource availability and manufacturing capabilities, to where reducing the input resources per cumulative energy throughput is valued. Using electric vehicles as an example, a practical realization of this is to acknowledge that the average consumer does not travel 500 km per trip on a regular basis, and perhaps only 150

km is needed for the vast majority of uses. A smaller and less energy dense battery could likely be used, but if it can outlive the car, service many cycles of vehicle-to-grid distributed storage, and participate in second-use applications, it could be a greater net usage of the materials for society.

In Chapters 4 and 6, cells were cycled following cycle-hold protocols. These were introduced as more aggressive due to longer time spent in an anodically harsh configuration, but also mentioned as realistic tests for devices that spend a long time connected to a charger, beyond reaching full charge. Cells tested with cycle-hold methods showed faster failure than those tested with CCCV methods. This should be troubling to makers of devices that commonly remain connected to a charger at full state-of-charge for many hours, once per day, but rely on manufacturer data sheets or other testing data sourced from CCCV experiments. Common examples of this are laptops or cell phones, or electric vehicles owned by individuals with range anxiety. This identifies the need for test methods, either new, or existing, that match the target application, or improved predictive methods that can deliver results in less time with higher degrees of certainty than presently exist. Additionally, the results here show that smart charging schemes which minimize time spent at full charge and/or limit charging to lower levels of charge should be implemented in devices wherever possible.

8.2 Future Work

The work presented in this thesis approaches the issue of lifetime from many angles and utilizes several different cell types. This provides many opportunities for new work and starting points for continued development and learning, in different directions.

8.2.1 Further Development and Use of NMC640

The NMC532 cells discussed in Chapter 4 showed great high voltage lifetime, while the low voltage NMC532 cells discussed in Chapter 7 showed incredibly long lifetime potential. Chapter 5 discussed NMC640 cells and introduced them as a more sustainable successor to NMC532 cells. NMC640 contains no Co and less Ni than contemporary positive electrodes, both of which are considered elements of risk for the future of Li-ion economics. The NMC640 cells described in Chapter 5 had some possible problems with positive electrode longevity that did not exist with NMC532 cells tested in Chapter 4. Material improvements that can improve NMC640 performance such that it is comparable to NMC532 are desirable, at which point, repeating the experiments in Chapter 4 with NMC640 cells, and expanding the test parameters to more additive combinations, alternate solvent systems and alternate salts, with a full optimization of the entire electrolyte composition for use at high voltage. This would enable the use of NMC640 at high voltage, with sufficient lifetime and energy density to make it a compelling choice compared to the positive electrode materials that are common today.

NMC640 cells could just as easily be implemented in the same cell design as the low voltage NMC532 cells described in Chapter 7. This would presumably achieve a long

lived NMC640 cell, which would have very few of the problems identified in Chapter 5, at the expense of energy density, and therefore represent a cost saving over low voltage NMC532 cells. For both high voltage and low voltage cell designs, a careful cost analysis is required to determine if the $/Wh calculated using both a single cycle and the cumulative energy stored over the lifetime of the cells makes for a compelling comparison with cheaper (e.g., LFP) or more energy dense (e.g., NMC811) cells.

8.2.2   Further Development of Low Voltage Cells at High Temperature

The low voltage NMC532 cells discussed in Chapter 7 showed excellent lifetime capability, particularly at high temperatures. At the time of the writing, the low voltage NMC532 cell containing LiFSI is the cell that has undergone the longest period of continuous cycling at 70°C at the author's institution, and promises to continue onward, past traditional end-of-life by implementing constant capacity charging methods. Testing and improving performance at higher temperatures is desirable for applications such as mining, where power tools may be exposed to extreme temperatures, biomedical, where devices with a sealed battery that can withstand autoclave temperatures would increase sanitation, and stationary storage, where joule heating under use in hot, equatorial locations could see cells reach extreme temperatures.

The low charge endpoint voltage enforced by the cell design and compatibility with LiFSI makes these cells well suited for higher temperature applications, but additional work is required to determine electrolytes, particularly solvents that are compatible with higher temperatures. This includes study of the boiling point as a function of solvent types, solvent ratio, and salt concentration. The solvents and additives must be thermally and

electrochemically stable at temperatures of interest while also enabling excellent performance. Some of this work is already underway, being led by Tina Taskovic,[221] but much more work is required to fully optimize electrolyte for this application. It is also likely that development in this area will require improvements to other areas of the cell, such as separators, cell housing and sealing techniques.

8.2.3   Optimization of Lifetime Using Constant Capacity Charging

The low voltage NMC cells discussed in Chapter 7 were shown to yield extremely long service life by combining conventional CCCV cycling between charge and discharge endpoint voltage limits, followed by cycling with a constant capacity charge and allowing the charge endpoint voltage to increase as necessary. The cells utilized in Chapter 7 are constructed such that at beginning of life, they are balanced for charging to 3.8 V or less. It was stated in Chapter 7 that the constant capacity charging regime will be stopped when the charge endpoint voltage reaches 4.3 V. This means that there is 0.5 V of charge endpoint voltage increase that can be tolerated.

If cells were constructed anew, balancing the cells for charging to lower voltages (e.g., 3.7 V) would result in prolonged lifetime during CCCV and more charge endpoint voltage increase during constant capacity cycling before reaching 4.3 V, but at the expense of reduced energy density stored per cycle. Constructing cells that are balanced for charging to higher voltages (e.g., 3.9 V) would have the opposite effect. Exploration of the lifetime, failure rate and general cell performance under variation of the cell balance with the constraints of certain applications is required to determine an acceptable compromise of single cycle energy density, cumulative energy stored and lifetime. This would

undoubtedly require years of testing. This point draws attention to the need for predictive methods. This includes testing at higher temperatures, where results can be obtained quickly, as degradation is rapid, and using those results to estimate lifetime at ambient temperature. Ambient temperature is perhaps the most relevant temperature to most devices, however, obtaining test results in this temperature range requires prohibitively long times.

The optimization problem of low voltage NMC cells becomes more complex as the contrast of $LiPF_6$ and LiFSI is considered. $LiPF_6$ has good anodic stability and can readily tolerate allowing the charge endpoint voltage to increase to 4.3 V, or even higher during cycling with constant capacity charging. LiFSI, as has been mentioned, can cause cell failure due to corrosion of the positive electrode current collector when cell voltages exceed 4.0 V. This means there is 0.3 V less tolerable charge endpoint voltage increase in cells containing LiFSI. Chapter 7 showed that low voltage NMC cells containing LiFSI have longer lifetime than those containing $LiPF_6$ during CCCV cycling. Less room for charge endpoint voltage increase may result in shorter lifetime for cells containing LiFSI during cycling with constant capacity charging. It remains unknown, when the combined lifetime of CCCV cycling and cycling with constant capacity charging is considered, whether $LiPF_6$ or LiFSI is superior.

Finally, implementation of this in devices may be a problem of electrical engineering and battery management system (BMS) design. Constant capacity charging requires detailed knowledge of the instantaneous electrode alignment, at least at the switchover point from CCCV charging to constant capacity charging. This could be monitored via continuous coulomb counting by the BMS, with corrections and calibrations

adjusted every time cells are fully charged and balanced. In devices that see regular servicing, such as electric vehicles, the switchover could be implemented based on offline testing performed on the battery, to obtain electrode alignment with high precision and accuracy, during a service.

8.2.4 Application of Low Voltage Cell Design to Sodium Ion Cells

The low voltage NMC cells discussed in Chapter 7 are somewhat novel in their construction, in terms of utilizing less of the positive electrode than normal and only having sufficient graphite for that usage. The ability to reliably charge to a voltage that corresponds to 50% of the positive electrode capacity and the ability to access the reservoir of unused capacity in the positive electrode are both because NMC materials have a sloping voltage curve. As such, any positive electrode material that has a sloped voltage curve could be incorporated into a similar cell design and used in a similar manner to the cells described in Chapter 7.

Sodium ion (Na-ion) cells are of interest to supplant Li-ion cells in certain applications because they are typically comprised of more abundant and affordable materials.[272] Oxide type positive electrodes for Na-ion cells can have sloping voltage curves[273] and therefore may be able to leverage the techniques described in Chapter 7 to achieve improved lifetime.

8.2.5 Electrolytes for Olivine Cells Operated at High State of Charge

Chapter 6 showed that LFP cells that spend extended duration at full state of charge fail faster than those that undergo simple CCCV cycling. A number of applications were mentioned, where LFP cells in the field could be exposed to long times at full state of charge. It was suggested based on the results of Chapter 6, that HF production at full state of charge, as a result of $LiPF_6$ decomposition, contributes to failure of LFP cells. Replacing $LiPF_6$ with LiFSI appears to alleviate this problem, but the topic requires extra attention and understanding.

Classes of acid scavenging electrolyte additives,[274] additives that may establish passivation films robust against acid attack or $LiPF_6$ decomposition, or artificial means of passivation like particle coatings all require study in cells tested with cycle-hold or similar methods, with both $LiPF_6$ and LiFSI based electrolytes. This work may become increasingly relevant as the development of $LiMnPO_4$ (LMP) cells progresses. LMP is an olivine material, like LFP, but the replacement of Fe with Mn results in a two-phase material which intercalates Li at 4.1 V vs Li^+/Li.[275] This is higher than for LFP, which may result in greater amounts of $LiPF_6$ hydrolysis and HF generation, along with possibly precluding the use of LiFSI due to corrosion concerns. In this case, LMP cells may rely on the above or other means of controlling vulnerability to $LiPF_6$ decomposition products.

8.2.6 Developments in Support of Long Lifetime Cells

Increases of lifetime of Li-ion cells will be achieved by eliminating or reducing the rate at which primary failure mechanisms occur for a given combination of cell type and application parameters. It is likely that as lifetime is increased, other failure mechanisms or deleterious effects which were not relevant at shorter lifetimes will play a significant

role in cell failure. For instance, in certain circumstances, electrolyte "dry out" has been shown to occur, where electrolyte has been consumed due to parasitic reactions in the cell and cell failure occurs due to insufficient electrochemical contact with the active materials.[271] As cell lifetime increases, "dry out" may become increasingly prevalent. Extremely long-lived cells may require extra electrolyte loading at the time of construction to account for future consumption. Research is required into the optimum electrolyte quantity based on the chemistry, application and expected lifetime. An alternative means of resolving this possible issue would be the development of a Li-ion battery that can be serviced or maintained. This design could involve a housing that would allow replenishment of electrolyte at regular intervals, or as needed. Due to the air and moisture sensitivity of the materials inside a cell, casings are usually designed to be hermetically sealed and off no opportunity for controlled ingress. A possible solution would be integration of a septum into the casings which could allow for electrolyte refilling via a needle.

Cells with extreme lifetimes will also place greater demands on cells materials and sealing integrity. It has been observed that conventional liquid electrolytes for Li-ion batteries can cause deterioration of both pouch cell casings[276] and cylindrical cell cans.[277] It has recently been shown that even the tape used in cell assembly can undergo reactions with electrolyte that negatively affect performance.[268] The casing, assembly materials and all other components that are assumed to be inert inside a cell must be truly non-reactive over long timescales, in the application specific temperature and electrochemical windows for long lifetimes to be realized. It is unclear if this will be achieved by changes in casing and assembly materials, improvements in electrolyte that are less reactive, or engineered

protection via films and coatings. All these avenues are worthy of study. In addition to materials, cell assembly techniques must also improve such that seals remain hermetic over many decades and control structures internal to the cell, such as a pressure, temperature, current switch, or a current interrupt device, do not fail prematurely.

REFERENCES

1. Y. Nishi, in *Lithium-Ion Batteries: Advances and Applications,*, p. 21–39, Elsevier (2014).

2. J. B. Goodenough and Y. Kim, *Chem. Mater.*, **22**, 587–603 (2010) doi: 10.1021/cm901452z.

3. J. B. Goodenough and K. S. Park, *J. Am. Chem. Soc.*, **135**, 1167–1176 (2013) doi: 10.1021/ja3091438.

4. Y. A. Wu, A. W. Ng, Z. Yu, J. Huang, K. Meng, and Z. Y. Dong, *Energy Policy*, **148**, 111983 (2021) doi: 10.1016/j.enpol.2020.111983.

5. P. von Brockdorff and G. Tanti, *Case Stud. Transp. Policy*, **5**, 509–517 (2017) doi: 10.1016/j.cstp.2017.05.002.

6. S. Hardman, A. Chandan, G. Tal, and T. Turrentine, *Renew. Sustain. Energy Rev.*, **80**, 1100–1111 (2017) doi: 10.1016/j.rser.2017.05.255.

7. D. P. Tuttle and R. Baldick, *Electr. J.*, **28**, 29–43 (2015) doi: 10.1016/j.tej.2015.07.008.

8. K. Y. Bjerkan, T. E. Nørbech, and M. E. Nordtømme, *Transp. Res. Part D Transp. Environ.*, **43**, 169–180 (2016) doi: 10.1016/j.trd.2015.12.002.

9. N. Melton, J. Axsen, and S. Goldberg, *Energy Policy*, **107**, 381–393 (2017) doi: 10.1016/j.enpol.2017.04.052.

10. H. C. Hesse, M. Schimpe, D. Kucevic, and A. Jossen, *Energies*, **10**, 2107 (2017) doi: 10.3390/en10122107.

11. X. Sun, H. Hao, P. Hartmann, Z. Liu, and F. Zhao, *Mater. Today Energy*, **14**, 100347 (2019) doi: 10.1016/j.mtener.2019.100347.

12. X. Sun, Z. Liu, F. Zhao, and H. Hao, *Environ. Sci. Technol.*, **55**, 12180–12190 (2021) doi: 10.1021/acs.est.1c03376.

13. Federal Consortium for Advanced Batteries, *National Blueprint for Lithium Batteries 2021–2030*, Washington, DC, (2021).

14. International Energy Agency, *World Energy Outlook 2020*, Paris, (2020).

15. C. P. Aiken, T. Taskovic, and J. R. Dahn, *J. Electrochem. Soc.*, **169**, 090523 (2022) doi: 10.1149/1945-7111/AC91AC.

16. Benchmark Mineral Intelligence, *Lithium Ion Battery Gigafactory Assessment - June 2022 Assessment*, London, (2022).

17. B. K. Sovacool, J. Kester, L. Noel, and G. Zarazua de Rubens, *Renew. Sustain. Energy Rev.*, **131**, 109963 (2020) doi: 10.1016/J.RSER.2020.109963.

18. S. Goel, R. Sharma, and A. K. Rathore, *Transp. Eng.*, **4**, 100057 (2021) doi: 10.1016/J.TRENG.2021.100057.

19. E. Martinez-Laserna, I. Gandiaga, E. Sarasketa-Zabala, J. Badeda, D. I. Stroe, M. Swierczynski, and A. Goikoetxea, *Renew. Sustain. Energy Rev.*, **93**, 701–718 (2018) doi: 10.1016/j.rser.2018.04.035.

20. Y. Akira, S. Kenichi, and N. Takayuki, (1987) https://lens.org/069-807-549-790-419.

21. K. Mizushima, P. C. Jones, P. J. Wiseman, and J. B. Goodenough, *Mater. Res. Bull.*, **15**, 783–789 (1980) doi: 10.1016/0025-5408(80)90012-4.

22. W. R. McKinnon and R. R. Haering, *Mod. Asp. Electrochem.*, 235–304 (1983) doi: 10.1007/978-1-4615-7461-3_4.

23. D. Guyomard and J. -M Tarascon, *Adv. Mater.*, **6**, 408–412 (1994) doi: 10.1002/adma.19940060516.

24. R. Koksbang, J. Barker, H. Shi, and M. Y. Saïdi, *Solid State Ionics*, **84**, 1–21 (1996) doi: 10.1016/S0167-2738(96)83001-3.

25. B. Scrosati, *J. Electrochem. Soc.*, **139**, 2776–2781 (1992) doi: 10.1149/1.2068978.

26. K. Tagawa and R. J. Brodd, in *Lithium-Ion Batteries: Science and Technologies*, M. Yoshio, R. J. Brodd, and A. Kozawa, Editors, p. 181–194, Springer New York, New York, NY (2009).

27. T. Marks, S. Trussler, A. J. Smith, D. Xiong, and J. R. Dahn, *J. Electrochem. Soc.*, **158**, A51 (2011) doi: 10.1149/1.3515072.

28. J. E. Harlow, X. Ma, J. Li, E. Logan, Y. Liu, N. Zhang, L. Ma, S. L. Glazier, M. M. E. Cormier, M. Genovese, S. Buteau, A. Cameron, J. E. Stark, and J. R. Dahn, *J. Electrochem. Soc.*, **166**, A3031–A3044 (2019) doi: 10.1149/2.0981913jes.

29. M. Zhao, S. Kariuki, H. D. Dewald, F. R. Lemke, R. J. Staniewicz, E. J. Plichta, and R. A. Marsh, *J. Electrochem. Soc.*, **147**, 2874 (2000) doi: 10.1149/1.1393619.

30. M. N. Obrovac and V. L. Chevrier, *Chem. Rev.*, **114**, 11444–11502 (2014) doi: 10.1021/cr500207g.

31. W. Li, B. Song, and A. Manthiram, *Chem. Soc. Rev.*, **46**, 3006–3059 (2017) doi: 10.1039/c6cs00875e.

32. B. L. Ellis, K. T. Lee, and L. F. Nazar, *Chem. Mater.*, **22**, 691–714 (2010) doi: 10.1021/cm902696j.

33. W. Luo, F. Zhou, X. Zhao, Z. Lu, X. Li, and J. R. Dahn, *Chem. Mater.*, **22**, 1164–1172 (2010) doi: 10.1021/CM902593N.

34. Z. Lu, D. D. MacNeil, and J. R. Dahn, *Electrochem. Solid-State Lett.*, **4**, A191 (2001) doi: 10.1149/1.1407994.

35. C. H. Chen, J. Liu, M. E. Stoll, G. Henriksen, D. R. Vissers, and K. Amine, *J. Power Sources*, **128**, 278–285 (2004) doi: 10.1016/j.jpowsour.2003.10.009.

36. S. Yamada, M. Fujiwara, and M. Kanda, *J. Power Sources*, **54**, 209–213 (1995) doi: 10.1016/0378-7753(94)02068-E.

37. N. Nitta, F. Wu, J. T. Lee, and G. Yushin, *Mater. Today*, **18**, 252–264 (2015) doi: 10.1016/J.MATTOD.2014.10.040.

38. Y. Wang, J. Jiang, and J. R. Dahn, *Electrochem. commun.*, **9**, 2534–2540 (2007) doi: 10.1016/j.elecom.2007.07.033.

39. C. M. Julien and A. Mauger, *Energies*, **13**, 6363 (2020) doi: 10.3390/en13236363.

40. K. Zaghib, A. Guerfi, P. Hovington, A. Vijh, M. Trudeau, A. Mauger, J. B. Goodenough, and C. M. Julien, *J. Power Sources*, **232**, 357–369 (2013) doi: 10.1016/j.jpowsour.2012.12.095.

41. H. J. Noh, S. Youn, C. S. Yoon, and Y. K. Sun, *J. Power Sources*, **233**, 121–130 (2013) doi: 10.1016/J.JPOWSOUR.2013.01.063.

42. C. P. Aiken, E. R. Logan, A. Eldesoky, H. Hebecker, J. M. Oxner, J. E. Harlow, M. Metzger, and J. R. Dahn, *J. Electrochem. Soc.*, **169**, 050512 (2022) doi: 10.1149/1945-7111/AC67B5.

43. H. Li, A. Liu, N. Zhang, Y. Wang, S. Yin, H. Wu, and J. R. Dahn, *Chem. Mater.*, **31**, 7574–7583 (2019) doi: 10.1021/ACS.CHEMMATER.9B02372.

44. Y. K. Sun, *ACS Energy Lett.*, **7**, 1774–1775 (2022) doi: 10.1021/acsenergylett.2c00908.

45. A. K. Padhi, K. S. Nanjundaswamy, and J. B. Goodenough, *J. Electrochem. Soc.*, **144**, 1188 (1997) doi: 10.1149/1.1837571.

46. A. Ritchie and W. Howard, *J. Power Sources*, **162**, 809–812 (2006) doi: 10.1016/j.jpowsour.2005.07.014.

47. E. A. Olivetti, G. Ceder, G. G. Gaustad, and X. Fu, *Joule*, **1**, 229–243 (2017) doi: 10.1016/J.JOULE.2017.08.019.

48. K. Turcheniuk, D. Bondarev, V. Singhal, and G. Yushin, *Nature*, **559**, 467–470 (2018) doi: 10.1038/d41586-018-05752-3.

49. A. W. Golubkov, David Fuchs, Julian Wagner, Helmar Wiltsche, Christoph Stangl, Gisela Fauler, Gernot Voitic, Alexander Thaler, and Viktor Hacker, *RSC Adv.*, **4**, 3633–3642 (2013) doi: 10.1039/C3RA45748F.

50. J. Jiang and J. R. Dahn, *Electrochem. commun.*, **6**, 39–43 (2004) doi: 10.1016/J.ELECOM.2003.10.011.

51. S. L. Glazier, S. A. Odom, A. P. Kaur, and J. R. Dahn, *J. Electrochem. Soc.*, **165**, A3449–A3458 (2018) doi: 10.1149/2.0761814jes.

52. J. Li, H. Liu, J. Xia, A. R. Cameron, M. Nie, G. A. Botton, and J. R. Dahn, *J. Electrochem. Soc.*, **164**, A655 (2017) doi: 10.1149/2.0651704JES.

53. H. Li, J. Li, X. Ma, and J. R. Dahn, *J. Electrochem. Soc.*, **165**, A1038–A1045 (2018) doi: 10.1149/2.0951805jes.

54. J. Li, H. Li, W. Stone, R. Weber, S. Hy, and J. R. Dahn, *J. Electrochem. Soc.*, **164**, A3529–A3537 (2017) doi: 10.1149/2.0401714JES.

55. L. Ma, M. Nie, J. Xia, and J. R. Dahn, *J. Power Sources*, **327**, 145–150 (2016) doi: 10.1016/J.JPOWSOUR.2016.07.039.

56. W. Xu, J. Wang, F. Ding, X. Chen, E. Nasybulin, Y. Zhang, and J. G. Zhang, *Energy Environ. Sci.*, **7**, 513–537 (2014) doi: 10.1039/c3ee40795k.

57. O. (Youngman) Chusid, E. Ein Ely, D. Aurbach, M. Babai, and Y. Carmeli, *J. Power Sources*, **43**, 47–64 (1993) doi: 10.1016/0378-7753(93)80101-T.

58. K. Ozawa, *Solid State Ionics*, **69**, 212–221 (1994) doi: 10.1016/0167-2738(94)90411-1.

59. K. Sekai, H. Azuma, A. Omaru, S. Fujita, H. Imoto, T. Endo, K. Yamaura, Y. Nishi, S. Mashiko, and M. Yokogawa, *J. Power Sources*, **43**, 241–244 (1993) doi: 10.1016/0378-7753(93)80120-E.

60. J. R. Dahn, T. Zheng, Y. Liu, and J. S. Xue, *Science (80-.).*, **270**, 590–593 (1995) doi: 10.1126/science.270.5236.590.

61. S. L. Glazier, J. Li, A. J. Louli, J. P. Allen, and J. R. Dahn, *J. Electrochem. Soc.*, **164**, A3545–A3555 (2017) doi: 10.1149/2.0421714jes.

62. B. Liu, J. G. Zhang, and W. Xu, *Joule*, **2**, 833–845 (2018) doi: 10.1016/j.joule.2018.03.008.

63. R. Weber, M. Genovese, A. J. Louli, S. Hames, C. Martin, I. G. Hill, and J. R. Dahn, *Nat. Energy*, **4**, 683–689 (2019) doi: 10.1038/s41560-019-0428-9.

64. J. Y. Li, Q. Xu, G. Li, Y. X. Yin, L. J. Wan, and Y. G. Guo, *Mater. Chem. Front.*, **1**, 1691–1708 (2017) doi: 10.1039/C6QM00302H.

65. A. J. Louli, A. Eldesoky, R. Weber, M. Genovese, M. Coon, J. DeGooyer, Z. Deng, R. T. White, J. Lee, T. Rodgers, R. Petibon, S. Hy, S. J. H. Cheng, and J. R. Dahn, *Nat. Energy*, **5**, 693–702 (2020) doi: 10.1038/s41560-020-0668-8.

66. L. Y. Beaulieu, K. W. Eberman, R. L. Turner, L. J. Krause, and J. R. Dahn, *Electrochem. Solid-State Lett.*, **4**, A137 (2001) doi: 10.1149/1.1388178.

67. P. Li, H. Kim, S. T. Myung, and Y. K. Sun, *Energy Storage Mater.*, **35**, 550–576 (2021) doi: 10.1016/j.ensm.2020.11.028.

68. E. Peled, *J. Electrochem. Soc.*, **144**, L208 (1997) doi: 10.1149/1.1837858.

69. K. Edström, M. Herstedt, and D. P. Abraham, *J. Power Sources*, **153**, 380–384 (2006) doi: 10.1016/j.jpowsour.2005.05.062.

70. J. O. Besenhard, M. Winter, J. Yang, and W. Biberacher, *J. Power Sources*, **54**, 228–231 (1995) doi: 10.1016/0378-7753(94)02073-C.

71. M. S. Ding, K. Xu, and T. R. Jow, *J. Electrochem. Soc.*, **147**, 1688 (2000) doi: 10.1149/1.1393419.

72. G.-C. Chung, H.-J. Kim, S.-I. Yu, S.-H. Jun, J. Choi, and M.-H. Kim, *J. Electrochem. Soc.*, **147**, 4391 (2000) doi: 10.1149/1.1394076.

73. E. R. Logan, E. M. Tonita, K. L. Gering, J. Li, X. Ma, L. Y. Beaulieu, and J. R. Dahn, *J. Electrochem. Soc.*, **165**, A21–A30 (2018) doi: 10.1149/2.0271802jes.

74. R. Petibon, C. P. Aiken, L. Ma, D. Xiong, and J. R. Dahn, *Electrochim. Acta*, **154**, 287–293 (2015) doi: 10.1016/j.electacta.2014.12.093.

75. J. Li, H. Li, X. Ma, W. Stone, S. Glazier, E. Logan, E. M. Tonita, K. L. Gering, and J. R. Dahn, *J. Electrochem. Soc.*, **165**, A1027–A1037 (2018) doi: 10.1149/2.0861805jes.

76. S. S. Zhang, T. R. Jow, K. Amine, and G. L. Henriksen, *J. Power Sources*, **107**, 18–23 (2002) doi: 10.1016/S0378-7753(01)00968-5.

77. N. Takami, T. Ohsaki, and K. Inada, *J. Electrochem. Soc.*, **139**, 1849–1854 (1992) doi: 10.1149/1.2069510.

78. J. S. Gnanaraj, E. Zinigrad, M. D. Levi, D. Aurbach, and M. Schmidt, in *Journal of Power Sources,*, vol. 119–121, p. 799–804, Elsevier (2003).

79. S. E. Sloop, J. K. Pugh, S. Wang, J. B. Kerr, and K. Kinoshita, *Electrochem. Solid-State Lett.*, **4**, A42 (2001) doi: 10.1149/1.1353158.

80. J. Jiang and J. R. Dahn, *Electrochem. Solid-State Lett.*, **6**, A180 (2003) doi: 10.1149/1.1592911.

81. X. Ma, J. E. Harlow, J. Li, L. Ma, D. S. Hall, S. Buteau, M. Genovese, M. Cormier, and J. R. Dahn, *J. Electrochem. Soc.*, **166**, A711–A724 (2019) doi: 10.1149/2.0801904jes.

82. R. Marom, O. Haik, I. C. Halalay, and D. Aurbach, *ECS Meet. Abstr.*, **MA2010-03**, 142–142 (2010) doi: 10.1149/ma2010-03/1/142.

83. J. T. Dudley, D. P. Wilkinson, G. Thomas, R. LeVae, S. Woo, H. Blom, C. Horvath, M. W. Juzkow, B. Denis, P. Juric, P. Aghakian, and J. R. Dahn, *J. Power Sources*, **35**, 59–82 (1991) doi: 10.1016/0378-7753(91)80004-H.

84. W. Xu and C. A. Angell, *Electrochem. Solid-State Lett.*, **4**, E1 (2001) doi: 10.1149/1.1344281.

85. G. H. Newman, R. W. Francis, L. H. Gaines, and B. M. L. Rao, *J. Electrochem. Soc.*, **127**, 2025–2027 (1980) doi: 10.1149/1.2130056.

86. R. Jasinski and S. Carroll, *J. Electrochem. Soc.*, **117**, 218 (1970) doi: 10.1149/1.2407468.

87. L. J. Krause, W. Lamanna, J. Summerfield, M. Engle, G. Korba, R. Loch, and R. Atanasoski, *J. Power Sources*, **68**, 320–325 (1997) doi: 10.1016/S0378-7753(97)02517-2.

88. C. Luo, Y. Li, W. Sun, P. Xiao, S. Liu, D. Q. Wang, and C. Zheng, *Electrochim. Acta*, **419**, 140353 (2022) doi: 10.1016/j.electacta.2022.140353.

89. E. R. Logan, A. Eldesoky, E. Eastwood, H. Hebecker, C. P. Aiken, M. Metzger, and J. R. Dahn, *J. Electrochem. Soc.*, **169**, 040560 (2022) doi: 10.1149/1945-7111/AC67F9.

90. S. S. Zhang, *J. Power Sources*, **162**, 1379–1394 (2006) doi: 10.1016/j.jpowsour.2006.07.074.

91. Y. Wang, S. Nakamura, K. Tasaki, and P. B. Balbuena, *J. Am. Chem. Soc.*, **124**, 4408–4421 (2002) doi: 10.1021/ja017073i.

92. S. Leroy, F. Blanchard, R. Dedryvère, H. Martinez, B. Carré, D. Lemordant, and D. Gonbeau, *Surf. Interface Anal.*, **37**, 773–781 (2005) doi: 10.1002/sia.2072.

93. S.-K. Jeong, M. Inaba, T. Abe, and Z. Ogumi, *J. Electrochem. Soc.*, **148**, A989 (2001) doi: 10.1149/1.1387981.

94. J. C. Burns, G. Jain, A. J. Smith, K. W. Eberman, E. Scott, J. P. Gardner, and J. R. Dahn, *J. Electrochem. Soc.*, **158**, A255 (2011) doi: 10.1149/1.3531997.

95. C. Burns, A. Kassam, N. N. Sinha, L. Downie, L. Solnickova, B. Way, and J. Dahn, *ECS Meet. Abstr.*, **MA2013-02**, 1211–1211 (2013) doi: 10.1149/ma2013-02/14/1211.

96. L. Ma, D. Y. Wang, L. E. Downie, J. Xia, K. J. Nelson, N. N. Sinha, and J. R. Dahn, *J. Electrochem. Soc.*, **161**, A1261–A1265 (2014) doi: 10.1149/2.0541409jes.

97. L. Ma, J. Xia, and J. R. Dahn, *J. Electrochem. Soc.*, **161**, A2250–A2254 (2014) doi: 10.1149/2.1041414jes.

98. X. Zuo, C. Fan, X. Xiao, J. Liu, and J. Nan, *J. Power Sources*, **219**, 94–99 (2012) doi: 10.1016/j.jpowsour.2012.07.026.

99. R. Petibon, N. N. Sinha, J. C. Burns, C. P. Aiken, H. Ye, C. M. Vanelzen, G. Jain, S. Trussler, and J. R. Dahn, *J. Power Sources*, **251**, 187–194 (2014) doi: 10.1016/j.jpowsour.2013.11.054.

100. L. Xia, D. Wang, H. Yang, Y. Cao, and X. Ai, *Electrochem. commun.*, **25**, 98–100 (2012) doi: 10.1016/j.elecom.2012.09.038.

101. Y. S. Kim, T. H. Kim, H. Lee, and H. K. Song, *Energy Environ. Sci.*, **4**, 4038–4045 (2011) doi: 10.1039/c1ee01272j.

102. D. Aurbach, Y. Talyosef, B. Markovsky, E. Markevich, E. Zinigrad, L. Asraf, J. S. Gnanaraj, and H.-J. Kim, *Electrochim. Acta*, **50**, 247–254 (2004) doi: 10.1016/j.electacta.2004.01.090.

103. D. Y. Wang, J. Xia, L. Ma, K. J. Nelson, J. E. Harlow, D. Xiong, L. E. Downie, R. Petibon, J. C. Burns, A. Xiao, W. M. Lamanna, and J. R. Dahn, *J. Electrochem. Soc.*, **161**, A1818–A1827 (2014) doi: 10.1149/2.0511412jes.

104. Q. Zhao, S. Stalin, C. Z. Zhao, and L. A. Archer, *Nat. Rev. Mater.*, **5**, 229–252 (2020) doi: 10.1038/s41578-019-0165-5.

105. A. Manthiram, X. Yu, and S. Wang, *Nat. Rev. Mater.*, **2**, 1–16 (2017) doi: 10.1038/natrevmats.2016.103.

106. P. Verma, P. Maire, and P. Novák, *Electrochim. Acta*, **55**, 6332–6341 (2010) doi: 10.1016/j.electacta.2010.05.072.

107. P. Novák, F. Joho, M. Lanz, B. Rykart, J.-C. Panitz, D. Alliata, R. Kötz, and O. Haas, *J. Power Sources*, **97**–**98**, 39–46 (2001) doi: 10.1016/S0378-7753(01)00586-9.

108. K. Edström, T. Gustafsson, and J. O. Thomas, *Electrochim. Acta*, **50**, 397–403 (2004) doi: 10.1016/j.electacta.2004.03.049.

109. E. Peled, *J. Electrochem. Soc.*, **126**, 2047 (1979) doi: 10.1149/1.2128859.

110. J. Christensen and J. Newman, *J. Electrochem. Soc.*, **152**, A818 (2005) doi: 10.1149/1.1870752.

111. A. J. Smith, J. C. Burns, D. Xiong, and J. R. Dahn, *J. Electrochem. Soc.*, **158**, A1136–A1142 (2011) doi: 10.1149/1.3625232.

112. R. Fong, U. von Sacken, and J. R. Dahn, *J. Electrochem. Soc.*, **137**, 2009–2013 (1990) doi: 10.1149/1.2086855.

113. E. Peled, *J. Electrochem. Soc.*, **143**, L4 (1996) doi: 10.1149/1.1836372.

114. M. Broussely, S. Herreyre, P. Biensan, P. Kasztejna, K. Nechev, and R. J. Staniewicz, *J. Power Sources*, **97**–**98**, 13–21 (2001) doi: 10.1016/S0378-7753(01)00722-4.

115. A. J. Smith, J. C. Burns, X. Zhao, D. Xiong, and J. R. Dahn, *J. Electrochem. Soc.*, **158**, A447 (2011) doi: 10.1149/1.3557892.

116. F. Single, B. Horstmann, and A. Latz, *Phys. Chem. Chem. Phys.*, **18**, 17810–17814 (2016) doi: 10.1039/c6cp02816k.

117. K. R. Lawless, *Reports Prog. Phys.*, **37**, 231 (1974) doi: 10.1088/0034-4885/37/2/002.

118. P. G. Kitz, P. Novák, and E. J. Berg, *ACS Appl. Mater. Interfaces*, **12**, 15934–15942 (2020) doi: 10.1021/acsami.0c01642.

119. H. Bryngelsson, M. Stjerndahl, T. Gustafsson, and K. Edström, *J. Power Sources*, **174**, 970–975 (2007) doi: 10.1016/j.jpowsour.2007.06.050.

120. L. Madec, J. Xia, R. Petibon, K. J. Nelson, J. P. Sun, I. G. Hill, and J. R. Dahn, *J. Phys. Chem. C*, **118**, 29608–29622 (2014) doi: 10.1021/jp509731y.

121. P. Lu and S. J. Harris, *Electrochem. commun.*, **13**, 1035–1037 (2011) doi: 10.1016/j.elecom.2011.06.026.

122. S. J. Harris and P. Lu, *J. Phys. Chem. C*, **117**, 6481–6492 (2013) doi: 10.1021/jp311431z.

123. P. Lu, C. Li, E. W. Schneider, and S. J. Harris, *J. Phys. Chem. C*, **118**, 896–903 (2014) doi: 10.1021/jp4111019.

124. S. K. Heiskanen, J. Kim, and B. L. Lucht, *Joule*, **3**, 2322–2333 (2019) doi: 10.1016/j.joule.2019.08.018.

125. E. Peled and S. Menkin, *J. Electrochem. Soc.*, **164**, A1703–A1719 (2017) doi: 10.1149/2.1441707JES.

126. F. A. Soto, Y. Ma, J. M. Martinez De La Hoz, J. M. Seminario, and P. B. Balbuena, *Chem. Mater.*, **27**, 7990–8000 (2015) doi: 10.1021/acs.chemmater.5b03358.

127. L. D. Ellis, J. P. Allen, I. G. Hill, and J. R. Dahn, *J. Electrochem. Soc.*, **165**, A1529–A1536 (2018) doi: 10.1149/2.1091807jes.

128. M. Moshkovich, M. Cojocaru, H. E. Gottlieb, and D. Aurbach, *J. Electroanal. Chem.*, **497**, 84–96 (2001) doi: 10.1016/S0022-0728(00)00457-5.

129. M. G. S. R. Thomas, P. G. Bruce, and J. B. Goodenough, *J. Electrochem. Soc.*, **132**, 1521–1528 (1985) doi: 10.1149/1.2114158.

130. D. Guyomard and J. M. Tarascon, *J. Electrochem. Soc.*, **139**, 937–948 (1992) doi: 10.1149/1.2069372.

131. H. Wang, X. Li, F. Li, X. Liu, S. Yang, and J. Ma, *Electrochem. commun.*, **122**, 106870 (2021) doi: 10.1016/j.elecom.2020.106870.

132. Y. Wu, X. Liu, L. Wang, X. Feng, D. Ren, Y. Li, X. Rui, Y. Wang, X. Han, G. L. Xu, H. Wang, L. Lu, X. He, K. Amine, and M. Ouyang, *Energy Storage Mater.*, **37**, 77–86 (2021) doi: 10.1016/j.ensm.2021.02.001.

133. K. Xu, *Chem. Rev.*, **104**, 4303–4417 (2004) doi: 10.1021/cr030203g.

134. S. P. Kühn, K. Edström, M. Winter, I. Cekic-Laskovic, S. P. Kühn, M. Winter, I. Cekic-Laskovic, and K. Edström, *Adv. Mater. Interfaces*, **9**, 2102078 (2022) doi: 10.1002/ADMI.202102078.

135. C. Ye, W. Tu, L. Yin, Q. Zheng, C. Wang, Y. Zhong, Y. Zhang, Q. Huang, K. Xu, and W. Li, *J. Mater. Chem. A*, **6**, 17642–17652 (2018) doi: 10.1039/c8ta06150e.

136. M. S. Ding and T. Richard Jow, *J. Electrochem. Soc.*, **151**, A2007 (2004) doi: 10.1149/1.1809575.

137. E. R. Logan, E. M. Tonita, K. L. Gering, L. Ma, M. K. G. Bauer, J. Li, L. Y. Beaulieu, and J. R. Dahn, *J. Electrochem. Soc.*, **165**, A705–A716 (2018) doi: 10.1149/2.0981803jes.

138. L. Doucey, M. Revault, A. Lautié, A. Chaussé, and R. Messina, *Electrochim. Acta*, **44**, 2371–2377 (1999) doi: 10.1016/S0013-4686(98)00365-X.

139. D. J. Xiong, M. Bauer, L. D. Ellis, T. Hynes, S. Hyatt, D. S. Hall, and J. R. Dahn, *J. Electrochem. Soc.*, **165**, A126–A131 (2018) doi: 10.1149/2.0511802jes.

140. K. Xu, *Chem. Rev.*, **114**, 11503–11618 (2014) doi: 10.1021/cr500003w.

141. E. Endo, M. Ata, K. Tanaka, and K. Sekai, *J. Electrochem. Soc.*, **145**, 3757–3764 (1998) doi: 10.1149/1.1838870.

142. M. Ue, A. Murakami, and S. Nakamura, *J. Electrochem. Soc.*, **149**, A1572 (2002) doi: 10.1149/1.1517579.

143. K. I. Chung, M. W. Chung, W. S. Kim, S. K. Kim, Y. E. Sung, and Y. K. Choi, *Bull. Korean Chem. Soc.*, **22**, 189–193 (2001).

144. M. Nie, D. P. Abraham, D. M. Seo, Y. Chen, A. Bose, and B. L. Lucht, *J. Phys. Chem. C*, **117**, 25381–25389 (2013) doi: 10.1021/jp409765w.

145. M. Winter, *Zeitschrift fur Phys. Chemie*, **223**, 1395–1406 (2009) doi: 10.1524/zpch.2009.6086.

146. Q. Liu, H. Xu, F. Wu, D. Mu, L. Shi, L. Wang, J. Bi, and B. Wu, *ACS Appl. Energy Mater*, **2**, 8878–8884 (2019) doi: 10.1021/acsaem.9b01917.

147. R. Sahore, D. C. O'Hanlon, A. Tornheim, C.-W. Lee, J. C. Garcia, H. Iddir, M. Balasubramanian, and I. Bloom, *J. Electrochem. Soc.*, **167**, 020513 (2020) doi: 10.1149/1945-7111/AB6826.

148. W. Liu, J. Li, W. Li, H. Xu, C. Zhang, and X. Qiu, *Nat. Commun.*, **11**, 1–11 (2020) doi: 10.1038/s41467-020-17396-x.

149. S. Klein, J. M. Wrogemann, S. van Wickeren, P. Harte, P. Bärmann, B. Heidrich, J. Hesper, K. Borzutzki, S. Nowak, M. Börner, M. Winter, J. Kasnatscheew, and T. Placke, *Adv. Energy Mater.*, **12**, 2102599 (2022) doi: 10.1002/AENM.202102599.

150. L. Ma, L. Ellis, S. L. Glazier, X. Ma, Q. Liu, J. Li, and J. R. Dahn, *J. Electrochem. Soc.*, **165**, A891–A899 (2018) doi: 10.1149/2.0381805jes.

151. L. Liu, S. Gu, S. Wang, X. Zhang, and S. Chen, *RSC Adv.*, **10**, 1704–1710 (2020) doi: 10.1039/c9ra09841k.

152. J. Chen, L. Xing, X. Yang, X. Liu, T. Li, and W. Li, *Electrochim. Acta*, **290**, 568–576 (2018) doi: 10.1016/j.electacta.2018.09.077.

153. C. P. Aiken, J. E. Harlow, R. Tingley, T. Hynes, E. R. Logan, S. L. Glazier, A. S. Keefe, and J. R. Dahn, *J. Electrochem. Soc.*, **167**, 130541 (2020) doi: 10.1149/1945-7111/ABBE5B.

154. A. C. Martinez, S. Rigaud, S. Grugeon, P. Tran-Van, M. Armand, D. Cailleu, S. Pilard, and S. Laruelle, *Electrochim. Acta*, **426**, 140765 (2022) doi: 10.1016/j.electacta.2022.140765.

155. I. Li, D. D. MacNeil, and J. R. Dahn, *J. Electrochem. Soc.*, **148**, 1205–1210 (2001) doi: 10.1149/1.1407245.

156. F. Guo, Y. Ozaki, K. Nishimura, N. Hashimoto, and O. Fujita, *Combust. Flame*, **213**, 314–321 (2020) doi: 10.1016/j.combustflame.2019.12.001.

157. S. Qiao, X. Meng, W. Cao, S. Yu, C. Liu, and Q. Huang, *Case Stud. Therm. Eng.*, **30**, 101741 (2022) doi: 10.1016/j.csite.2021.101741.

158. Y. Yamada, K. Usui, C. H. Chiang, K. Kikuchi, K. Furukawa, and A. Yamada, *ACS Appl. Mater. Interfaces*, **6**, 10892–10899 (2014) doi: 10.1021/am5001163.

159. Y. Yamada, K. Furukawa, K. Sodeyama, K. Kikuchi, M. Yaegashi, Y. Tateyama, and A. Yamada, *J. Am. Chem. Soc.*, **136**, 5039–5046 (2014) doi: 10.1021/ja412807w.

160. M. Wang, L. Huai, G. Hu, S. Yang, F. Ren, S. Wang, Z. Zhang, Z. Chen, Z. Peng, C. Shen, and D. Wang, *J. Phys. Chem. C*, **122**, 9825–9834 (2018) doi: 10.1021/acs.jpcc.8b02314.

161. B. Ravikumar, M. Mynam, and B. Rai, *J. Phys. Chem. C*, **122**, 8173–8181 (2018) doi: 10.1021/acs.jpcc.8b02072.

162. Y. Ein-Eli, S. F. McDevitt, and R. Laura, *J. Electrochem. Soc.*, **145**, L1–L3 (1998) doi: 10.1149/1.1838196.

163. A. J. Gmitter, I. Plitz, and G. G. Amatucci, *J. Electrochem. Soc.*, **159**, A370–A379 (2012) doi: 10.1149/2.016204jes.

164. R. McMillan, H. Slegr, Z. X. Shu, and W. Wang, *J. Power Sources*, **81**–**82**, 20–26 (1999) doi: 10.1016/S0378-7753(98)00201-8.

165. D. Aurbach, K. Gamolsky, B. Markovsky, Y. Gofer, M. Schmidt, and U. Heider, *Electrochim. Acta*, **47**, 1423–1439 (2002) doi: 10.1016/S0013-4686(01)00858-1.

166. H. Ota, Y. Sakata, A. Inoue, and S. Yamaguchi, *J. Electrochem. Soc.*, **151**, A1659 (2004) doi: 10.1149/1.1785795.

167. M. C. Smart, B. V. Ratnakumar, L. D. Whitcanack, K. B. Chin, S. Surampudi, H. Croft, D. Tice, and R. Staniewicz, in *Journal of Power Sources*, vol. 119–121, p. 349–358, Elsevier (2003).

168. R. Petibon, J. Xia, L. Ma, M. K. G. Bauer, K. J. Nelson, and J. R. Dahn, *J. Electrochem. Soc.*, **163**, A2571–A2578 (2016) doi: 10.1149/2.0321613jes.

169. L. Ma, S. L. Glazier, R. Petibon, J. Xia, J. M. Peters, Q. Liu, J. Allen, R. N. C. Doig, and J. R. Dahn, *J. Electrochem. Soc.*, **164**, A5008–A5018 (2017) doi: 10.1149/2.0191701jes.

170. J. Xia, R. Petibon, D. Xiong, L. Ma, and J. R. Dahn, *J. Power Sources*, **328**, 124–135 (2016) doi: 10.1016/j.jpowsour.2016.08.015.

171. M. S. Ding, K. Xu, and T. R. Jow, *J. Electrochem. Soc.*, **147**, 1688 (2000) doi: 10.1149/1.1393419.

172. K. Xu, Y. Lam, S. S. Zhang, T. R. Jow, and T. B. Curtis, *J. Phys. Chem. C*, **111**, 7411–7421 (2007) doi: 10.1021/jp068691u.

173. E. M. Erickson, E. Markevich, G. Salitra, D. Sharon, D. Hirshberg, E. de la Llave, I. Shterenberg, A. Rosenman, A. Frimer, and D. Aurbach, *J. Electrochem. Soc.*, **164**, X5–X5 (2017) doi: 10.1149/2.0991704jes.

174. L. Hu, Z. Xue, K. Amine, and Z. Zhang, *J. Electrochem. Soc.*, **161**, A1777–A1781 (2014) doi: 10.1149/2.0141412jes.

175. I. A. Profatilova, S. S. Kim, and N. S. Choi, *Electrochim. Acta*, **54**, 4445–4450 (2009) doi: 10.1016/j.electacta.2009.03.032.

176. K. C. Möller, T. Hodal, W. K. Appel, M. Winter, and J. O. Besenhard, in *Journal of Power Sources,*, vol. 97–98, p. 595–597, Elsevier (2001).

177. J. I. Yamaki, I. Yamazaki, M. Egashira, and S. Okada, *J. Power Sources*, **102**, 288–293 (2001) doi: 10.1016/S0378-7753(01)00805-9.

178. J. Xia, M. Nie, J. C. Burns, A. Xiao, W. M. Lamanna, and J. R. Dahn, *J. Power Sources*, **307**, 340–350 (2016) doi: 10.1016/j.jpowsour.2015.12.132.

179. Z. Zhang, L. Hu, H. Wu, W. Weng, M. Koh, P. C. Redfern, L. A. Curtiss, and K. Amine, *Energy Environ. Sci.*, **6**, 1806–1810 (2013) doi: 10.1039/c3ee24414h.

180. E. Markevich, G. Salitra, Y. Talyosef, U. H. Kim, H. H. Ryu, Y. K. Sun, and D. Aurbach, *ACS Appl. Energy Mater.*, **1**, 2600–2607 (2018) doi: 10.1021/acsaem.8b00304.

181. M. Takehara, S. Watanabe, N. Nanbu, M. Ue, and Y. Sasaki, *Synth. Commun.*, **34**, 1367–1375 (2004) doi: 10.1081/SCC-120030685.

182. R. Jung, M. Metzger, D. Haering, S. Solchenbach, C. Marino, N. Tsiouvaras, C. Stinner, and H. A. Gasteiger, *J. Electrochem. Soc.*, **163**, A1705 (2016) doi: 10.1149/2.0951608JES.

183. R. Petibon, J. Harlow, D. B. Le, and J. R. Dahn, *Electrochim. Acta*, **154**, 227–234 (2015) doi: 10.1016/j.electacta.2014.12.084.

184. E. R. Logan and J. R. Dahn, *Trends Chem.*, **2**, 354–366 (2020) doi: 10.1016/J.TRECHM.2020.01.011.

185. E. R. Logan and J. R. Dahn, *J. Electrochem. Soc.*, **168**, 120526 (2021) doi: 10.1149/1945-7111/AC405B.

186. S. L. Glazier, J. Li, X. Ma, L. D. Ellis, J. P. Allen, K. L. Gering, and J. R. Dahn, *J. Electrochem. Soc.*, **165**, A867–A875 (2018) doi: 10.1149/2.0451805jes.

187. T. T. Hagos, B. Thirumalraj, C. J. Huang, L. H. Abrha, T. M. Hagos, G. B. Berhe, H. K. Bezabh, J. Cherng, S. F. Chiu, W. N. Su, and B. J. Hwang, *ACS Appl. Mater. Interfaces*, **11**, 9955–9963 (2019) doi: 10.1021/acsami.8b21052.

188. L. J. Lyons, T. Derrah, S. Sharpe, S. Yoon, S. Beecher, M. Usrey, A. Peña-Hueso, T. Johnson, and R. West, *MRS Commun.*, **9**, 1200–1205 (2019) doi: 10.1557/mrc.2019.131.

189. K. Yoshida, M. Nakamura, Y. Kazue, N. Tachikawa, S. Tsuzuki, S. Seki, K. Dokko, and M. Watanabe, *J. Am. Chem. Soc.*, **133**, 13121–13129 (2011) doi: 10.1021/ja203983r.

190. K. J. Nelson, G. L. d'Eon, A. T. B. Wright, L. Ma, J. Xia, and J. R. Dahn, *J. Electrochem. Soc.*, **162**, A1046–A1054 (2015) doi: 10.1149/2.0831506jes.

191. S.-K. Jeong, M. Inaba, R. Mogi, Y. Iriyama, T. Abe, and Z. Ogumi, *Langmuir*, **17**, 8281–8286 (2001) doi: 10.1021/la015553h.

192. D. Y. Wang, J. C. Burns, and J. R. Dahn, *J. Electrochem. Soc.*, **161**, 1278–1283 (2014) doi: 10.1149/2.0611409jes.

193. Y. Liu, L. Ma, and J. R. Dahn, *J. Electrochem. Soc.*, **168**, 080537 (2021) doi: 10.1149/1945-7111/ac1eb7.

194. L. Ma, L. Ellis, S. L. Glazier, X. Ma, Q. Liu, J. Li, and J. R. Dahn, *J. Electrochem. Soc.*, **165**, A891–A899 (2018) doi: 10.1149/2.0381805jes.

195. V. Murray, D. S. Hall, and J. R. Dahn, *J. Electrochem. Soc.*, **166**, A329–A333 (2019) doi: 10.1149/2.1171902jes.

196. E. R. Logan, H. Hebecker, A. Eldesoky, A. Luscombe, M. B. Johnson, and J. R. Dahn, *J. Electrochem. Soc.*, **167**, 130543 (2020) doi: 10.1149/1945-7111/ABBBBE.

197. I. Hamam, N. Zhang, A. Liu, M. B. Johnson, and J. R. Dahn, *J. Electrochem. Soc.*, **167**, 130521 (2020) doi: 10.1149/1945-7111/abb9cd.

198. J. R. Dahn, S. Trussler, S. Dugas, D. J. Coyle, J. J. Dahn, and J. C. Burns, *J. Electrochem. Soc.*, **160**, A251–A258 (2013) doi: 10.1149/2.047302jes.

199. A. J. Louli, M. Genovese, R. Weber, and J. R. Dahn, *ECS Meet. Abstr.*, **MA2019-03**, 88–88 (2019) doi: 10.1149/ma2019-03/1/88.

200. H. Maleki and J. N. Howard, *J. Power Sources*, **160**, 1395–1402 (2006) doi: 10.1016/j.jpowsour.2006.03.043.

201. R. Guo, L. Lu, M. Ouyang, and X. Feng, *Sci. Rep.*, **6**, 1–9 (2016) doi: 10.1038/srep30248.

202. K. J. Nelson, J. E. Harlow, and J. R. Dahn, *J. Electrochem. Soc.*, **165**, A456–A462 (2018) doi: 10.1149/2.0041803jes.

203. A. J. Smith, J. C. Burns, S. Trussler, and J. R. Dahn, *J. Electrochem. Soc.*, **157**, A196 (2010) doi: 10.1149/1.3268129.

204. T. M. Bond, J. C. Burns, D. A. Stevens, H. M. Dahn, and J. R. Dahn, *J. Electrochem. Soc.*, **160**, A521–A527 (2013) doi: 10.1149/2.014304jes.

205. I. Bloom, A. N. Jansen, D. P. Abraham, J. Knuth, S. A. Jones, V. S. Battaglia, and G. L. Henriksen, *J. Power Sources*, **139**, 295–303 (2005) doi: 10.1016/j.jpowsour.2004.07.021.

206. I. Bloom, J. Christophersen, and K. Gering, *J. Power Sources*, **139**, 304–313 (2005) doi: 10.1016/j.jpowsour.2004.07.022.

207. I. Bloom, J. P. Christophersen, D. P. Abraham, and K. L. Gering, *J. Power Sources*, **157**, 537–542 (2006) doi: 10.1016/j.jpowsour.2005.07.054.

208. I. Bloom, L. K. Walker, J. K. Basco, D. P. Abraham, J. P. Christophersen, and C. D. Ho, *J. Power Sources*, **195**, 877–882 (2010) doi: 10.1016/j.jpowsour.2009.08.019.

209. K. Honkura, H. Honbo, Y. Koishikawa, and T. Horiba, *ECS Meet. Abstr.*, **MA2008-01**, 115–115 (2008) doi: 10.1149/ma2008-01/5/115.

210. H. M. Dahn, A. J. Smith, J. C. Burns, D. A. Stevens, and J. R. Dahn, *J. Electrochem. Soc.*, **159**, A1405–A1409 (2012) doi: 10.1149/2.013209jes.

211. A. S. Keefe, S. Buteau, I. G. Hill, and J. R. Dahn, *J. Electrochem. Soc.*, **166**, A3272–A3279 (2019) doi: 10.1149/2.0541914jes.

212. D. W. Abarbanel, K. J. Nelson, and J. R. Dahn, *J. Electrochem. Soc.*, **163**, A522–A529 (2016) doi: 10.1149/2.0901603jes.

213. L. J. Krause, L. D. Jensen, and J. R. Dahn, *J. Electrochem. Soc.*, **159**, A937–A943 (2012) doi: 10.1149/2.021207jes.

214. S. L. Glazier, thesis, Dalhousie University (2018).

215. L. M. Thompson, W. Stone, A. Eldesoky, N. K. Smith, C. R. M. McFarlane, J. S. Kim, M. B. Johnson, R. Petibon, and J. R. Dahn, *J. Electrochem. Soc.*, **165**, A2732–A2740 (2018) doi: 10.1149/2.0721811jes.

216. A. Eldesoky, E. R. Logan, M. B. Johnson, C. R. M. McFarlane, and J. R. Dahn, *J. Electrochem. Soc.*, **167**, 130539 (2020) doi: 10.1149/1945-7111/ABBA62.

217. R. P. Day, J. Xia, R. Petibon, J. Rucska, H. Wang, A. T. B. Wright, and J. R. Dahn, *J. Electrochem. Soc.*, **162**, A2577–A2581 (2015) doi: 10.1149/2.0181514jes.

218. T. Bond, R. Gauthier, A. Eldesoky, J. Harlow, and J. R. Dahn, *J. Electrochem. Soc.*, **169**, 020501 (2022) doi: 10.1149/1945-7111/AC4B83.

219. S. Azam, Q. Meisner, C. P. Aiken, W. Song, Q. Liu, D.-J. Yoo, A. Eldesoky, Z. Zhang, and J. R. Dahn, *J. Electrochem. Soc.*, **169**, 100552 (2022) doi: 10.1149/1945-7111/ac9c36.

220. T. Taskovic, L. M. Thompson, A. Eldesoky, M. D. Lumsden, and J. R. Dahn, *J. Electrochem. Soc.*, **168**, 010514 (2021) doi: 10.1149/1945-7111/abd833.

221. T. Taskovic, A. Eldesoky, W. Song, M. Bauer, and J. R. Dahn, *J. Electrochem. Soc.*, **169**, 040538 (2022) doi: 10.1149/1945-7111/ac6453.

222. C. P. Aiken, J. Xia, D. Y. Wang, D. A. Stevens, S. Trussler, and J. R. Dahn, *J. Electrochem. Soc.*, **161**, A1548–A1554 (2014) doi: 10.1149/2.0151410jes.

223. P. Gasper, N. Collath, H. C. Hesse, A. Jossen, and K. Smith, *J. Electrochem. Soc.*, **169**, 080518 (2022) doi: 10.1149/1945-7111/ac86a8.

224. I. Bloom, B. W. Cole, J. J. Sohn, S. A. Jones, E. G. Polzin, V. S. Battaglia, G. L. Henriksen, C. Motloch, R. Richardson, T. Unkelhaeuser, D. Ingersoll, and H. L. Case, *J. Power Sources*, **101**, 238–247 (2001) doi: 10.1016/S0378-7753(01)00783-2.

225. K. L. Gering, *Electrochim. Acta*, **225**, 175–189 (2017) doi: 10.1016/j.electacta.2016.12.083.

226. A. Eldesoky, E. R. Logan, A. J. Louli, W. Song, R. Weber, S. Hy, R. Petibon, J. E. Harlow, S. Azam, E. Zsoldos, and J. R. Dahn, *J. Electrochem. Soc.*, **169**, 010501 (2022) doi: 10.1149/1945-7111/ac42f1.

227. R. Gauthier, A. Luscombe, T. Bond, M. Bauer, M. Johnson, J. Harlow, A. Louli, and J. R. Dahn, *J. Electrochem. Soc.*, **169**, 020518 (2022) doi: 10.1149/1945-7111/ac4b82.

228. J. Xia, K. J. Nelson, Z. Lu, and J. R. Dahn, *J. Power Sources*, **329**, 387–397 (2016) doi: 10.1016/j.jpowsour.2016.08.100.

229. Y. Zhu, Y. Li, M. Bettge, and D. P. Abraham, *Electrochim. Acta*, **110**, 191–199 (2013) doi: 10.1016/j.electacta.2013.03.102.

230. R. Petibon, L. Madec, D. W. Abarbanel, and J. R. Dahn, *J. Power Sources*, **300**, 419–429 (2015) doi: 10.1016/j.jpowsour.2015.09.090.

231. J. Li, H. Li, W. Stone, S. Glazier, and J. R. Dahn, *J. Electrochem. Soc.*, **165**, A626–A635 (2018) doi: 10.1149/2.0971803jes.

232. D. M. Seo, S. Reininger, M. Kutcher, K. Redmond, W. B. Euler, and B. L. Lucht, *J. Phys. Chem. C*, **119**, 14038–14046 (2015) doi: 10.1021/acs.jpcc.5b03694.

233. Z. Feng, K. Higa, K. S. Han, and V. Srinivasan, *J. Electrochem. Soc.*, **164**, A2434–A2440 (2017) doi: 10.1149/2.0941712jes.

234. L. E. Downie, K. J. Nelson, R. Petibon, V. L. Chevrier, and J. R. Dahn, *ECS Electrochem. Lett.*, **2**, A106 (2013) doi: 10.1149/2.010310EEL.

235. T. Sasaki, T. Nonaka, H. Oka, C. Okuda, Y. Itou, Y. Kondo, Y. Takeuchi, Y. Ukyo, K. Tatsumi, and S. Muto, *J. Electrochem. Soc.*, **156**, A289 (2009) doi: 10.1149/1.3076136.

236. R. Mondal, H. Ratnawat, S. Kumar, A. Kumar, and P. Singh, *RSC Adv.*, **10**, 17845–17853 (2020) doi: 10.1039/d0ra03050c.

237. L. D. Ellis, J. Xia, A. J. Louli, and J. R. Dahn, *J. Electrochem. Soc.*, **163**, A1686–A1692 (2016) doi: 10.1149/2.0851608jes.

238. T. Kawamura, S. Okada, and J. ichi Yamaki, *J. Power Sources*, **156**, 547–554 (2006) doi: 10.1016/j.jpowsour.2005.05.084.

239. L. O. Valøen and J. N. Reimers, *J. Electrochem. Soc.*, **152**, A882 (2005) doi: 10.1149/1.1872737.

240. M. Li and J. Lu, *Science (80-.).*, **367**, 979–980 (2020) doi: 10.1126/science.aba9168.

241. T. Liu, L. Yu, J. Liu, J. Lu, X. Bi, A. Dai, M. Li, M. Li, Z. Hu, L. Ma, D. Luo, J. Zheng, T. Wu, Y. Ren, J. Wen, F. Pan, and K. Amine, *Nat. Energy*, **6**, 277–286 (2021) doi: 10.1038/s41560-021-00776-y.

242. Shanghai Metals Markets, https://www.metal.com/.

243. J. R. Dahn, J. C. Burns, and D. A. Stevens, *Electrochem. Soc. Interface*, **25**, 75–78 (2016) doi: 10.1149/2.F07163if.

244. Y. Liu, J. Harlow, and J. Dahn, *J. Electrochem. Soc.*, **167**, 020512 (2020) doi: 10.1149/1945-7111/ab6288.

245. M. Stich, M. Göttlinger, M. Kurniawan, U. Schmidt, and A. Bund, *J. Phys. Chem. C*, **122**, 8836–8842 (2018) doi: 10.1021/acs.jpcc.8b02080.

246. M. Liu, J. Vatamanu, X. Chen, L. Xing, K. Xu, and W. Li, *ACS Energy Lett.*, **6**, 2096–2102 (2021) doi: 10.1021/acsenergylett.1c00707.

247. T. Boulanger, A. Eldesoky, S. Buechele, T. Taskovic, S. Azam, C. Aiken, E. Logan, and M. Metzger, *J. Electrochem. Soc.*, **169**, 040518 (2022) doi: 10.1149/1945-7111/ac62c6.

248. T. Taskovic, A. Eldesoky, C. P. Aiken, and J. R. Dahn, *J. Electrochem. Soc.*, **169**, 100547 (2022) doi: 10.1149/1945-7111/ac9a81.

249. O. C. Harris, S. E. Lee, C. Lees, and M. Tang, *J. Phys. Energy*, **2**, 032002 (2020) doi: 10.1088/2515-7655/AB8B68.

250. C. Y. Jhu, Y. W. Wang, C. Y. Wen, and C. M. Shu, *Appl. Energy*, **100**, 127–131 (2012) doi: 10.1016/J.APENERGY.2012.05.064.

251. S. Jaffe, *Joule*, **1**, 225–228 (2017) doi: 10.1016/J.JOULE.2017.09.021.

252. Z. Lu, D. D. MacNeil, and J. R. Dahn, *Electrochem. Solid-State Lett.*, **4**, A191 (2001) doi: 10.1149/1.1407994.

253. D. J. Miller, C. Proff, J. G. Wen, D. P. Abraham, and J. Bareño, *Adv. Energy Mater.*, **3**, 1098–1103 (2013) doi: 10.1002/AENM.201300015.

254. X. Zhu, Y. Chen, H. Chen, and W. Luan, *Int. J. Mech. Sci.*, **178**, 105608 (2020) doi: 10.1016/J.IJMECSCI.2020.105608.

255. P. Yan, J. Zheng, M. Gu, J. Xiao, J.-G. Zhang, and C.-M. Wang, *Nat. Commun. 2017 81*, **8**, 1–9 (2017) doi: 10.1038/ncomms14101.

256. J. N. Reimers and J. R. Dahn, *J. Electrochem. Soc.*, **139**, 2091 (1992) doi: 10.1149/1.2221184.

257. R. Jung, M. Metzger, F. Maglia, C. Stinner, and H. A. Gasteiger, *J. Electrochem. Soc.*, **164**, A1361 (2017) doi: 10.1149/2.0021707JES.

258. R. Jung, M. Metzger, F. Maglia, C. Stinner, and H. A. Gasteiger, *J. Phys. Chem. Lett.*, **8**, 4820–4825 (2017) doi: 10.1021/ACS.JPCLETT.7B01927.

259. Yirui Zhang, Yu Katayama, Ryoichi Tatara, Livia Giordano, Yang Yu, Dimitrios Fraggedakis, J. Guangwen Sun, Filippo Maglia, Roland Jung, M. Z. Bazant, and Yang Shao-Horn, *Energy Environ. Sci.*, **13**, 183–199 (2020) doi: 10.1039/C9EE02543J.

260. A. T. S. Freiberg, J. Sicklinger, S. Solchenbach, and H. A. Gasteiger, *Electrochim. Acta*, **346**, 136271 (2020) doi: 10.1016/j.electacta.2020.136271.

261. V. L. Chevrier, L. J. Krause, L. D. Jensen, C. Huynh, M. Triemert, E. L. Bowen, and J. Thorson, *J. Electrochem. Soc.*, **165**, A2968–A2977 (2018) doi: 10.1149/2.0351813jes.

262. D. J. Xiong, L. D. Ellis, R. Petibon, T. Hynes, Q. Q. Liu, and J. R. Dahn, *J. Electrochem. Soc.*, **164**, A340–A347 (2017) doi: 10.1149/2.1091702jes.

263. C. Martin, M. Genovese, A. J. Louli, R. Weber, and J. R. Dahn, *Joule*, **4**, 1296–1310 (2020) doi: 10.1016/J.JOULE.2020.04.003.

264. B. Gyenes, D. A. Stevens, V. L. Chevrier, and J. R. Dahn, *J. Electrochem. Soc.*, **162**, A278–A283 (2015) doi: 10.1149/2.0191503jes.

265. H. Zhou, F. Xin, B. Pei, and M. S. Whittingham, *ACS Energy Lett.*, **4**, 1902–1906 (2019) doi: 10.1021/acsenergylett.9b01236.

266. A. Guéguen, L. Castro, R. Dedryvère, E. Dumont, J. Bréger, C. Tessier, and D. Gonbeau, *J. Electrochem. Soc.*, **160**, A387 (2012) doi: 10.1149/2.019303JES.

267. S. J. Kang, K. Park, S. H. Park, and H. Lee, *Electrochim. Acta*, **259**, 949–954 (2018) doi: 10.1016/j.electacta.2017.11.018.

268. S. Buechele, A. Adamson, A. Eldesoky, T. Boetticher, L. Hartmann, T. Boulanger, S. Azam, M. B. Johnson, T. Taskovic, E. Logan, and M. Metzger, *J. Electrochem. Soc.*, **170**, 010511 (2023) doi: 10.1149/1945-7111/acaf44.

269. J. Zhang, I. A. Shkrob, R. S. Assary, S. Zhang, B. Hu, C. Liao, Z. Zhang, and L. Zhang, *J. Power Sources*, **378**, 264–267 (2018) doi: 10.1016/j.jpowsour.2017.12.059.

270. W. Song, J. Harlow, E. Logan, H. Hebecker, M. Coon, L. Molino, M. Johnson, J. Dahn, and M. Metzger, *J. Electrochem. Soc.*, **168**, 090503 (2021) doi: 10.1149/1945-7111/ac1e55.

271. Z. Deng, Z. Huang, Y. Shen, Y. Huang, H. Ding, A. Luscombe, M. Johnson, J. E. Harlow, R. Gauthier, and J. R. Dahn, *Joule*, **4**, 2017–2029 (2020) doi: 10.1016/j.joule.2020.07.014.

272. E. Goikolea, V. Palomares, S. Wang, I. R. de Larramendi, X. Guo, G. Wang, and T. Rojo, *Adv. Energy Mater.*, **10**, 2002055 (2020) doi: 10.1002/aenm.202002055.

273. K. Kubota, M. Dahbi, T. Hosaka, S. Kumakura, and S. Komaba, *Chem. Rec.*, **18**, 459–479 (2018) doi: 10.1002/tcr.201700057.

274. M. H. Choo, C. C. Nguyen, S. Hong, Y. H. Kwon, S. W. Woo, J. Y. Kim, and S. W. Song, *Electrochim. Acta*, **112**, 252–257 (2013) doi: 10.1016/j.electacta.2013.08.121.

275. G. Li, H. Azuma, and M. Tohda, *Electrochem. Solid-State Lett.*, **5**, A135 (2002) doi: 10.1149/1.1475195.

276. B. K. Park, Y. K. Jeong, S. Y. Yang, S. Kwon, J. H. Yang, Y. M. Kim, and K. J. Kim, *J. Power Sources*, **506**, 230222 (2021) doi: 10.1016/j.jpowsour.2021.230222.

277. X. Wu and Z. Du, *Electrochem. commun.*, **129**, 107088 (2021) doi: 10.1016/j.elecom.2021.107088.

APPENDIX A CELL DETAILS

Table A.1. Build specifications of pouch cells used in this thesis. *Includes thickness of carbon coating. **Based on requested specifications, not measured/received specifications.

Positive Electrode

Active Material	Zhenhua BDA5000 NMC532	Zhenhua E6000 NMC640	Pulead LFP	Zhenhua BDA5000 NMC532	XTC M83B + M83E200 NMC811 (Ni83)	90 wt.% Pulead LFP + 10 wt.% Zhenhua E6000 NMC640
Area (cm^2)	66.8	56.2	123.8	86.6		85.5
Coating Thickness (um)	61	64	55	47	64**	69
Loading (mg/cm^2)	19.3	20.0	12.3	15.8	21**	17.8
Foil Thickness (um)	13	13	26*	13	13	26*
Separator Thickness (um)	15	15	15	15	15	15

Negative Electrode

|						
Active Material	Kaijin AML400 graphite	Kaijin AML400 graphite	Kaijin AML400 graphite	Kaijin AML400 graphite	Zichen F1-Z graphite	Novonix GX-23 graphite
Area (cm^2)	78.7	66.9	142.0	99.4		99.4
Coating Thickness (um)	84	97	48	36	76**	63
Loading (mg/cm^2)	12.4	13.9	6.6	5.1	11.8**	8.7
Foil Thickness (um)	8	8	8	8	8	8
Cell Balance (V)	4.40	4.50	3.65	3.80	4.06	3.80
Capacity at C/3 (mAh)	240	225	210	130	220	210
Average Discharge Voltage at C/3 (V)	3.75	3.80	3.23	3.59	3.65	3.27
Chapter in this Thesis	4	5	6,7	6,7	7	7

APPENDIX B EXTRA FIGURES
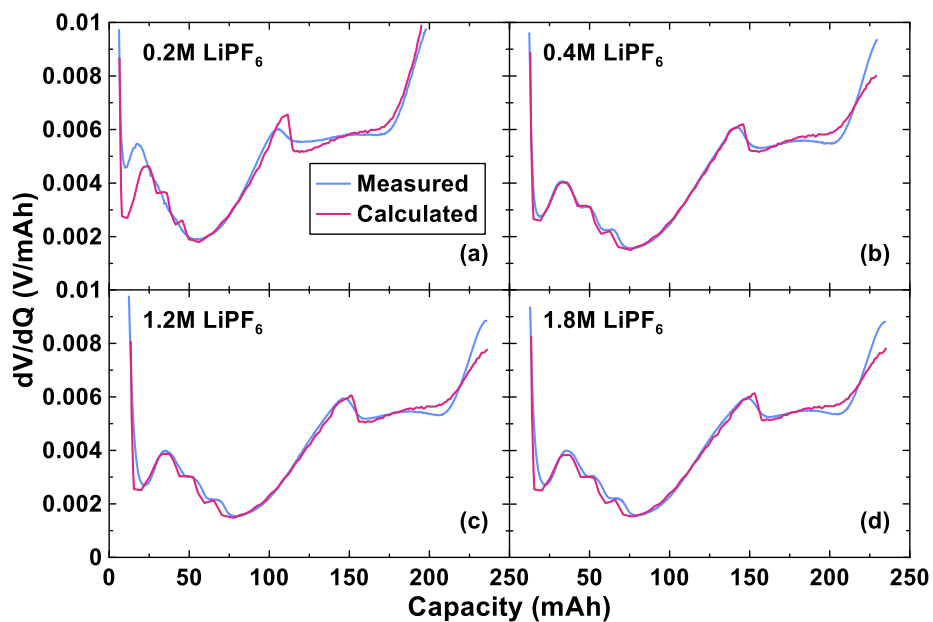
Figure B.1 Measured and calculated differential voltage curves for Li[Ni$_{0.5}$Mn$_{0.3}$Co$_{0.2}$]O$_2$/graphite cells containing 2% FEC + 1% DTD. Cells contained electrolytes with either (a) 0.2M LiPF$_6$, (b) 0.4M LiPF$_6$, (c) 1.2M LiPF$_6$, (d) 1.8M LiPF$_6$. Fitting parameters are reported in Figure 4.11.
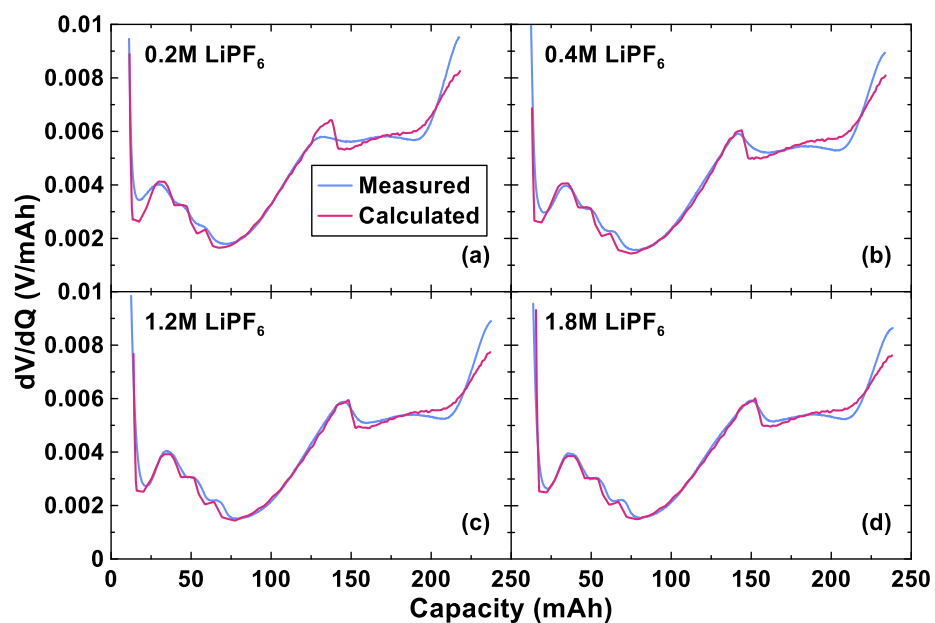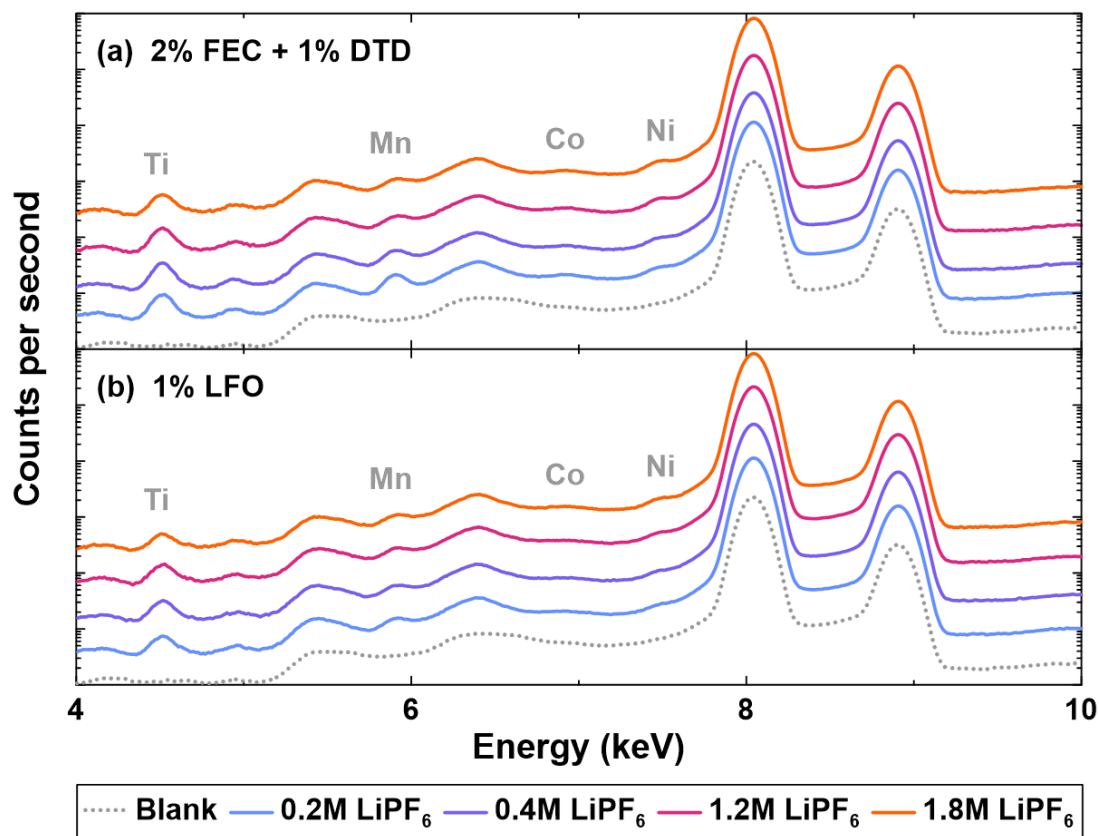
Figure B.2. Measured and calculated differential voltage curves for Li[$Ni_{0.5}Mn_{0.3}Co_{0.2}$]O_2/graphite cells containing 1% LFO. Cells contained electrolytes with either (a) 0.2M $LiPF_6$, (b) 0.4M $LiPF_6$, (c) 1.2M $LiPF_6$, (d) 1.8M $LiPF_6$. Fitting parameters are reported in Figure 4.11.

Figure B.3. X-ray fluorescence spectra from which results in Figure 4.12, for cycled cells, were obtained. Measurements were performed on Li[Ni$_{0.5}$Mn$_{0.3}$Co$_{0.2}$]O$_2$/graphite pouch cells after approximately 40 cycles. Cells contained electrolytes with one of four LiPF$_6$ concentrations and either (a) 2% FEC + 1% DTD or (b) 1% LFO electrolyte additives. The XRF energy of coating and bulk active material metals of note are labelled. The large features at 8.0 keV and 8.9 keV are the Cu K$_\alpha$ and K$_\beta$ signals respectively, from the substrate (or current collector). Spectra are offset vertically for clarity.
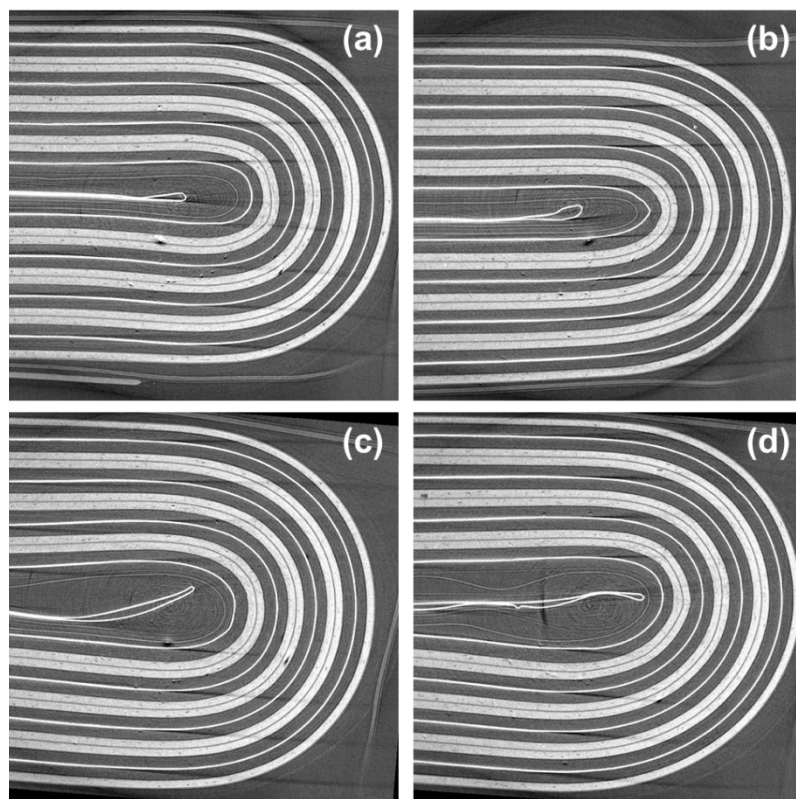
Figure B.4. Synchrotron X-ray tomography images from which thickness measurements in Figure 4.13 were obtained. Imaging was performed on Li[Ni$_{0.5}$Mn$_{0.3}$Co$_{0.2}$]O$_2$/graphite pouch cells after approximately 40 cycles. Due to beamline availability constraints, only cells with (a,b) 0.2M or (c,d) 1.8M LiPF$_6$ were measured. Cells contained either (a,c) 2% FEC + 1% DTD or (b,d) 1% LFO electrolyte additives.
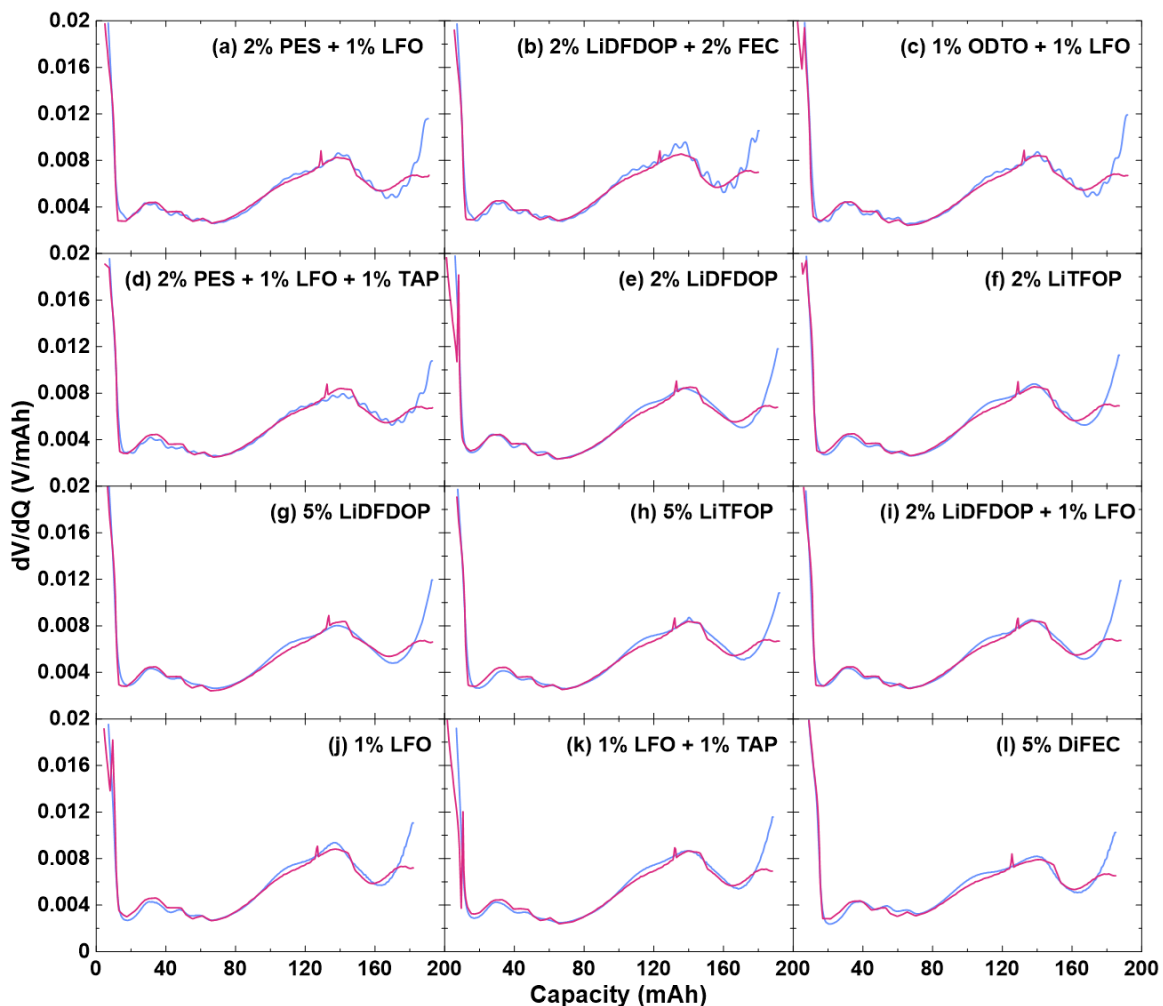
Figure B.5. Differential voltage analysis fits based on UHPC measurements conducted at C/40 at 40°C, with charging to 4.4 V on NMC640 cells after reaching end-of-life. Cells were tested with CCCV cycling methods prior to UHPC measurement, with charging to 4.4 V at 40°C at a C/3 rate. Data (blue) and fits (pink) are shown for each panel. Electrolyte additive formulation indicated in text labels. Representative fitting in more detail is shown in Figure 5.7 and a summary of one fit parameter, positive electrode mass loss, is shown in Figure 5.8a.
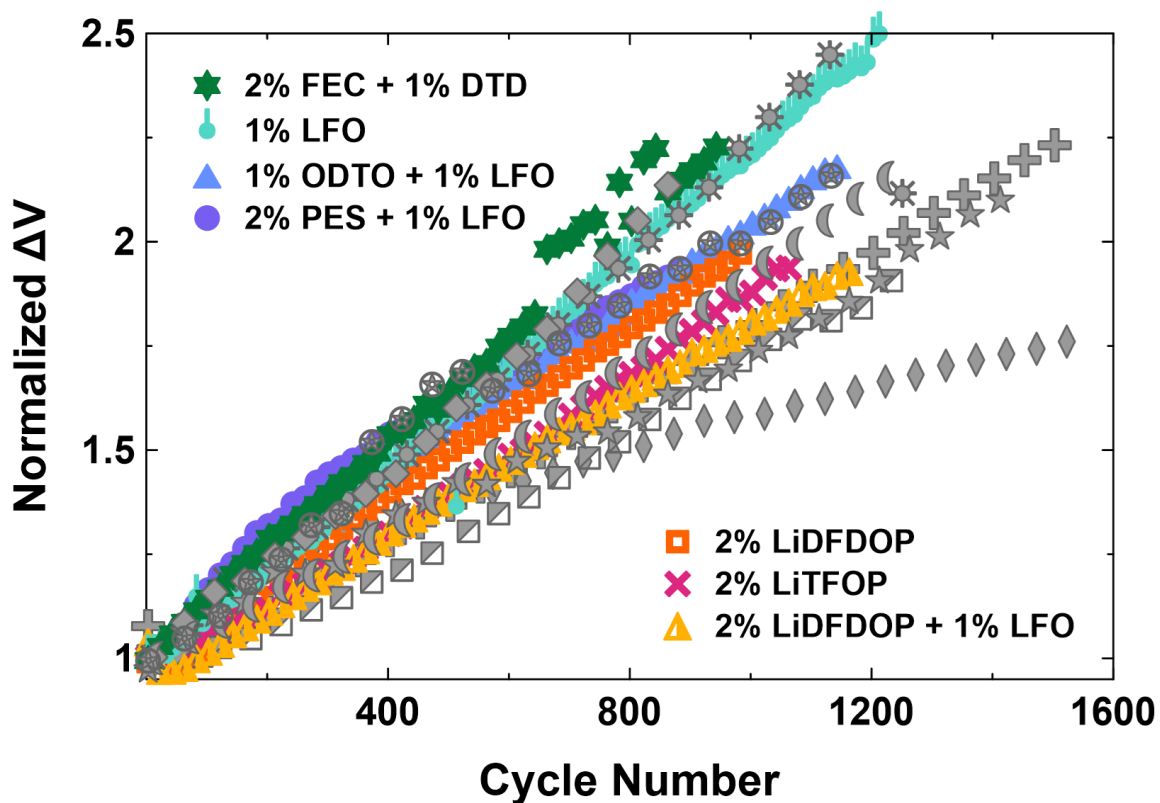
Figure B.6. Normalized or fractional ΔV versus cycle number measured during long-term electrochemical cycling for NMC640 cells subjected to CCCV test methods. Cells were charged to 4.4 V during cycling conducted at 40°C at a C/3 rate. Data shown here is used in the calculation of quantities in Figure 5.8c. Due to the high number of data series most data are identically colored grey to avoid unnecessary visual clutter. Select symbols are colored to match those in Figure 5.6. For the interested reader curious as to which additive formulation corresponds to the "best" results, the grey diamonds that track the lowest are from a cell containing 2% PES + 1% LFO + 1% TAP.
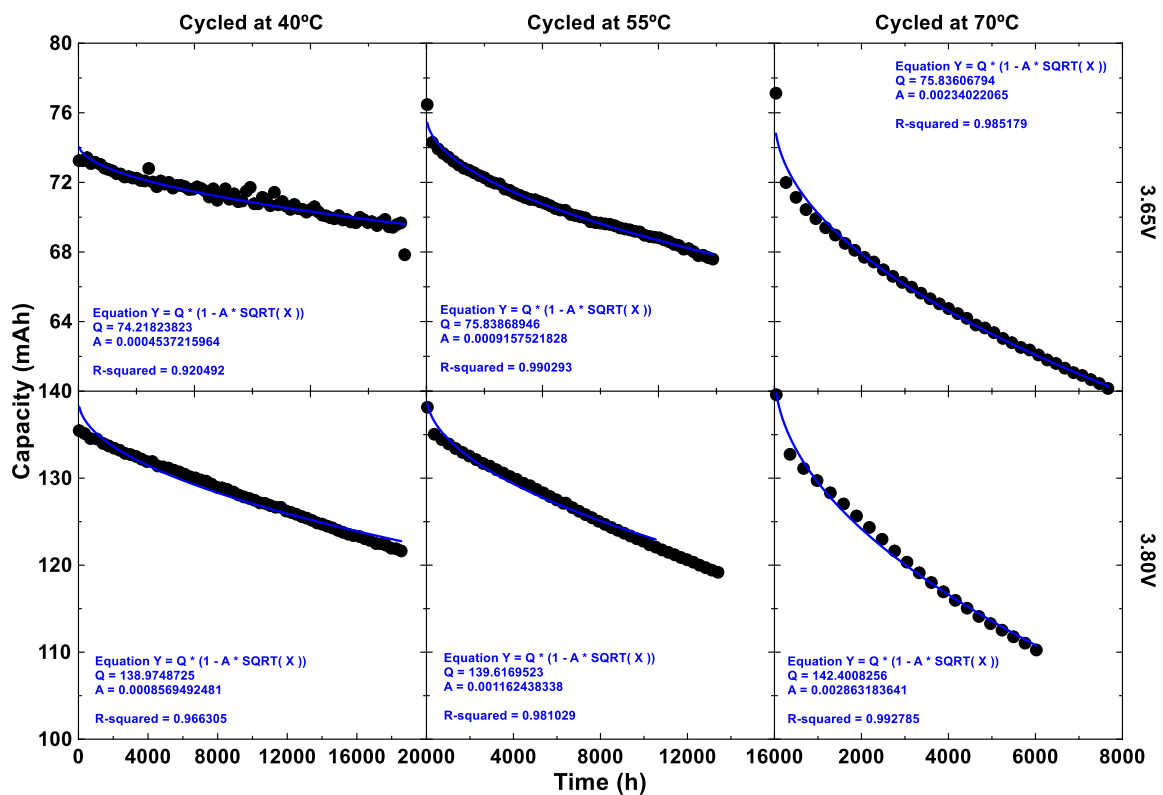
Figure B.7. Discharge capacity of C/20 cycles versus time, obtained from Figure 7.8, for low voltage Li[Ni$_{0.5}$Mn$_{0.3}$Co$_{0.2}$]O$_2$//graphite (NMC) cells, containing LiPF$_6$ electrolyte, cycled at a), d) 40°C, b), e) 55°C and e), f) 70°C. Cells were charged to either a), b), c) 3.65 V or d), e), f) 3.80 V. Also shown is the fit of a simple capacity loss model which follows a parabolic growth law: Q/Q$_0$ = 1 – At^{½}.
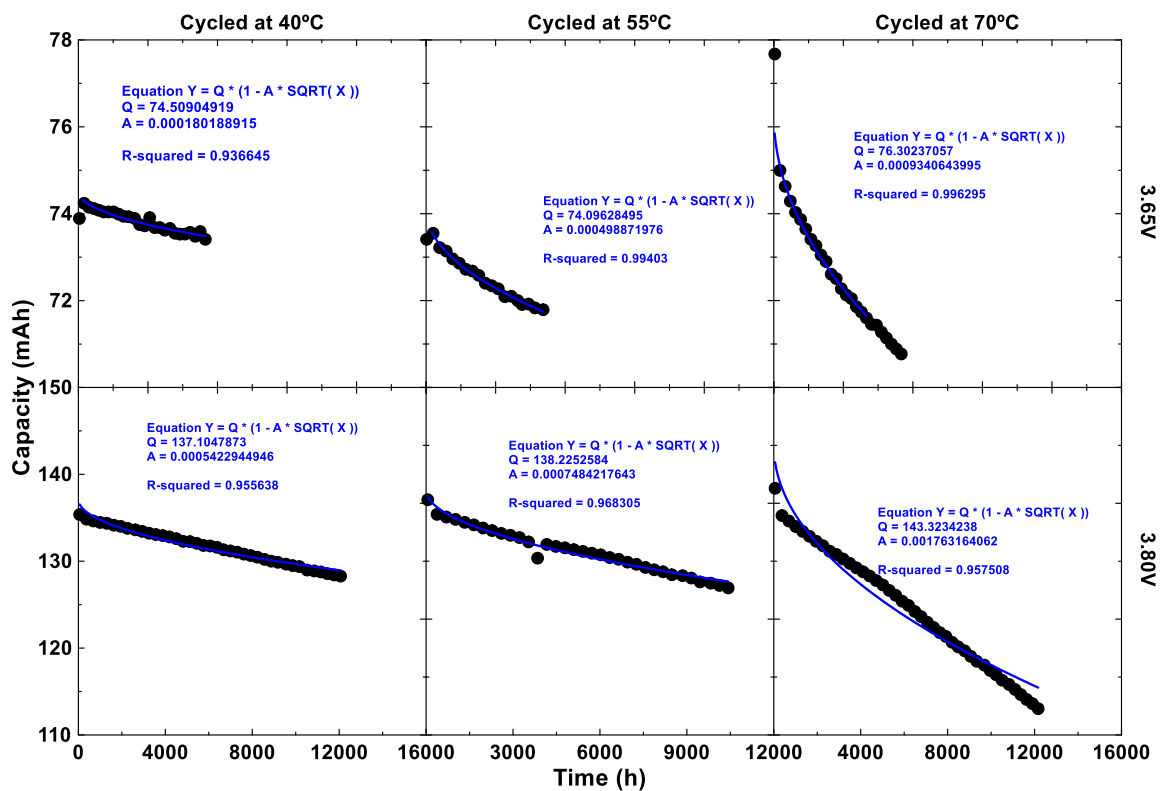
Figure B.8. Discharge capacity of C/20 cycles versus time, obtained from Figure 7.8, for low voltage Li[Ni$_{0.5}$Mn$_{0.3}$Co$_{0.2}$]O$_2$//graphite (NMC) cells, containing LiFSI electrolyte, cycled at a), d) 40°C, b), e) 55°C and e), f) 70°C. Cells were charged to either a), b), c) 3.65 V or d), e), f) 3.80 V. Also shown is the fit of a simple capacity loss model which follows a parabolic growth law: $Q/Q_0 = 1 - At^{1/2}$.
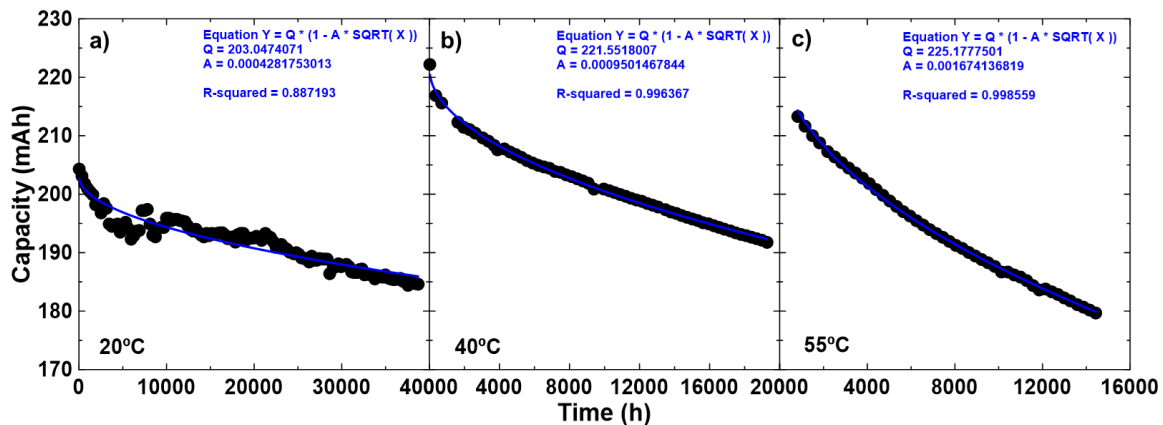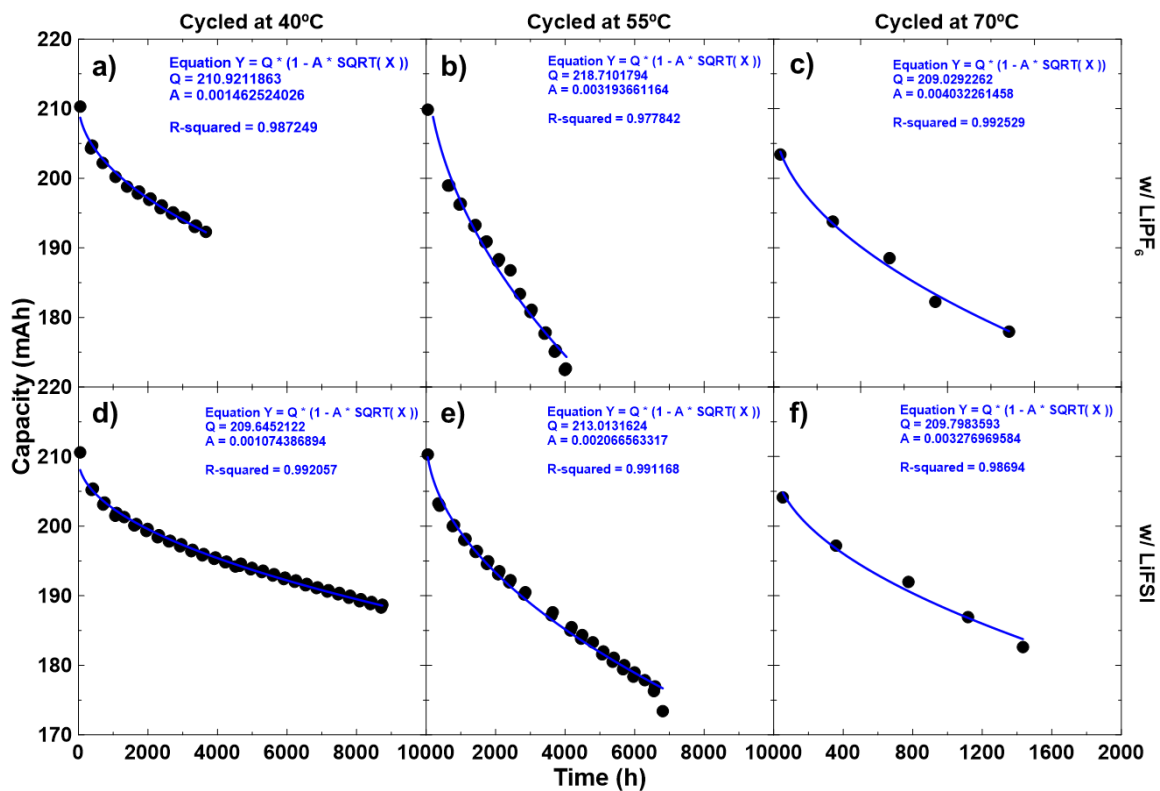
Figure B.9. Figure S4. Discharge capacity of C/20 cycles versus time, obtained from Figure 7.8, for conventional Li[Ni$_{0.5}$Mn$_{0.3}$Co$_{0.2}$]O$_2$//graphite (NMC) cells, operated to 4.20V, containing LiPF$_6$ electrolyte, cycled at a), d) 40°C, b), e) 55°C and e), f) 70°C. Also shown is the fit of a simple capacity loss model which follows a parabolic growth law: Q/Q$_0$ = 1 – At^{½}.

Figure B.10. Discharge capacity of C/20 cycles versus time, obtained from Figure 7.8, for LiFePO$_4$//graphite (LFP) cells, containing LiPF$_6$ and LiFSI electrolyte, cycled at a), d) 40°C, b), e) 55°C and e), f) 70°C. Cells contained either a), b), c) LiPF$_6$ or d), e), f) LiFSI electrolyte. Also shown is the fit of a simple capacity loss model which follows a parabolic growth law: $Q/Q_0 = 1 - At^{1/2}$.